

***Progress Report on the Development
of a Geologic Framework Model
Capability to Support GDSA***

Fuel Cycle Research & Development

Prepared for
US Department of Energy
Spent Fuel and Waste Disposition
Milestone M4SF-19LA010304021

M. Gross
G. Bussod
C.W. Gable
R. Kelley
A. Lavadie-Bulnes
D. Milazzo
E. Miller
T.A. Miller
R. Roback
P.H. Stauffer
E. Swanson

Los Alamos National Laboratory

F. Perry
Sandia National Laboratory

August 8, 2019

Los Alamos National Laboratory Document LA-UR-19-27943



DISCLAIMER

This information was prepared as an account of work sponsored by an agency of the U.S. Government. Neither the U.S. Government nor any agency thereof, nor any of their employees, makes any warranty, expressed or implied, or assumes any legal liability or responsibility for the accuracy, completeness, or usefulness, of any information, apparatus, product, or process disclosed, or represents that its use would not infringe privately owned rights. References herein to any specific commercial product, process, or service by trade name, trade mark, manufacturer, or otherwise, does not necessarily constitute or imply its endorsement, recommendation, or favoring by the U.S. Government or any agency thereof. The views and opinions of authors expressed herein do not necessarily state or reflect those of the U.S. Government or any agency thereof.

APPENDIX E
NTRD DOCUMENT COVER SHEET ¹

Name/Title of Deliverable/Milestone/Revision No. M4SF-19LA010304021-Progress report on development of geologic framework model capability to support GDSA

Work Package Title and Number SF-19LA01030402 GDSA-Geologic Modeling-LANL

Work Package WBS Number 1.08.01.03.04

Responsible Work Package Manager Michael Gross
(Name/Signature)

Date Submitted

Quality Rigor Level for Deliverable/Milestone ²	<input type="checkbox"/> QRL-1 <input type="checkbox"/> Nuclear Data	<input type="checkbox"/> QRL-2	<input type="checkbox"/> QRL-3	<input checked="" type="checkbox"/> QRL 4 Lab QA Program ³
--	---	--------------------------------	--------------------------------	--

This deliverable was prepared in accordance with Michael Gross, Los Alamos National Laboratory
(Participant/National Laboratory Name)

QA program which meets the requirements of
 DOE Order 414.1 NQA-1 Other

This Deliverable was subjected to:

Technical Review

Technical Review (TR)

Review Documentation Provided

- Signed TR Report or,
- Signed TR Concurrence Sheet or,
- Signature of TR Reviewer(s)

below **Name and Signature of Reviewers**


Peer Review

Peer Review (PR)

Review Documentation Provided

- Signed PR Report or,
- Signed PR Concurrence Sheet or,
- Signature of PR Reviewer(s) below

Name and Signature of Reviewers

Kirsten Sauer 

NOTE 1: Appendix E should be filled out and submitted with each deliverable. Or, if the PICS: NE system permits, completely enter all applicable information in the PICS: NE Deliverable Form. The requirement is to ensure that all applicable information is entered either in the PICS: NE system or by using the NTRD Document Cover Sheet.

- In some cases there may be a milestone where an item is being fabricated, maintenance is being performed on a facility, or a document is being issued through a formal document control process where it specifically calls out a formal review of the document. In these cases, documentation (e.g., inspection report, maintenance request, work planning package documentation or the documented review of the issued document through the document control process) of the completion of the activity, along with the Document Cover Sheet, is sufficient to demonstrate achieving the milestone.

NOTE 2: If QRL 1, 2, or 3 is not assigned, then the QRL 4 box must be checked, and the work is understood to be performed using laboratory QA requirements. This includes any deliverable developed in conformance with the respective National Laboratory / Participant, DOE or NNSA-approved QA Program.

NOTE 3: If the lab has an NQA-1 program and the work to be conducted requires an NQA-1 program, then the QRL-1 box must be checked in the work Package and on the Appendix E cover sheet and the work must be performed in accordance with the Lab's NQA-1 program. The QRL-4 box should not be checked.

Table of Contents

List of Figures	vii
List of Tables	xiii
List of Acronyms	1
1 Introduction	2
2 Alluvial Basins in the Basin and Range Province.....	5
2.1 Tectonics and Structure	5
2.2 Stratigraphy and Lithologies	6
3 Mimbres Basin as a Generic Case Study	10
3.1 Overview of the Mimbres Basin	10
3.2 Geology, Structure and Geophysics of the Mimbres Basin	12
3.3 Alluvial Sediments of the Mimbres Basin: Lithologies and Thickness.....	19
3.3.1 Stratigraphy and Lithofacies of Basin-fill Sediments	19
3.4 Thickness and Distribution of Basin-fill Sediments	21
3.5 Hydrology of the Mimbres Basin	24
4 Geo-Database Compilation	27
4.1 Imported Maps and Data for the Mimbres Basin	27
4.2 Defining the Area of Interest (AOI)	31
4.3 Water Table Surface.....	32
4.4 Top of Precambrian Surface	34
4.5 Alluvium Thickness and Base of Alluvium Surface	35
4.6 3D Visualization of Surfaces	40
5 Subsurface Characterization for GFM Input.....	41
5.1 Structural Characterization of Bedrock.....	41
5.1.1 Overview	41
5.1.2 Interpretation of Seismic Refraction Lines	44
5.1.3 Construction of Structural Cross-Sections	48
5.1.4 Fault network for the structural GFM	59
5.1.5 Exporting data to JewelSuite GFM	61
5.2 Development of the Mimbres Alluvial GFM	62
5.2.1 Overview	62
5.2.2 Climate Variation from Miocene to Present	62
5.2.3 Alluvial Sedimentation and Lithostratigraphy.....	62

5.2.4	Stratigraphy of the Santa Maria DB R&R Well	63
5.2.5	Conceptual Model of the Alluvial Deming Sub-basin	68
6	The Geologic Framework Model (GFM).....	74
6.1	Overview.....	74
6.2	Data Import and Model Boundaries	74
6.3	Surfaces	76
6.4	Volumes.....	80
6.5	GFM Assessment.....	84
7	The Hydrologic Framework Model (HFM).....	86
7.1	Porosity.....	86
7.2	Permeability.....	87
7.2.1	Grain Size	87
7.2.2	Cementation	88
7.2.3	Depth of Burial	88
7.2.4	Faults and Fractures	88
7.2.5	Permeabilities in study area basin	88
7.3	Saturation	92
7.4	Sorption Properties	92
7.5	Unsaturated Hydraulic Properties	93
7.6	Hydraulic Gradient	94
8	Meshing Workflow for Alluvial Basin Case.....	96
8.1	Cube Test 1: Horizontal Layers	98
8.1.1	JewelSuite GFM exports for Meshing Workflow.....	99
8.1.2	Mesh Generation.....	99
8.1.3	Computational Mesh and Model Setup Files.....	100
8.2	Cube Test 2: Wedge	101
8.2.1	JewelSuite GFM exports for Meshing Workflow.....	101
8.2.2	Mesh Generation.....	101
8.2.3	Computational Mesh and Model Setup Files.....	103
8.3	Cube Test 3: Lens	104
8.3.1	JewelSuite GFM exports for Meshing Workflow.....	104
8.3.2	Mesh Generation.....	105
8.3.3	Computational Mesh and Model Setup Files.....	106

8.4	Cube Test 4: Fault	107
8.4.1	JewelSuite GFM exports for Meshing Workflow.....	107
8.4.2	Mesh Generation.....	107
8.4.3	Computational Mesh and Model Setup Files.....	109
9	FEHM Verification of Mesh and Model Setup.....	111
9.1	Test Case 1 – Horizontal Layers	113
9.1.1	Scenario 1.1.....	113
9.1.2	Scenario 1.2.....	114
9.1.3	Scenario 1.3.....	116
9.1.4	Scenario 1.4.....	117
9.2	Test Case 2 – Wedge	118
9.2.1	Scenario 2.1.....	118
9.2.2	Scenario 2.2.....	119
9.2.3	Scenario 2.3.....	121
9.2.4	Scenario 2.4.....	121
9.3	Test Case 3 – Lens	122
9.3.1	Scenario 3.1.....	122
9.3.2	Scenario 3.2.....	123
9.3.3	Scenario 3.3.....	124
9.3.4	Scenario 3.4.....	125
9.4	Test Case 4 – Fault	126
9.4.1	Scenario 4.1.....	126
9.4.2	Scenario 4.2.....	128
9.4.3	Scenario 4.3.....	129
9.4.4	Scenario 4.4.....	130
9.5	Diagnostic output data.....	131
9.6	Conclusions.....	132
10	References.....	134
11	Appendix 1 – Geological Time Scale	144
12	Appendix 2 – File Format for Exporting Data from Structural Cross-Sections to JewelSuite.....	145

List of Figures

Figure 1-1 Flowchart for a Geological Disposal Safety Assessment of a generic alluvial basin. The process is iterative at all steps.	4
Figure 1-2 Conceptual model for a generic alluvial basin in the Basin and Range province. Note that slip on the basin-bounding fault provides the accommodation space for a thick accumulation of alluvium (brown colors) of varying lithologies and depositional environments.	4
Figure 2-1. A. Map of the Basin and Range province (stippled pattern) in western North America and its relation to other tectonic elements. From Parsons (2006). B. Digital elevation model showing the geomorphology of the Basin and Range dominated by linear ridges and valleys (source: USGS).....	5
Figure 2-2 Schematic diagram showing groundwater flow in alluvial aquifers of the Basin and Range province (from Sweetkind et al, 2010a). Note thick accumulations of alluvial sediments in the tilted hanging wall blocks. FW=footwall, HW=hanging wall.	6
Figure 2-3 Hydrogeologic units for Basin and Range alluvial aquifers proposed by Anderson (1995).	8
Figure 2-4 Model of alluvial depositional facies within (A) continental half graben and (B) continental full graben, from Mack and Stout (2005).....	9
Figure 2-5 Generalized representation of stratigraphy and permeabilities for an alluvium-filled basin (from Perry et al., 2018). UZ=unsaturated zone, SZ=saturated zone.	10
Figure 3-1 Location of the Mimbres Basin among the alluvial basins of the greater Basin and Range Province.....	11
Figure 3-2 Sub-basins and mountain ranges in the Mimbres Basin (from Heywood, 2002). CP=Colorado Plateau, BR=Basin and Range, RG=Rio Grande Rift.	12
Figure 3-3 Stratigraphy of the southern Florida Mountains, an uplifted block bordering the Deming sub-basin to the east (from Brown and Clemons, 1983).	13
Figure 3-4 Timing of middle and late Cenozoic block faulting and volcanism in southwestern New Mexico as summarized from various sources by Mack (2004). The Mimbres Basin falls within the Basin and Range province (red box).	14
Figure 3-5 Portion of the Geologic Map of New Mexico (1:500,000) with outlines of the Mimbres Basin (blue line), focused area of interest (black box) and major faults (red). Arrows point to Treasure Mountain fault (TMF) and West Florida Mountain fault (WFMF).	16
Figure 3-6 Geologic cross section from Mimbres Basin showing development of alluvial basins in the hanging wall blocks of range-bounding normal faults (Seager, 1995). Note basin geometries and offset of Tertiary volcanics (Tv) as well as Bouguer gravity plot above.	17
Figure 3-7 Seismic refraction surveys conducted by the USGS and their interpretations (Ackermann et al, 1994; Klein et al, 1995). (a) Location of the 6 refraction lines; (b) Velocity interpretation of Line 4 (10x vertical exaggeration); (c) Identification of faults, top to basement and alluvium thickness on portion of Line 4 crossing the Mimbres Basin (10x vertical exaggeration); (d) Our interpretation of seismic line 4 with no vertical exaggeration.....	18
Figure 3-8 Correlation chart of middle and late Cenozoic basin fill sediments and associated volcanic rocks in southwestern New Mexico (From Mack, 2004). Ages in parentheses are in millions of years. Note especially the section for "Cedar, Florida, Tres Hermanas Mountains" which corresponds to the Mimbres Basin.....	20

Figure 3-9 Main lithostratigraphic and hydrostratigraphic units proposed by Kennedy et al. (2000) for Neogene and Quaternary basin-fill sediments in southwestern New Mexico.....	20
Figure 3-10 A small portion of Plate 1 from Hawley et al. (2000) depicting surface geology and hydrostratigraphic units of southwestern New Mexico focusing on the Deming sub-basin (our AOI for the GFM) and the Florida Mountains. Note the detailed mapping of the surficial alluvial deposits. Refer to Figure 3-5 for geologic context.	21
Figure 3-11 Maps of alluvial sediment thickness for the Mimbres Basin of southwestern New Mexico. (A) Geographic sectors of constant alluvium thickness (estimates) in feet from Hanson et al. (1994); (B) Gravity measurement points and contoured map of isostatic residual gravity used to calculate alluvium thickness (Heywood, 2002); (C) Contoured map of alluvium thickness in meters calculated from isostatic residual gravity map (Heywood, 2002); (D) Alluvium thickness map contoured in feet compiled from a variety of sources (Finch et al, 2008).	23
Figure 3-12 (A) Conceptual hydrogeological models for intermontane basins, including undrained, partly drained and drained basins. From Kennedy et al. (2000) modified from Eakin et al. (1976); (B) The four hydrogeological zones for the Mimbres Basin proposed by Finch et al. (2008).	25
Figure 3-13 Differences in depth to ground water table between 1950-1959 and 2000-2009 for the Mimbres Basin. Kriging interpolations are shown in 10 ft contour intervals; areas of bedrock are dark gray. From Rhinehart et al. (2015).	26
Figure 4-1 Geologic map for Mimbres Basin. This is a portion of the Geologic Map of New Mexico, from the New Mexico Bureau of Geology and Mineral Resources in cooperation with the U.S. Geological Survey (scale: 1:500,000).	28
Figure 4-2 Digital elevation model (DEM) of surface elevation with fault traces in red.	29
Figure 4-3 Map of water wells (blue dots) and deep boreholes (red dots) drilled in the Mimbres Basin and surrounding areas. The shallow water wells are used to map the depth to water table surface and the deep boreholes provide limited information about the pre-alluvium bedrock geology.	30
Figure 4-4 The area of interest (AOI) selected for detailed analysis within the Mimbres Basin (black rectangle 50 x 70 km surrounded by 10 km buffer).	31
Figure 4-5 Map showing water table elevation in the AOI. We used the original water table depth recorded prior to pumping. Note the general regional groundwater flow from north (highlands) to south (basin floors).	33
Figure 4-6 Map of top to Precambrian surface for the Mimbres Basin, using data from deep exploratory boreholes.....	34
Figure 4-7 Structure map of top of Precambrian surface for the state of New Mexico from Broadhead et al. (2009). Note lack of contours in the Mimbres Basin (blue box) due to scarcity of data.	35
Figure 4-8 Map showing distinction between alluvial sediments (beige) and bedrock outcroppings (blue) for the AOI and adjacent areas.....	36
Figure 4-9 Procedures for generating alluvium thickness map for the Mimbres Basin. (A) Georeferenced map of alluvial sediment thickness from Finch et al. (2008) with thickness contours (purple) digitized in ArcPro. (B) Digitized contours of alluvium thickness (white) superimposed on isostatic residual gravity map of Heywood (2002) showing very close agreement. Gravity lows (purple-blue) correspond to thick alluvium whereas gravity highs (yellow-red) correspond to uplifted basement blocks, i.e., thin or no alluvium.	37
Figure 4-10 Map of alluvium thickness for the Mimbres Basin derived from digitizing the contour map of Finch et al. (2008).	38

Figure 4-11 Map of depth to base of alluvium created by subtracting the alluvium thickness from surface elevation.....	39
Figure 4-12 Three-dimensional visualization of the ground surface, water table, base of alluvium and top of Precambrian.	40
Figure 5-1 Map of Mimbres Basin AOI (solid black rectangle), GFM boundaries (dashed rectangle) and surrounding area showing locations of deep boreholes (yellow dots), shot points of seismic refraction surveys (green dots), main faults (red lines) and contours of alluvium thickness (blue) derived from gravity. Structural cross-section lines are numbered 1-6.	43
Figure 5-2 Ranges of seismic velocities and their inferred lithologies used by Klein et al. (1995) to build 2D velocity models for the seismic refraction surveys conducted in southwestern New Mexico.	44
Figure 5-3 Seismic velocity profile for survey line 7 from Klein et al. (1995). Velocities are in km/s and the profile as a 10x vertical exaggeration.	46
Figure 5-4 Structural interpretations for the three seismic refraction lines that cross the Mimbres Basin, based on velocity sections from Ackermann et al. (1994) and Klein et al. (1995). Shot point locations are presented in Figure 5-1.	47
Figure 5-5 Close-up map of the GFM area (dashed rectangle) with the six structural cross section lines (blue) and the three alluvial stratigraphy lines (brown). Deep boreholes are yellow dots and seismic shot points are blue dots.	50
Figure 5-6 Profiles of surface elevation (red line) and base of alluvium (blue line) for the six structural cross sections. Surface elevation was extracted from the DEM surface and the elevation of base of alluvium was extracted from the gravity-derived surface.	51
Figure 5-7 Structural cross section #1 for the Deming sub-basin. Refer to Figure 5-5 for location.....	53
Figure 5-8 Structural cross section #2 for the Deming sub-basin. Refer to Figure 5-5 for location.....	54
Figure 5-9 Structural cross section #3 for the Deming sub-basin. Refer to Figure 5-5 for location.....	55
Figure 5-10 Structural cross section #4 for the Deming sub-basin. Refer to Figure 5-5 for location.....	56
Figure 5-11 Structural cross section #5 for the Deming sub-basin. Refer to Figure 5-5 for location.	57
Figure 5-12 Structural cross section #6 for the Deming sub-basin. . Refer to Figure 5-5 for location.	58
Figure 5-13 Revised fault map for the AOI with three new faults (red dashed) added to the map from this study. Fault #1 is the main basin-bounding fault, known as the West Florida Mountain Fault (WFMF) in the Deming sub-basin to the south and as the Treasure Mountain Fault (TMF) adjacent to the Mangas Trench (San Vicente) sub-basin to the north. Fault #3 is the antithetic fault that bounds the Deming sub-basin to the west. Faults #2 and #4 are synthetic to the main basin-bounding faults (#1). U = upthrown fault block, D = downthrown fault block.	60
Figure 5-14 Contour Map of Alluvial Thicknesses for the Mimbres. The Florida Mountains divide the Mimbres Basin into a western section (WMB) dominated by Basin and Range extension and an eastern section (EMB) which is a zone of transition between Basin and Range and Rio Grande Rift structures. Yellow circle is the Santa Maria DB R&R well.	65
Figure 5-15 Stratigraphic Column of the Santa Maria DB R&R well. The section is representative of the Gila Group for this basin in which three hydrostratigraphic units (HSUs) are identified and used as basis of 3-D Deming Sub-basin model. Unit 1: Holocene channel and basin fill fan deposits; Unit 2: Late Pleistocene conglomerates; Unit 3: Late Pliocene to Early Pleistocene lacustrine pluvial lake deposits.....	67

Figure 5-16 Lithofacies Assemblages (LFAs) Classification of Kennedy et al. (2000). Late Quaternary climatic change from a temperate interglacial Pleistocene period to an arid Holocene may be reflected by overlapping or inset sequences of terraces or fans (UNITs 1 and 2; Figure 5-20). Major basin aggradation however was terminated in most southwestern US basins by the deposition of relatively thin, coarse-grained pediment alluvial fans above mildly discordant erosion surfaces (Unit 2). 67

Figure 5-20 NNW (left)-SSE (right) Cross-section Line 7 of Alluvial Deming Sub-basin GFM. NW from the Mexican Highland valley (channel fill) towards the Central basin beneath the city of Deming to the SE. SM-DB: Santa Maria – Deming Basin well location. East bounding W Florida Mountain fault and antithetic fault zone #3 are in red. Channel and basin fill descriptions are provided in text. 71

Figure 5-18 Contour Map of Deming Basin Alluvial Basin Fill Thicknesses. Also included are the locations of cross-section lines used for Deming sub-basin alluvial basin fill reconstruction. Cross-section lines used to build 3-D conceptual alluvial framework and alluvial GFM models are shown (Lines #2, #3, #6, #7 and #9). Location of well SM-DB on cross-section Line #7 is also shown (yellow dot). Note the location of the NNW-SSE trending Mexican Highland valley channel to the deep basin and its relation to the bounding normal faults of the Florida Mountain Fault (FM) to the East and the Treasure Mountain Fault (TM) to the North. Also shown are the traces of the proposed ancestral perennial Mimbres and San Vicente River systems. 73

Figure 6-1 (A) JewelSuite representation of synthetic vertical wells from the structural cross sections intersecting the ground surface derived from the digital elevation model; (B) Outline of model box superimposed on ground elevation; (C) Map view perspective of 3-dimensional well trajectories located along the six structural cross sections; (D) Outline of model box for the GFM superimposed on well trajectories with GFM dimensions (33.6 x 22.8 km). 75

Figure 6-2 Tops of bedrock units ("markers") from well data extracted from the six structural cross sections. (A) Top of Precambrian; (B) Top of Paleozoic; (C) Top of Tertiary; (D) All marker tops for all bedrock units. 76

Figure 6-3 Fault and bedrock horizon surfaces created for the GFM presented in 3D perspective and 2D map view for top of Precambrian (A,B), tops of Precambrian and Paleozoic (C,D), tops of Precambrian, Paleozoic and Tertiary volcanics (E,F). 78

Figure 6-4 Fault and horizon surfaces of bedrock and alluvium created for the GFM presented in 3D perspective and 2D map view for tops of bedrock and alluvium unit 1 (A,B), tops of bedrock, alluvium unit 1 and alluvium unit 2 (C,D), tops of bedrock, alluvium unit 1, alluvium unit 2 and alluvium unit 3 (E,F). 79

Figure 6-5 Cross sectional view looking to the north of all horizon and fault surfaces in the GFM. 80

Figure 6-6 Three-dimensional gridded volumes of the GFM in oblique perspective and map view for the Precambrian (A, B), Precambrian and Paleozoic (C, D) and Precambrian, Paleozoic and Tertiary volcanics (E, F). 82

Figure 6-7 Three-dimensional gridded volumes of the GFM for all bedrock units as viewed in cross section (A) and oblique (B) perspectives. Note the symmetric graben geometry in the wide south portion of the basin as well as the topography on top of the Tertiary volcanics. 83

Figure 6-8 Comparison of structural Cross Section #1 (A) to the GFM cross section at the same location (B). The vertical black lines in the GFM are the synthetic wells and the horizontal yellow lines are the three alluvium tops. 84

Figure 6-9 2D perspective map view of (A) surface geology from Hawley et al, 2001; (B) Fault traces and contours of alluvium thickness from this study; and (C) Surface geology and faults from the GFM.	85
Figure 7-1 Map of model-produced values for hydraulic conductivity of the aquifer in ft/day from Hanson et al, 1994 (text converts to m/d).	90
Figure 7-2 Map of the water table elevation over the study area, based on the data from the water wells indicated with black dots.	95
Figure 8-1 Exported GFM tetrahedral mesh representing 4 material zones (left) and extracted boundary surfaces and internal interfaces (right).	99
Figure 8-2 shows the Delaunay triangulation used for stacking (left), the stacked point distribution connected into a Delaunay mesh with material zones (middle), and a detail showing the mesh vertices and elements with material zone colors (right).	99
Figure 8-3 Exported GFM tetrahedral mesh representing 3 material zones (left) and extracted boundary surfaces and internal interfaces (right).	101
Figure 8-4 The hexahedral mesh with 3 levels of octree refinement (top left), the point distribution connected into a Delaunay mesh with interpolated material zones (top right), and detail showing the mesh vertices and elements with material zone colors (bottom).	102
Figure 8-5 Exported GFM tetrahedral mesh exploded to show the internal body (left) and the extracted boundary and internal surface (right).	104
Figure 8-6 The hexahedral mesh with 3 levels of octree refinement (top left), the point distribution connected into a Delaunay mesh with interpolated material zones (top right), and detail showing the mesh vertices and elements with material zone colors (bottom). The mesh has been clipped to show the internal lens.	105
Figure 8-7 Exported GFM tetrahedral mesh represented as 5 material zones (left) and the extracted boundary and interface surfaces (right).	107
Figure 8-8 The hexahedral mesh with 3 levels of octree refinement (top left), the point distribution connected into a Delaunay mesh with interpolated material zones (top right), and detail showing the mesh vertices and elements with material zone colors (bottom).	108
Figure 9-1 Scenario 1.1. Water pressure contours for up flowing single phase water in the absence of gravity (FEHM).	113
Figure 9-2 Layered permeability for the saturated layered case 1.2 (FEHM).	115
Figure 9-3 Scenario 1.2. Pressure contours for upwelling in a layered permeability field (FEHM).	116
Figure 9-4 Scenario 1.2. Pressure contours for upwelling in a layered permeability field as generated by PFLOTRAN.	116
Figure 9-5 Scenario 1.3. Saturation profile for 10 mm/yr infiltration flux on an isotropic material property field (Santa Fe Group).	117
Figure 9-6 Scenario 1.4. Saturation profile for 10 mm/yr infiltration flux on a layered material property field (Santa Fe Group top and bottom, Otowi in the middle).	118
Figure 9-7 Scenario 2.1. Up flowing single phase water in the absence of gravity for the wedge mesh (test case 2).	119
Figure 9-8 Wedge permeability (log ₁₀ (perm m ²)) for the saturated case 2.2. Slice is at y = 10 m, through the center of the 3-D domain.	119
Figure 9-9 Scenario 2.2. FEHM version of pressure contours for upwelling with the low permeability wedge. Slice is at y = 10 m, through the center of the 3-D domain.	120

Figure 9-10 Scenario 2.2. PFLOTRAN version of pressure contours for upwelling with the low permeability wedge. Slice is at $y = 10$ m, through the center of the 3-D domain.....	120
Figure 9-11 Scenario 2.3. Saturation profile for 10 mm/yr infiltration flux on an isotropic material property field (Santa Fe Group).....	121
Figure 9-12 Scenario 2.4. Saturation profile for 10 mm/yr infiltration flux. The wedge is composed of Otowi tuff and the rest of the domain is Santa Fe Group. The slice plane is at $y = 10$ m.....	122
Figure 9-13 Scenario 3.1. Up flowing single phase water in the absence of gravity for the lens mesh (test case 3). Slice plane is $y = 10$ m.....	123
Figure 9-14 Lens permeability ($\log_{10}(\text{perm m}^2)$) for the saturated case 3.2. Slice is at $y = 10$ m, through the center of the 3-D domain.....	123
Figure 9-15 Scenario 3.2. Pressure contours for upwelling with the low permeability lens. Slice is at $y = 10$ m, through the center of the 3-D domain. (FEHM).....	124
Figure 9-16 Scenario 3.2. PFLOTRAN simulation showing pressure contours for upwelling with the low permeability lens. Slice is at $y = 10$ m, through the center of the 3-D domain.....	124
Figure 9-17 Scenario 3.3. Saturation profile for 10 mm/yr infiltration flux on an isotropic material property field (Santa Fe Group). Slice plane through the lens at $X = 10$ m.....	125
Figure 9-18 Scenario 3.4. Saturation profile for 10 mm/yr infiltration flux. The wedge is composed of Otowi tuff and the rest of the domain is Santa Fe Group.....	126
Figure 9-19 Scenario 4.1. Up flowing single phase water in the absence of gravity for the fault mesh (test case 4). Slice plane is $x = 10$ m.....	127
Figure 9-20 Fault permeability ($\log_{10}(\text{perm m}^2)$) for the saturated case 4.2. Slice is at $x = 10$ m, through the center of the 3-D domain.....	128
Figure 9-21 Scenario 4.2. Pressure contours for upwelling with low permeability layers forcing flow up from the lower left to the upper right. Slice is at $x = 10$ m, through the center of the 3-D domain.....	129
Figure 9-22 Scenario 4.2. PFLOTRAN simulation of pressure contours for upwelling with low permeability layers forcing flow up from the lower left to the upper right. Slice is at $x = 10$ m, through the center of the 3-D domain.....	129
Figure 9-23 Scenario 4.3. Saturation profile for 10 mm/yr infiltration flux on an isotropic material property field (Santa Fe Group).....	130
Figure 9-24 Scenario 3.4. Saturation profile for 10 mm/yr infiltration flux. The wedge is composed of Otowi tuff and the rest of the domain is Santa Fe Group.....	131

List of Tables

Table 2-1 Hydrogeologic units for the Great Basin carbonate and alluvial aquifer system (from Sweetkind et al., 2010b).....	8
Table 5-1 Ranges of seismic compressional velocities and their inferred lithologies used to interpret the seismic refraction lines from the Mimbres Basin.	45
Table 5-2 Structural data prepared for JewelSuite that defines the well properties for synthetic well number 2-36000, located on Cross Section #2, 36 km. All depths are in meters.....	61
Table 5-3 Structural data prepared for JewelSuite that provides the formation tops for synthetic well number 2-36000, located at Cross Section #2, 36 km. All depths are in meters.	61
Table 5-4 Model Hydrostratigraphic Unit Descriptions. Deming channel and basin fill descriptions and their equivalence to LFAs and HSUs from Kennedy et al. (2000) are placed in the context of the alluvial conceptual framework in this study. Model layer thicknesses are also shown and in the central and deepest area of the basin are constant (Figure 5-20).	68
Table 5-5 Proposed Tectonic and Climate Reconstruction Used for Mimbres Conceptual Model. Schematic illustration of chronologic relation and interplay between tectonic setting and climate in the development of southwestern structures and B&R formation.....	72
Table 7-1 Hydrogeologic properties from bedrock and basin-fill sediments in the Mimbres Basin (from Finch et al, 2008). Last column is added to show in m/d for better comparison with other data sources.	91
Table 7-2 Sorption properties for alluvium provided by Mariner et al. (2018) in their Table 5-7. Radionuclide sorption coefficients in mL/g for alluvium at the Nevada National Security Site....	93
Table 7-3 Unsaturated alluvium hydraulic properties values from the Greater Confinement Disposal Boreholes, Nevada National Security Site (Table 5-2 in Mariner et al., 2018).	94
Table 8-1 Cube Tests 1-4 Computational Mesh Summary	98
Table 9-1 Information for the 16 test case scenarios.....	112
Table 9-2 Hydrologic properties for the 4 test case scenarios.....	113
Table 9-3 Thicknesses and permeabilities for the layers in Scenario 1.2	114
Table 9-4 Diagnostic output information for the 16 test case scenarios	132

List of Acronyms

AOI	Area of interest
DEM	Digital Elevation Model
DFE	Drilling Floor Elevation
DOE	Department of Energy
DOE-EM	DOE Office of Environmental Management
DOE-NE	DOE Office of Nuclear Energy
ESRI	Environmental Systems Research Institute
FEHM	Finite Element Heat and Mass Transfer
FY	fiscal year (October-September)
GDSA	geologic disposal safety assessment
GFM	geologic framework model
GPF	Geothermal Play Fairways (DOE sponsored program)
HFM	hydrologic framework model
HLW	high level nuclear waste
HSU	hydrostratigraphic units
LANL	Los Alamos National Laboratory
LFA	Lithofacies assemblages
Ma	Millions of years ago
MD	Measured Depth
MSL	Mean Sea Level (amsl = above mean sea level; bmsl = below mean sea level)
NMBGMR	New Mexico Bureau of Geology and Mineral Resources
NMT	New Mexico Tech
PA	performance assessment
PFLOTRAN	parallel flow and transport (simulation code)
R&D	research and development
RGIS	New Mexico Resource Geographic Information System
SFWD	Spent Fuel & Waste Disposition (DOE-NE program)
SNF	Spent nuclear fuel
SNL	Sandia National Laboratories
TOUGH	Transport of Unsaturated Groundwater and Heat (simulation code)
TVDSS	Total Vertical Depth Sub-sea
US	United States
USGS	United States Geological Survey
UWI	Unique Well Identifier
UZ	Unsaturated Zone

1 Introduction

This report documents progress on the development of a geologic framework model (GFM) for the alluvium/unsaturated zone reference case, part of the larger Spent Fuel and Waste Disposition (SFWD) campaign to evaluate alternative geologic media for the disposal of spent nuclear fuel and high level nuclear waste. The primary objectives of the FY2019 work are to (1) develop a workflow for the performance assessment (PA) of a generic alluvial basin, from initial geologic characterization through flow and transport modeling, and (2) apply the workflow to a specific “case study” alluvial basin that requires the integration of all available datasets as well as contending with subsurface complexities and uncertainties.

We begin this report with an overview of the Basin and Range province in the western U.S. (Chapter 2), which contains numerous alluvial basins that may serve as potential examples for the unsaturated zone reference case. This is followed by a detailed description of the Mimbres Basin of southwestern New Mexico (Chapter 3), which we selected for the in-depth case study. Chapter 4 documents the compilation of the geo-database within ArcPro GIS software and the various geospatial analyses that contributed to the successful execution of the project workplan. The GFM relies entirely on the quality and scientific integrity of the subsurface geological characterization, which is the focus of Chapter 5. The chapter is divided into two sections: structural characterization of the bedrock units and the characterization of the alluvial basin-fill sediments. The first iteration of the GFM is presented in Chapter 6, built in JewelSuite software from geologic cross sections (Chapter 5) and surfaces extracted from the GIS (Chapter 4). The framework for hydrological modeling is presented in Chapter 7 and includes a discussion of physical properties of hydrostratigraphic units (e.g., porosity, permeability, saturation) and properties relevant to the unsaturated zone. Numerical modeling proceeded in parallel with the geological characterization to ensure compatibility between JewelSuites’ GFM output and LANL’s computational meshing algorithm (LaGriT). Chapter 8 details the computational meshes and set up files generated in LaGriT for four test case scenarios of GFM created in JewelSuite. In Chapter 9, flow simulators FEHM and PFLOTRAN are used to test the validity of the meshes for transport modeling.

Advances made during FY2019 for the GDSA alluvium reference case include:

- Compilation of a geo-database to facilitate the geospatial analysis of large datasets, which is required to evaluate and model the surface and subsurface of a generic alluvial basin.
- A workflow to build a GFM for a generic alluvial basin in the Basin and Range province.
- Structural and lithologic characterization of tectonic sub-basin for Mimbres Basin case study.
- Characterization of alluvial basin fill for Mimbres Basin case study.
- First iteration GFM focusing on structural and stratigraphic geometry of Deming sub-basin.
- Successful testing of GFM export from JewelSuite into LaGriT for computational meshing.
- Validation of computational meshes for transport modeling using FEHM and PFLOTRAN.

A flowchart outlining the proposed workflow for evaluating the GDSA of a generic alluvial basin is presented in Figure 1-1. Many basins within the Basin and Range province have broad

similarities, enabling the creation of a conceptual model that applies to most of these basins (Figure 1-2). Displacement along a range-bounding normal fault generates a structural basin that accommodates the accumulation of alluvial sediments. The geologic characteristics, and hence hydrologic properties, of these alluvial layers may vary according to distance from range front, tectonics, climate and other factors. Evaluating the GDSA for a real alluvial basin, in contrast to a conceptual one, will require the ability of the workflow to handle conflicting data, geologic heterogeneity and subsurface uncertainty. For this reason we selected a generic “case study” basin where we could develop a process for integrating real data into flow simulations. During this work, we discovered that digital databases and computational algorithms readily available in a GIS program provided geologically unreasonable constraints to the GFM. Therefore, we found it necessary to obtain additional existing data (seismic surveys, descriptions of well cuttings) and to employ classic geologic techniques (hand-drawn cross sections, inferring depositional environments) in order to construct a viable GFM for the Mimbres Basin case study. We include in this report the detailed geologic information behind the decisions needed for GFM creation that required technical expertise and judgement. We also describe the workflow we used to get from raw geologic data to a viable flow model. While we show here that numerical flow simulation and their dependent meshing processes accurately incorporate many of the complexities that exist in the Mimbres and other basins, future work is needed to integrate the entire GFM into the flow simulations.

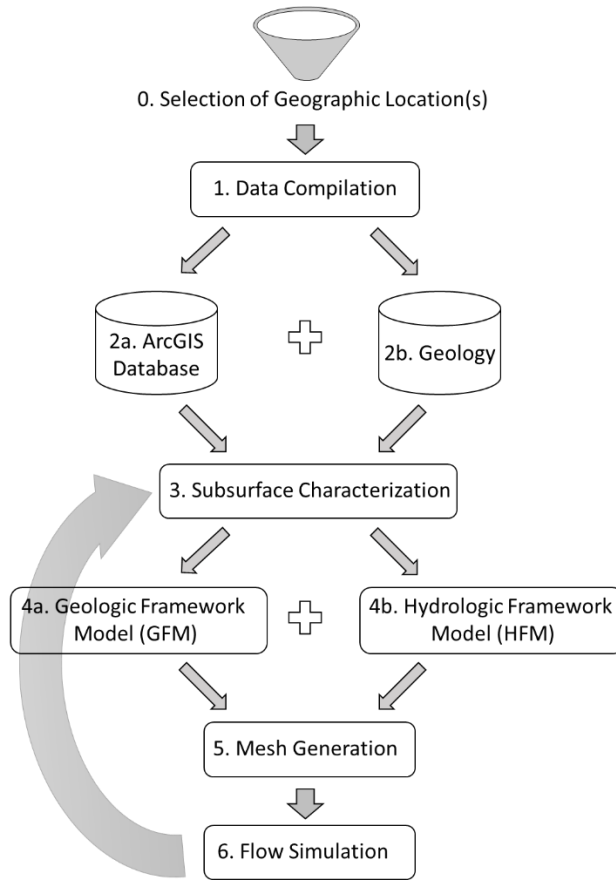


Figure 1-1 Flowchart for a Geological Disposal Safety Assessment of a generic alluvial basin. The process is iterative at all steps.

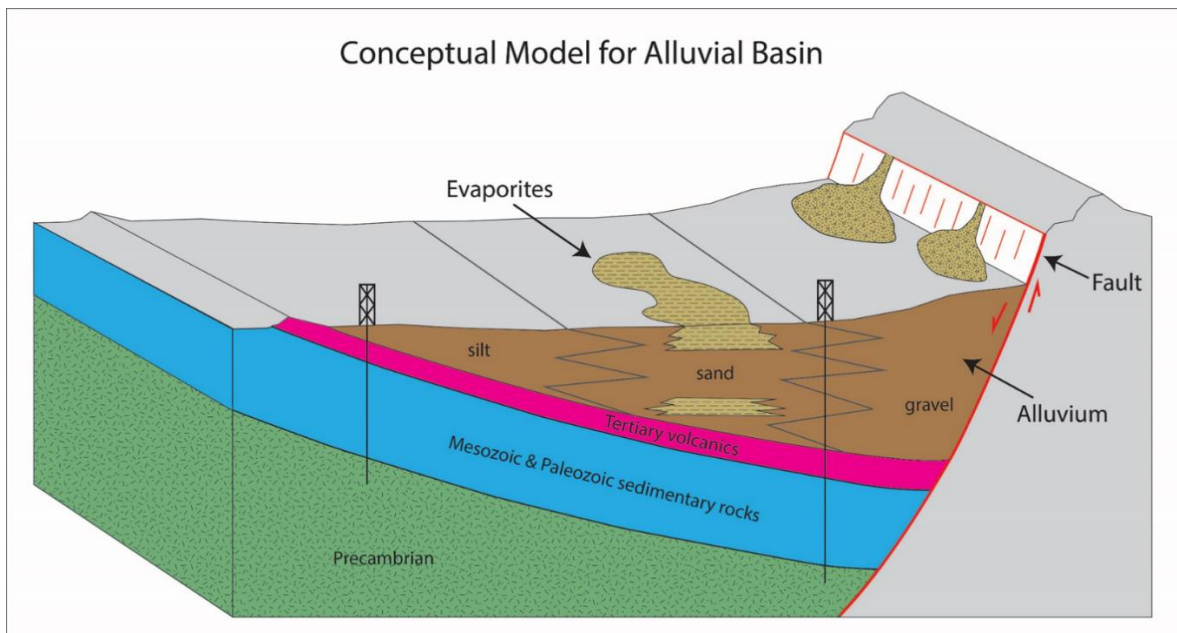


Figure 1-2 Conceptual model for a generic alluvial basin in the Basin and Range province. Note that slip on the basin-bounding fault provides the accommodation space for a thick accumulation of alluvium (brown colors) of varying lithologies and depositional environments.

2 Alluvial Basins in the Basin and Range Province

2.1 Tectonics and Structure

Alluvial basins of the Basin and Range province have been proposed as a potentially suitable geologic environment to host a repository in the unsaturated zone (Winograd, 1981), as this setting benefits from an arid environment (and therefore low water flux) and relatively high sorption capacity. An updated conceptual model of alluvial basins was presented by Perry et al. (2018) to support development of a new generic reference case for unsaturated alluvium. The Basin and Range covers portions of nine states and northern Mexico. It is bounded to the west by the Sierra Nevada-Cascade ranges and to the east by the Rocky Mountains, Colorado Plateau and Rio Grande rift (Figure 2-1). East-west directed extension of the Basin and Range initiated around 15 Ma and continues through the present, resulting in north-south oriented ridges (“ranges”) and adjacent valleys (“basins”). Range-bounding normal faults separate upthrown footwall blocks from downthrown hanging wall blocks (Figure 2-2). Fault throws (i.e., the vertical component of displacement) are typically greater than 1 km and place bedrock spanning in age from Precambrian to Tertiary in the upthrown ranges. The adjacent hanging wall blocks often dip toward the range-bounding fault, forming half-graben geometries (Figure 2-2). The combination of large fault displacements and tilted strata in the hanging wall result in the formation of deep, asymmetric basins in valleys adjacent to the uplifted fault blocks. These basins develop thick accumulations of alluvial sediments, which are the target geological medium for hosting the repository considered in this study.

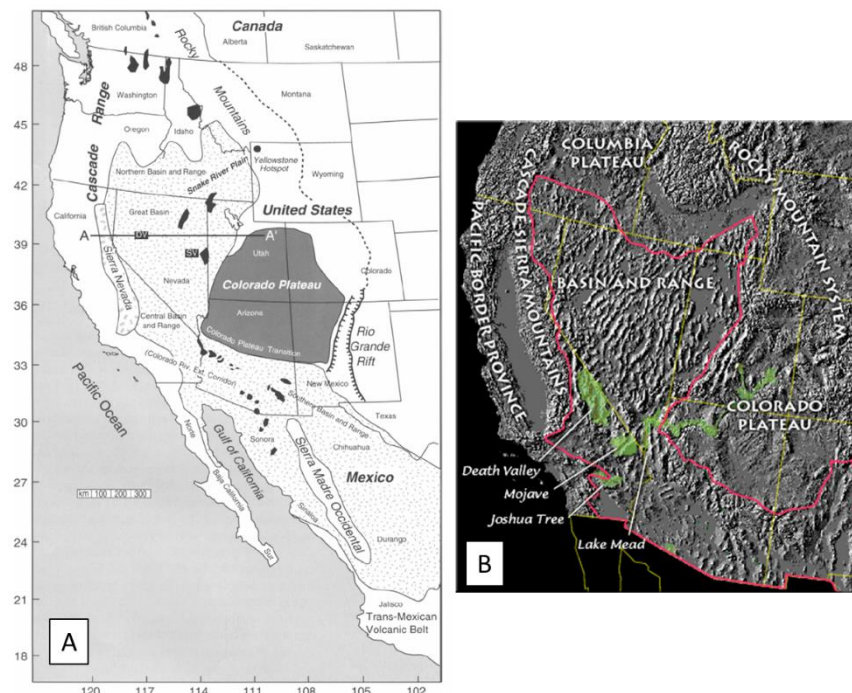


Figure 2-1. A. Map of the Basin and Range province (stippled pattern) in western North America and its relation to other tectonic elements. From Parsons (2006). B. Digital elevation model showing the geomorphology of the Basin and Range dominated by linear ridges and valleys (source: USGS).

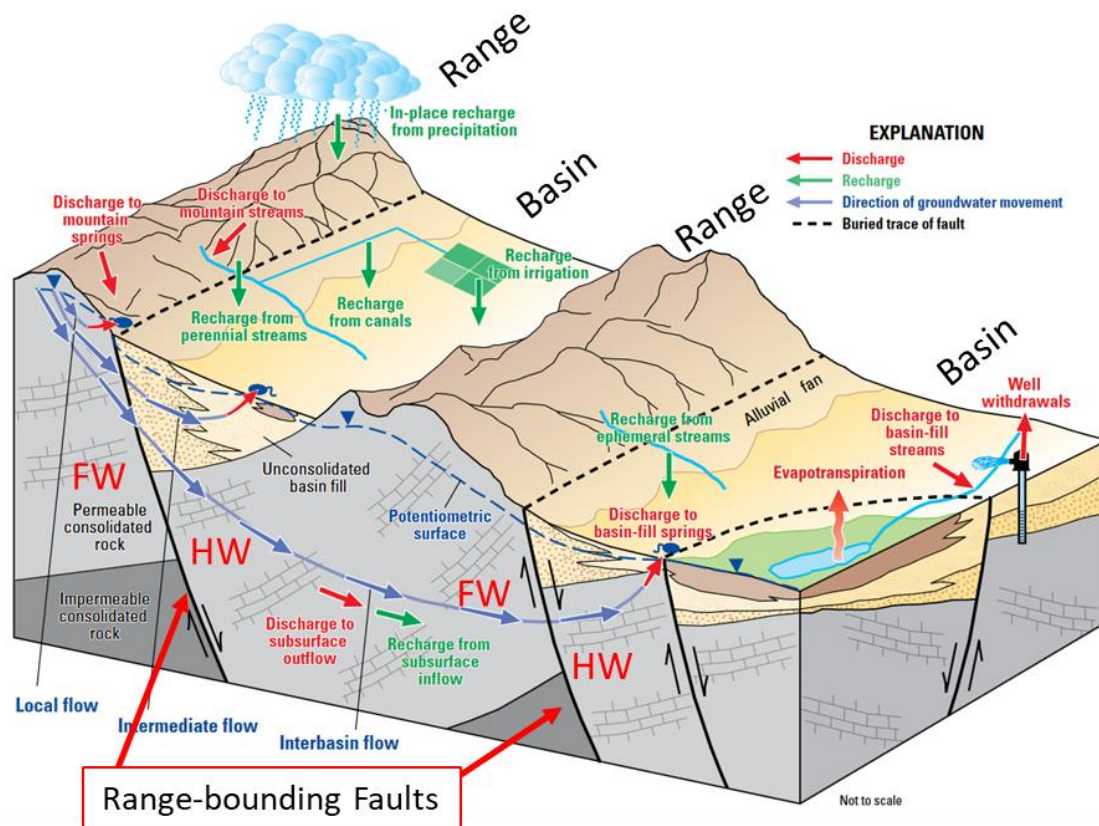


Figure 2-2 Schematic diagram showing groundwater flow in alluvial aquifers of the Basin and Range province (from Sweetkind et al, 2010a). Note thick accumulations of alluvial sediments in the tilted hanging wall blocks. FW=footwall, HW=hanging wall.

2.2 Stratigraphy and Lithologies

Although the stratigraphy of the Basin and Range province varies according to geographic location, general commonalities persist through geologic time when placed within the context of the tectonic evolution of the U.S. Cordillera (DeCelles, 2004; Chapman et al, 2018). Crystalline basement is composed of 2.2 to 1.0 Ga accreted terranes that formed along the margin of the supercontinent Laurentia during the Proterozoic (Whitmeyer and Karlstrom, 2007). Breakup of the supercontinent in the late Proterozoic was followed by the development of a passive continental margin during much of the Paleozoic. The Proterozoic and Paleozoic geologic history of the Basin and Range resulted in two important features for this study. First, Proterozoic structures, such as shear zones and faults in crystalline basement rock, are deep-seated zones of weakness that were candidates for reactivation during subsequent episodes of deformation such as Laramide convergence, Rio Grande rifting and Basin and Range extension (Karlstrom et al, 2004). Second, the sedimentation along the Paleozoic passive margin resulted in the deposition of thick carbonate sequences on a shallow marine platform. The carbonate rocks serve as deep bedrock aquifers that underlie much of the Basin and Range, and are the

primary conduit for interbasin flow due to their high permeabilities (Figure 2-2; Heilweil and Brooks, 2010; Perry et al., 2018).

Continental arc magmatism due to the subduction of oceanic lithosphere beneath the North American plate initiated during the Triassic, resulting in magmatism in the Sierra Nevada Range and pulses of tectonic convergence and uplift in the foreland, culminating in the Laramide orogeny between 80 and 40 Ma (Miller et al., 1992; Saleeby, 2003; Chapman et al., 2018). Mesozoic clastic rocks are largely absent in portions of the Basin and Range province due to non-deposition and/or erosion, most notably in southwestern New Mexico (Lucas, 2004). The main exceptions are Late Cretaceous-Paleocene syn-orogenic, non-marine, clastic sedimentary rocks related to the Laramide orogeny (De los Santos et al., 2018). At around 40 Ma the U.S. Cordillera transitioned from contractional to extensional tectonics, accelerated by the development of the San Andreas transform and subduction of the mid-ocean spreading center around 20Ma (Atwater and Stock, 1998). East-west directed extension occurred in two phases, an early phase (30–15 Ma) that includes initiation of the Rio Grande rift and the exhumation of metamorphic core complexes (Dickinson, 1991), followed by Basin and Range extension from 15 Ma to the present (Wernicke et al., 1988; Parsons, 2006). Intense volcanism accompanied tectonic extension, leading to thick deposits of Tertiary volcanics of varying compositions. Large differences in elevation resulting from Basin and Range topography led to erosion and thick accumulations of alluvial sediments, locally interbedded with volcanic deposits.

Regional studies of alluvial aquifers in the Basin and Range province simplify the geologic section and group bedrock formations and lithologies into main hydrologic units, while focusing greater attention on the basin fill. In a regional study of alluvial basins centered around south-central Arizona, Anderson (1995) groups underlying bedrock into two hydrologic units, “bedrock of the mountains” (presumably crystalline basement of Precambrian age) and “pre-basin and range sedimentary and volcanic rocks”, which includes all sedimentary and volcanic rocks from the Paleozoic through the Paleogene (Figure 2-3). Sweetkind et al. (2010b) identify five hydrologic units within the bedrock of the Great Basin overlapping Nevada, Utah and parts of adjacent states. They include two aquifers in the Paleozoic carbonate rocks, an intervening Paleozoic confining unit comprised of siliciclastic rocks, an underlying non-carbonate confining rock (presumably crystalline basement and sedimentary rocks of Precambrian age), and overlying Cenozoic volcanic rocks (Table 2-1). Note the maximum thicknesses of the aquifers and their hydraulic conductivities, and especially the similarities in hydraulic conductivity between the Paleozoic carbonate rock aquifers and the Cenozoic basin-fill aquifer sediments.

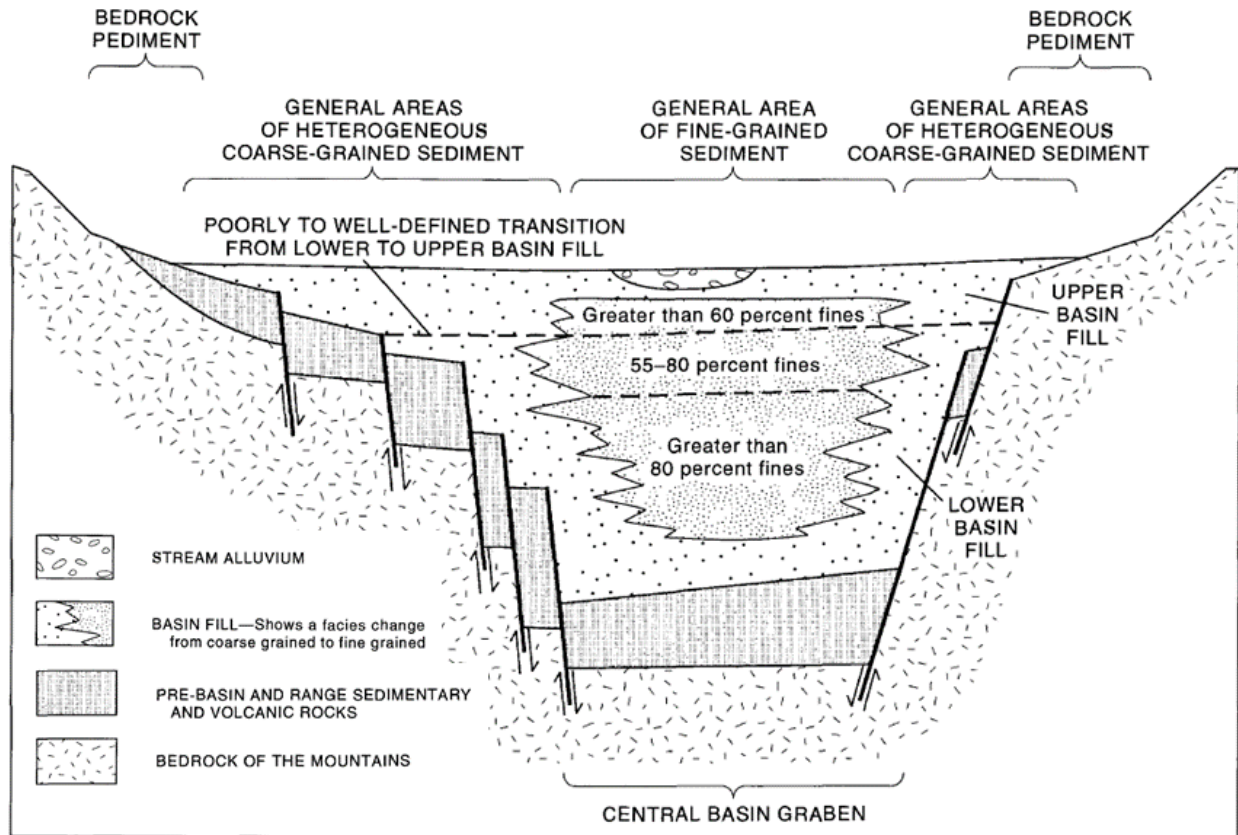


Figure 2-3 Hydrogeologic units for Basin and Range alluvial aquifers proposed by Anderson (1995).

Table 2-1 Hydrogeologic units for the Great Basin carbonate and alluvial aquifer system (from Sweetkind et al., 2010b).

[Modified from Belcher and others, 2001; 2002. >, greater than; NC, not calculated; LBFAU, lower basin-fill aquifer unit; UBFAU, upper basin-fill aquifer unit; VU, volcanic unit; UCAU, upper carbonate aquifer unit; USCU, upper siliciclastic confining unit; LCAU, lower carbonate aquifer unit; NCCU, noncarbonate confining unit]

Major hydrogeologic unit	Hydrogeologic unit abbreviation	Maximum unit thickness (feet)	Hydraulic conductivity (feet per day)				
			Arithmetic mean	Geometric mean	Minimum	Maximum	Count
Cenozoic basin-fill aquifer sediments	LBFAU and UBFAU ¹	36,000	31	4	0.0001	431	71
Cenozoic volcanic rock	VU	3,300 (>13,000 in calderas)	20	3	0.04	179	26
Upper Paleozoic carbonate rock	UCAU	24,000	62	0.4	0.0003	1,045	28
Upper Paleozoic siliciclastic confining rock	USCU	>5,000	0.4	0.06	0.0001	3	22
Lower Paleozoic carbonate rock	LCAU ²	16,500	169	4	0.009	2,704	45
Noncarbonate confining rock	NCCU ³	NC	0.8	0.008	0.00000009	15	26

Anderson (1995) and Sweetkind et al. (2010b) divide the alluvium into lower basin fill and upper basin fill units. Both units grade from coarse-grained sediments near the mountain fronts to fine-grained sediments toward the basin center (Figure 2-3). The lower basin fill tends to be consolidated, whereas the upper basin fill remains unconsolidated, which contributes to a general decrease in permeability (i.e., hydraulic conductivity) as a function of increasing depth (Anderson et al, 1992; Belcher et al., 2001). Mack and Stout (2005) present schematic models

of the distribution of depositional facies (alluvial fan, lacustrine, axial fluvial and aeolian) within continental extensional basins, distinguishing between an asymmetric half graben and the more symmetric full graben (Figure 2-4).

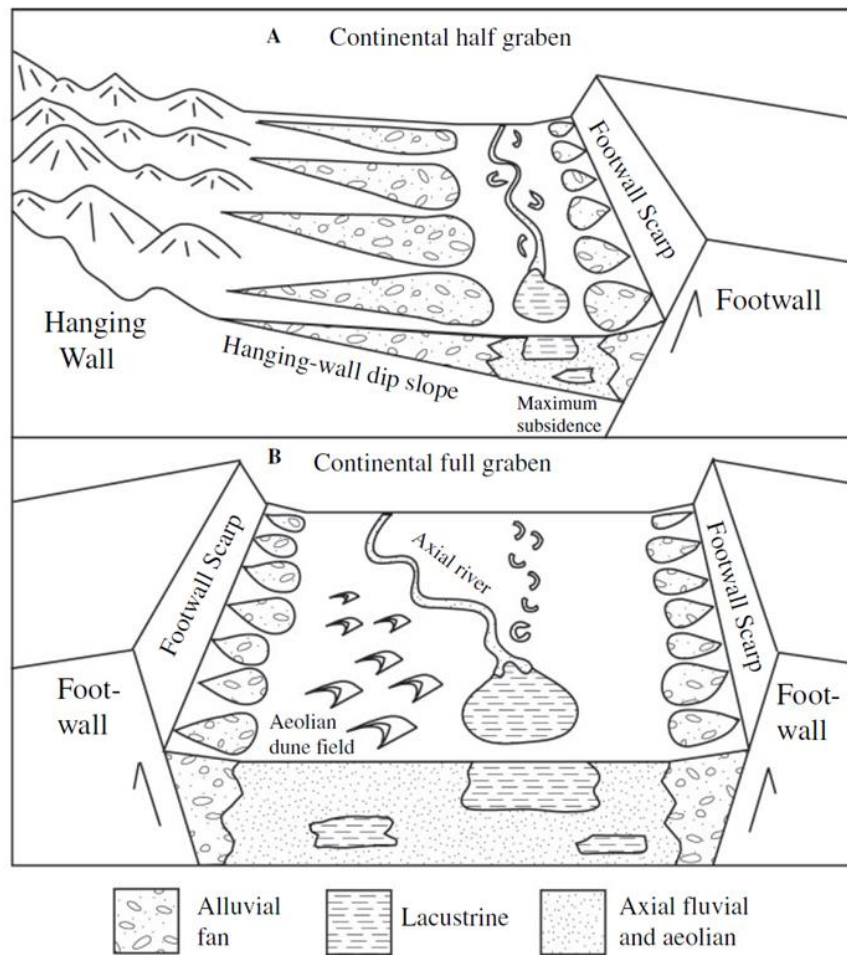


Figure 2-4 Model of alluvial depositional facies within (A) continental half graben and (B) continental full graben, from Mack and Stout (2005).

Perry et al. (2018) present a simplified stratigraphy and permeability framework for alluvial deposits in support of the generic repository case (Figure 2-5). The repository is placed in the unsaturated zone at a depth of 250 m within the upper basin fill. The water table sits at 450 m depth at the top of a sand/gravel aquifer at the base of the upper basin fill. The lower basin fill extends from 500 to 1000 m depth and lies within the saturated zone. Perry et al. (2018) assigned bulk permeability values of $1e^{-12} \text{ m}^2$ for the upper basin fill, $1e^{-13} \text{ m}^2$ for the lower basin fill, $1e^{-14} \text{ m}^2$ for clay-rich deposits in the upper fill, and $1e^{-11} \text{ m}^2$ for the sand/gravel aquifer based on data compiled from Thomas (1989), Plume (1996) and Belcher et al. (2001) (Figure 2-5).

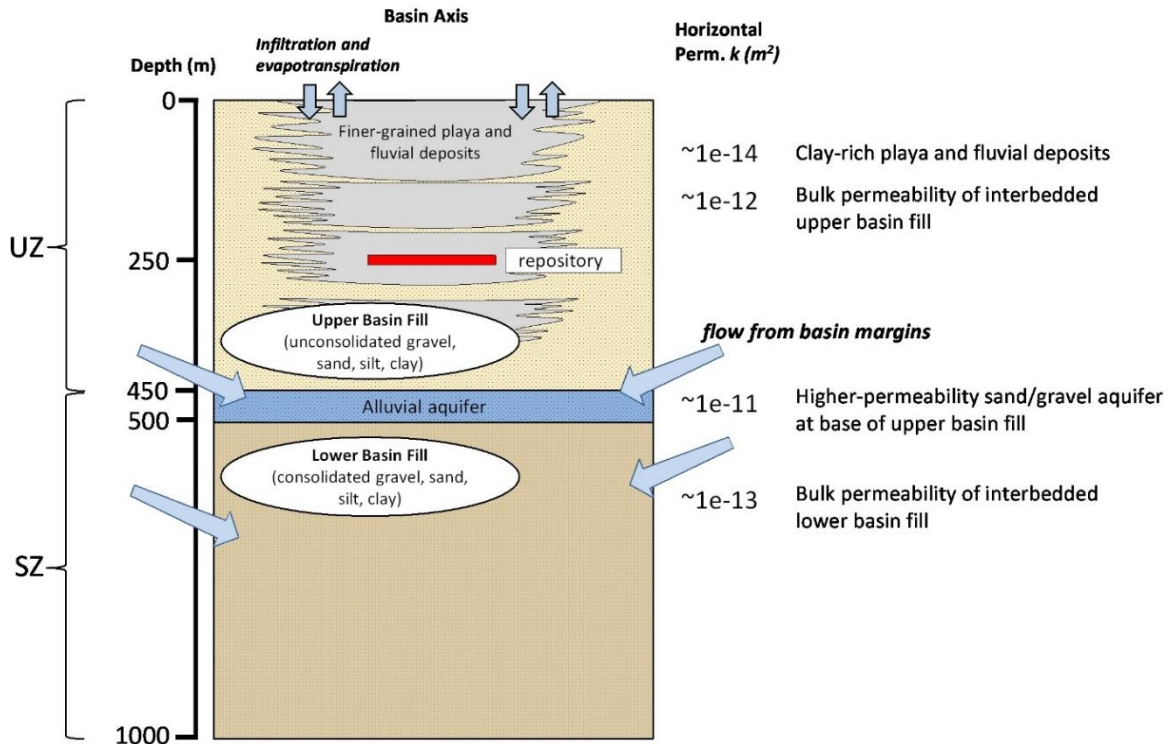


Figure 2-5 Generalized representation of stratigraphy and permeabilities for an alluvium-filled basin (from Perry et al., 2018). UZ=unsaturated zone, SZ=saturated zone.

3 Mimbres Basin as a Generic Case Study

In order to develop and demonstrate the capability to bring geologic data into the flow models, we needed a real basin with existing geologic data. For this, we chose the Mimbres Basin, as it contains numerous geometric complexities of the types that future flow models must be capable of incorporating. In addition, this basin has a relatively thick section of alluvium and there is sufficient geologic and well data available for the creation of a realistic GFM.

3.1 Overview of the Mimbres Basin

The Mimbres Basin of southwestern New Mexico and northern Mexico covers about 13,300 km², of which 11,300 km² overlap portions of the New Mexico counties of Luna, Grant, Dona Ana and Sierra (Kennedy et al, 2000). It is located in the eastern-most sector of the southern Basin and Range (Figure 3-1), at the junction of three physiographic provinces: the Basin and Range province to the west, the Colorado Plateau to the north and the Rio Grande rift to the east (Figure 3-2). The Mimbres Basin was selected as a candidate for the generic case study due to its thick (> 1000 m) accumulations of alluvial sediments within structurally-controlled sub-basins, numerous ground water wells drilled for irrigation, deep boreholes that intersect Precambrian basement, geophysical surveys, hydrologic studies and detailed geologic mapping of bedrock and alluvial sediments (e.g., Clemons, 1986; Hanson et al, 1994; Seager, 1995; Klein, 1995; Hawley et al, 2000; Heywood, 2002; Finch et al., 2008). The Mimbres Basin is

characterized by north- and northwest-trending intrabasin ranges such as Cooke's Range, the Florida Uplift, and the Hermanas Mountains, which divide the basin into the Deming, Columbus, Seventy-six, Florida, San Vicente (also known as the Mangas trench), and the Tres Hermanas sub-basins (Figure 3-2). Overall, the Mimbres Basin is a part of a larger network of alluvium-filled extensional basins that developed in southwestern New Mexico over the past 25 million years.

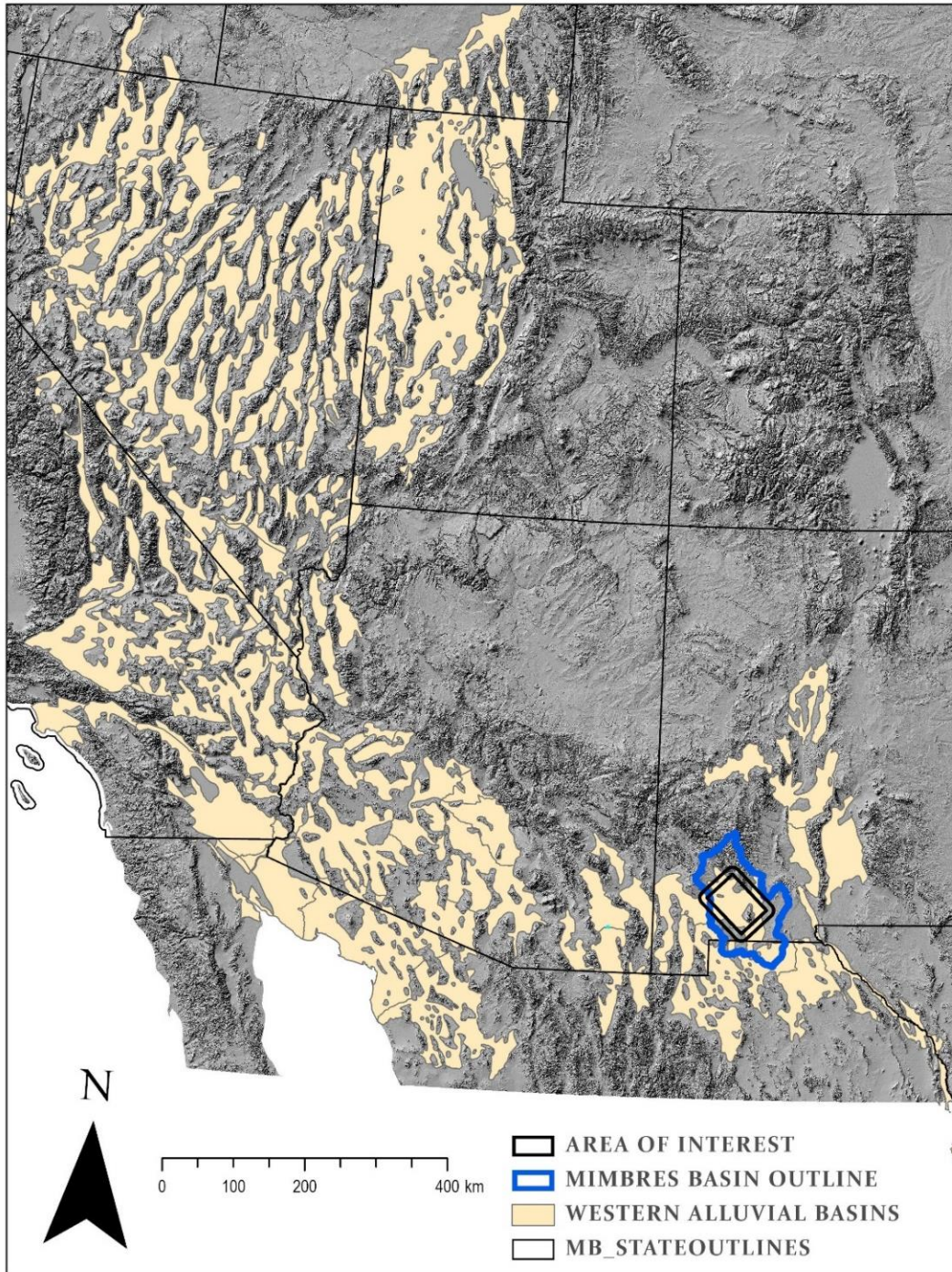


Figure 3-1 Location of the Mimbres Basin among the alluvial basins of the greater Basin and Range Province.

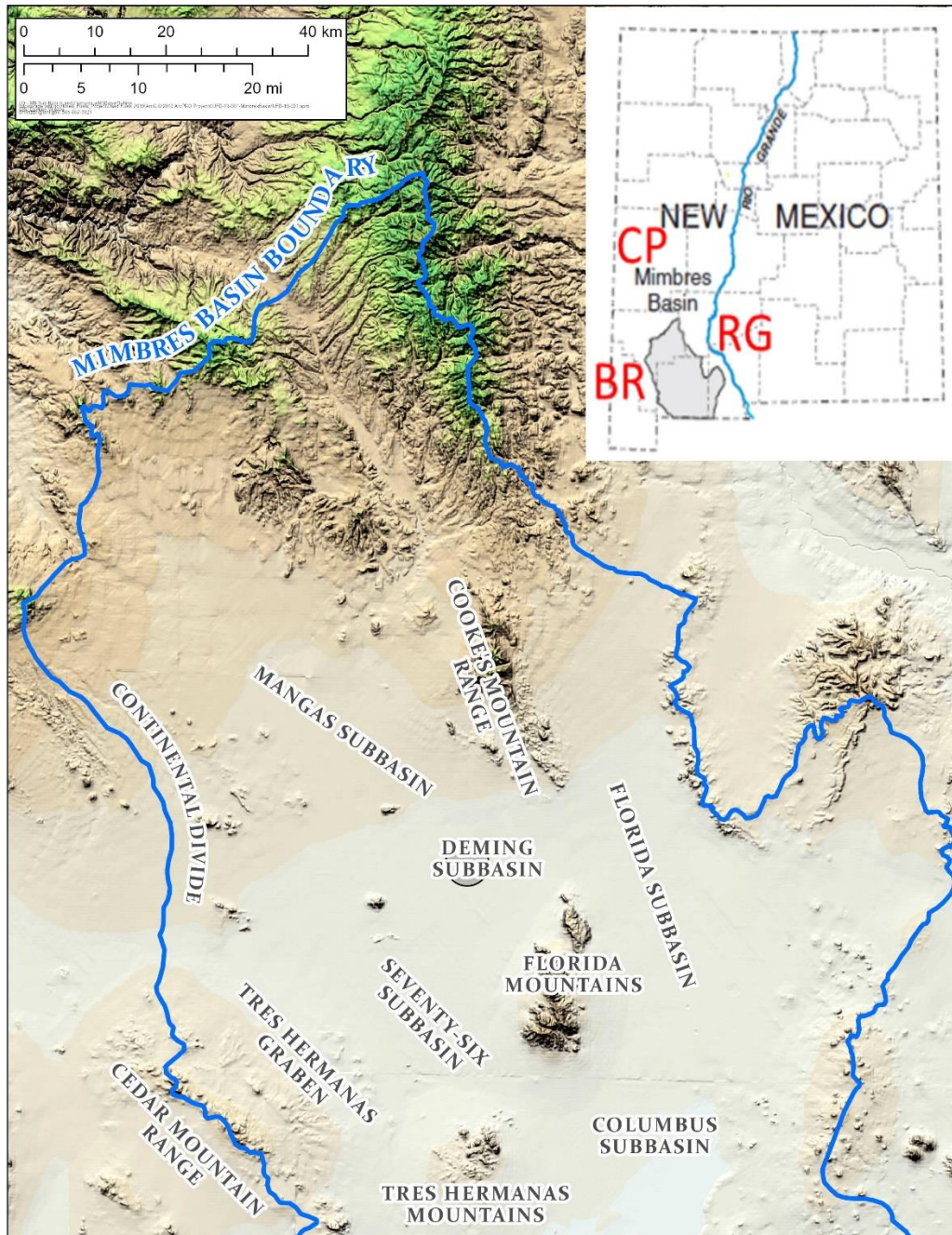


Figure 3-2 Sub-basins and mountain ranges in the Mimbres Basin (from Heywood, 2002). CP=Colorado Plateau, BR=Basin and Range, RG=Rio Grande Rift.

3.2 Geology, Structure and Geophysics of the Mimbres Basin

Geologic units within the Mimbres Basin can be divided into two main groups: (1) Precambrian through Tertiary bedrock, and (2) alluvial sediments that fill the deep structural basins and cover the valley surface. In general, the Proterozoic continental lithosphere that underlies southwestern New Mexico belongs to the 1.7–1.6 Ga Mazatzal terrane (Karlstrom et al., 2004;

Chapman et al., 2018). Pre-Tertiary bedrock geology is characterized from outcrop exposures in uplifted fault blocks (e.g., Florida Mountains, Cooke's Range) and deep oil and gas exploration wells in the basin (Thompson et al., 1978; Brown and Clemons, 1983; Clemons, 1986; Seager, 1995; Amato, 2000). Precambrian and Paleozoic rocks described from outcrops and well cuttings in the Mimbres Basin include granites, syenites and metamorphic rocks and have a wide range of ages (~1600–371 Ma; Clemons, 1986; Seager, 1995). A thick section of mostly carbonate rocks accumulated during the Paleozoic (Figure 3-3; Brown and Clemons, 1983), reflecting deposition on a stable, shallow marine platform. An angular unconformity separates Permian limestones from overlying Late Cretaceous rocks (Lobo Formation); therefore, Triassic through Early Cretaceous strata are absent in the Mimbres Basin (Lucas, 2004; Lawton, 2004).

System	Stratigraphic units	Thick. (ft)	Description
Quaternary	colluvial and alluvial deposits	0–200	Present day arroyo deposits. Silt, sand, gravel; locally carbonate cemented, fan and bajada deposits.
	<i>angular unconformity</i>		
Tertiary	diorite/andesite	—	Intrusive dikes and small plugs.
	<i>angular unconformity</i>		
Lower Tertiary	Lobo Formation	500	Conglomerate; reddish, cobble to boulder; minor sandstone.
Upper Cretaceous			
	<i>angular unconformity</i>		
Permian	Hueco Limestone	410	Limestone; dark gray, medium to massive bedded, fossiliferous.
	<i>disconformity</i>		
Mississippian	Rancheria Formation	220	Limestone, chert, shale; bedded chert well developed at top.
	<i>disconformity</i>		
Devonian	Percha Shale	250	Shale; olive gray. One-ft limestone bed at base.
	<i>disconformity</i>		
Silurian	Fusselman Dolomite	1,480	Dolomite; six alternating dark and light units, thin to thick bedded. Bedded chert at top. Silicified corals.
	<i>disconformity</i>		
	Cutter Member	180	Limestone/dolomite; limy and fossil-rich at base, dolomite increases upward, chert lenses near top.
	Aleman Member	150	Dolomite/limestone/chert; buff gray carbonate with abundant nodular and bedded chert. Fossiliferous.
	Montoya Formation		
	<i>disconformity</i>		
	Upham Member	60	Dolomite; dark gray, massive. Five-ft Cable Canyon sandy zone at base.
Ordovician			
	<i>disconformity upper</i>	190	Limestone and chert; medium to dark gray. Similar to middle unit but with abundant chert. Fossiliferous.
	middle	900	Limestone; light to medium gray, thin to medium bedded, many textural variations, very fossiliferous.
	El Paso Formation		
	lower	160	Dolomite; dark gray, thin to medium bedded, coarse crystalline, silty at base, abundant oncolites.
	<i>disconformity</i>		
Cambrian	Bliss Sandstone	110	Arkosic to quartzose sandstone. Grades upward to calcareous sandstone and silty limestone/dolomite.
	<i>nonconformity</i>		
Precambrian	syenite, granite diorite	—	Alkali-feldspar syenite and granite; interlayered diorite south of reverse fault.

Figure 3-3 Stratigraphy of the southern Florida Mountains, an uplifted block bordering the Deming sub-basin to the east (from Brown and Clemons, 1983).

Convergence during the Laramide orogeny (80-40 Ma) led to the development of foreland basins and the syn-orogenic deposition of the Lobo Formation overlapping the Late Cretaceous and Early Tertiary (De los Santos et al, 2018). The Lobo Formation has a measured thickness of ~150 m in the Florida Mountains (Brown and Clemons, 1983). A thick sequence of volcanic rocks blankets the Lobo Formation, recording pulses of magmatic activity that occurred in response to continental extension during the Eocene and Oligocene. In the Deming Basin and Florida mountains, this volcanic section attains a thickness of ~2000 m, and consists of mostly andesitic Rubio Peak Formation overlain by flow-banded rhyolites (Seager, 1995). These volcanics predate Basin and Range extension and are offset by range-bounding and intra-basin normal faults, often appearing in surface outcrops of uplifted footwall blocks. Further, the Tertiary volcanics serve as the depositional surface (i.e., basal contact) for the overlying alluvial sediments that accumulated in structural sub-basins of the Mimbres Basin. Timing of Cenozoic volcanism and block faulting in the Basin and Range province of southwestern New Mexico is summarized by Mack (2004) in Figure 3-4.

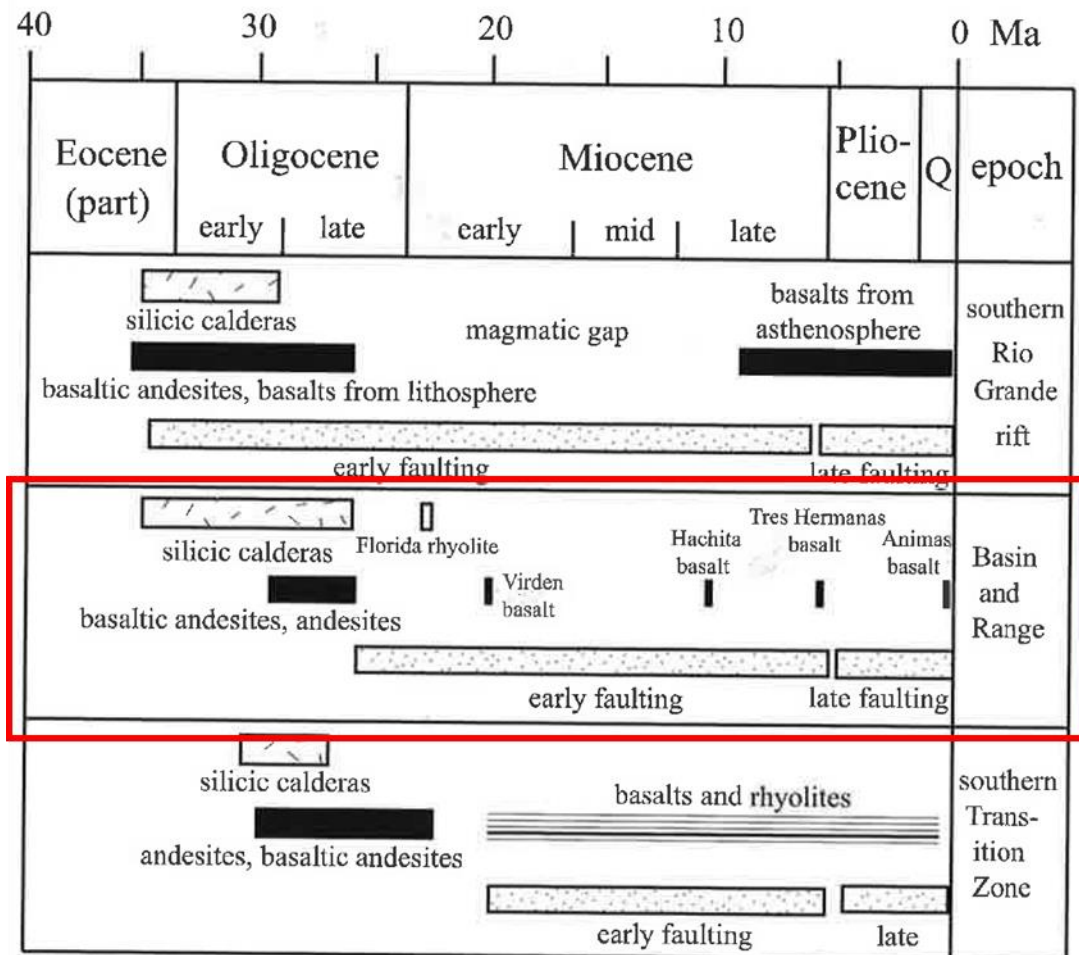


Figure 3-4 Timing of middle and late Cenozoic block faulting and volcanism in southwestern New Mexico as summarized from various sources by Mack (2004). The Mimbres Basin falls within the Basin and Range province (red box).

Structures in the Mimbres Basin and surrounding areas are dominated by north- and northwest-trending normal faults, resulting in a landscape characterized by upthrown horsts (ranges) and downthrown grabens (basins) (Figure 3-5). Basin geometries include symmetric full grabens and asymmetric half-grabens, depending upon the dip direction and magnitude of displacement across range-bounding faults (Figure 3-6). The N-S oriented normal faults are consistent with dip-slip motion and the E-W directed extension that prevailed from the mid-Tertiary through the present. The NW-SE oriented faults, however, are not compatible with pure shear extension in the present-day stress field, and likely represent Laramide-age contractional structures (e.g., Seager et al, 1997; Seager, 2004) that were subsequently reactivated in extension during the mid-late Tertiary. The linkage of NW and N trending structures can lead to complex fault geometries, as is the case for the Treasure Mountain – West Florida Mountains fault, a curving fault zone that marks the eastern and northern boundaries of the Deming sub-basin (Figure 3-5).

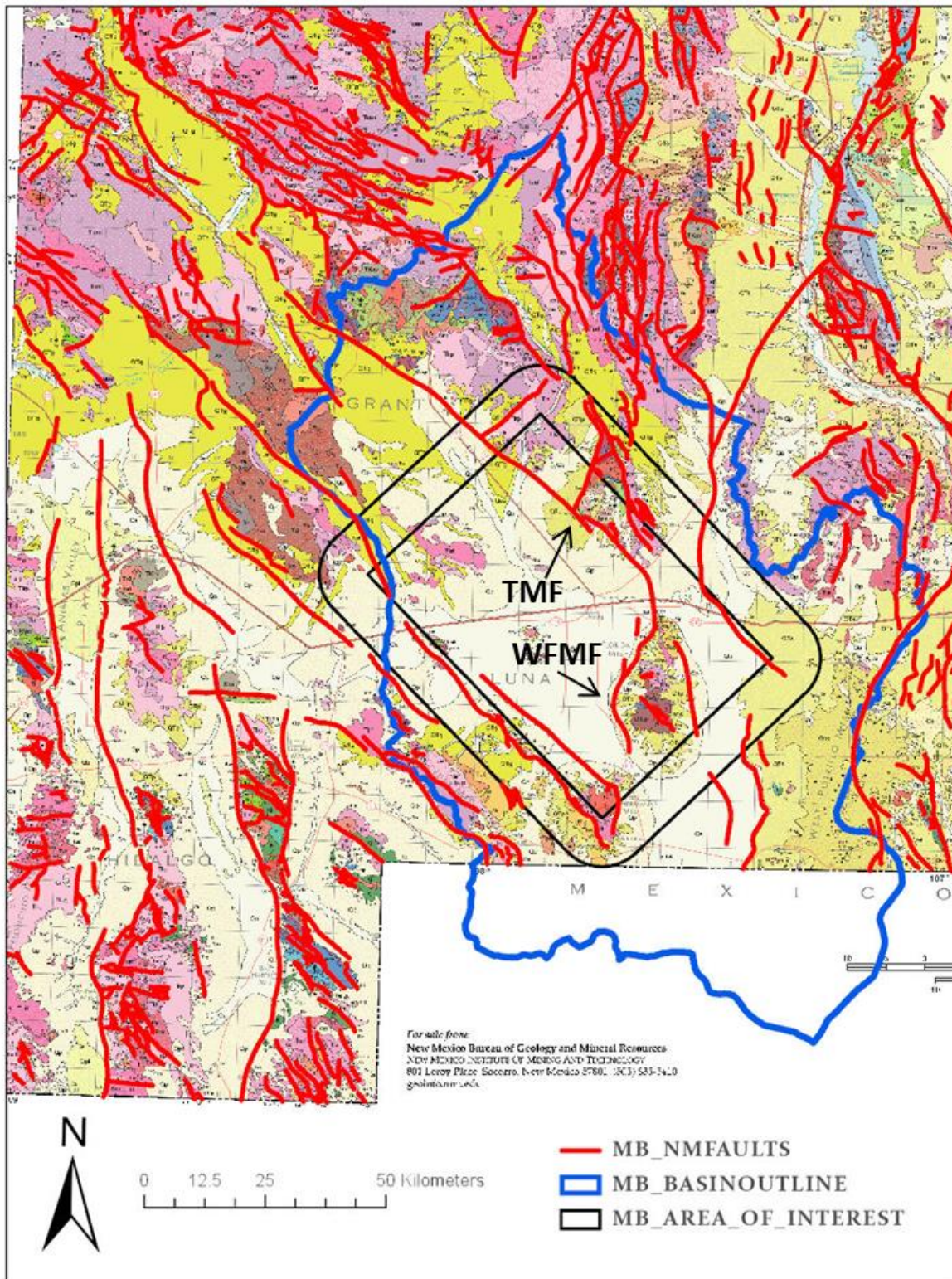


Figure 3-5 Portion of the Geologic Map of New Mexico (1:500,000) with outlines of the Mimbres Basin (blue line), focused area of interest (black box) and major faults (red). Arrows point to Treasure Mountain fault (TMF) and West Florida Mountain fault (WFMF).

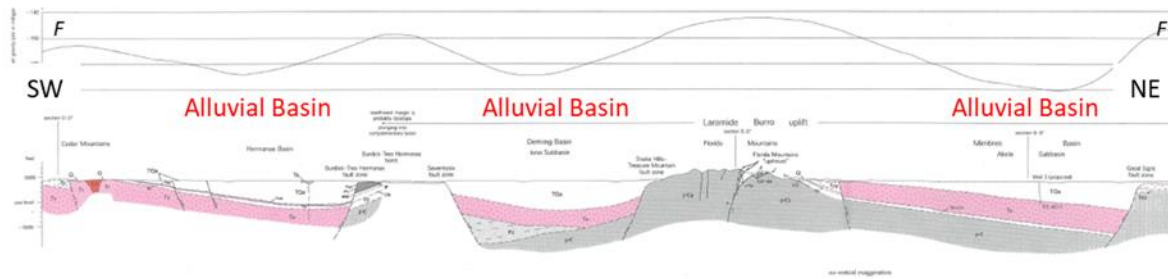


Figure 3-6 Geologic cross section from Mimbres Basin showing development of alluvial basins in the hanging wall blocks of range-bounding normal faults (Seager, 1995). Note basin geometries and offset of Tertiary volcanics (Tv) as well as Bouguer gravity plot above.

Seismic refraction surveys conducted by the USGS in southwestern New Mexico provide considerable insight into subsurface structural geometries, depth to crystalline basement and thickness of alluvial sediments (Ackermann et al, 1994; Klein, 1995). Three of the six regional surveys (Lines 4, 5 and 7) overlap portions of the Mimbres Basin (Figure 3-7a). The velocity section for Line 4 interpreted by Klein (1995) is shown in Figure 3-7b. Note the very low seismic velocities for alluvial sediments (< 3.5 km/s) and the high velocities for crystalline basement (> 4.5 km/s). Normal faults and the contact between crystalline basement and overlying sedimentary rocks can be identified and mapped from sharp contrasts in seismic velocity (Figure 3-7c; note 10:1 vertical exaggeration in seismic profiles). Our structural interpretation of seismic line 4 shows uplifted basement blocks, full and half-graben sub-basins and dipping normal faults that can be matched with faults mapped on surface geological maps (Figure 3-7d).

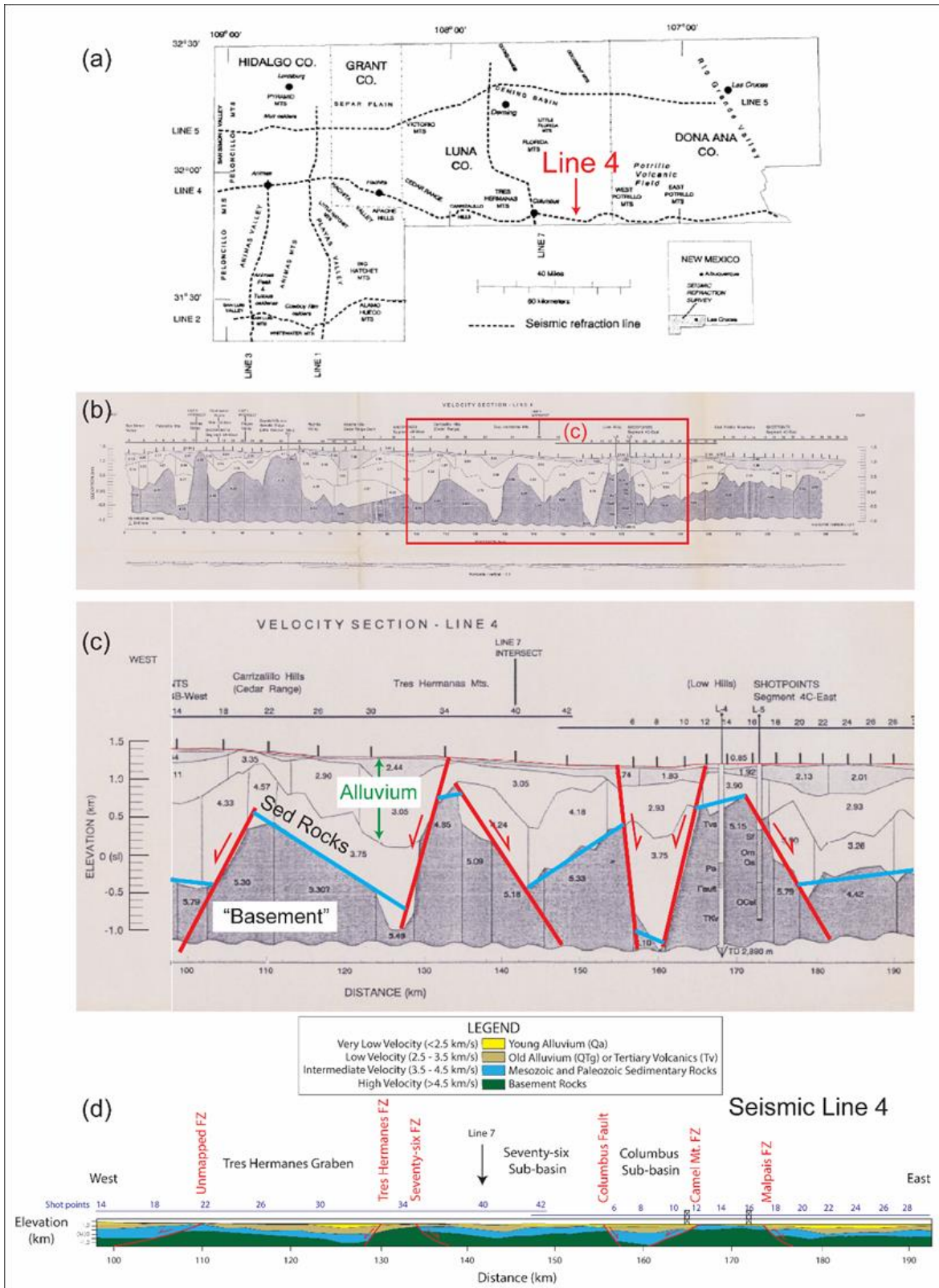


Figure 3-7 Seismic refraction surveys conducted by the USGS and their interpretations (Ackermann et al, 1994; Klein et al, 1995). (a) Location of the 6 refraction lines; (b) Velocity interpretation of Line 4 (10x vertical exaggeration); (c) Identification of faults, top to basement and alluvium thickness on portion of Line 4 crossing the Mimbres Basin (10x vertical exaggeration); (d) Our interpretation of seismic line 4 with no vertical exaggeration.

3.3 Alluvial Sediments of the Mimbres Basin: Lithologies and Thickness

As the alluvium is the host geological media for the repository, characterizing the lithologies, depositional facies and variations in thickness of the basin-fill sediments is crucial for building a viable geological framework model (GFM). This section provides a general overview of the basin-fill sediments in order to provide context for the spatial distribution and thickness of the alluvial sediments that accumulated in the fault-bounded sub-basins of the Mimbres Basin. A more detailed description of the alluvial stratigraphy is presented in Section 5.2 as part of the subsurface characterization for the GFM.

3.3.1 Stratigraphy and Lithofacies of Basin-fill Sediments

The Gila Group (or “Conglomerate”) is the stratigraphic unit commonly assigned to locally thick deposits of sediment that accumulated in Neogene basins of the American southwest (Mack, 2004). Its origin dates back to Gilbert’s expeditionary geological surveys of the Basin and Range (Gilbert, 1875). Subsequent mapping has identified numerous formation and/or members of the Gila Group, often restricted to individual basins due to variations in local geology, timing of volcanism and basin development (Figure 3-8). Deposition of the Gila Formation initiated as early as the Late Oligocene and continued through the Early Pleistocene (Kennedy et al., 2000). It is overlain by a relatively thin blanket of alluvium (mostly fluvial and lacustrine facies) deposited in the Quaternary (Love and Seager, 1996; Finch et al., 2008).

In order to maintain consistency with other studies and to correlate with Santa Fe Group sediments in Rio Grande rift basins, Hawley et al. (2000) and Kennedy et al. (2000) adopt the general subdivision of the Gila Group into Lower (LG), Middle (MG) and Upper (UG, UG1, UG2) units (Figure 3-9). Perhaps the most detailed lithostratigraphy for Gila and post-Gila alluvial sediments in southwestern New Mexico is proposed by Hawley et al. (2000) and Kennedy et al. (2000). They subdivide the Gila Group into twelve lithofacies and the post-Gila alluvium into five lithofacies, each with its own inferred depositional setting (e.g., alluvial fan, braided plain channel) and textural classes (e.g., silty clay, boulder gravel). The lithofacies of intermontane basin fill are grouped into three main hydrostratigraphic units: piedmont slope, basin floor and valley fill. The products of this description and classification are detailed surface maps and cross sections (Plate 1 of Hawley et al, 2000; Figure 3-10) that we used to build our model for the alluvial component of the GFM.

	Virден area	Alma basin, Mangas Trench	Gila Wilderness	San Lorenzo, Lake Roberts	Cedar, Florida, Tres Hermanas Mountains	southern Rio Grande rift
Quaternary						0.78
Pliocene	late 3.6	up p i l e a	Pearson Mesa Mbr		Camp Rice/ Mimbres/ upper Gila	pumice (3.1, 2.2, 1.5, 1.3) Camp Rice/ Palomas
	early		ashes (2.0, 2.1) Gila Cgl/ Alma Beds Harve Gulch basalt (5.6)			basalts (4.5, 3.1, 2.9, 2.1)
Miocene	late 5.3				basalt (5.2)	
	mid 11.2				Fanglomerate of Little Florida Mountains Florida Rhyolite (23.6)	Selden Basalt (9.6)
	early 16.4	G i l i a	Nichols Canyon Mbr basalt (20.6)	Gila Cgl		
Oligocene	late 23.8	o l d e r	Wilson Mine Mbr			Hayner Ranch
	early 28.5		Basaltic Andesite	older volcanic rocks		Thurman (27-27.4) Uvas Basaltic Andesite (26-28)
late Eocene	early 33.7		older volcanic rocks	older volcanic rocks	Basaltic Andesite	Bell Top
	37.0				older volcanic rocks	Upper Sed. 28.5 Lower Sed. 33.5 34.9

Figure 3-8 Correlation chart of middle and late Cenozoic basin fill sediments and associated volcanic rocks in southwestern New Mexico (From Mack, 2004). Ages in parentheses are in millions of years. Note especially the section for "Cedar, Florida, Tres Hermanas Mountains" which corresponds to the Mimbres Basin.

		Age	Basin-Fill Allostratigraphic and Lithostratigraphic units		Basin-Fill Hydrostratigraphic units (HSUs)		
QUATERNARY	L	Holocene	Informal Allostratigraphic units		Valley-Fill facies	Basin-Floor facies	Piedmont-Slope facies
					VA, AA, AR, AU, RA, RM, RCG, RG	AB, BF, BFP, LB, LS, LL, LP	PA, PAU
	M	Pleistocene	Lithostratigraphic units				
			West	East			
TERTIARY	NEOGENE	Pliocene	Gila Group ("Conglomerate")	Mimbres Fm.	Palomas Fm.	UG: Upper Gila hydrostratigraphic units	USF: Upper Santa Fe hydrostratigraphic units
						UG2 Basin Floor Facies	UG1 Piedmont Facies
		Miocene	Middle	Rincon Valley Fm.	Santa Fe Group	MG: Middle Gila hydrostratigraphic units	MSF: Middle Santa Fe hydrostratigraphic units
PALEOGENE	Oligocene	Lower	Hayner Ranch Fm.		LG: Lower Gila hydrostratigraphic units	MLG & MLS	LSF: Lower Santa Fe hydrostratigraphic units
		Many Units of Formation Rank		Basaltic Andesites Sedimentary and Volcaniclastic rocks Silicic and intermediate volcanic and plutonic rocks			
		Eocene					

Figure 3-9 Main lithostratigraphic and hydrostratigraphic units proposed by Kennedy et al. (2000) for Neogene and Quaternary basin-fill sediments in southwestern New Mexico.

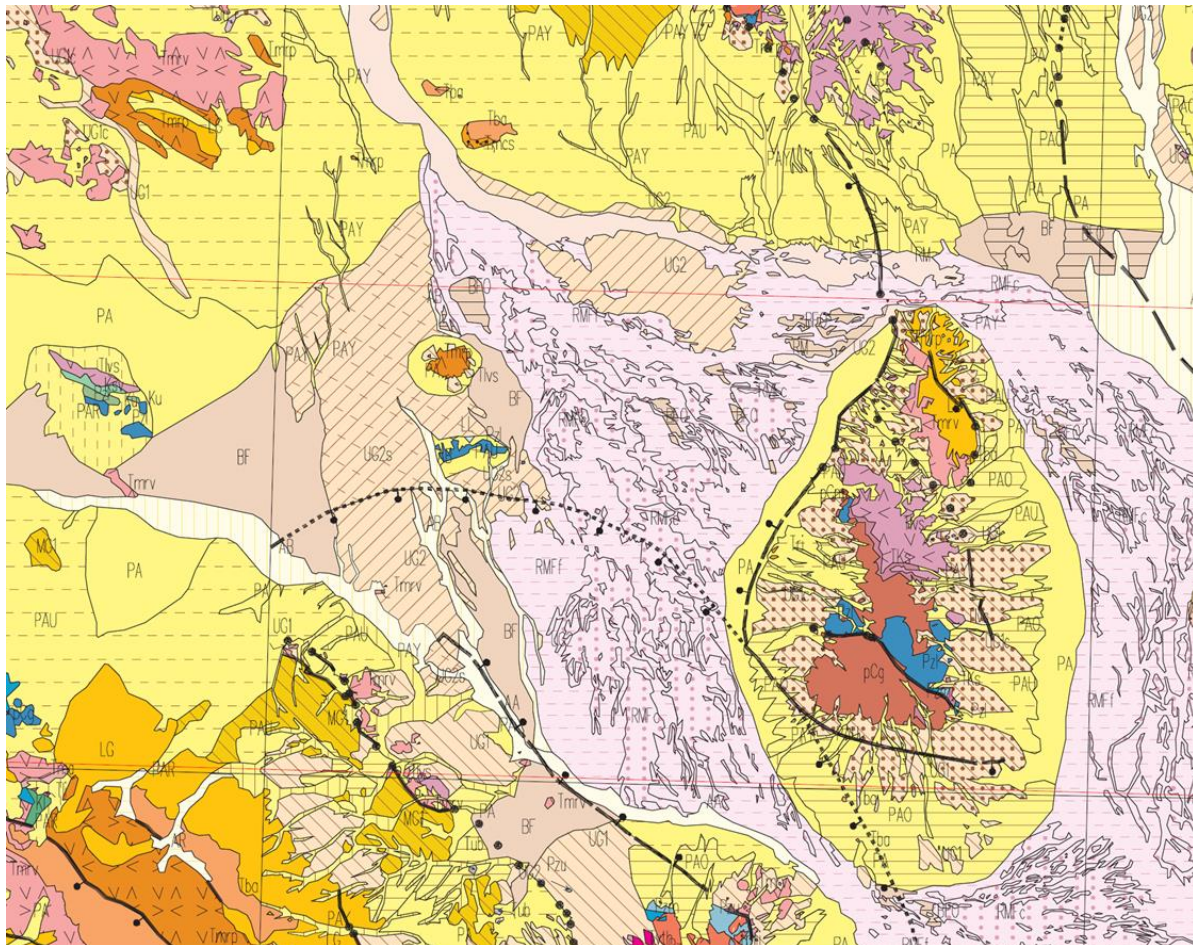


Figure 3-10 A small portion of Plate 1 from Hawley et al. (2000) depicting surface geology and hydrostratigraphic units of southwestern New Mexico focusing on the Deming sub-basin (our AOI for the GFM) and the Florida Mountains. Note the detailed mapping of the surficial alluvial deposits. Refer to Figure 3-5 for geologic context.

3.4 Thickness and Distribution of Basin-fill Sediments

Datasets that provide information on the thickness of alluvial sediments in the Mimbres Basin fall into two main categories: direct measurements of alluvium thickness from deep wellbores, and indirect methods via geophysical surveys. Most of the groundwater and monitoring wells in the Mimbres Basin are drilled to a maximum depth of several hundred meters, where they access the productive aquifer intervals of the Upper Gila (Mimbres Formation). However, around a dozen deep wellbores targeted the Paleozoic section for oil and gas exploration (Thompson et al, 1978; Clemons, 1986). These wells record the tops of the various bedrock units, in some cases including Precambrian crystalline basement. Around the City of Deming, two deep wellbores record thicknesses of 963 m and 1244 m, whereas ~ 30 km further west, a cluster of (3-4) wells consistently report thicknesses less than 100 m. The thickest interval of basin-fill sediments directly measured in the subsurface is 1417 m, encountered in a wellbore in the southeast corner of the basin, east Columbus. Details from the deep exploratory wellbores

relevant to our study are provided in Chapters 4 and 5. Although relatively few in number and scattered across the basin, these deep wellbores demonstrate the highly variable thicknesses of alluvium and also provide verification for thickness estimates derived from indirect geophysical measurements.

Ackermann et al. (1994) and Klein et al. (1995) produced 2D (cross-sectional) velocity structures for the six refraction survey lines to depths of ~ 3 km (Figure 3-7). The sections are divided into polygons roughly 4–10 km in horizontal extent, each assigned a specific acoustic compressional velocity (Figure 3-7 B, C). Klein et al. (1995) assigned a velocity range of 1.6–3.0 km/sec for “alluvium” (unconsolidated to poorly consolidated gravel, sand, clay and possibly thin volcanic layers), which is considerably less than velocities for sedimentary rocks (2.7–4.5 km/sec) and seismic basement (4.0–6.1 km/sec). Their cross sections reveal uplifted blocks and downthrown basins in the subsurface as manifested by vertically-shifted depths to high-velocity seismic basement (Figure 3-7 B-D). Further, the distribution of low-velocity alluvium provides insight into the geometry of structurally-controlled basins and estimates of thickness for the basin-fill alluvium. Klein et al. (1995) report maximum thicknesses of 200–600 m for sub-basins imaged by the 2D seismic surveys. For the Deming sub-basin within the larger Mimbres Basin, Klein et al. (1995) estimate a maximum thickness for alluvial sediments of ~500 m along a section of Line #5 east of Deming and west of the Florida Mountains. These are minimum thicknesses as Line #5 does not cross the deepest part of the sub-basin. Hanson et al. (1994) generated the first map of alluvial sediment thickness for the Mimbres Basin. They relied in large part on interpretations of the seismic refraction surveys in combination with well data to define geographic sectors of alluvial sediment thickness (Figure 3-11A).

One of the most valuable source of data for building the GFM is the three-dimensional map of alluvial-fill thickness generated by Heywood (2002) from an interpretation of gravity anomalies. Basin fill thickness for the Mimbres Basin was calculated by separating anomalies of isostatic residual gravity for low density alluvial fill (1800 – 2300 kg/m³) from regional bedrock gravity trends with higher densities. Measurements taken throughout the basin were used to compute alluvium thickness and to generate a mathematically continuous surface at a 1 km grid spacing (Figure 3-11 B, C). The resulting map shows (a) large areas of the basin are covered by a thin (< 100 m) veneer of alluvium; (b) Deep NW and N trending structural basins are located adjacent to range-bounding faults; and (c) alluvial sediment thickness in the structural basins is highly variable, with thickness in some localities exceeding 2000 m (Figure 3-11 C). Estimates of maximum thickness for basin fill sediments are 200 m for the Columbus sub-basin, 500 m for the Tres Hermanas graben, 874 m for the Seventy-six sub-basin and 2200 m for the Deming/Mangas Trench sub-basin (Figure 3-2; Figure 3-11). Heywood (2002) constrained thickness estimates calculated from gravity with exploratory deep boreholes, seismic refraction profiles and geologic maps. In general, there is good agreement between gravity-derived thicknesses and the other methods used to estimate alluvium thickness. The spatial distribution of alluvium thickness depicted in the maps of Heywood (2002) and their subsequent derivatives (Finch et al., 2008; Figure 3-11 D) provide us the opportunity to generate a 3D surface of the base of alluvium (top of bedrock) and map alluvium thickness in our area of interest, two essential components for building the GFM.

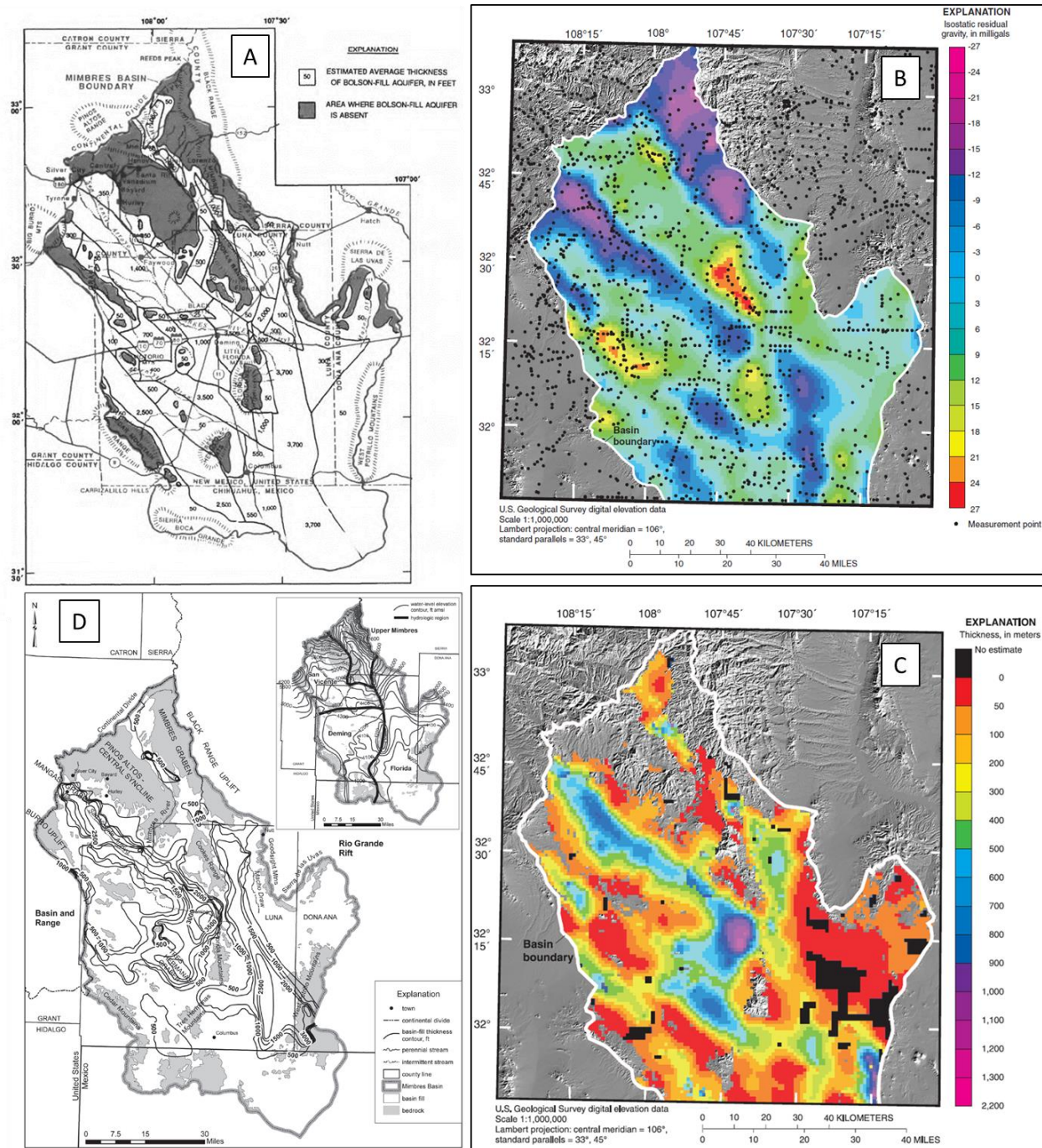


Figure 3-11 Maps of alluvial sediment thickness for the Mimbres Basin of southwestern New Mexico. (A) Geographic sectors of constant alluvium thickness (estimates) in feet from Hanson et al. (1994); (B) Gravity measurement points and contoured map of isostatic residual gravity used to calculate alluvium thickness (Heywood, 2002); (C) Contoured map of alluvium thickness in meters calculated from isostatic residual gravity map (Heywood, 2002); (D) Alluvium thickness map contoured in feet compiled from a variety of sources (Finch et al, 2008).

3.5 Hydrology of the Mimbres Basin

Surface elevations in the Mimbres Basin range from 1175 m above sea level in the playa floors of northern Mexico up to a maximum of 3051 m above sea level at Reeds Peak in the northern highlands of New Mexico (Hawley et al., 2000). The Mimbres Basin has an arid to semi-arid climate, with annual precipitations increasing from ~23 cm per year in low-lying areas up to 72 cm per year at higher elevations (Hanson et al, 1994; Finch et al, 2008; Hawley et al, 2000). Annual rainfall in the population center of Deming, New Mexico (located within our area of interest for the GFM) is 23.4 cm per year. As is typical for most arid regions, only a very small percentage (<2%) of basin wide precipitation contributes to ground water recharge (Hanson et al, 1994; Hawley et al, 2000).

The Mimbres surface water basin is bounded to the west and north by the continental divide, to the east by the Goodnight Mountains and West Potrillo volcanic field, and to the south by the extensive perennial-lake plains of the Bolson de los Muertos (Hawley et al., 2000). Kennedy et al. (2000) classify the Mimbres as an “open basin”, with surface water flowing down-gradient from piedmont slopes to axial streams that discharge into lower-lying areas outside of the basin. The Mimbres River is a perennial stream only along a 32 mile reach in the northern highlands. Elsewhere it and other stream systems in the basin are ephemeral (Finch, 2008). Occasionally high-magnitude precipitation events and snow melts result in the flow of the Mimbres River across the Deming sub-basin and into the Florida sub-basin via the topographic saddle between the Florida Mountains and Cooke’s Range.

Ground water in the Mimbres Basin generally flows from the northern highlands to the interior sub-basins and southward toward the U.S.-Mexico border (Hawley et al, 2000). It is therefore classified as a hydrologically “drained basin” in terms of groundwater flow (Eakin et al, 1976; Kennedy et al, 2000), with interbasin flow across sub-basins ultimately discharging into a regional sink (Figure 2-2; Figure 3-12A). Regional groundwater flow models provide widely varying estimates of annual recharge for the basin. Using a two dimensional regional flow model developed by the US Geological Survey, Hanson et al. (1994) estimate the mountain-front component of annual recharge at $6.8 \times 10^7 \text{ m}^3$ (55,300 acre-feet), with lesser amounts of recharge derived from spring and river infiltration, as well as underflow (interbasin flow) from adjacent valleys. Finch et al. (2008) estimate a total annual recharge of 29,000 ac-ft for the Mimbres Basin based on their calibrated three-dimensional ground water flow model. About 30% of the modeled recharge is from direct infiltration of precipitation into bedrock above elevations of 1525 m above sea level, referred to as “areal recharge”, whereas the remaining 70% is “mountain front recharge”. The latter refers to recharge from runoff redistributed from mountains to basin fringe sub-basins. Infiltration occurs in arroyos incised into the basin fill and in coarse-grained, high permeability facies of the basin fill adjacent to mountain fronts (Finch et al, 2008). Ground water recharge, however, is not distributed evenly across the Mimbres Basin. The San Vicente hydrogeologic region of Finch et al. (2018) accounts for 63% of total basin recharge, whereas the Deming and Florida regions only account for 26% and 5%, respectively (Figure 3-12B).

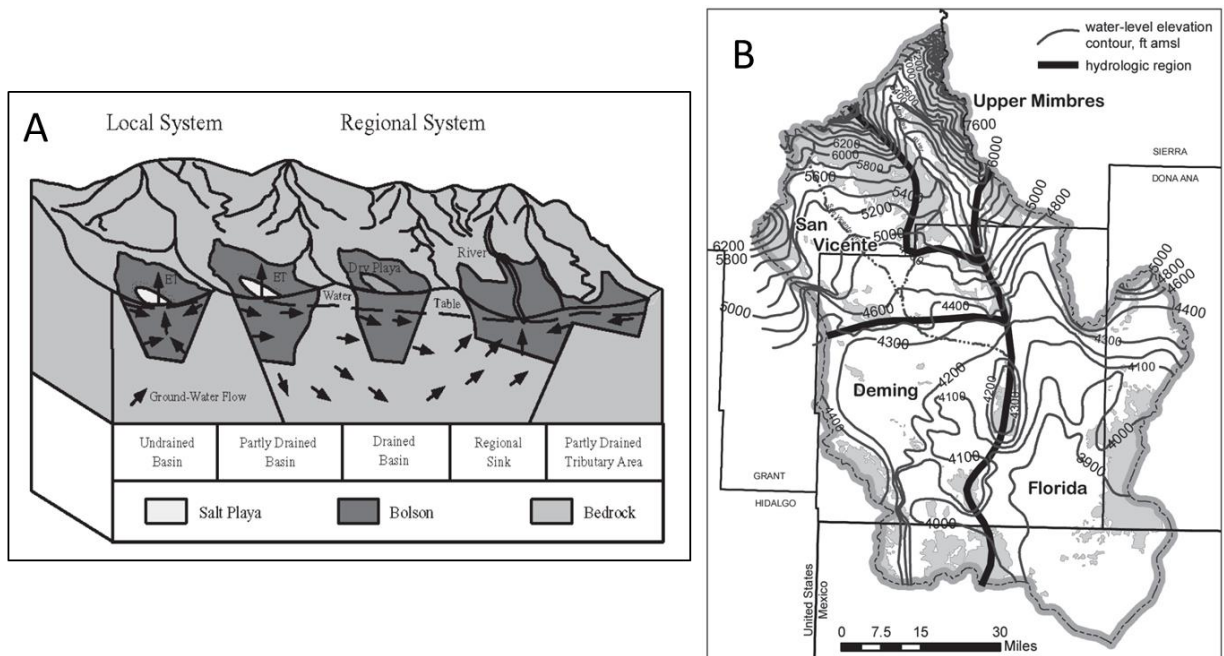


Figure 3-12 (A) Conceptual hydrogeological models for intermontane basins, including undrained, partly drained and drained basins. From Kennedy et al. (2000) modified from Eakin et al. (1976); (B) The four hydrogeological zones for the Mimbres Basin proposed by Finch et al. (2008).

Due to the arid climate and scarcity of surface water, the majority of water supplied for municipal, agricultural, mining and industrial usage comes from groundwater. According to Finch et al. (2008) and references cited therein, more than $1.2 \times 10^8 \text{ m}^3$ (100,000 acre-feet per year) of groundwater are pumped from the Mimbres Basin, with 94% coming from basin fill (alluvium and Gila Group aquifers) and only 6% from bedrock. This discharge via well pumping far exceeds the natural recharge for the basin estimated from hydrogeological models. Using the Aquifer Mapping Database developed by the New Mexico Bureau of Geology and Mineral Resources, Rinehart et al. (2015) examined changes in ground water levels over 10 year intervals for the Mimbres Basin. In some areas, changes in depth to groundwater exceeded 35 m over a 50 year period, with major areas of decline south of Deming and west of Columbus (Figure 3-13). They calculated a negative change in groundwater storage of approximately $3.1 \times 10^9 \text{ m}^3$ (2.5 million acre-feet) between the 1950's and the 2000's. Eight USGS-monitored wells near Deming, New Mexico indicate an average rate of decline of 0.23 m per year (City of Deming, 2009). Surface deformation in the form of earth fissures has accompanied groundwater withdrawal from the alluvial aquifers in the Deming sub-basin (Contaldo and Mueller, 1991). Measured lengths of these fractures range from 15 to 615 m, with some attaining depths greater than 13 m.

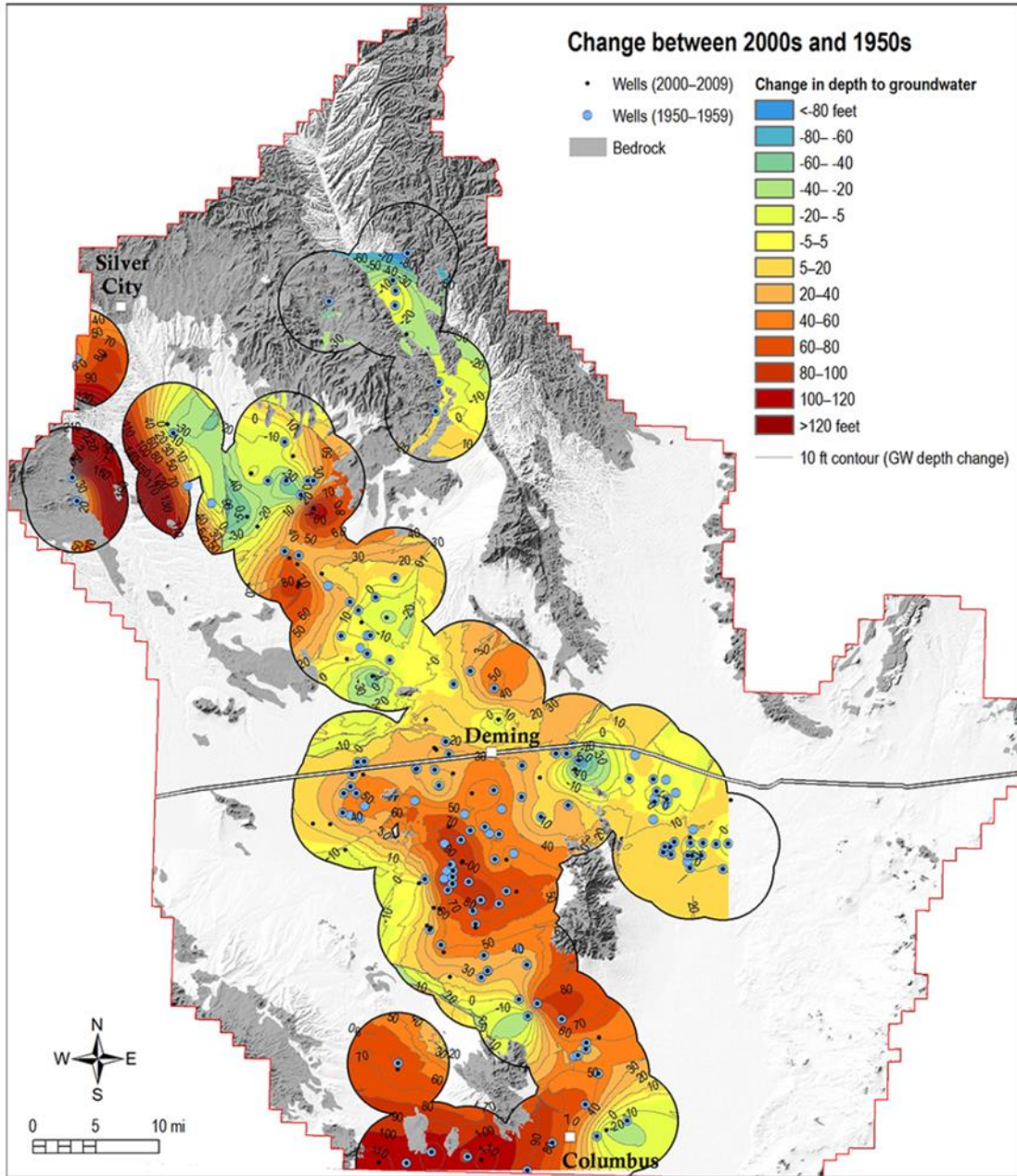


Figure 3-13 Differences in depth to ground water table between 1950-1959 and 2000-2009 for the Mimbres Basin. Kriging interpolations are shown in 10 ft contour intervals; areas of bedrock are dark gray. From Rhinehart et al. (2015).

4 Geo-Database Compilation

Our case study of the Mimbres Basin alluvium benefited greatly from data and analyses compiled by LANL for the DOE sponsored investigation of Geothermal Play Fairways (GPF) in New Mexico (Bielicki et al., 2015). The legacy project amassed datasets of water wells, deep exploratory wells, surface geologic maps, regional gravity, magnetics and aquifer information that enabled us to evaluate various alluvial basins in the Basin and Range province of New Mexico, and ultimately select the Mimbres Basin for our case study.

Once the Mimbres Basin was identified as the region of focus, we conducted a thorough literature search and acquired digital data from a variety of sources (e.g., USGS, NMBGR/NMT, RGIS, WebGIS, Esri ArcGIS Living Atlas) in order to characterize the surface topography and subsurface geology. Much of the data was available in digital, georeferenced format which enabled direct input into our ArcPro project. Other data sources such as map plates and journal figures were scanned and georeferenced so they could be added to the project geodatabase. The geodatabase maintains the location of each imported file and its relationship to other files. All imported data were referenced to a common geographic coordinate system (NAD 1983 UTM Zone 13) to maintain consistent georeferencing and visualization.

4.1 Imported Maps and Data for the Mimbres Basin

The geologic map for Mimbres Basin and surrounding areas was one of the first maps created as it is foundational for our project (Figure 4-1). It is a portion of the New Mexico Geological Map (1:500,000 scale) made available by the NMBGR/NMT in pdf and raster format. The raster files can be downloaded and imported directly into the ArcPro software, where different geologic units can be displayed and analyzed. A map of surface elevation is an integral part of the GFM because in areas covered by alluvium it defines the top surface of basin-fill sediments. The surface elevation map was created from the 30 m digital elevation model accessed from Resource Geographic Information System (RGIS) provided by the Earth Data Analysis Center of the University of New Mexico. It is presented in a map layout with traces of surface faults (Figure 4-2), one of the many shape-files that accompany the New Mexico Geological Map. A map showing the locations of shallow water wells compiled by the USGS and deep boreholes from the New Mexico Oil Conservation Division is shown Figure 4-3.

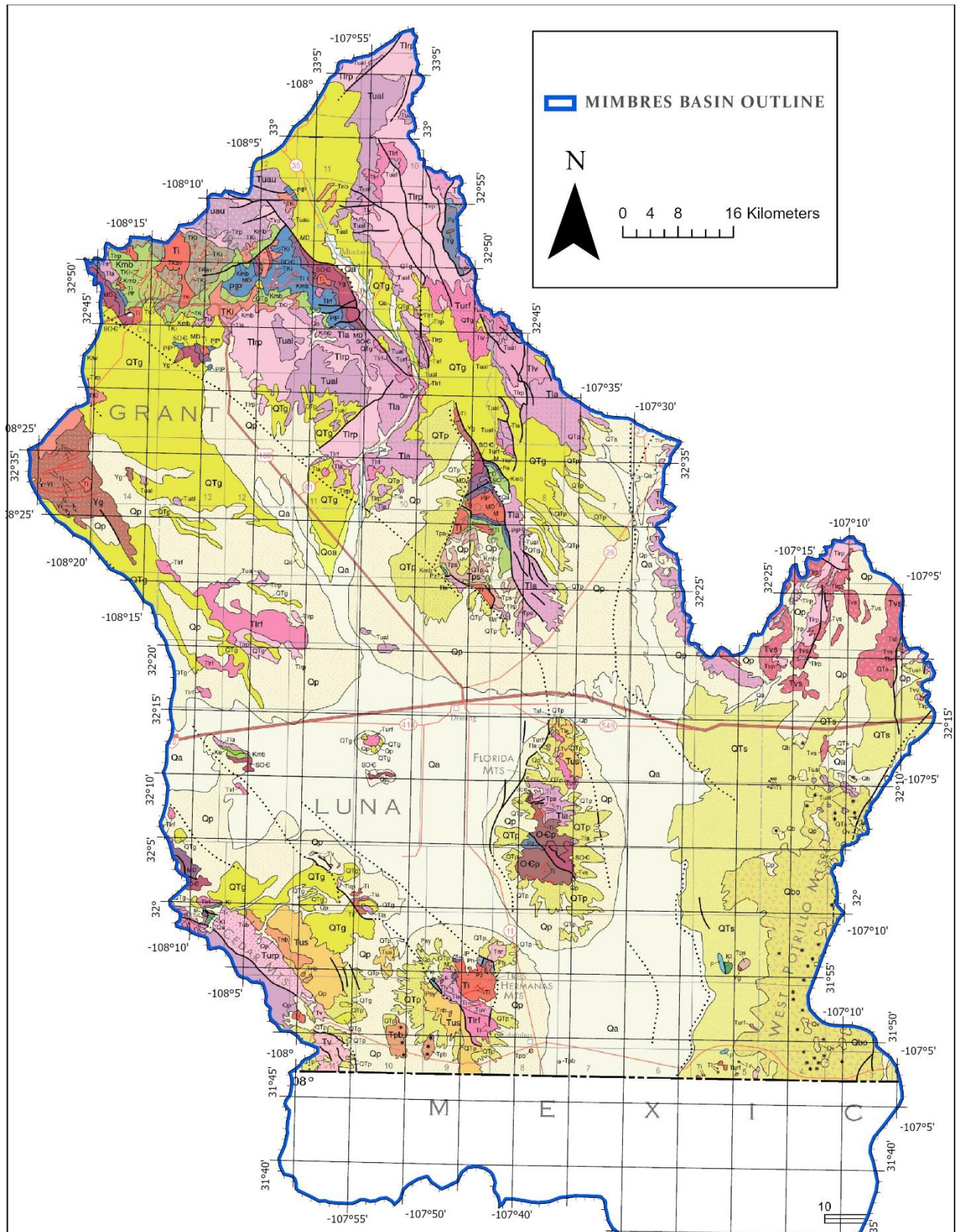


Figure 4-1 Geologic map for Mimbres Basin. This is a portion of the Geologic Map of New Mexico, from the New Mexico Bureau of Geology and Mineral Resources in cooperation with the U.S. Geological Survey (scale: 1:500,000).

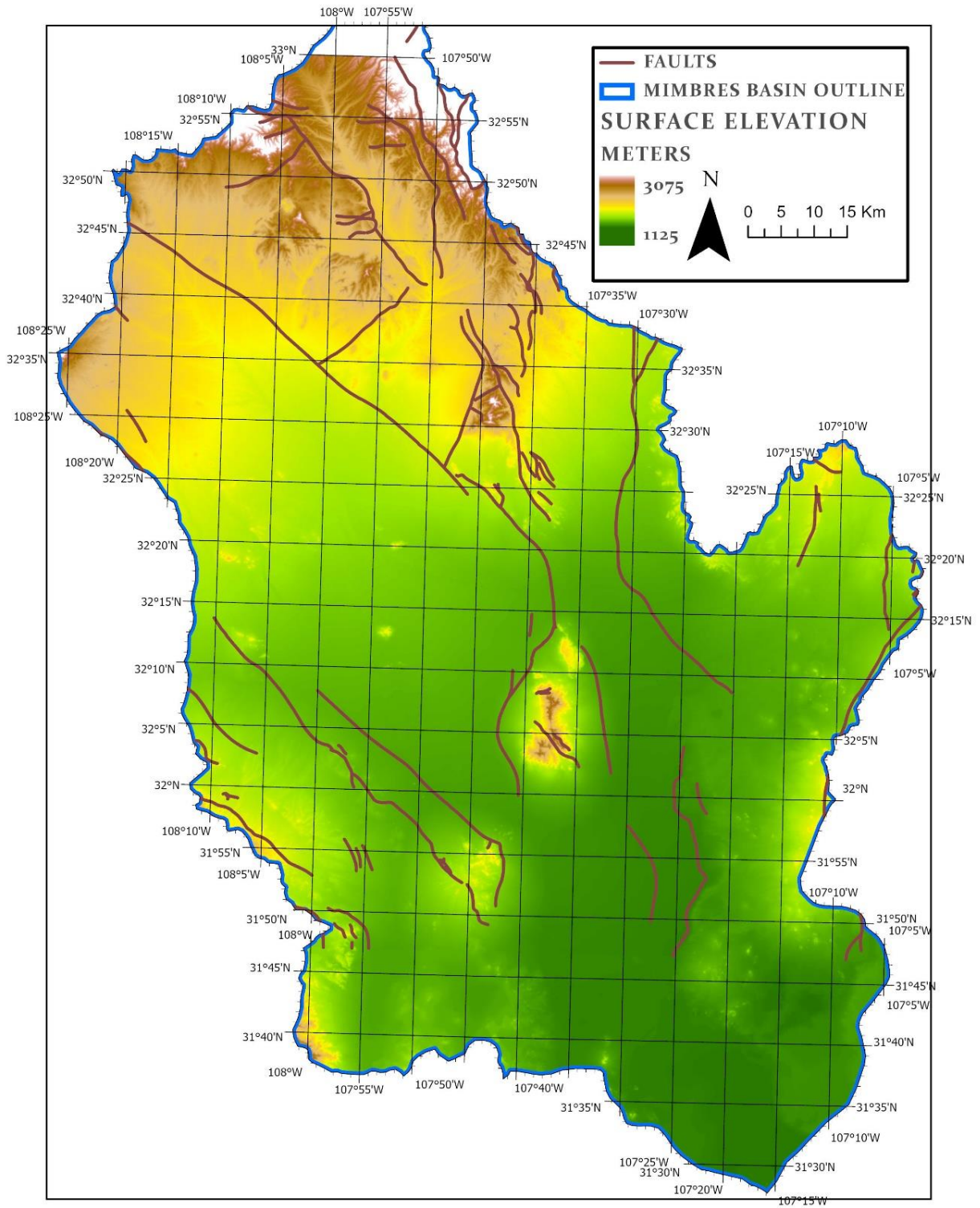


Figure 4-2 Digital elevation model (DEM) of surface elevation with fault traces in red.

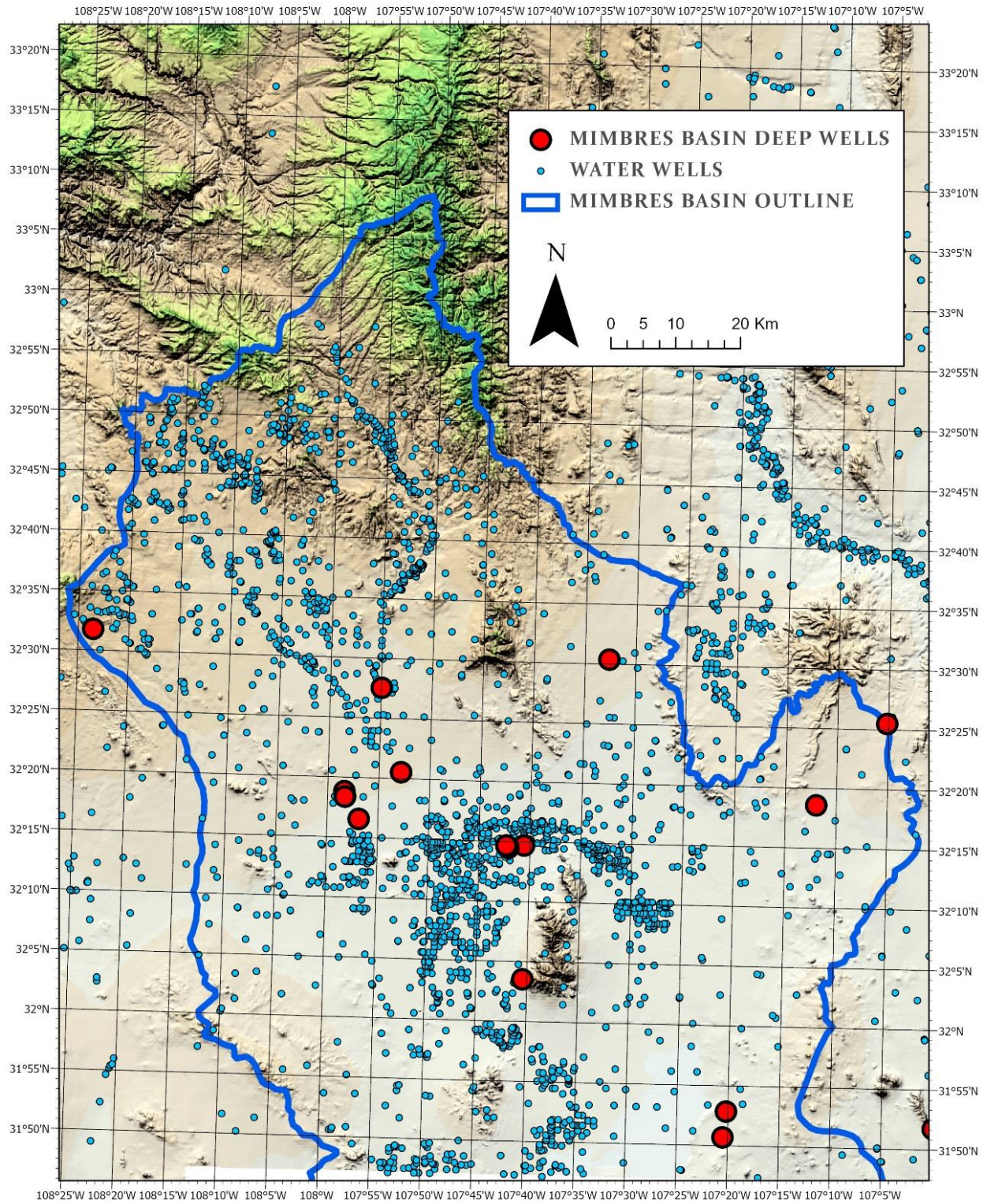


Figure 4-3 Map of water wells (blue dots) and deep boreholes (red dots) drilled in the Mimbres Basin and surrounding areas. The shallow water wells are used to map the depth to water table surface and the deep boreholes provide limited information about the pre-alluvium bedrock geology.

4.2 Defining the Area of Interest (AOI)

It was necessary for us to define an area of interest (AOI) within the larger Mimbres Basin that would allow us to focus on specific sub-basins for building the GFM and ultimately siting a hypothetical repository. This process allows us to exclude data that falls outside the prescribed boundaries of the AOI, thereby lowering processing and storage demands for data-intensive computations. The AOI is a 50 x 70 km rectangle with an additional 10 km buffer zone. The long side of the rectangle is aligned NW-SE, parallel to the dominant basin-wide structural trend (Figure 4-4). We added a 10 km buffer around the AOI in order to avoid edge effects in map computations along the boundaries. The AOI includes the Deming sub-basin and portions of the Seventy-six, Florida, and Mangas Trench (San Vicente) sub-basins (Figure 3-2). It was selected for its thick accumulations of alluvial sediments and to include the largest number of deep boreholes, which provide constraints on depths to underlying bedrock units. For completeness, main basin-bounding faults (Treasure Mountain, West Florida Mountain) and portions of uplifted footwall blocks are included in the AOI.

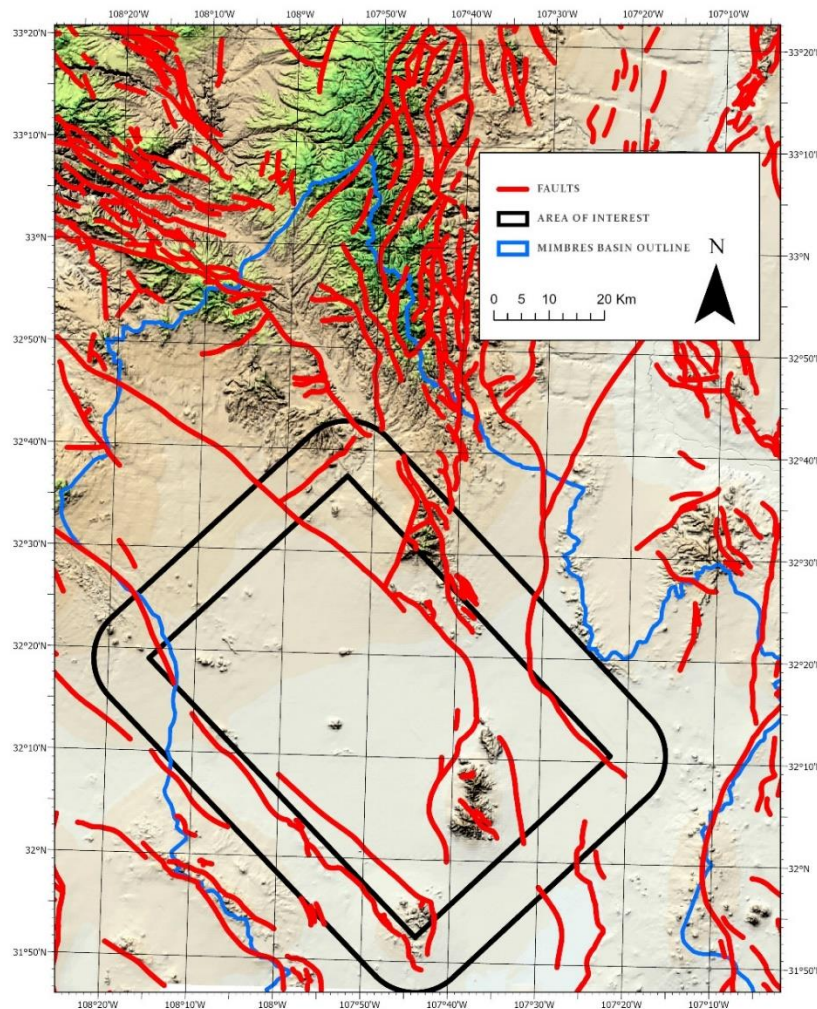


Figure 4-4 The area of interest (AOI) selected for detailed analysis within the Mimbres Basin (black rectangle 50 x 70 km surrounded by 10 km buffer).

4.3 Water Table Surface

The generic case for the alluvial basin repository calls for the waste to be buried in the unsaturated zone; therefore, generating an accurate water table surface is an important component of subsurface characterization. Further, constraining the hydrologic framework model (HFM) is crucial, as it determines the thickness of the unsaturated zone, groundwater gradient, and direction of groundwater flow. The hundreds of wells in the Mimbres Basin with water table measurements provide excellent constraints on the pre-development water table surface and groundwater movement in the AOI.

The USGS database of nearly 1000 water wells for southern New Mexico was imported into the GIS, which in addition to the latitude and longitude, includes the original depth to water table measurements taken from each well prior to pumping. We used the initial water table measurements in order to characterize the natural groundwater system prior to human intervention. The water table surface was generated through an interpolation technique (discretized thin plate spline technique of Wahba, 1990) offered in the ArcGIS Pro toolbox. The resulting map shows a general north to south movement of groundwater, from the highlands in the northern sectors of the Mimbres Basin to the low-lying basins to the south (Figure 4-5). In the alluvial plains surrounding the city of Deming and west of the Florida Mountains, the pre-development groundwater table is ~50 to 100 meters below the surface.

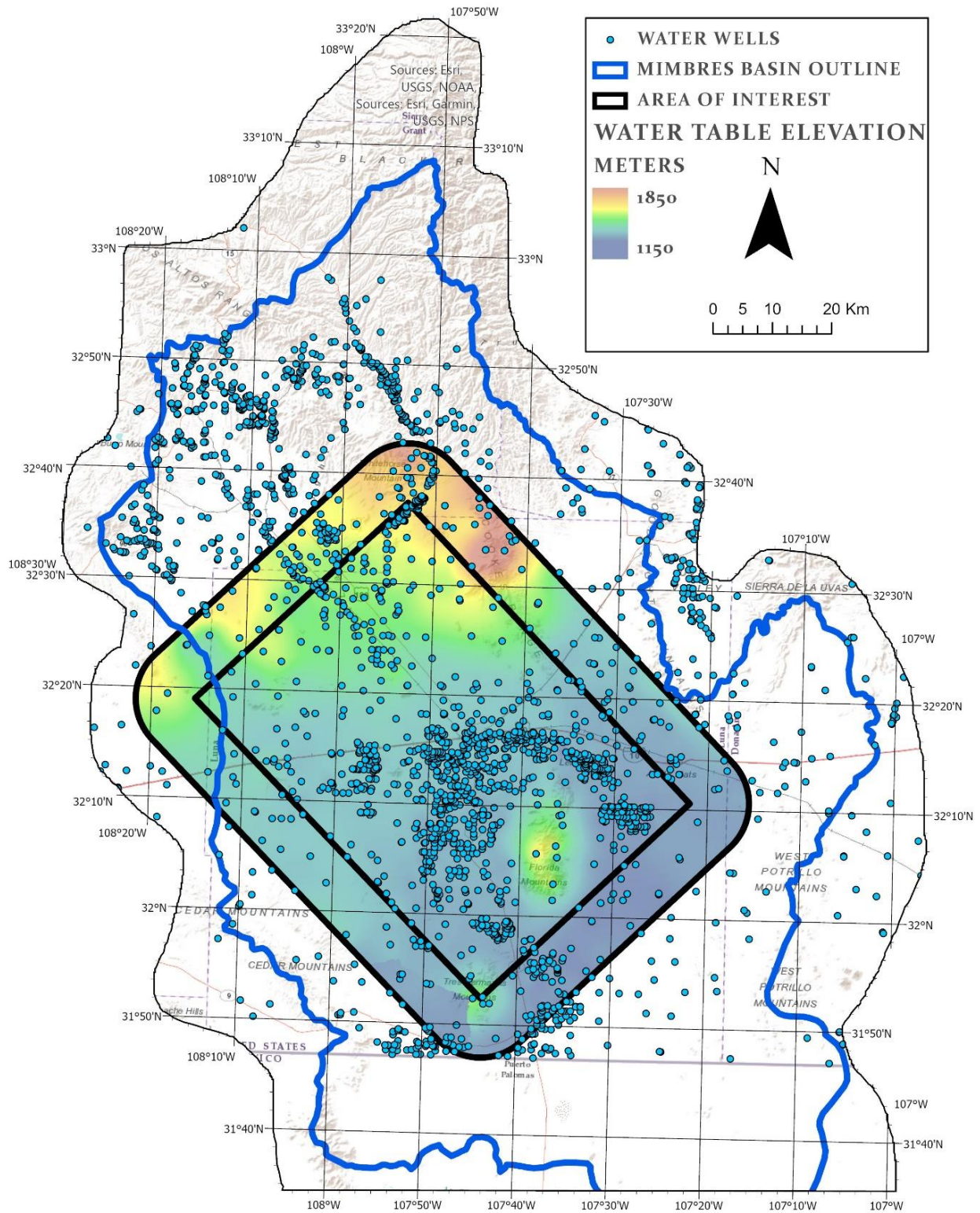


Figure 4-5 Map showing water table elevation in the AOI. We used the original water table depth recorded prior to pumping. Note the general regional groundwater flow from north (highlands) to south (basin floors).

4.4 Top of Precambrian Surface

A map of depth to Precambrian crystalline basement was generated in the same manner as the water table surface, using the tops recorded in the deep exploratory boreholes (Figure 4-6). However, of the approximately dozen boreholes in the Mimbres Basin that drilled into bedrock, only five report intersecting Precambrian basement. Thus, the resulting surface is poorly-constrained and unreliable for characterizing the Precambrian bedrock underlying the basin. As an example, the Precambrian surface map shows decreasing in elevation from the Deming sub-basin eastward across the Florida Mountains (Figure 4-6), despite crossing a major range-bounding normal fault resulting in the uplift of the Florida Mountains, with Precambrian rocks cropping out in the footwall block. Further, in the map generated by Broadhead et al. (2009) of the top of the Precambrian surface for the entire state of New Mexico, the Mimbres Basin is not contoured due to a lack of control points (Figure 4-7). Therefore, another method is needed to characterize the top of crystalline basement for the GFM in our AOI. The process we used is described in detail in Section 5.1, but can be summarized as creating geologically reasonable cross-sections, then exporting that information into JewelSuite using synthetic wells.

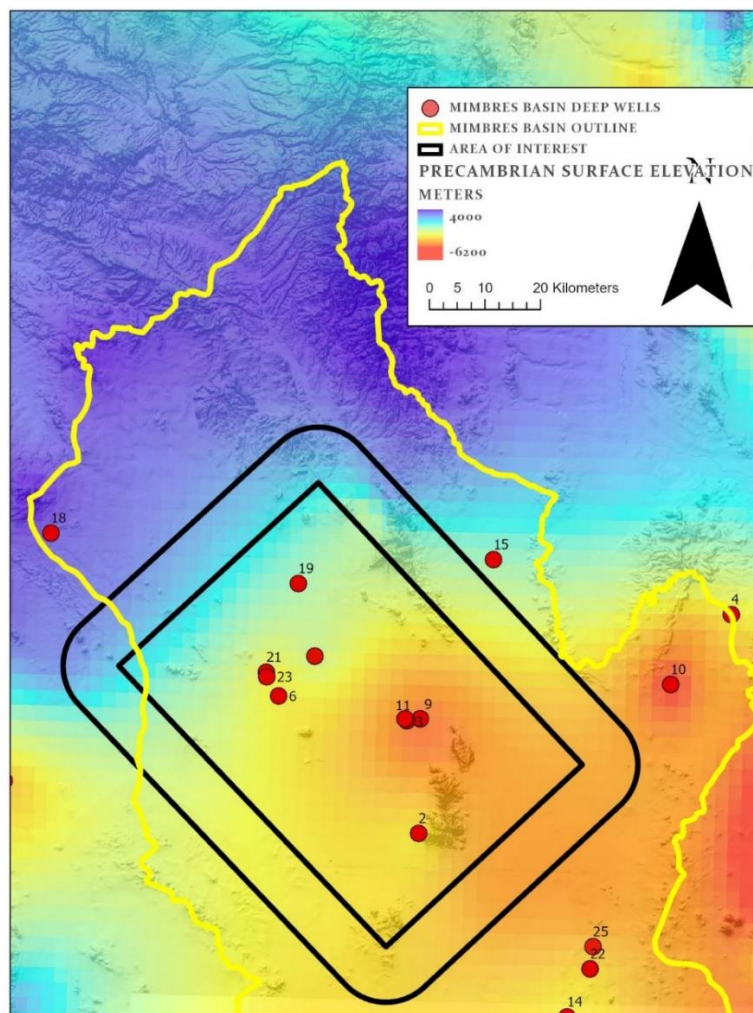


Figure 4-6 Map of top to Precambrian surface for the Mimbres Basin, using data from deep exploratory boreholes.

Structure on Precambrian Surface

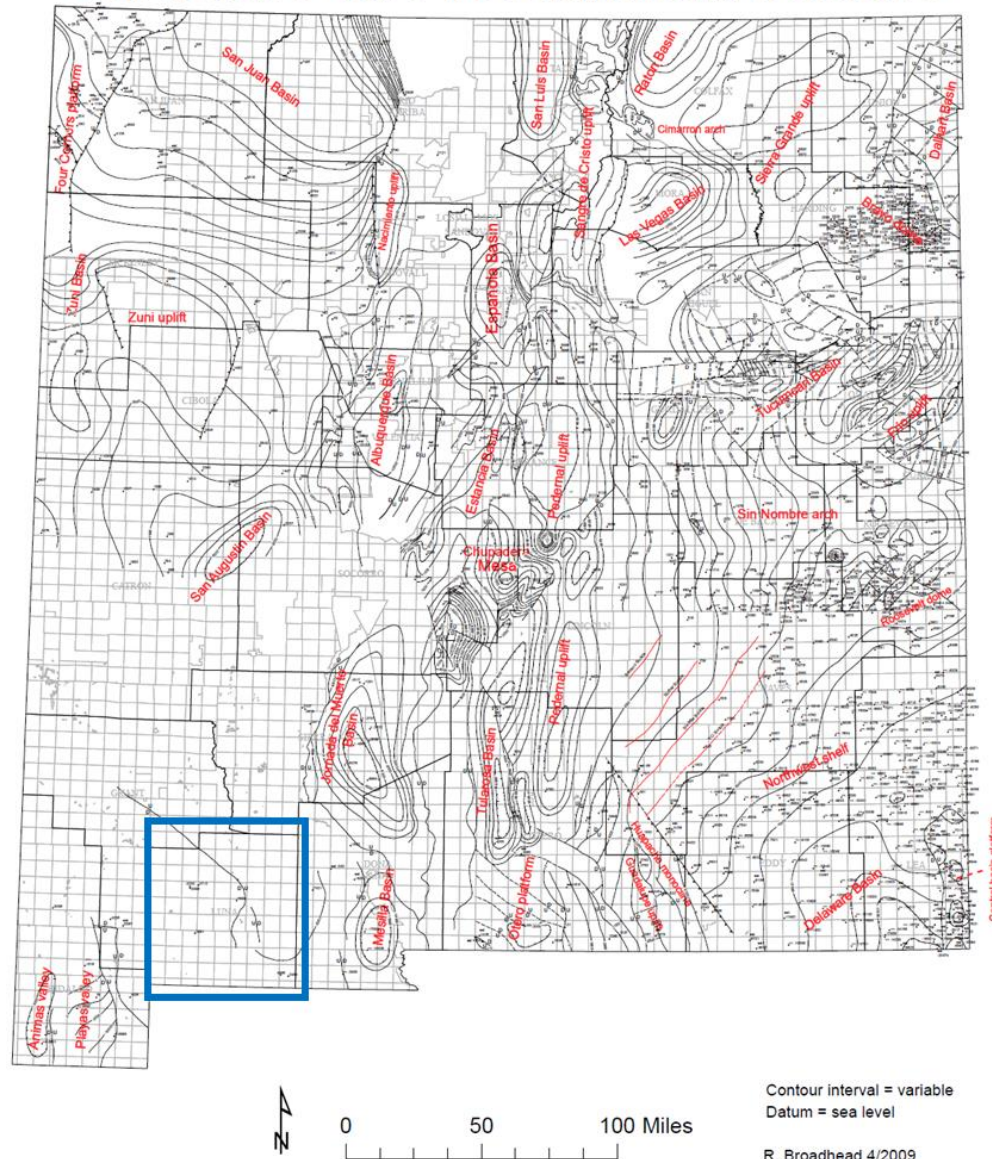


Figure 4-7 Structure map of top of Precambrian surface for the state of New Mexico from Broadhead et al. (2009). Note lack of contours in the Mimbres Basin (blue box) due to scarcity of data.

4.5 Alluvium Thickness and Base of Alluvium Surface

Establishing the contact between bedrock and alluvial sediments was accomplished using the raster dataset from the NMBGR/NMT Geologic Map of New Mexico (Section 4.1) and creating an SQL Query that excludes all units that are not alluvial or unconsolidated surficial deposits. The result is a binary map that distinguishes bedrock from alluvium (Figure 4-8). All contacts between bedrock and alluvium represent the zero contour line of alluvium thickness.

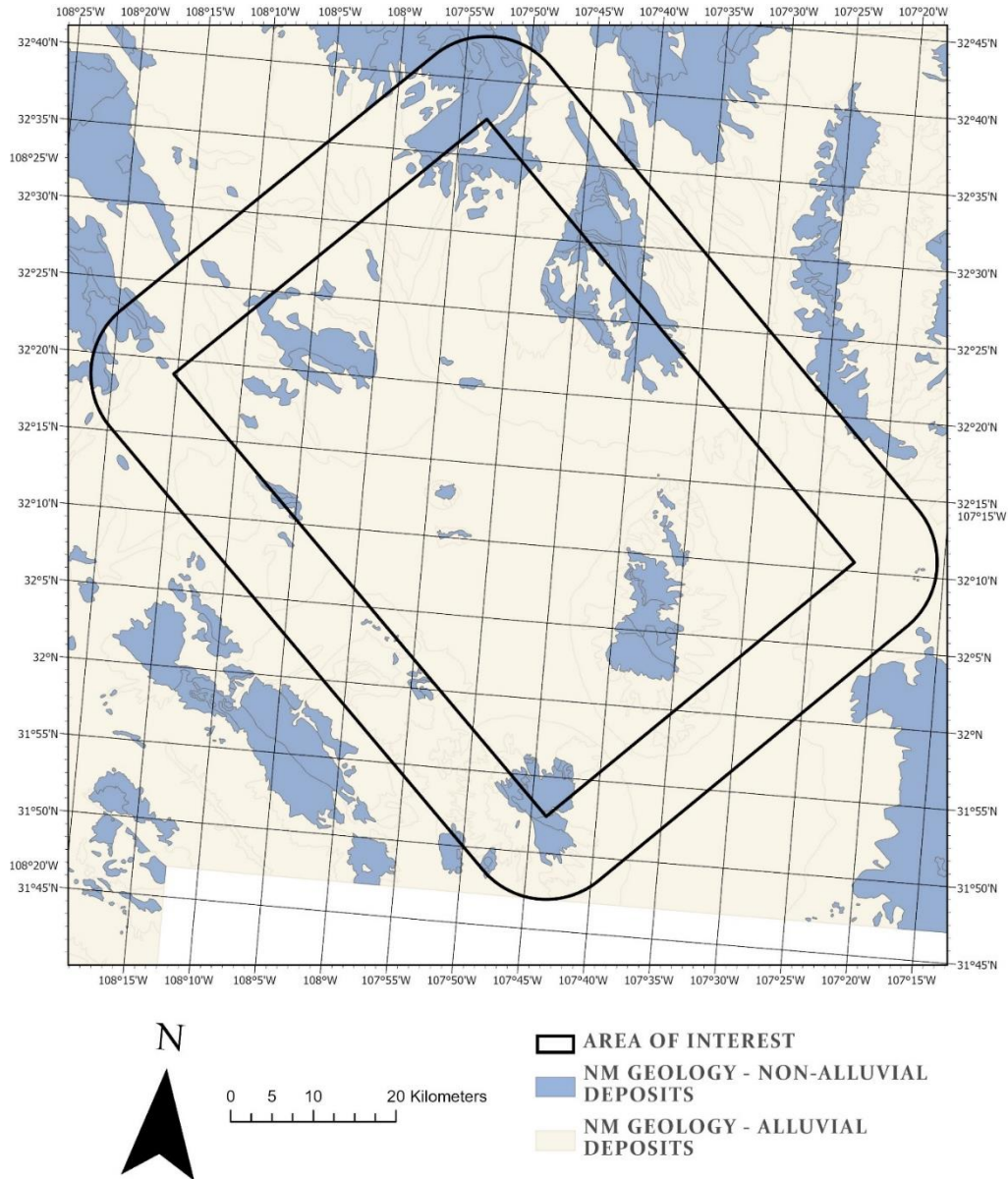


Figure 4-8 Map showing distinction between alluvial sediments (beige) and bedrock outcroppings (blue) for the AOI and adjacent areas.

Next, the contoured map of alluvium thickness from Finch et al. (2008) was scanned and georeferenced within the ArcGIS Pro project and carefully digitized to capture the geometry of the basin-fill sediments (Figure 4-9A). The resulting contour map of alluvium thickness corresponds well with the residual gravity map of Heywood (2002; Figure 4-9B), confirming the accuracy of the digitizing procedure. We then used the “Topo to Raster” tool to convert the digitized contour map into a raster map having a cell size of 50 m. The resulting map (Figure 4-10) shows the dramatic variation in alluvial sediment thickness across the basin. Thick accumulations of alluvium are found in NW and N linear trends that parallel, and abut against, the main basin-boundary faults. Note especially the thick section of alluvial sediments in the Deming sub-basin where a cluster of deep boreholes also helps to constrain the base of

alluvium and the underlying bedrock stratigraphy. As a note regarding units, thickness contours in the map of Finch et al. (2008) are in feet (Figure 4-9A), whereas the thickness map of Heywood (Figure 3-11D) and the maps of thickness and elevation presented in this report are in meters.

The surface representing the base of the alluvium was generated by subtracting the alluvial basin thickness map from the surface elevation map (Figure 4-11). This surface also represents the structure map for the top of the Tertiary volcanic sequence (Tv) in the subsurface. It is an important element for the GFM and defines a major hydrologic boundary as it separates basin-fill sediment from solid bedrock.

As explained in Section 5.1.3, we use the digitized alluvium thickness map as one of many inputs to build the structural cross sections, and ultimately the GFM (Section 6). It serves as an excellent starting point for characterizing the basin geometry.

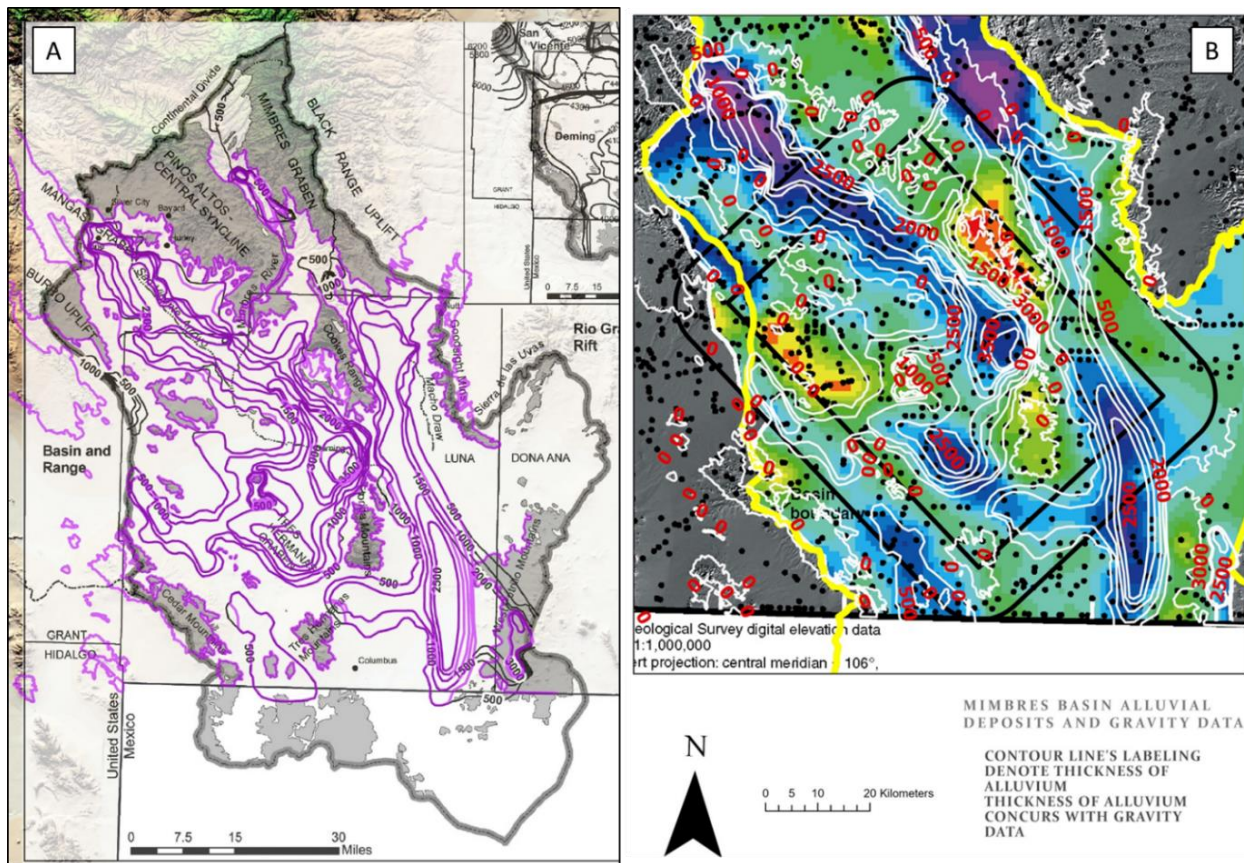


Figure 4-9 Procedures for generating alluvium thickness map for the Mimbres Basin. (A) Georeferenced map of alluvial sediment thickness from Finch et al. (2008) with thickness contours (purple) digitized in ArcPro. (B) Digitized contours of alluvium thickness (white) superimposed on isostatic residual gravity map of Heywood (2002) showing very close agreement. Gravity lows (purple-blue) correspond to thick alluvium whereas gravity highs (yellow-red) correspond to uplifted basement blocks, i.e., thin or no alluvium.

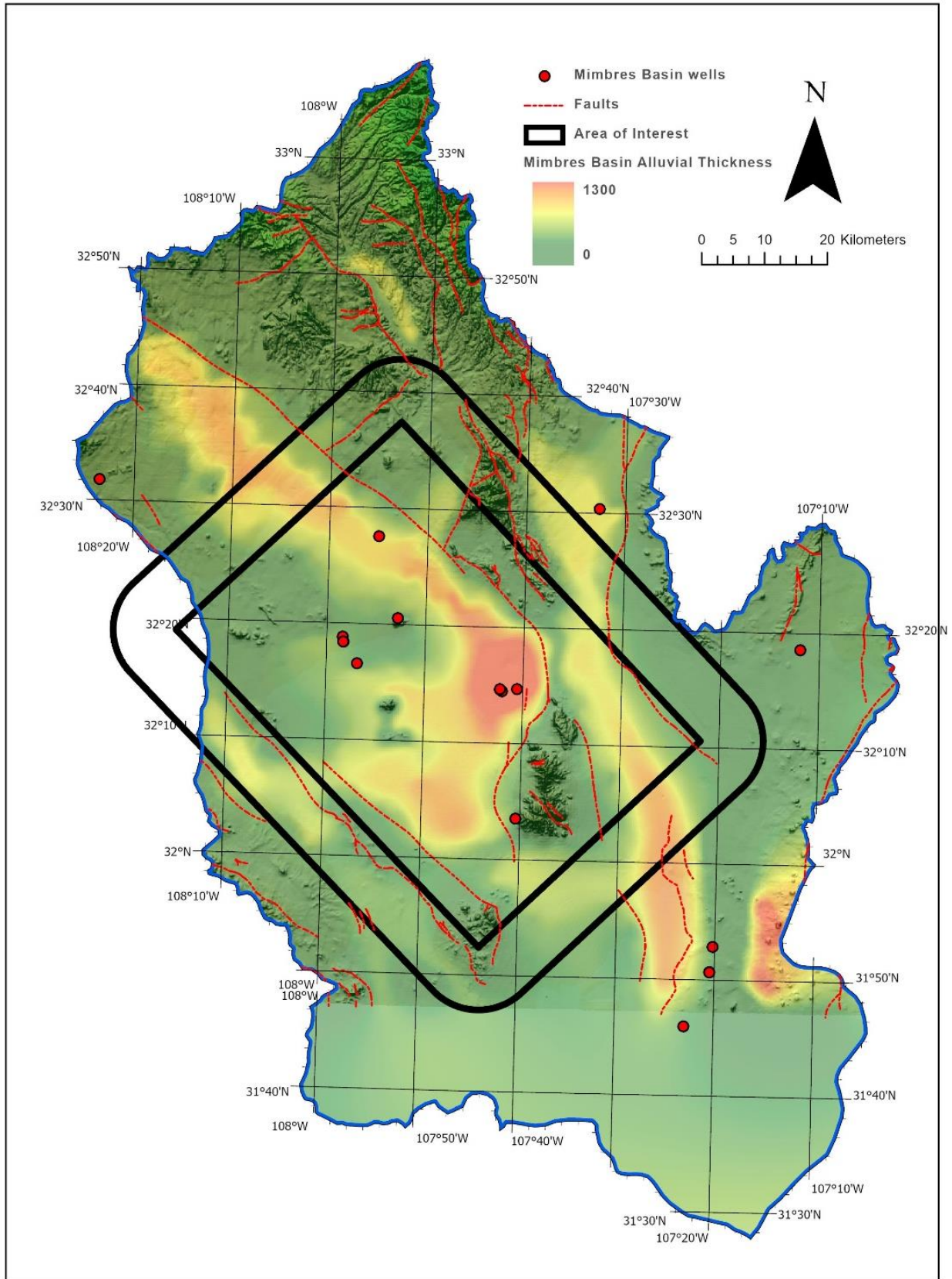


Figure 4-10 Map of alluvium thickness for the Mimbres Basin derived from digitizing the contour map of Finch et al. (2008).

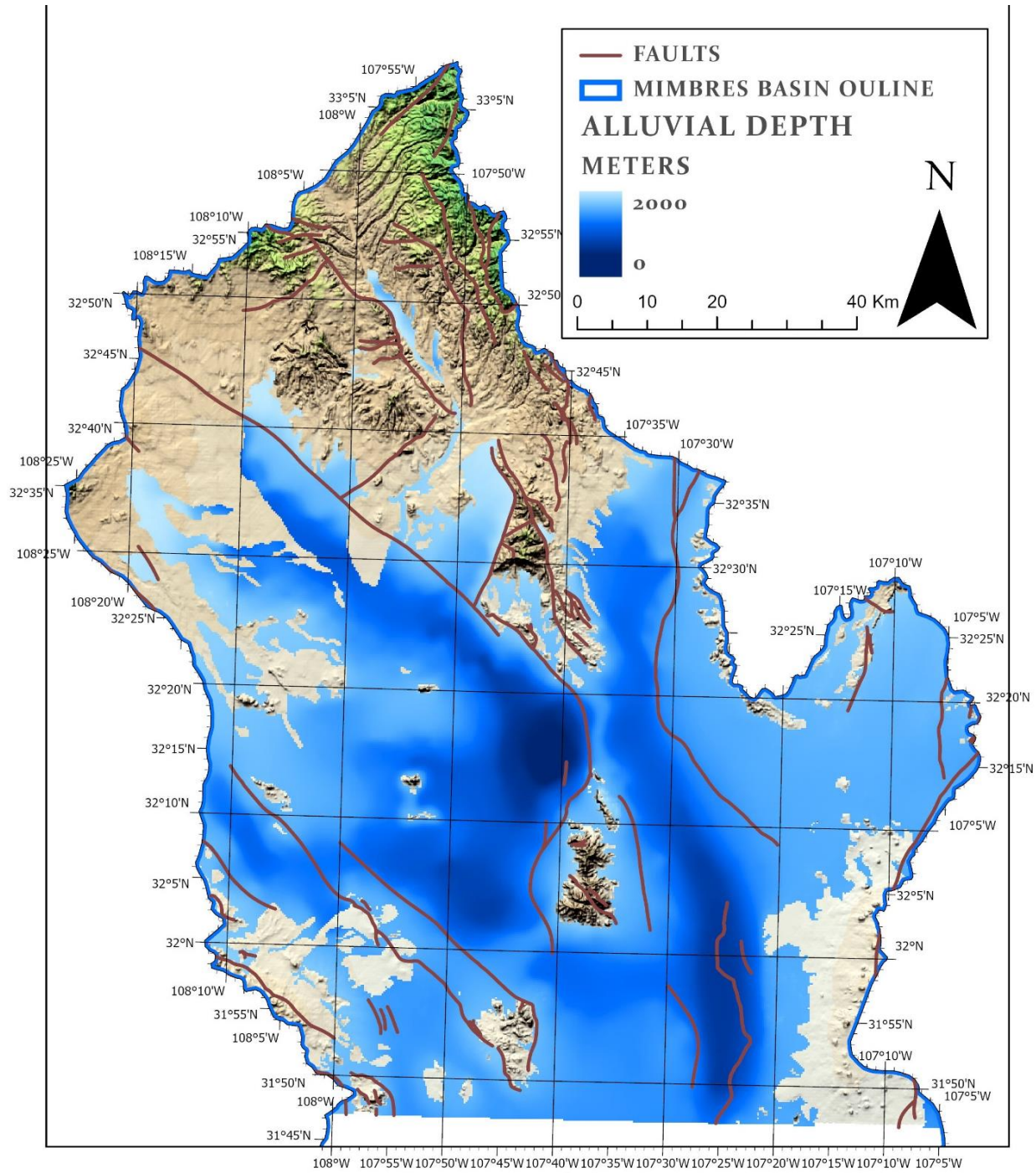


Figure 4-11 Map of depth to base of alluvium created by subtracting the alluvium thickness from surface elevation.

4.6 3D Visualization of Surfaces

The surfaces generated in the GIS are visualized in three dimensions in Figure 4-12. All of the surfaces are presented in units of elevation with respect to sea level, and are offset by an arbitrary vertical distance to enhance the visualization. Note that in the Mimbres Basin the water table is relatively shallow and in real space sits just below the ground surface and far above the base of alluvium surface. The topography displayed by the base of alluvium surface shows the location and geometry of the deep, linear-trending sub-basins that accommodated thick accumulations of basin fill (Figure 4-12).

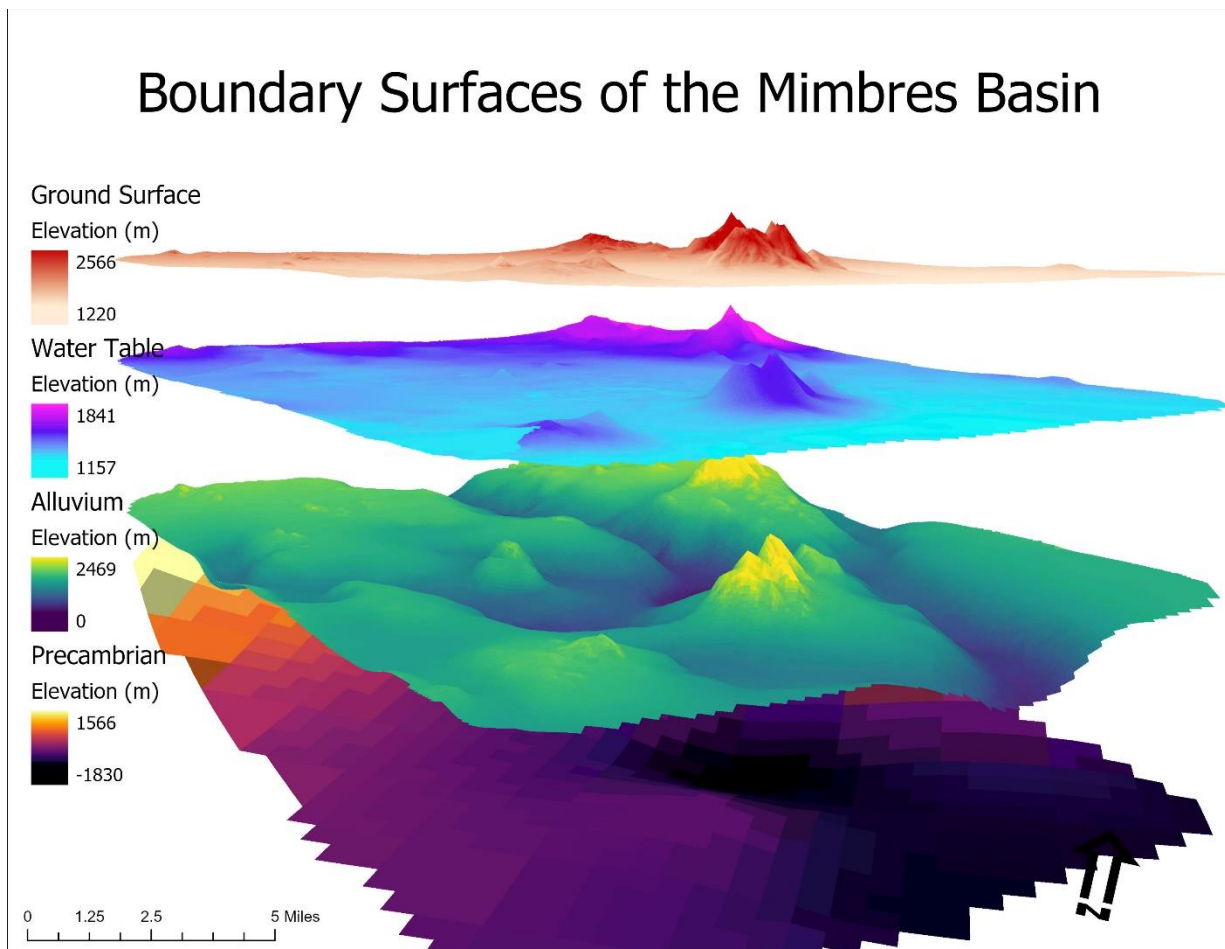


Figure 4-12 Three-dimensional visualization of the ground surface, water table, base of alluvium and top of Precambrian.

5 Subsurface Characterization for GFM Input

The subsurface characterization falls into two main categories – the structural geometry of the Precambrian through Tertiary bedrock and the nature of the alluvial sediments that filled the structural basins. They are presented below in two separate sections, with the structural characterization in Section 5.1 and the alluvium characterization in Section 5.2.

Given that the automated tools for interpreting raw data and incorporating them into a GFM produced geologically unrealistic results, we used a different method. This method uses classical geological techniques such as cross-section creation and analysis, which is imported into JewelSuite with the use of synthetic well data created from those cross-sections, resulting in a more geologically plausible GFM. We detail the method below, starting with the geologic data used for the subsurface characterization, the analysis of that data, and then importing into JewelSuite. We also discuss how this process resulted in the identification of previously unidentified faults within the Mimbres Basin, and its effects on repository siting.

5.1 Structural Characterization of Bedrock

5.1.1 Overview

The structural model is the foundational framework for the GFM, and can be envisioned as the “container” that will be filled with alluvial sediments such as sand, gravel and silt. The container develops in response to movement along range-bounding faults, thus the steep sides of the container are likely normal faults and the bottom of the container is the tilted upper surface of downthrown bedrock, capped by Tertiary volcanics. The structural model defines the basin geometry–orientation, shape and depth of sub-basins within the larger Mimbres Basin, and is the cumulative product of tectonic activity since at least the early Tertiary.

Building a geologically viable structural model requires the integration of all available sources of data. For the AOI in the Mimbres Basin, the following data sources were incorporated into the structural characterization study:

- Surficial geologic maps
- Deep exploratory wellbores
- Seismic refraction surveys
- Gravity surveys
- Tectonic and basin history

Each data source provides valuable insight and makes important contributions to the structural model, although each method has limitations. Geologic maps from the state of New Mexico at scales of 1:500,000 and 1:125,000 (Seager et al., 1982; Seager, 1995; Geologic Map of New Mexico, 2003) supplemented by map plates found in various publications (Hanson et al., 1994; Hawley et al., 2000; Heywood, 2002) delineate the spatial distribution of bedrock and alluvial units at the earth’s surface (Figure 4-1 and Figure 4-8). They are often accompanied by regional

cross sections which offer interpretations on structural style of deformation and basin geometry (e.g., Figure 3-6). The geologic maps also provide the locations of major faults, stratigraphy, lithologic descriptions and bedding orientations where bedrock is exposed on the surface. Main limitations are the inability to constrain stratigraphic units and their thicknesses in the subsurface, as well as to constrain subsurface basin geometry.

Deep exploratory wells provide the depth to stratigraphic tops, unit thicknesses in the subsurface, missing and/or repeated sections and confirmation of alluvium thickness for calibration of indirect geophysical methods. The main limitation is their scarcity in numbers, with only eight deep wellbores in the AOI (Figure 5-1). Confusion arises from inconsistencies in stratigraphic nomenclature and varying depths for formation tops picked by different operators. Seismic refraction lines are excellent at identifying faults in the subsurface, estimating depth to basement and defining basin and range geometries. They are limited to two-dimensional, vertical sections to depths of ~3km and do not traverse the deepest parts of the sub-basins (Figure 5-1). Further, the overlap in seismic compressional velocity between the older alluvium (QTg, i.e., Gila Formation) and Tertiary volcanics (Tv) makes distinguishing between basin fill sediments and underlying bedrock difficult (Figure 5-2). The gravity surveys yield maps of alluvium thickness throughout the basin (Figure 5-1d), an invaluable contribution which can be used to map the elevation of the base of alluvium (top bedrock) in three dimensions (Figure 4-11). It is the only technique that can provide reliable estimates of maximum alluvium thickness for each sub-basin. However, gravity survey data cannot directly image faults in the subsurface and depict an unrealistically smooth surface for the base of alluvium, likely the product of averaging physical properties and uneven bedrock topography. As is the case for seismic velocities, alluvial basin fill and Tertiary volcanic rocks have similar (overlapping) densities, and thus differentiating these lithologies in the subsurface on the basis of gravity data is problematic (Heywood, 2002).

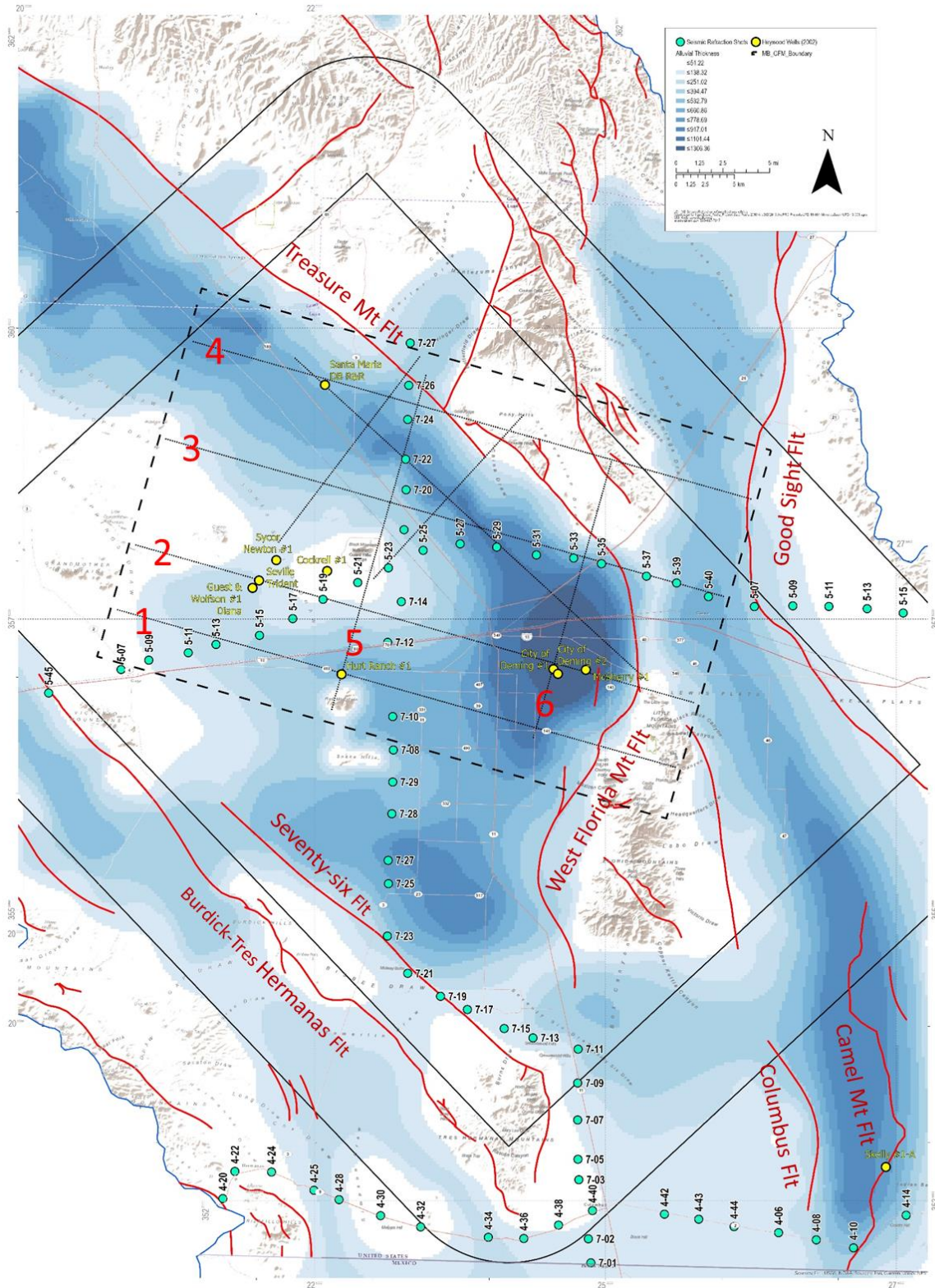


Figure 5-1 Map of Mimbres Basin AOI (solid black rectangle), GFM boundaries (dashed rectangle) and surrounding area showing locations of deep boreholes (yellow dots), shot points of seismic refraction surveys (green dots), main faults (red lines) and contours of alluvium thickness (blue) derived from gravity. Structural cross-section lines are numbered 1-6.

5.1.2 Interpretation of Seismic Refraction Lines

Seismic refraction lines selected for analysis and interpretation are the portions of lines 4, 5 and 7 that cross the Mimbres Basin (green dots in Figure 5-1). For the purposes of this study, it was necessary to reclassify the velocity-defined layers in terms of their inferred lithologies. Klein et al. (1995) were mostly interested in identifying potential mineral resources from the refraction surveys, and focused their attention on the position of basement and buried fault zones in the subsurface. They defined three main units, including a seismic “basement” comprised of crystalline Precambrian rocks grouped together with Paleozoic sedimentary rocks (Figure 5-2; Table 5-1). Further, they grouped Tertiary volcanic rocks together with Mesozoic sedimentary rocks (Table 5-1). Our structural model requires differentiating between Tertiary volcanic rocks and older sedimentary rocks, as well as between Precambrian crystalline “basement” and overlying Paleozoic sedimentary rocks. Thus, we divided the subsurface into four layers according to their ranges of seismic velocities and inferred lithologies: young alluvium, old alluvium, Mesozoic and Paleozoic sedimentary rocks, and Precambrian crystalline basement (Table 5-1). Our subdivision of basin-fill sediments for interpreting the seismic surveys is consistent with gravity and hydrostratigraphic classifications of alluvial sediments (Kennedy et al., 2000; Heywood, 2002).

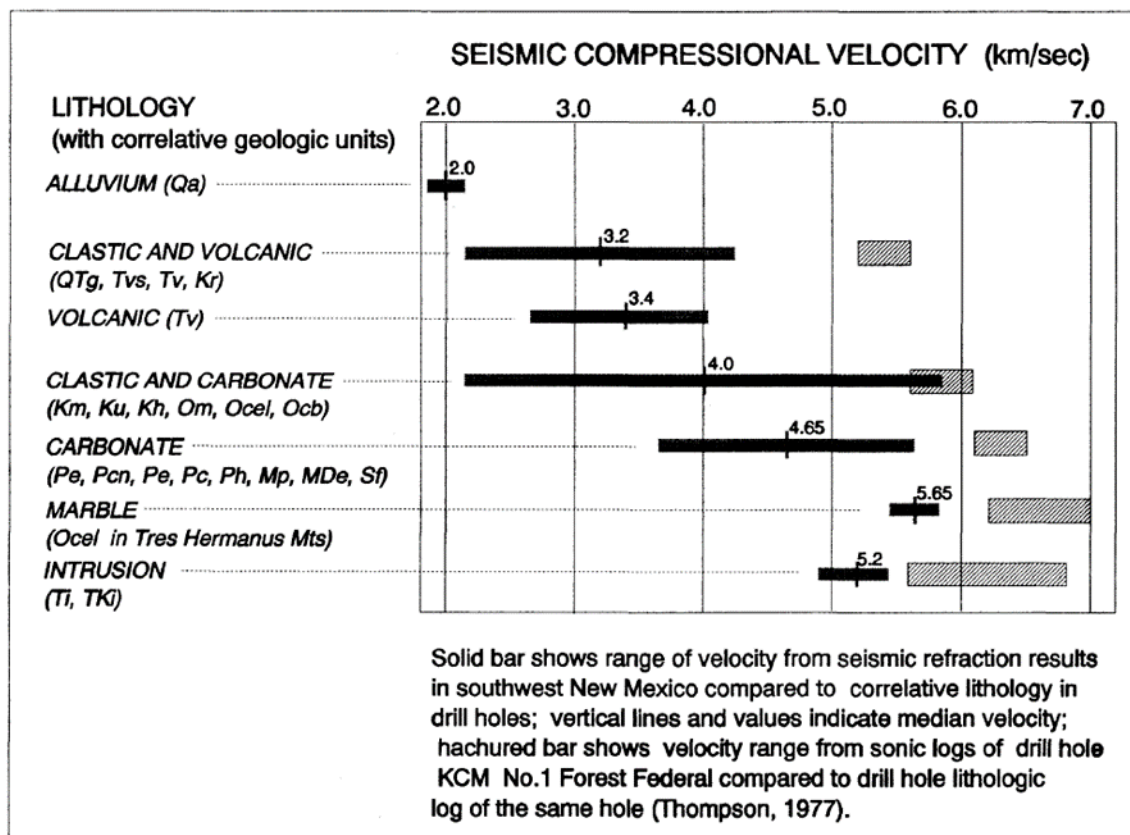


Figure 5-2 Ranges of seismic velocities and their inferred lithologies used by Klein et al. (1995) to build 2D velocity models for the seismic refraction surveys conducted in southwestern New Mexico.

Table 5-1 Ranges of seismic compressional velocities and their inferred lithologies used to interpret the seismic refraction lines from the Mimbres Basin.

Klein et al (1995)			This Study		
Layer	Seismic Velocity	Lithologies	Layer	Seismic Velocity	Lithologies
	Vp, (km/s)			Vp, (km/s)	
0	0.85	Weathered, near surface material	1	< 2.5	Young alluvium (Qa)
1	1.6 to 3.0	Alluvium - unconsolidated to poorly consolidated gravel, sand and clay and possible thin volcanic layers	2	2.5-3.5	Old alluvium (QTg) or Tertiary Volcanics (Tv)
2	2.7 to 4.5	Tertiary and Mesozoic clastic and volcanic rock; encompasses many rock types	3	3.5-4.5	Mesozoic and Paleozoic sedimentary rocks
3	4.0 to 6.1	Seismic basement, forms core of mountain ranges and basin floors. Plutonic, metamorphic, carbonate, silica-cemented sedimentary rocks and welded volcanic rocks	4	> 4.5	Basement rocks (Precambrian)

The original seismic velocity profiles are presented by Klein et al. (1995) as cross sections with 10x vertical exaggeration (Figure 3-7B). We identify the faults and stratigraphic layering on the 10x sections (Figure 3-7C), then provide our structural interpretations in cross sections at a 1:1 scale (Figure 3-7D). The structural interpretation attempts to honor the velocity polygons, even though adjacent polygons may have very different seismic velocities. The consequence is that lateral thicknesses of units are highly variable due to variability in polygon dimensions. In many cases, reducing the vertical exaggeration of cross sections to a 1:1 scale results in fault dips that are unrealistically shallow, although their locations along the profile lines remain accurate.

We begin our interpretation with seismic line 7, which runs north-south from the U.S. border with Mexico near the intersection with seismic line 4, parallel to the Seventy-six fault zone along the western margin of the Columbus sub-basin, across western Deming sub-basin, seismic line 5, the Mangas sub-basin, and terminating just north of the Treasure Mountain fault (Figure 5-1). At ~90 km length it is the shortest of the three interpreted lines with simple basin geometries that can be used to illustrate our principles of structural interpretation (Figure 5-3). The crystalline basement (shaded gray in Figure 5-3) stands out by virtue of its high velocity (mostly > 5.0 km/s) and its contrast with lower velocity sedimentary rocks. At a distance of 40-50 km along the profile, the contact between high velocity basement (5.03-5.33 km/s) and very low velocity basin-fill sediment (<3.2 km/s) is a surface that dips to the south (left) and marked in red (Figure 5-3). This is the Snake Hills fault, which projects onto the ground surface at shot point 7-29 (Figure 5-1; Figure 5-3). It should be noted that the Snake Hills fault, clearly imaged on seismic line 7, does not appear in many regional geologic maps (e.g., Geologic Map of New Mexico, 2003 and the GIS database), though it is mapped as a dashed fault in Seager (1995). A cursory glance at the alluvium thickness contours in Figure 5-1 indicates two separate depocenters (the Seventy-six and Deming sub-basins), thus necessitating a (buried) basin-bounding normal fault at the precise location indicated by the seismic profile. A similar south-dipping fault can be identified at a profile distance of 75-85 km, which projects to shot point 7-26, corresponding to the mapped Treasure Mountain fault (Figure 5-1; Figure 5-3). The

stratigraphic contact between basement and sedimentary rocks, marked by blue lines dipping to the north (right), defines a contrast in seismic velocity of ~1.25 km/s (Figure 5-3). The structural interpretation of seismic line 7 is two half-grabens, each bounded to the north by south-dipping normal faults (Figure 5-4).

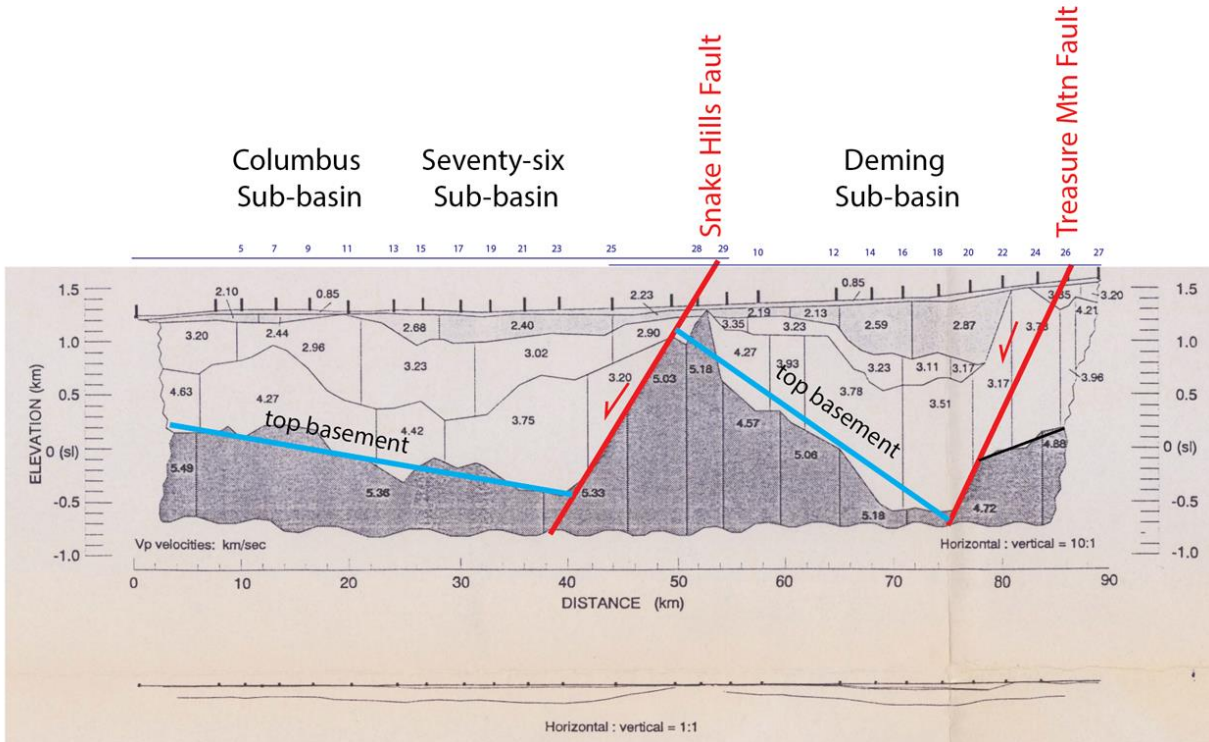


Figure 5-3 Seismic velocity profile for survey line 7 from Klein et al. (1995). Velocities are in km/s and the profile as a 10x vertical exaggeration.

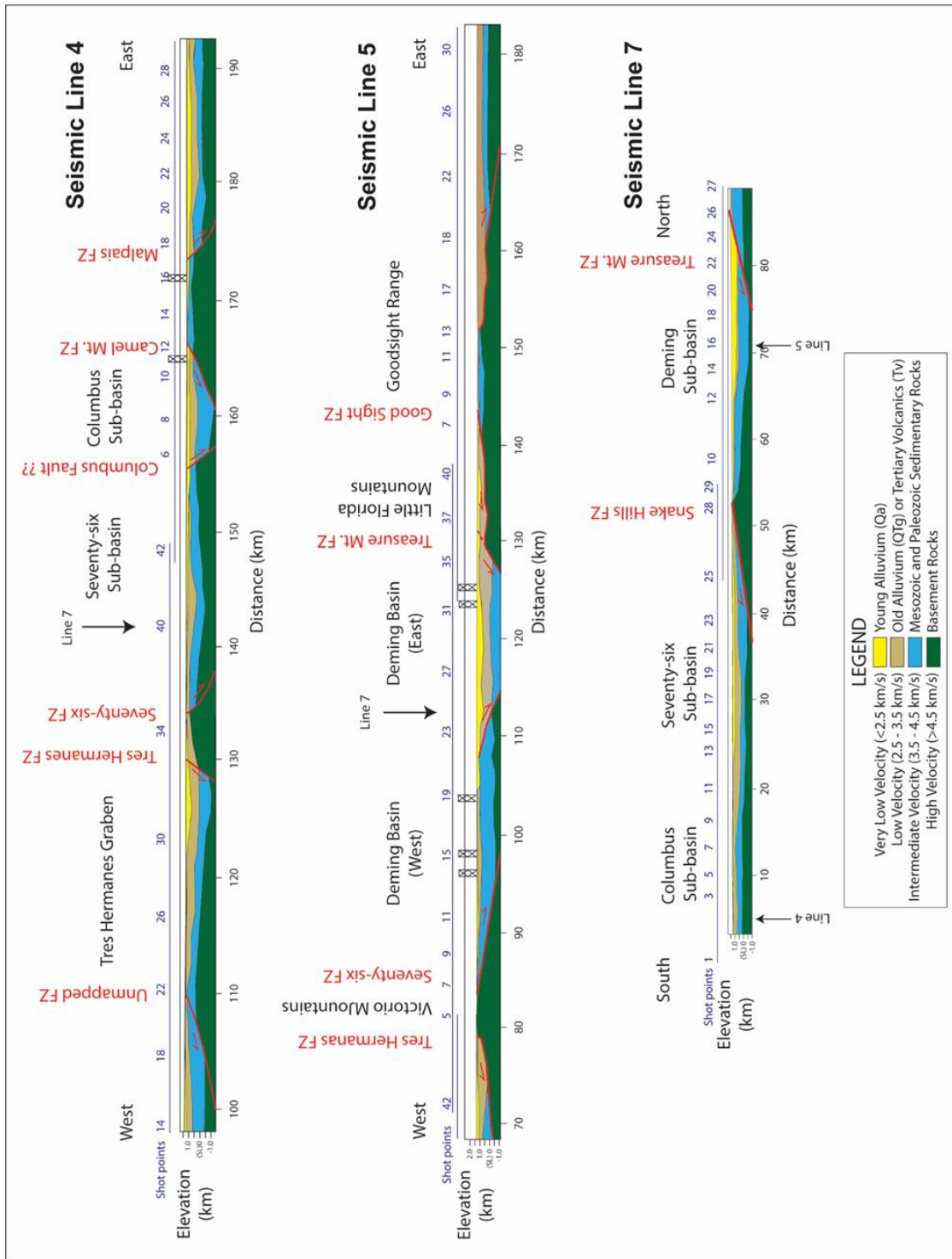


Figure 5-4. Structural interpretations for the three seismic refraction lines that cross the Mimbres Basin, based on velocity sections from Ackermann et al. (1994) and Klein et al. (1995). Shot point locations are presented in Figure 5-1.

The east-west trending Seismic line 4 lies south of our AOI, but illustrates classic Basin and Range structures in the subsurface (Figure 5-4). Discrete faults identified in the subsurface on the seismic profile can be matched with their corresponding fault traces on geologic maps (Figure 5-1; Figure 5-4). Relatively thick accumulations of alluvial sediments are apparent in the Columbus, Seventy-six, Tres Hermanas sub-basins and the unnamed sub-basin to the east

(Figure 5-4). For the most part these results compare favorably to thickness contours of alluvium derived from gravity, with the exception of the Tres Hermanas graben (~125 km on seismic profile 4; shot points 4-30 to 4-32) where the gravity estimates for thickness are less than 50 m (Figure 5-1).

Seismic line 5 runs east-west, from the margins of the Rio Grande rift on the east past the Victorio Mountains to the west (Figure 5-1). Importantly for our study, it crosses the Deming sub-basin, which is located in the center of the AOI and is the focus of the GFM. At a profile distance of 130 km it traverses the buried Treasure Mountain–West Florida Mountain fault zone, which projects to shot point 5-37 on the ground surface (Figure 5-4). The seismic profile defines this fault zone as a west-dipping normal fault that marks the eastern boundary of the Deming sub-basin. At a profile distance of ~110 km, contrasts in seismic velocity across the basement and overlying sedimentary cover reveal unequivocally the existence of an east-dipping normal fault buried beneath the surface (Figure 5-4). Projected to intersect the ground surface between shot points 5-21 and 5-23, this antithetic fault divides the Deming sub-basin into a deep eastern basin and a very shallow western basin. By virtue of having oppositely-dipping normal faults at its boundaries, the east Deming sub-basin has a more symmetrical (“full graben”) geometry than other sub-basins bounded by a single fault. Formation tops from wellbores projected onto seismic line 5, albeit few in number, confirm a thick alluvial section in the eastern Deming sub-basin and a very thin cover of alluvium in the western sub-basin (Figure 5-4). Identifying the antithetic normal fault on the seismic profile has a profound impact on the structural interpretation of the basin, and hence the GFM.

5.1.3 Construction of Structural Cross-Sections

Structural cross sections provide the framework for building the three-dimensional model of an alluvial sub-basin. The sections capture the faults (orientations and displacement), bedrock stratigraphy (depth and thickness), basin geometry (shape and depth) and tectonics (regional extension, tilted fault blocks) of the rock volume. As outlined below, a number of assumptions and simplifications are inherent in assembling the structural sections. However, in light of the limited subsurface data available for the Mimbres Basin (which may indeed be the case for other alluvial basins selected for repository evaluation), we consider this approach the best-suited method for building a structural GFM of the basin.

A total of six section lines for structural modeling were strategically placed within the AOI, with four lines of 50 km length oriented WNW-ESE and two perpendicular lines 25-30 km in length oriented NNE-SSW. The rectangular outline of the section lines defines the area of the GFM (Figure 5-5). This area was selected by virtue of its thick sections of alluvial sediments (Deming sub-basin and Mangas Trench/San Vicente sub-basin), overlapping range bounding faults (West Florida Mountain – Treasure Mountain fault zone), uplifted footwall blocks (Florida Mountains, Cooke’s Range), seismic refraction surveys (lines 5 and 7), and the highest concentration of deep boreholes (Figure 5-1). The WNW-ESE section lines are numbered 1-4 from south to north. The shorter NNE-SSW lines are numbered 5 and 6 (Figure 5-5). The first structural cross section we built was for Section 2, as it is constrained by the most borehole data, crosses the

thickest alluvial section of the Deming sub-basin, and offers a transverse profile of the sub-basin perpendicular to the main range-bounding fault (Figure 5-1; Figure 5-5). Stratigraphic units and their thicknesses were defined by analyzing formation tops from the four key boreholes along Section 2 (McSherry #1, City of Deming #2, Seville Trident, Guest & Wolfson #1 Diana). This stratigraphy was then applied consistently to the other five, less-constrained sections.

The starting point for all of the structural cross sections are vertical profiles at a 1:1 scale (no vertical exaggeration) of surface elevation and the base of alluvium (Figure 5-6). The surface elevation profiles were extracted from the digital elevation model (Figure 4-2), whereas profiles of the base of alluvium were extracted from the surface created using the gravity-derived alluvium thickness (Figure 4-11). The base of the cross-sections was set at a depth of 3.5 km below sea level, resulting in cross-section thicknesses of ~ 5km. The following basic rules and assumptions guided the construction of the cross sections:

- Constant layer thickness was applied to all bedrock units (this excludes the alluvium and erosion of Tertiary volcanics).
- All normal faults dip 60°.
- Bedding orientations from geologic maps (e.g., Seager, 1995) were used to constrain the dips in uplifted fault blocks.
- Where possible, bedding dip remains uniform within each fault block (e.g., Cross Section #2). Where bedding dips change, a kink fold geometry is assumed (e.g., Cross Section #5).
- Layer thicknesses are constrained by wellbore data (formation tops); where there is conflicting terminology, lithologic descriptions and/or thicknesses, we used our understanding of the regional stratigraphy and tectonic history to make determinations.
- The gravity-derived thickness (red lines in profile sections, Figure 5-6) defines the maximum depth of alluvium on the structural cross sections. By definition this marks the top of Tertiary volcanics (Tv), which is a planar surface.
- Tie lines (the intersections of two perpendicular cross sections) must have identical stratigraphies (layers, tops, thicknesses).

For this first iteration of the GFM we divide the geologic section into four principal units:

- Precambrian – All Precambrian rocks (granite, metamorphic, etc.). This defines the “basement”. Five boreholes within the GFM focus area tagged Precambrian basement.
- “Paleozoic” – This unit includes all Paleozoic sedimentary rocks plus the Lobo Formation of Cretaceous-Tertiary age (Section 3.2). Recall that the Mesozoic section is largely absent from the Mimbres Basin, and we thought it prudent to group all sedimentary rocks between the Precambrian and Tertiary volcanics into a single unit. The thickness of the Paleozoic section is estimated as 590 m.
- Tertiary Volcanics (Tv) – The thick section of Tertiary volcanics that predates Basin and Range extensional faulting. It consists of the andesitic Rubio Peak Formation overlain by rhyolites. Total thickness for the Tertiary volcanics is 2100 m.

- Alluvium (QTal) – Includes all basin-fill alluvial sediments that were deposited in Neogene basins from the Oligocene to the present.

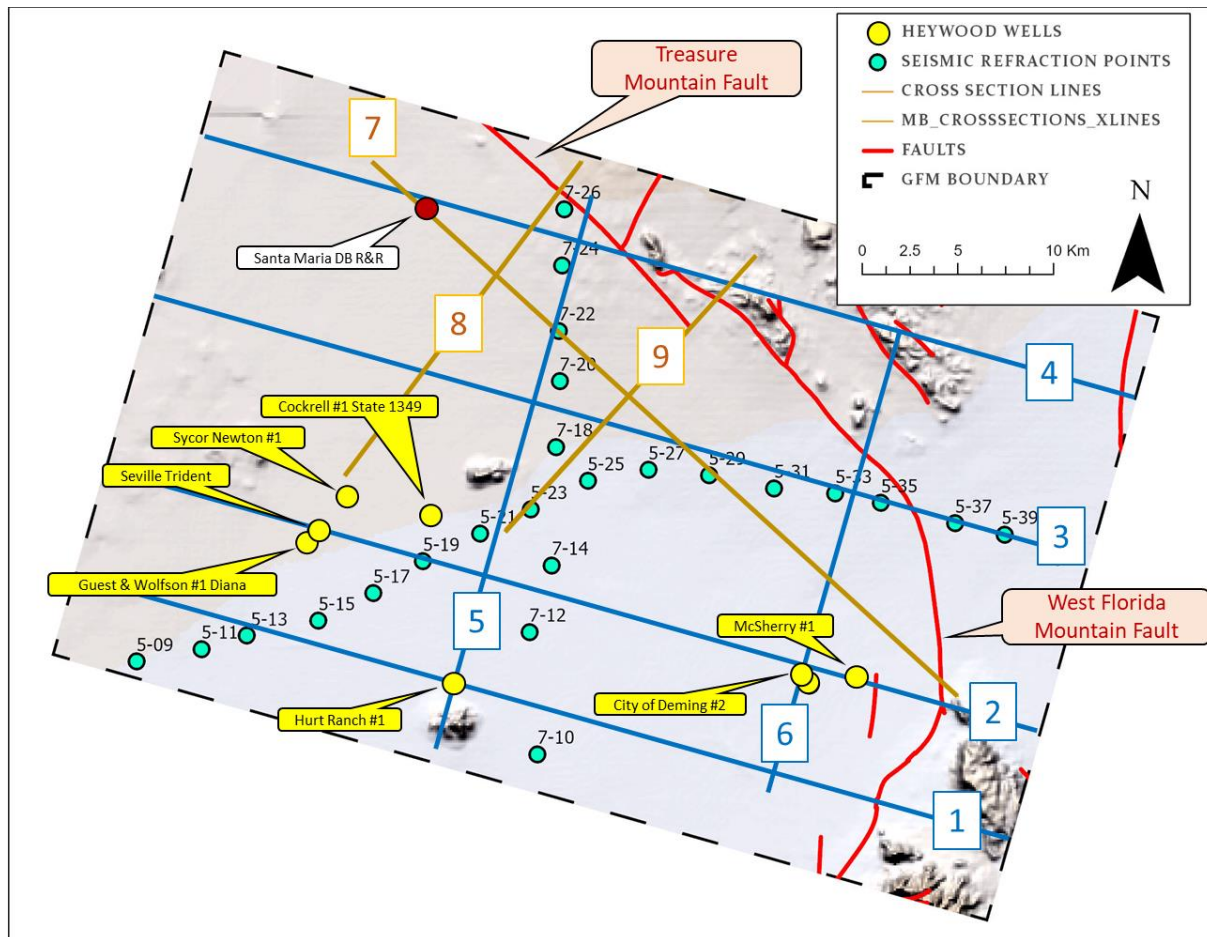


Figure 5-5 Close-up map of the GFM area (dashed rectangle) with the six structural cross section lines (blue) and the three alluvial stratigraphy lines (brown). Deep boreholes are yellow dots and seismic shot points are blue dots.

The six structural cross sections are shown in Figure 5-7 through Figure 5-12. We begin our description with Cross Section #2 as it is best constrained by subsurface data and thus serves as the template for building subsequent cross sections. The eastern part of Section #2 traverses the deepest part of the Deming sub-basin where alluvial sediments are thickest, in contrast to the thin alluvium found in the western portion (Figure 5-1). This is apparent in the profile section of surface elevation and base of alluvium for cross section #2 (Figure 5-6). Three normal faults are recognized in Cross Section #2, which divide the section into four fault blocks (labeled A, B, C and D from east to west in Figure 5-8). Fault #1 is the main range-bounding fault and its surface location at 45.3 km is taken directly from the geologic maps (e.g., Figure 3-5; Figure 5-5). This is the West Florida Mountain fault. Guided by cross-section B-B' found in geologic map GM-60 (Seager, 1995) and formation tops in the McSherry #1 wellbore (Figure 5-5), we imposed a throw of 2400 m on Fault #1. A regional eastward dip of 5° was applied to Block A east of Fault #1 based on bedding orientations measured in exposed bedrock (Seager, 1995). The top of Tertiary volcanics in the McSherry #1 is at 339 m amsl elevation,

corresponding to an alluvium thickness of 963 m, 240 m less than the thickness estimated from gravity (Figure 5-8). Applying an eastward dip of 5°, formation tops from the McSherry #1 and unit thicknesses discussed above completely constrain the geology within tilted block B (Figure 5-8).

The City of Deming #2 wellbore, located ~2.5 km west of the McSherry #1, places the top of Tertiary volcanics at an elevation of 62 m amsl. This corresponds to an alluvium thickness of 1245 m which is nearly identical to the estimate derived from gravity (Figure 5-8).

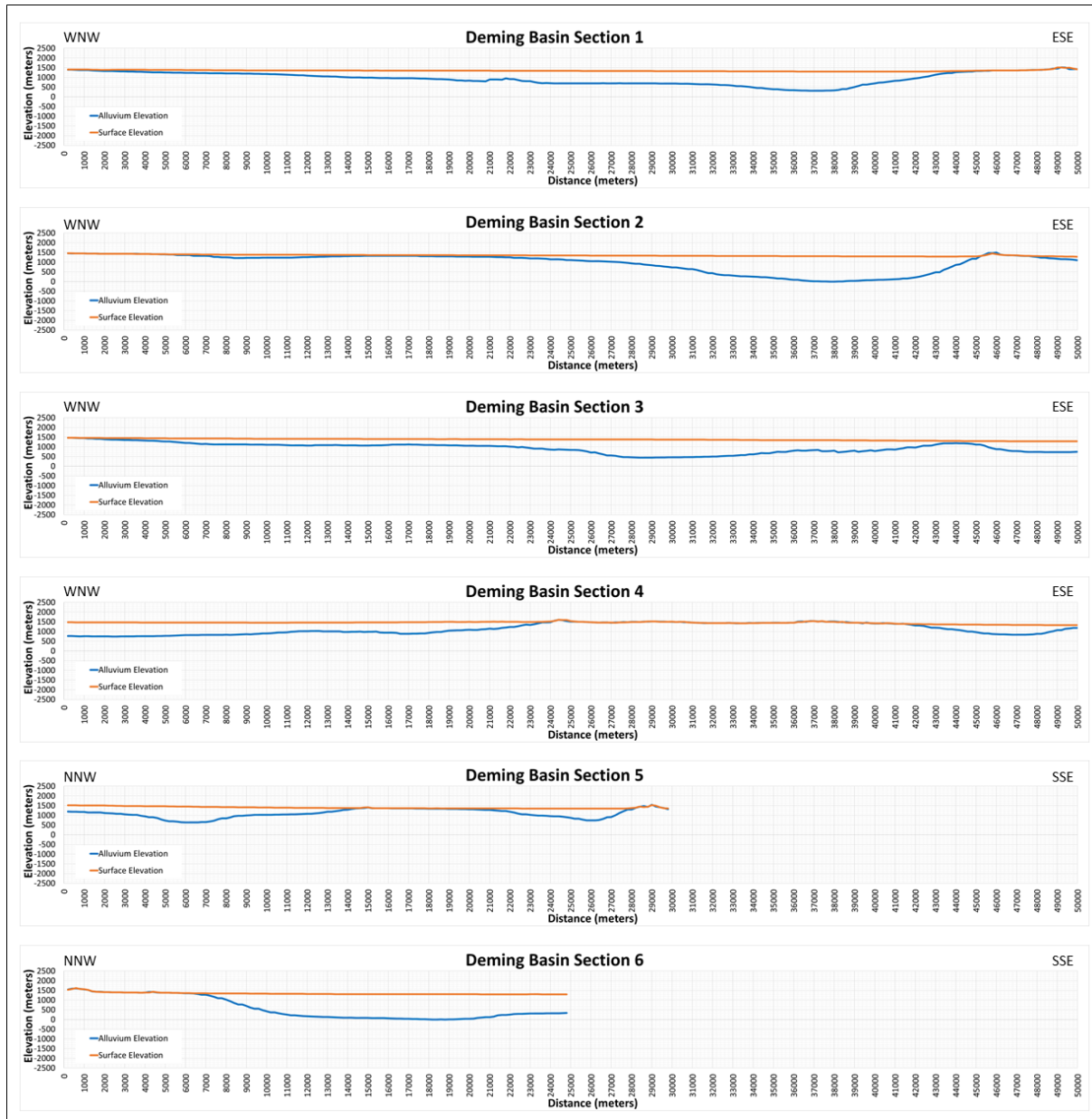


Figure 5-6 Profiles of surface elevation (red line) and base of alluvium (blue line) for the six structural cross sections. Surface elevation was extracted from the DEM surface and the elevation of base of alluvium was extracted from the gravity-derived surface.

The Paleozoic section is completely missing from the City of Deming #2, although 171 m of Lobo Formation was reported. The missing Paleozoic section, along with a ~275 m drop in elevation for the top of Tv between the McSherry #1 and the City of Deming #2, are strong indicators of a normal fault dipping to the west. This is mapped as Fault #2, synthetic to Fault #3 with its upper tip buried within the thick alluvium section (between 37 km and 39.5 km on the cross section of Figure 5-8). The throw on Fault #2 is ~ 500 m, considerably less than Fault #1, thus requiring a greater regional dip in Block B than in Block C.

The top of Tv in Block C is placed at the point of maximum alluvium thickness as derived from the gravity, which is in close proximity to the Tv formation top in the City of Deming #2 upon applying an eastward regional dip of 2°. Maintaining the regional dip and using established unit thicknesses completes the internal geology for Block C up until the intersection with Fault #3 to the west (Figure 5-8). Following the guidelines prescribed for building the structural cross sections results in an angular, wedge-shaped geometry for the alluvial basin, markedly different from the smooth, tapered profile derived from the gravity surveys (Figure 5-8). It also implies a much thicker section of alluvium in the western portion of Block C, confirmed by an estimated thickness of 900 m for alluvium from seismic refraction profile 7 (Figure 5-3), which intersects the section at 23.5 km (Figure 5-8).

Fault #3 is an east-dipping, antithetic normal fault that was identified on seismic (refer to Section 5.1.2). It is located between 21 km and 24 km distance along the section upon projection from seismic line 5 (between shot points 5-21 and 5-23) and marks the eastern boundary of upthrown Block D. The top and base of the Paleozoic section are at the same elevations in the Guest & Wolfson #1 Diana and the Seville Trident boreholes, implying horizontal strata for fault block D. Extending the Paleozoic boundaries eastward constrains the throw on Fault #3 to ~1000m.

Cross Section #1 is directly south of section #2 and shares a similar structural geometry, though the alluvium is thinner (Figure 5-6). The maximum alluvium thickness of 988 m as estimated from gravity is found at a profile distance of 37.2 km. This allows us to build a complete stratigraphic section at 37.2 km distance by placing the top of Tertiary volcanics (base alluvium) at 313 m amsl, the top of Paleozoics at 1787 m bmsl and the top of the Precambrian at 2377 m bmsl (Figure 5-7). Applying a regional dip of 2° constrains the geometry for Block C, the central graben bounded by Faults #2 and #3. We position antithetic normal Fault #3 so it intersects the disrupted base of alluvium profile at ~21 km distance. The Hurt Ranch #1 wellbore (20.3 km) indicates a shallow Paleozoic section (top Lobo Formation at 668 bmsl), resulting in an upthrown Block D and constraining the throw across Fault #3 to ~550 m. The trace of the West Florida Mountain Fault (Fault #1) intersects Cross Section #1 at 43.4 km. We applied the same throw of 2400 m for Fault #1 as we did in Section 2, which results in a tilted block geometry for Block B where the top of Tv matches very closely with the base of alluvium profile estimated from gravity (Figure 5-7). This gives us confidence to locate Fault #2 east of Tie Line 6.

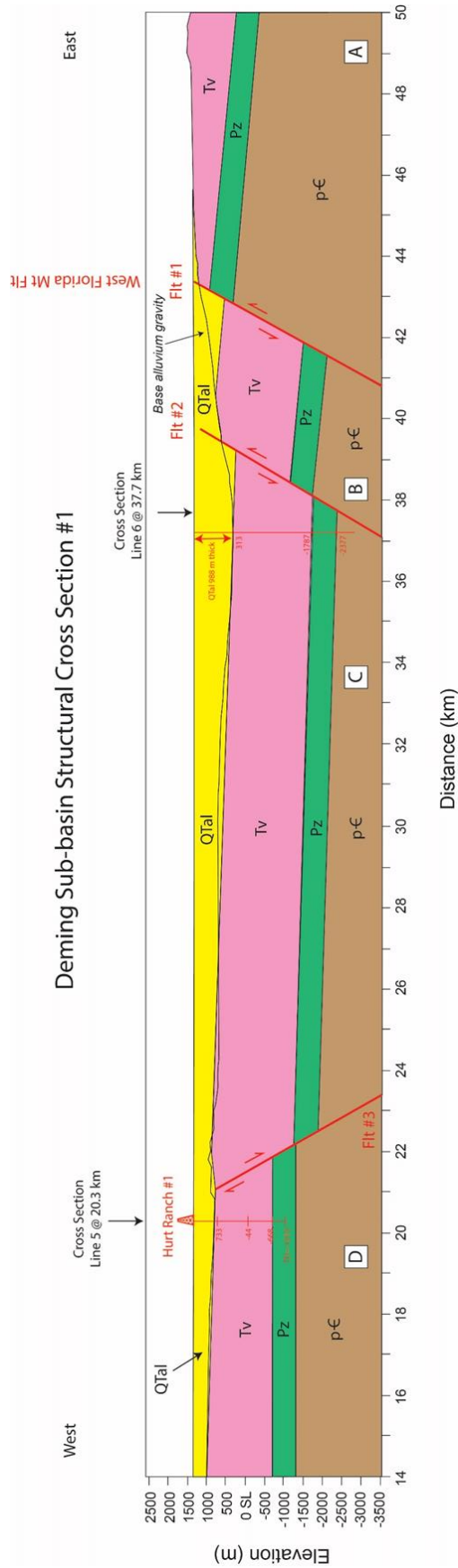


Figure 5-7 Structural cross section #1 for the Deming sub-basin. Refer to Figure 5-5 for location..

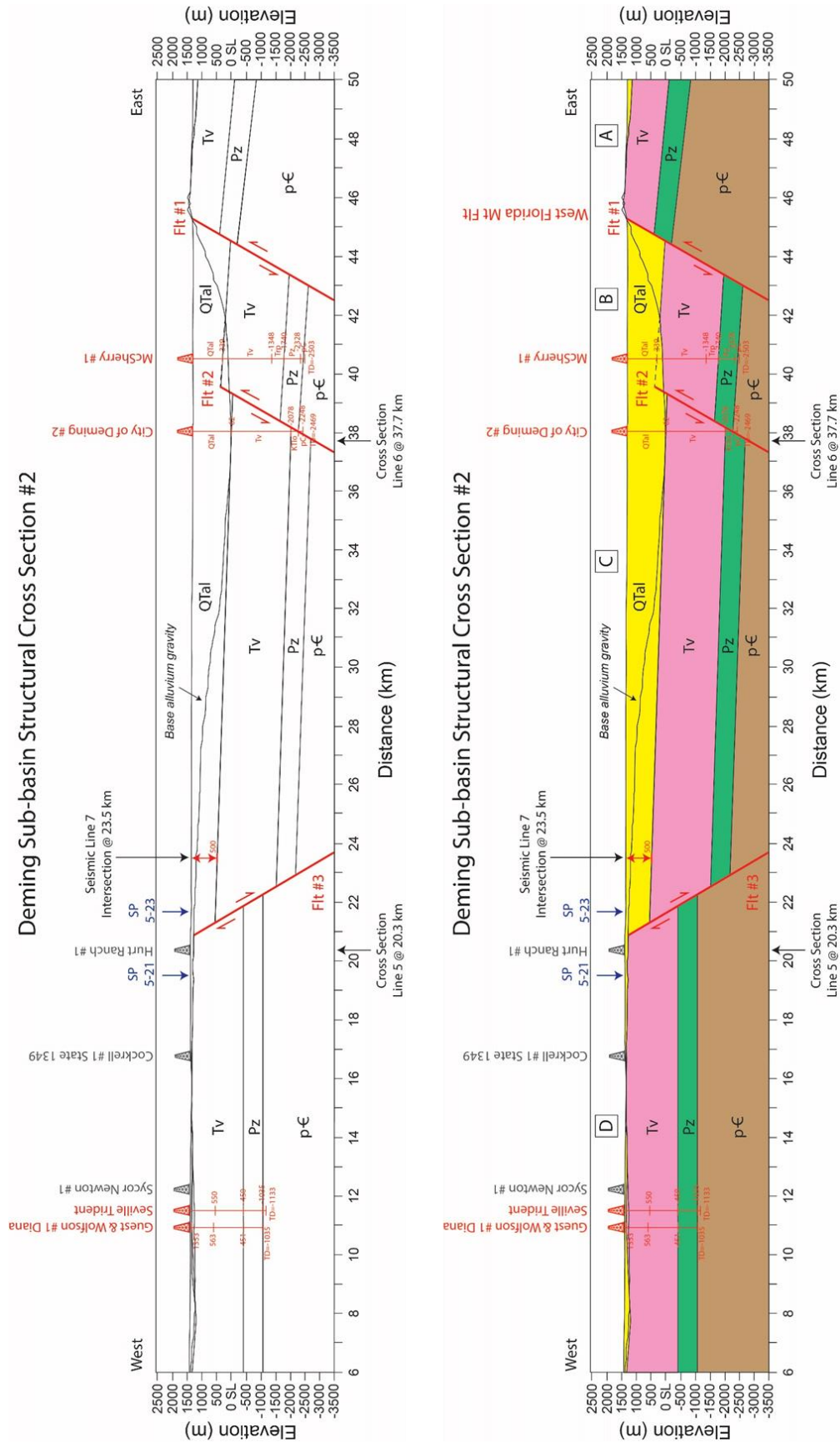


Figure 5-8 Structural cross section #2 for the Deming sub-basin. Refer to Figure 5-5 for location.

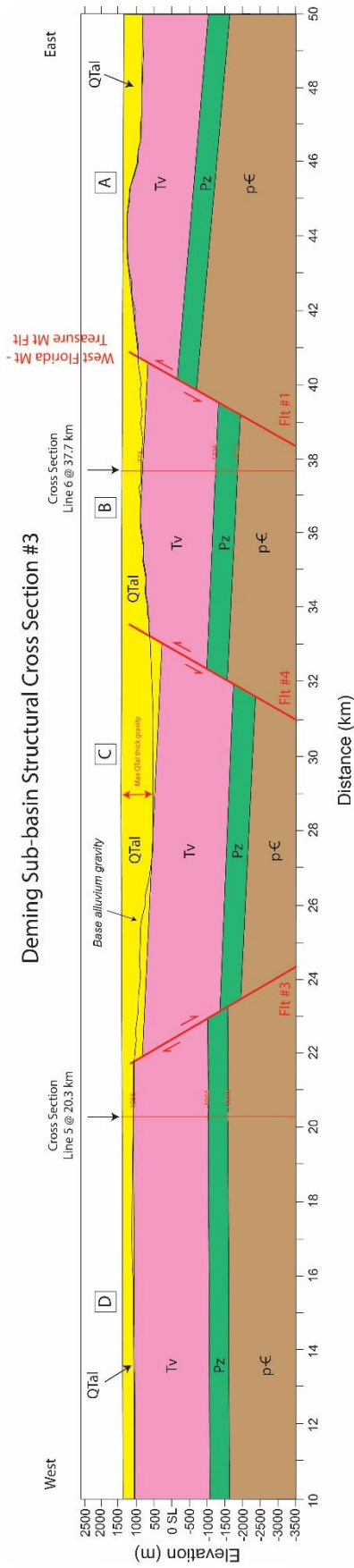


Figure 5-9 Structural cross section #3 for the Deming sub-basin. Refer to Figure 5-5 for location.

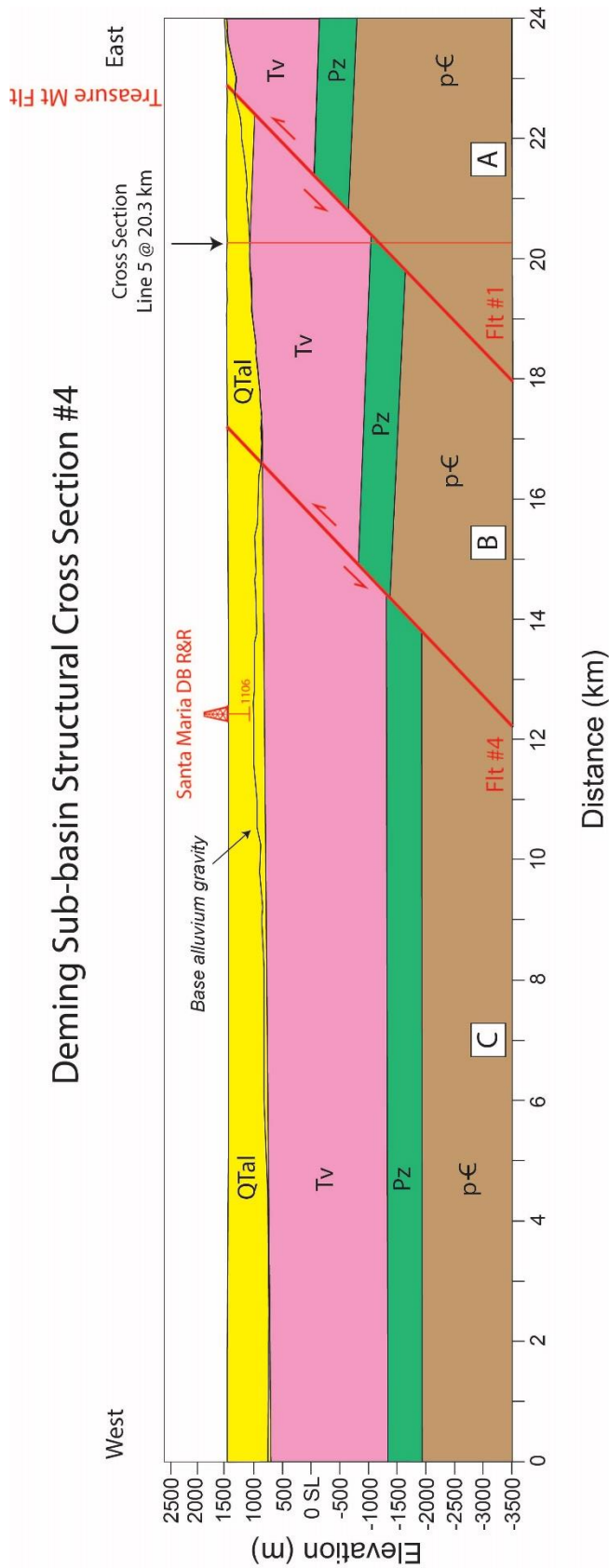


Figure 5-10 Structural cross section #4 for the Deming sub-basin. Refer to Figure 5-5 for location

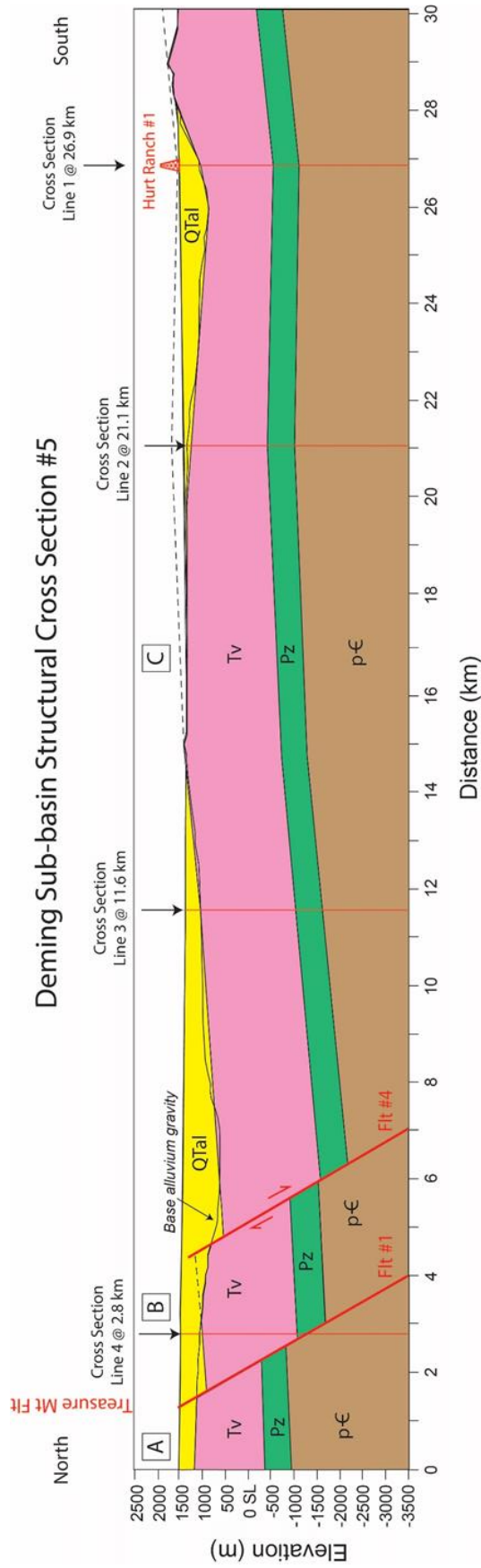


Figure 5-11. Structural cross section #5 for the Deming sub-basin. Refer to Figure 5-5 for location.

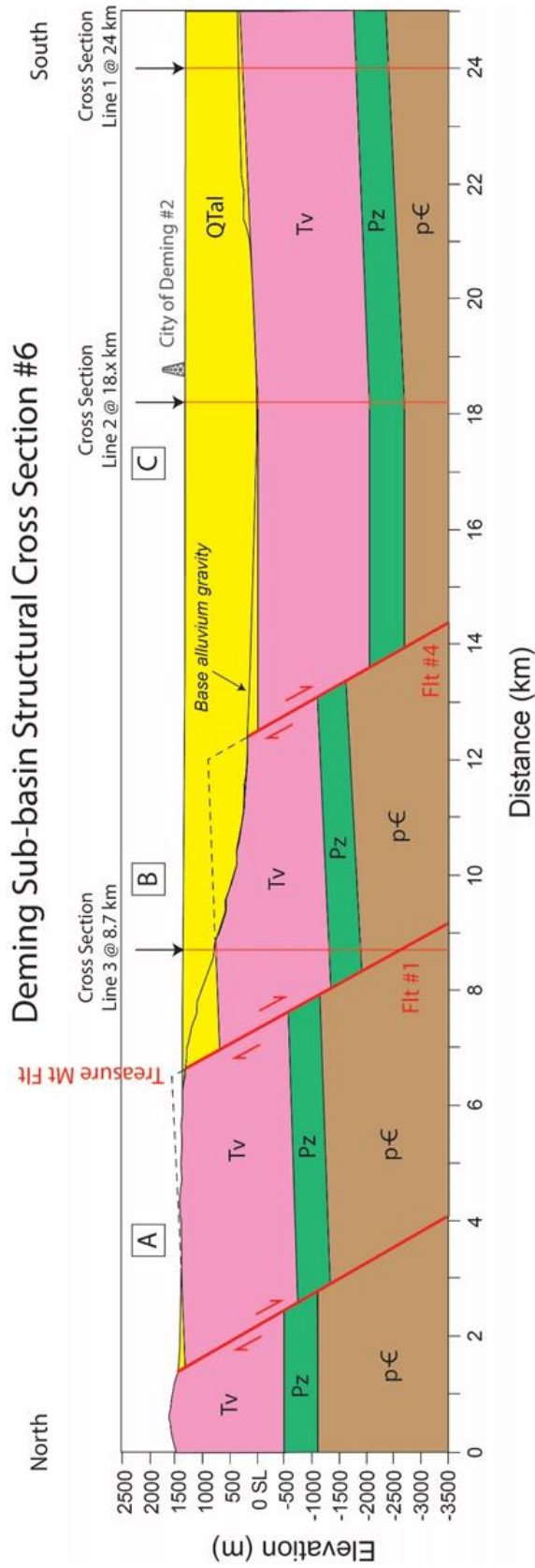


Figure 5-12 Structural cross section #6 for the Deming sub-basin. . Refer to Figure 5-5 for location.

Cross Sections #3 and #4 are located north of Cross Section #2. Though parallel to sections #1 and #2, the main basin-bounding fault has curved to a northwesterly orientation, thereby intersecting sections #3 and #4 at oblique angles (Figure 5-5) and reducing the sub-basin width. The main fault intersects Section #3 at 41 km whereas it intersects Section #4 at 22.9 km. We refer to the main fault (Fault #1) in sections #3 and #4 as the Treasure Mountain Fault to remain consistent with published geologic maps. The throw across the basin-bounding fault is 1200 m for Section #3 and 1000 m for Section #4 (Figure 5-9; Figure 5-10), a dramatic decrease (~50%) from the throw documented for the basin-bounding fault in Sections #1 and #2. This may indicate a different kinematic origin for the West Florida Mountain and Treasure Mountain fault segments. Both sections #3 and #4 require a synthetic fault in order to accommodate structural constraints, which we presume is aligned parallel to the Treasure Mountain fault, and hence labeled as Fault #4. We terminate the antithetic Fault #3 between Sections #3 and #4 in order to prevent intersection with synthetic Fault #4. Thus the central graben structure remains in Section #3 as required by seismic profile #5, but is absent from Section #4. This logically marks the transition from the N-S trending Deming sub-basin in the south to the NW-SE trending Mangas Trench / San Vicente sub-basin to the north.

Structural Cross Sections #5 and #6 are aligned perpendicular to Sections #1 through #4. Section #6 crosses the deepest part of the Deming sub-basin and passes through the City of Deming #2 wellbore (Figure 5-5). Section #5 is located just west of antithetic Fault #3, where alluvium is considerably thinner (Figure 5-1). In fact, Tertiary volcanic bedrock is exposed between 15 km and 20 km along Section #5, effectively demarcating two shallow sub-basins separated by exposed bedrock (Figure 5-11). The subsurface geology for Sections #5 and #6 is largely constrained by the stratigraphy (tops and thicknesses) from the tie lines created by the intersections of Sections #1 through #4 (Figure 5-11; Figure 5-12). This requires changes in dip within Block C (the down-dropped southern hanging wall block), which is accommodated by kink folding at the tie lines in order to maintain constant unit thickness. Considerable erosion of Tertiary volcanics is required in Block B of Section #6 and Block C of Section #5. It is also worthwhile to note the asymmetric, half-graben geometry for sub-basins that develop adjacent to the Treasure Mountain Fault (e.g., Section #5; Figure 5-11), in contrast to the more symmetric, full graben geometries for the Deming sub-basin adjacent to the West-Florida Mountain Fault (e.g., Section #2; Figure 5-8).

5.1.4 Fault network for the structural GFM

One of the important outcomes of the structural analysis is the identification of new faults in the subsurface, which in turn constrains the geometries of the alluvial sub-basins and the attitude of bedding within structural blocks. The main basin boundary faults, the Treasure Mountain Fault and the West Florida Mountain Fault (Figure 5-13), are classic range-bounding faults that appear on all published geological maps. They are mapped on the surface where uplifted blocks of bedrock are exposed and inferred where covered by alluvium. Seismic refraction surveys identify the main faults where buried, and confirm the continuity, or linkage, of the curving WFMF-TMF fault zone, which we label Fault #1 in our cross-sections and maps (Figure 5-7 through Figure 5-13). The largest amount of vertical displacement is observed

across the range-bounding Fault #1, with 2400 m of throw across the WFMF and ~1000 m of throw across the TMF. As a consequence, regional bedding within the hanging wall blocks dips eastward in the Deming sub-basin (towards the WFMF) and to the northeast in the Mangas Trench / San Vicente sub-basin (towards the TMF). Synthetic normal faults (Fault #2 and #4) parallel the main basin-bounding faults and are required to ensure validation of the structural cross sections. As confirmation, Fault #2 was intersected by the deep exploratory well City of Deming #2 in Cross Section #2 (Figure 5-8). Antithetic Fault #3, identified on seismic line #5 and confirmed by well data along Cross Sections #1 and #2, effectively marks the western boundary of the Deming sub-basin. This results in a full graben geometry for the Deming sub-basin in contrast to the half-graben geometry for the Mangas Trench / San Vicente sub-basin. The three buried faults identified in this study likely serve as major fluid-flow pathways and zones of mechanical weakness in the bedrock beneath the alluvial cover, and may impact the siting of a nuclear waste repository.

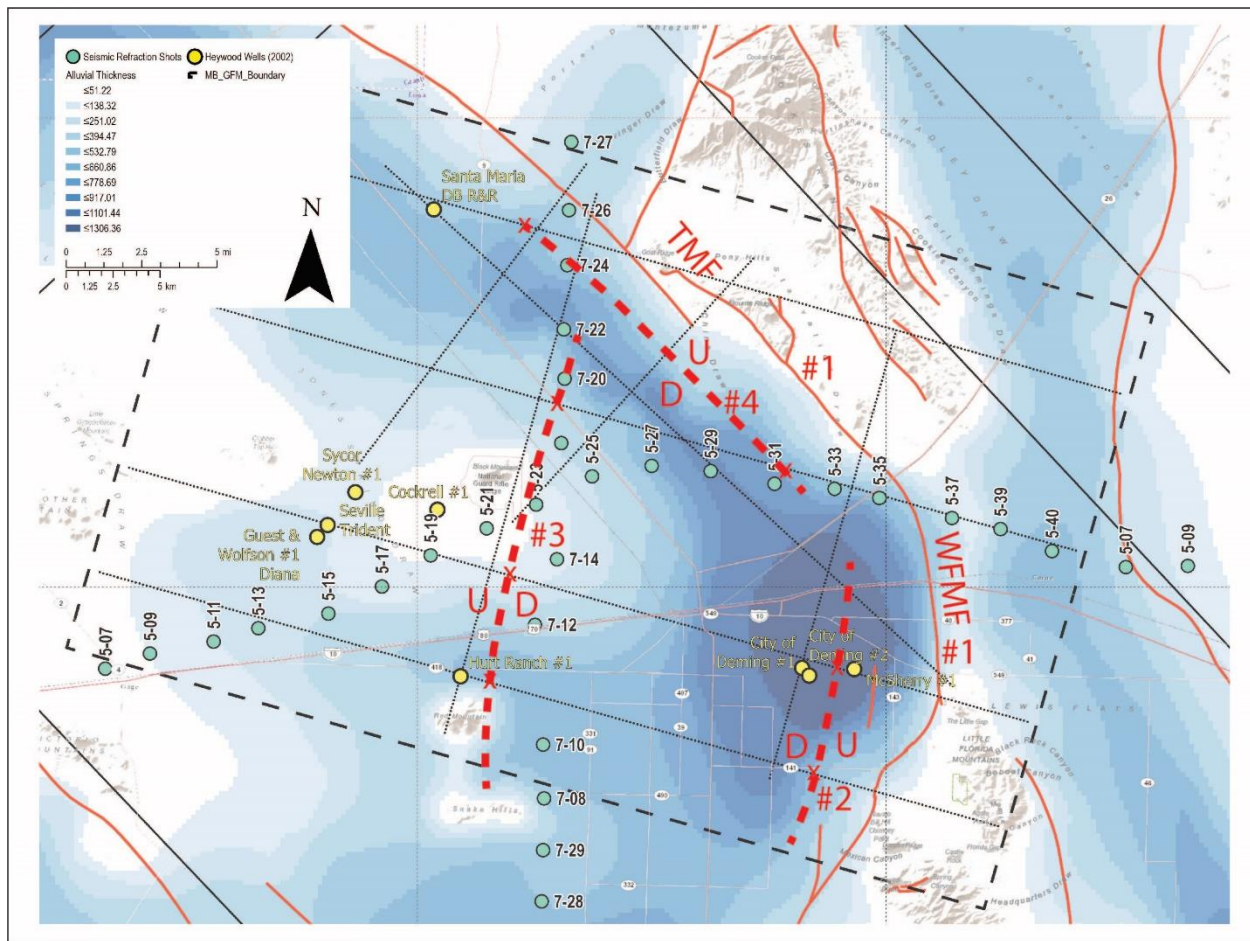


Figure 5-13 Revised fault map for the AOI with three new faults (red dashed) added to the map from this study. Fault #1 is the main basin-bounding fault, known as the West Florida Mountain Fault (WFMF) in the Deming sub-basin to the south and as the Treasure Mountain Fault (TMF) adjacent to the Mangas Trench (San Vicente) sub-basin to the north. Fault #3 is the antithetic fault that bounds the Deming sub-basin to the west. Faults #2 and #4 are synthetic to the main basin-bounding faults (#1). U = upthrown fault block, D = downthrown fault block.

5.1.5 Exporting data to JewelSuite GFM

Upon completion of the structural interpretation of the basin within the AOI, the next step is to transfer the information from the cross sections to JewelSuite in preparation for building the GFM. This was accomplished by extracting depth to formation tops from “synthetic” wells placed at 2 km spacing along each cross section. For example, a synthetic well located at a distance of 36 km along Cross Section #2 encounters alluvium at the surface (0 meters measured depth, MD), Tertiary volcanics at 1308 m MD, Paleozoic rocks at 3248 m MD and Precambrian rocks at 3928 m MD (Figure 5-8). This corresponds to elevations of 1308 m amsl, 0 m, 1940 m bmsl, and 2620 m bmsl, respectively.

JewelSuite requires two separate files to process the synthetic well data. One file describes the location and properties of the wells (Table 5-2) and the second file provides the depths of formation tops for each well (Table 5-3). Information for each well occupies two rows in the well properties table (Table 5-2). The well name identifier (UWI) and geographic coordinates (Northing and Easting) are the same for both rows. This is followed by TVDSS (total vertical depth sub-sea, with negative values above sea level and positive values below sea level), DFE (drilling floor elevation) and MD (measured depth). The inclination and azimuth are indicators of wellbore deviation. For a vertical wellbore both values are zero. Note that for the top row, TVDSS is the elevation of the drilling floor (ground surface in our case) and for the second row TVDSS, is 5000 m bmsl, i.e. the base of the JewelSuite model is set at 5 km bmsl.

In the formation top file each lithologic unit (or formation) occupies a single row for each well, thus Well 2-36000 is described by four rows (Table 5-3). In Appendix 2 we present the two files that describe synthetic well data extracted from Cross Section #2.

Table 5-2 Structural data prepared for JewelSuite that defines the well properties for synthetic well number 2-36000, located on Cross Section #2, 36 km. All depths are in meters.

UWI	Northing	Easting	TVDSS	DFE	MD	Inclination	Azimuth
2-36000	3571630	244086	-1308.4	1308.4	0	0	0
2-36000	3571630	244086	5000	1308.4	6308.4	0	0

Table 5-3 Structural data prepared for JewelSuite that provides the formation tops for synthetic well number 2-36000, located at Cross Section #2, 36 km. All depths are in meters.

Well	Lithologic Unit	TVDSS	DFE	MD
2-36000	Top Alluvium	-1308.40	1308.40	0.00
2-36000	Top Tertiary Volcanics	0.00	1308.40	1308.40
2-36000	Top Paleozoic	1940.00	1308.40	3248.40
2-36000	Top Precambrian	2620.00	1308.40	3928.40

5.2 Development of the Mimbres Alluvial Conceptual Model

5.2.1 Overview

This section illustrates the procedure used to build a conceptual alluvial basin framework model, which will be the basis for creating a 3D computational mesh used for vadose zone flow and transport simulations. Because available borehole data provides insufficient details regarding the stratigraphy within the basin, our process involves understanding basin formation, and using the depositional setting to predict the alluvial stratigraphy. The interplay between tectonic history and climate variation over time relates to the basin's hydrologic evolution, depositional and erosional environments and stratigraphic composition.

Though directly associated with uplift and graben formation, the basin-fill and valley-fill deposits within the Mimbres Basin are principally the product of post tectonic alluvial transport, composed of a wide variety of intercalated sediments including conglomerates, gravels, gravelly, clayey- and coarse to fine-sand mixtures, sandstones, and claystones. In this study, we assume that the formation of the Mimbres Basin structure was complete ca 8-5 Ma and that the first allogenic sediment deposited is found in the deepest area of the Deming sub-basin at a depth of 1,300 m.

5.2.2 Climate Variation from Miocene to Present

In the Mimbres Basin, the net basin fill aggradation is principally post tectonic and associated with the alluvial transport of sediments from newly uplifted source areas. From the mid-Miocene into the late-Miocene (16-11.6 Ma) a decreasing amount of rain was recorded in the Great Plains, possibly indicative of a drier southwestern environment as well. However, this period was followed by the onset (13-8 Ma) of new large-scale climate changes in the Western US possibly due to the uplift of plateaus, and global cooling in the northern hemisphere (8-7 Ma). In the west and southwestern US this corresponds to the establishment of more temperate climate conditions with seasonal precipitation during the late-Miocene, early-Pliocene (5.3-3.6 Ma) and the formation of pluvial lakes (i.e., lacustrine deposits) in the Great Basin province of the Basin and Range. In the southwest US the early Pliocene (5.3-3.6 Ma) corresponds to a relatively drier climate regime (Remeikam, 1988; Ferrester, 1991) until the late-Pliocene (3.6-2.6 Ma) and Pleistocene (3.6-0.013 Ma) Epochs when temperate wetter conditions prevailed. The modern Holocene (0.013 Ma - present day) is an arid and warm, post-glacial Epoch during which alluvial transport is greatly curtailed in the southwest US.

5.2.3 Alluvial Sedimentation and Lithostratigraphy

The Gila Group, as first described by Gilbert (1875), consists of (i) younger sedimentary deposits of alluvium from river valleys that unconformably overlay (ii) well-stratified, fine-grained, soft sandstones, tuffs, marly clays (and limestones when present), deposited in a body of standing water (lake beds) and rest over (iii) the older Gila sediments consisting of sand, gravel and coarser rock debris laid down by streams and derived from pre-Quaternary (>2.6 Ma) rocks that form basin floors of the area.

In terms of depositional environment, Gulluly (1956) proposed a useful timeline from early deposition to present day for the Gila Group in Arizona that includes:

1. Early aggradation of rock troughs with deposition of 100 ft of gravelly alluvium and construction of large steep alluvial slopes (i.e., ancient basin fill).
2. Erosion of alluvial slopes.
3. Submergence of the lower parts of the alluvial slopes by a lake with deposition of sand, tuff, and other sediments in the lake to a maximum depth of 240 m (800 feet) and continued erosion of the non-submerged slopes (i.e., lacustrine pluvial lake deposits).
4. Disappearance of the lake (due to regional changes in climate).
5. Partial refilling of river valleys through deposition by streams followed by slight changes in stream grade resulting in the formation of low terraces (i.e., alluvial fan deposits).

Based on the information above, the conceptual alluvial framework model for the Deming sub-basin is constructed using the overall Gila Group depositional history and the lithofacies assemblages (LFAs) and hydrostratigraphic units (HSUs) of Kennedy et al. (2000) and Hawley et al. (2000). The relation of these units to changes in depositional environment is also revisited and put in the context of known structural and climatic constraints applicable to the southwestern US.

Surface exposures of alluvial sediments in the AOI include sand-gravel ridges and channels contained in a complex system of anabranching fans and meandering patterns of distributary systems (Love and Seager, 1996). In the Deming sub-basin the fans consist of broad channels of sand and gravel, the latter locally containing cobble-sized clasts. The deposits forming the present surface are nearly unmodified by erosion and are presumed to be young (Holocene <30,000 years) as indicated by soil profiles at the top of fan deposits in the Deming and Columbus basins (Gile et al, 1981; Neher and Buchanan, 1980; Reeves 1969).

5.2.4 Stratigraphy of the Santa Maria DB R&R Well

The only borehole in the AOI that includes a lithologic description of the subsurface alluvial basin fill is the Santa Maria DB R&R well, located 45 km northwest of the city of Deming (Figure 5-14). It was drilled from a surface elevation of 1456 m to a total depth below the surface of 351 m. The stratigraphic sequence from the top to base of the well is shown in Figure 5-15 and listed as follows:

UNIT 1:

- Clay and caliche (3m)
- Sand and gravel (53m)

UNIT 2:

- Conglomerate (13m)
- Sandstone (4m)
- Conglomerate (43m)
- Clay and gravel (3m)
- Conglomerate (8m)
- Boulders (2m)
- Conglomerate (11m)
- Conglomerate with clay matrix (28m)

UNIT 3:

- Clay (29m)
- Very fine sand (54m)
- Sand (31m)
- Red sand and clay (68m)

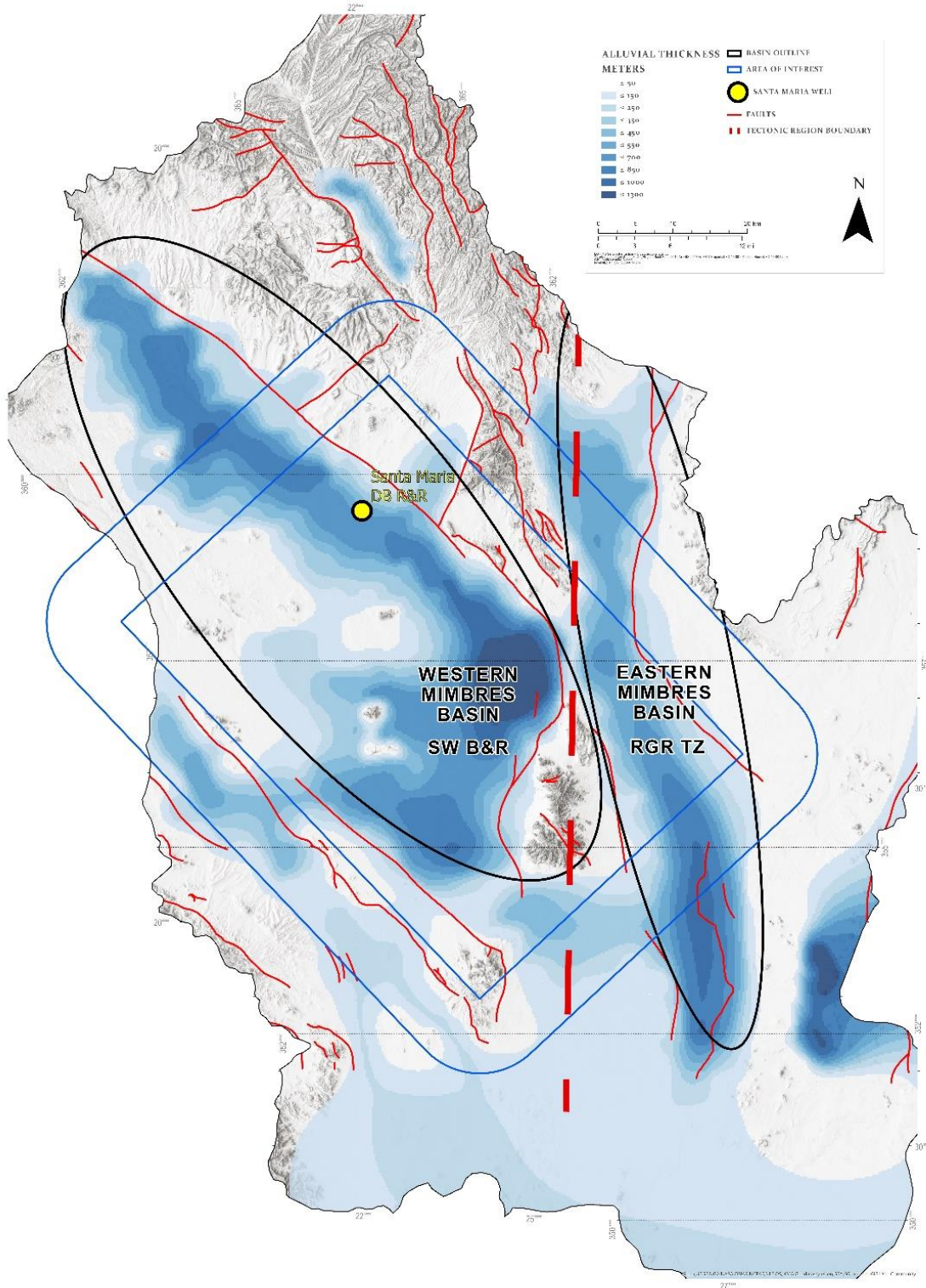


Figure 5-14 Contour Map of Alluvial Thicknesses for the Mimbres. The Florida Mountains divide the Mimbres Basin into a western section (WMB) dominated by Basin and Range extension and an eastern section (EMB) which is a zone of transition between Basin and Range and Rio Grande Rift structures. Yellow circle is the Santa Maria DB R&R well.

The lithostratigraphic facies encountered in the Santa Maria DB R&R well are presented in the stratigraphic column of Figure 5-15. They are grouped into three HSUs following the outline of Kennedy et al. (2000), but independent of their assigned depositional age. We adopt their proposed basin fill aquifer zones and their relation to the upper, middle and lower Gila HSUs as well as their LFAs (Figure 5-16). Consequently, within the constraints discussed above, the HSUs for the Santa Maria DB R&R well section are described as:

- **Unit 1** (50m thick): Channel and floodplain deposits from the perennial and ephemeral reaches of the Mimbres River and Animas creek. This unit represents an upper section of unconsolidated fluvial valley and basin facies associated with modern alluvial fan deposits (sand and gravel mixtures). This unit is equated to the fluvial facies a, b and c of Kennedy et al. (2000) in Figure 5-16, representing valley fills of late Quaternary age (<130,000ka) derived from the upper part of the Mimbres River channel. In the basin these facies include extensive fluvial-fan deposits (Fleischhauer & Stone, 1982; Love & Seager, 1996; Mack et al., 1997).
- **Unit 2** (120m): Gila conglomerate sequence composed of interlayered mixtures of cobbles, pebbles, sands, sandstones, and boulders with sand and clay matrices from reworked piedmont and valley fill sediments. In the model this unit represents the Upper Gila Group, and is the product of a higher energy depositional environment than Unit 1. In terms of the lithofacies classification of Kennedy et al. (2000), Unit 2 is equated with Basin and Valley LFAs 1, 2, and 3.
- **Unit 3** (180m): Lacustrine sediments from pluvial lake deposits possibly Pleistocene in age representing glacial and interglacial low energy depositional sequence of finely interlayered clays, very fine sands, silty sands and silts. In our model it is classified as Basin and Valley/Channel LFAs 4 and 9 (Kennedy et al, 2000) and belongs to the Upper to Middle Gila Group, possibly late Pliocene-Pleistocene, based on climate reconstruction.

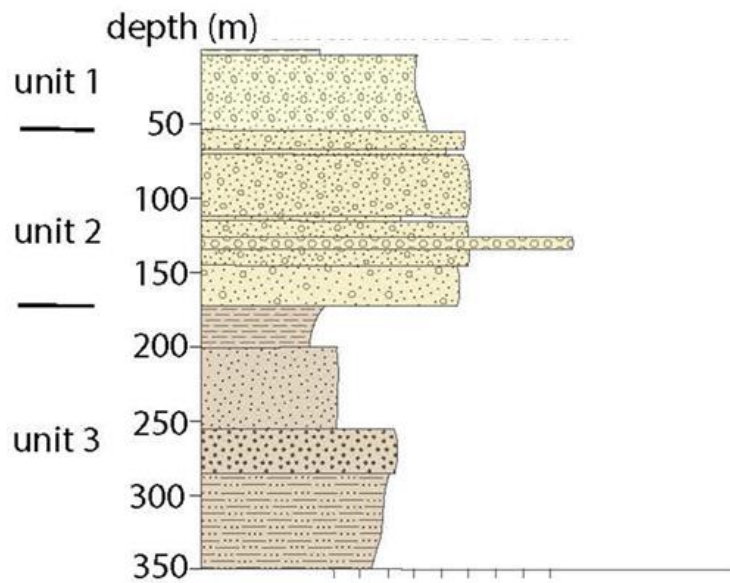


Figure 5-15 Stratigraphic Column of the Santa Maria DB R&R well. The section is representative of the Gila Group for this basin in which three hydrostratigraphic units (HSUs) are identified and used as basis of 3-D Deming Sub-basin model. Unit 1 (light yellow): Holocene channel and basin fill fan deposits; Unit 2 (medium yellow): Late Pleistocene conglomerates; Unit 3 (brown): Late Pliocene to Early Pleistocene lacustrine pluvial lake deposits.

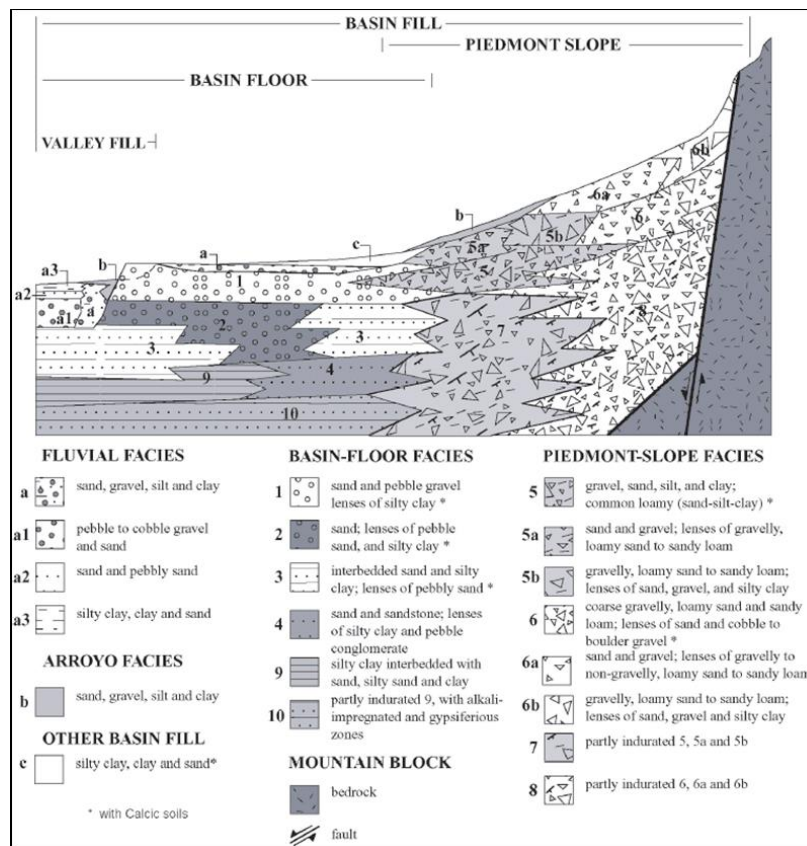


Figure 5-16 Lithofacies Assemblages (LFAs) Classification of Kennedy et al. (2000). Late Quaternary climatic change from a temperate interglacial Pleistocene period to an arid Holocene may be reflected by overlapping or inset sequences of terraces or fans (UNITs 1 and 2; Figure 5-17). Major basin aggradation however was terminated in most southwestern US basins by the deposition of relatively thin, coarse-grained pediment alluvial fans above mildly discordant erosion surfaces (Unit 2).

5.2.5 Conceptual Model of the Alluvial Deming Sub-basin

Due to the scarcity of data available to constrain the alluvial stratigraphy of the Mimbres Basin subsurface, the Santa Maria DB R&R well data was integrated into a “conceptual” basin fill stratigraphic model using the information presented in Section 5.2.4 and constraints from a range of published journal articles and USGS and NM State reports and maps.

We constructed an alluvial conceptual model for the Deming Sub-basin, with 6 units (Table 5-4) based on the LFAs from Kennedy et al. (2000) (Figure 5-16). Model layer descriptions listed below are based on (i) the stratigraphic column from the Santa Maria DB R&R well (i.e., Units 1, 2, 3), (ii) the descriptions of the Gila Group rocks from Section 5.2.3, and (iii) the LFAs and HSUs of Kennedy et al. (2000). The depositional time periods for each unit are inferred from the preliminary reconstruction of southwestern US climatic conditions throughout the Pliocene-Holocene and the initial late Miocene-early Pliocene age of formation of the Deming sub-basin (8-5Ma; Table 5-5).

Table 5-4 Model hydrostratigraphic unit descriptions for the Deming sub-basin alluvial conceptual model. Deming channel and basin fill descriptions and their equivalence to LFAs and HSUs from Kennedy et al. (2000) are placed in the context of the alluvial conceptual model in this study. Model layer thicknesses are also shown and in the central and deepest area of the basin are constant (Figure 5-17).

ACFM UNIT	Model Layer Thickness (m)	LFA	Assigned SM-DB/Model Descriptions	SM-DB Thickness (m)	HSU/Gila Group Description
UNIT - 1	0-50m	Fluvial Facies a, b, c	Holocene channel and basin fill fan deposits. Unconsolidated top layer of reworked fluvial (Mimbres river), arroyo, eolian, playa and basin fill deposits.	50	Post Gila Group fluvial, floodplain, and low terrace alluvial deposition.
UNIT - 2	120m	Valley and Basin Alluvial Facies 1, 2	Mostly reworked unconsolidated Late Pleistocene inter-layered sequence of reworked Mimbres River valley and Sub-basin piedmont footwall/piedmont slope deposits of cobbles, pebbles, sands, sandstones and boulders with sandy-clay matrix.	120	Upper Gila Conglomerate Group - UG Proximal to distal undivided piedmont slope UG1 and basin floor UG2 facies.
UNIT - 3	180m	Lacustrine Basin Floor Facies 3, 4, 9	Late Pliocene-Pleistocene interglacial/glacial lacustrine sequence of finely interlayered clays, very fine sands, silty sands and silts.	180	Upper to Middle Gila Group - UG/MG
UNIT - 4	0-356m	Channel and Basin Alluvial Facies 4, 9	Early- to Late Pliocene temperate climate deposits of fluvial and alluvial fan deposits. Compacted and partially cemented gravel, pebbles, sands and silty clay mixtures.	n/a	Middle Gila Group - MG
UNIT - 5	600m max	Ancestral Mimbres Basin Floor Facies 7, 8, 10	Earliest basin syn- to post-tectonic deposits of Late Miocene-Early Pliocene volcanoclastic piedmont slope deposits of locally sourced footwall deposits, cemented and indurated.	n/a	Lower Gila Group - LG Early basin floor deposition
UNIT - 6	variable	Piedmont-Slope Facies 5, 6, 7, 8	Continuous undifferentiated footwall slope deposits of gravel, cobbles, boulders, sand, loamy sand and clay.	n/a	Pre-Gila Group - LG deposition

The proposed alluvial basin-fill cross section along line 7 (Figure 5-17) was chosen to best capture the potential variability in HSUs described in Table 5-4. The cross-section is oriented NNW-SSE to illustrate both channel and basin LFAs captured in the basin model. Units 2, 4 and 5 are separated into alluvial valley fill-facies (i.e., Units -2a, -4a, -5a) and basin-fill facies (i.e., Units -2b, -4b, -5b) to capture the alluvial fan structure and lateral NW-SE variations in the coarseness of the alluvial sediment deposits based on proximity to sediment source areas and modes of deposition (e.g., episodic high energy transport from the Mimbres River valley vs. lower energy deposition of terrace and eolian sediments in the central basin).

The conceptual model we developed for the alluvium in the Deming sub-basin consists of the following units:

- **Unit 1** (Table 5-4) represents post-Gila Group fluvial channel and basin fill sediments deposited during the Holocene under arid to semi-arid conditions with seasonal winter precipitation and based on the Santa Maria DB R&R well stratigraphy (Figure 5-15). Late Quaternary climatic change from a temperate interglacial Pleistocene period to an arid Holocene may be reflected by overlapping or inset sequences of terraces or fans (Table 5-5). Major basin filling, however, was terminated in most southwestern US basins by the deposition of relatively thin, coarse-grained pediment alluvial fans above mildly discordant erosion surfaces. These fans are believed to record fluvial responses to initial climate fluctuations in late Pleistocene or early Quaternary time.
- **Unit 2** represents unconsolidated Upper Gila conglomerate sequence formed during the wetter late Pleistocene temperate climate (Table 5-5), which was characterized by strong seasonal precipitation variations. The sequence is also based on the the Santa Maria DB R&R well stratigraphic column (Figure 5-15). The depositional environment was likely episodically high-energy in comparison to the present, with transport of coarse alluvial deposits composed of sands with cobbles, gravels and pebbles intercalated with fine sands and clays.
- **Unit 3** (Table 5-4) is taken to represent a thick (180 m) lacustrine section of clays, very fine sands and silt layers likely deposited in a pluvial lake formed during a late Pliocene-early Pleistocene glacial-interglacial climate and a period of tectonic quiescence (Table 5-5). As for Units 1 and 2, the thickness and description of Unit 3 is based on the Santa Maria DB R&R well stratigraphy (Figure 5-15). Because this thick lake deposit is present in the Santa Maria DB R&R well within the Mexican Highland Valley, it is assumed to be a continuous layer extending SE into the central part of the Deming Basin floor presently beneath the city of Deming, and responsible for the shallow aquifer system in the area. This potential aquitard is also equated with the Upper to Middle Gila Group (Table 5-4).
- **Unit 4** unconformably underlies the lacustrine sequence (Unit-3) and represents a thick sequence of up to 356 meters of early to late Pliocene coarse, partially cemented fluvial and alluvial fan deposits of coarse sands, cobbles and gravels. This unit represents an undifferentiated mix of LFAs described in Table 5-4 and Figure 5-16 (Kennedy et al., 2000). The depositional environment for this layer corresponds to the onset of a cool and wet, temperate climate and the introduction of seasonal climate variations following a period of global cooling (8-7Ma). It also corresponds to a period of rapid uplift of the Colorado Plateau to the north in the late to mid-Miocene (Table 5-5).
- **Unit 5** represents the deepest and earliest ancestral basin floor deposits of the Deming Basin and formed syn- and post-tectonically at the end of southwestern B&R tectonics uplift (8-5Ma) along the western Florida Mountain- and the Treasure Mountain fault systems to the east and north of the basin respectively (c.f., Figure 5-14). It is linked to pre-Gila Group or Lower Gila deposition and in the model equated to late Miocene-early Pliocene mixed volcanoclastic and

very coarse angular piedmont slope deposits, which are locally sourced from footwalls and cemented and indurated.

- **Unit 6** in the model is an undifferentiated Piedmont slope facies formed episodically from the erosion of the hanging walls of basin-bounding faults. This unit is composed of boulders, gravels, cobbles, coarse sands, loamy sands and clays as described by Kennedy et al. (2000). This facies represents undifferentiated LFAs 5, 6, 7 and 8 of Kennedy et al. (2000), and is important as it is also the loci of mountain front recharge for the basin (Figure 5-16, Figure 5-17).

Ancient channel geomorphology, visible as changes in alluvial thickness, reveal a narrow early drainage system into the Deming sub-basin from the north and northwest along narrow fault-bound valleys that we propose drained into the Deming sub-basin (Figure 5-18). The drainage system was bound on three sides by the Treasure Mountain and Florida Mountain fault footwalls to the north and east respectively and an antithetic fault zone (#3) to the south and west (Figure 5-14). This seems to indicate that, unlike modern, ephemeral Mimbres river that mostly flows episodically into the Mimbres Basin between the Florida Mountains and the Cooke Mountains, from 5 Ma to the late Pleistocene, the ancient Mimbres river, and possibly its ancestral tributary (San Vincente River), were perennial and flowed through the Deming Basin, travelling south of the Florida Mountains into the Columbus Basin area and then into northern Mexico. The location and hydrostratigraphic composition of the well-defined channel at depth (Figure 5-17) indicates that the channel deposits may also represent an active subsurface groundwater pathway today. This feature is also important for reconstructing the source of the basin sediments.

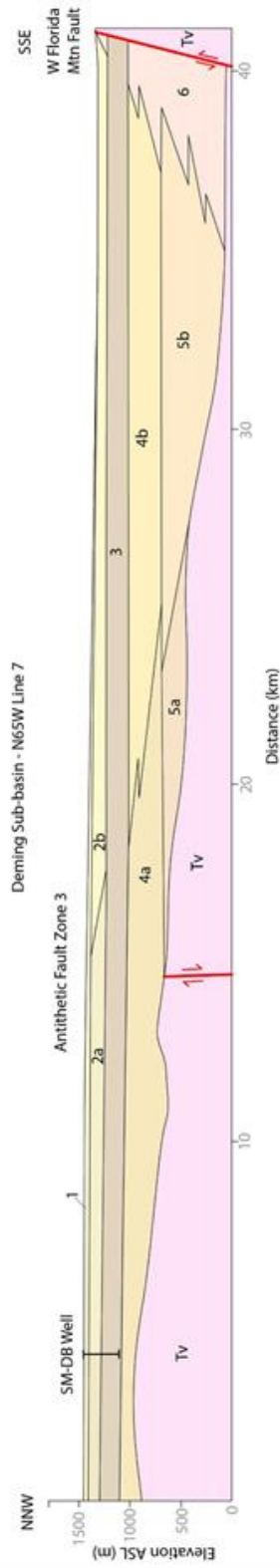


Figure 5-17 NNW (left)-SSE (right) Cross-section Line 7 of Alluvial Deming Sub-basin GFM. NW from the Mexican Highland valley (channel fill) towards the Central basin beneath the city of Deming to the SE. SM-DB: Santa Maria – Deming Basin well location. East bounding W Florida Mountain fault and antithetic fault zone #3 are in red. Channel and basin fill descriptions are provided in text.

Table 5-5 Proposed Tectonic and Climate Reconstruction Used for Mimbres Conceptual Model. Schematic illustration of chronologic relation and interplay between tectonic setting and climate in the development of southwestern structures and B&R formation.

GEOLOGIC TIMEFRAME		TECTONIC SETTING				TECTONIC CONTEXT		CLIMATE
EPOCH	AGE (Ma)	Basin & Range	Southwestern US	Coloabrd	Plateau			Western & Southwestern US
		Great Basin (GB)		Uplift/Erosion	Deformation			
Holocene	0.013 - present					B&R uplifts impede Pacific storm systems (Winoograd 1985)		Post Glacial: arid-warm
Late Pleistocene	1.8 - 0.013					3.6-1.8Ma: Climatic shifts during tectonic quiescence		Glacial-interglacial: drier/winter precipitation
Mid-Pleistocene	ca. 1.8							Temperature: Arid - Cooler
Late Pliocene	2.6 - 1.8							Temperature : Wet-Cooler 3.5-2.5Ma
Early Pleistocene	3.6 - 2.6							Temperature : Wet-Warm
Early Pliocene	5.3 - 3.6							Global Cooling 8-7Ma
Late Miocene	11.6 - 5.3							Decreased Rain Fall 15-8Ma (GB)
Mid Miocene	16 - 11.6							
Early Miocene	23 - 16							
Late Oligocene	28.1 - 23							
Early Oligocene	33.9 - 28.1							
Eocene	56-33.9							

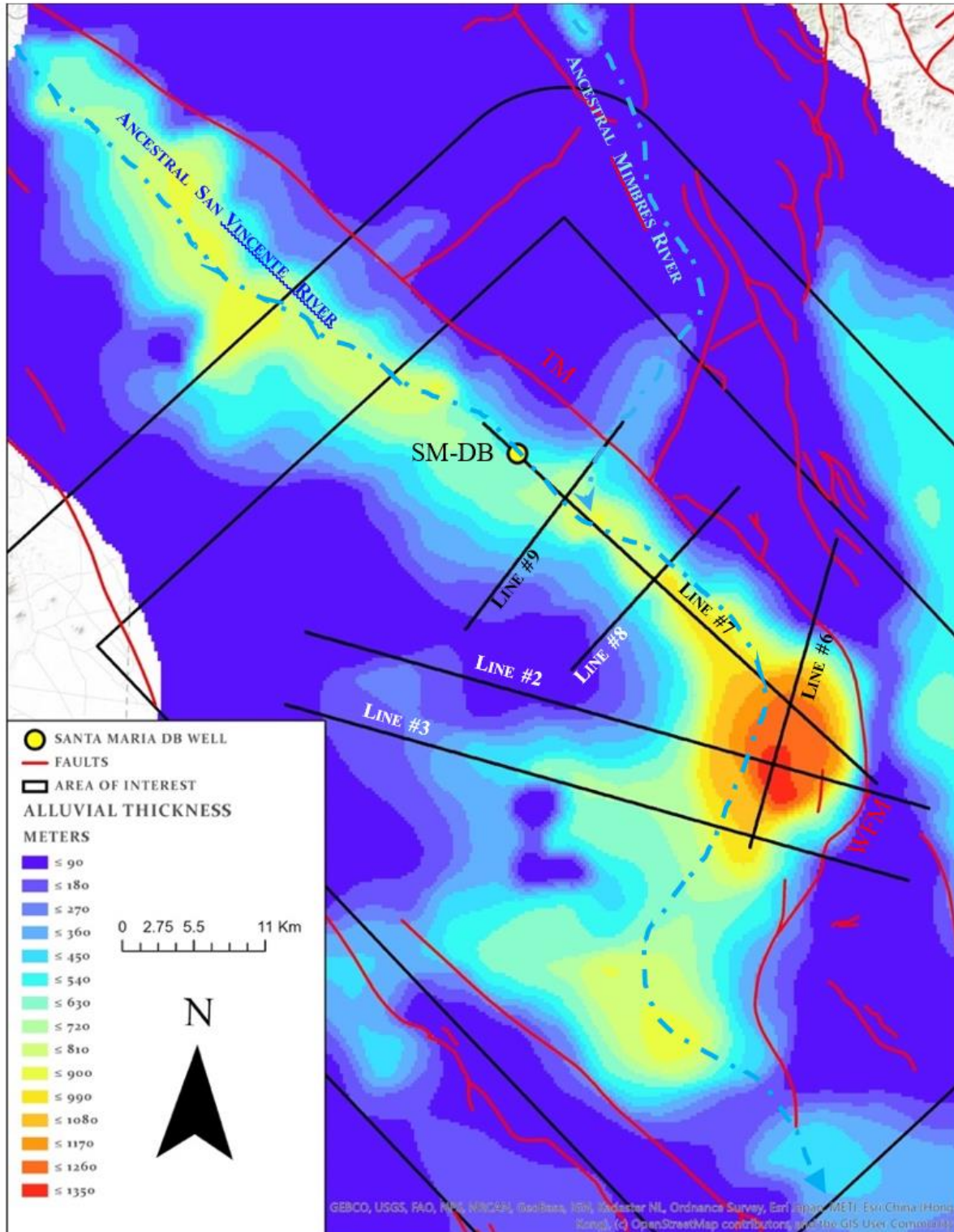


Figure 5-18 Contour Map of Deming Basin Alluvial Basin Fill Thicknesses. Also included are the locations of cross-section lines used for Deming sub-basin alluvial basin fill reconstruction. Cross-section lines used to build 3-D conceptual alluvial framework and alluvial GFM models are shown (Lines #2, #3, #6, #7 and #9). Location of well SM-DB on cross-section Line #7 is also shown (yellow dot). Note the location of the NNW-SSE trending Mexican Highland valley channel to the deep basin and its relation to the bounding normal faults of the Florida Mountain Fault (FM) to the East and the Treasure Mountain Fault (TM) to the North. Also shown are the traces of the proposed ancestral perennial Mimbres and San Vicente River systems.

6 The Geologic Framework Model (GFM)

6.1 Overview

A geologic framework model is needed to transform the characterization of bedrock and alluvium as described in Chapter 5 into a three-dimensional subsurface geological model, which in turn can be exported for numerical flow simulation to assess repository safety and assurance. The GFM must capture the geological elements that impact the siting and dynamic behavior of a potential repository, including basin geometry, alluvium stratigraphy, lithofacies and geologic structures. A proper evaluation requires building the GFM at different scales, from regional to site-specific. The first step, and the focus of our FY2019 efforts, is to establish the geologic elements that define the boundaries of the alluvial sub-basin, such as depth to bedrock, basin-bounding and intra-basin faults, and the geometry of the top Tertiary volcanics (Tv) surface upon which the alluvial basin-fill sediments were deposited. This can be viewed as the regional “basin structure” GFM. In this report, the basin structure GFM contains limited detail of the internal characteristics of the alluvium within the basin. In FY2020 we intend to focus on the internal characteristics of the alluvial basin GFM. We used the JewelSuite™ modeling software from Baker Hughes to construct the GFM.

6.2 Data Import and Model Boundaries

The GFM was constructed from the following data sources:

- Ground elevation surface exported from GIS (Figure 4-2),
- Six structural cross sections (Figure 5-7 through Figure 5-12), and
- Alluvial stratigraphy section #7 (Figure 5-17).

The ground elevation surface data were provided in XYZ (longitude, latitude, elevation) format at 30 m grid spacing. Data from the cross sections were captured as formation tops from synthetic vertical wells sampled at 2 km spacing along each profile line (Section 5.1.5). Representations of the imported wells, ground surface elevation and model dimensions are presented in Figure 6-1. The formation tops, or more precisely the bedrock unit marker tops, encountered in the wells are shown in Figure 6-2. These tops are used to interpolate stratigraphic horizons (i.e., surfaces) and to position the main faults in the model.

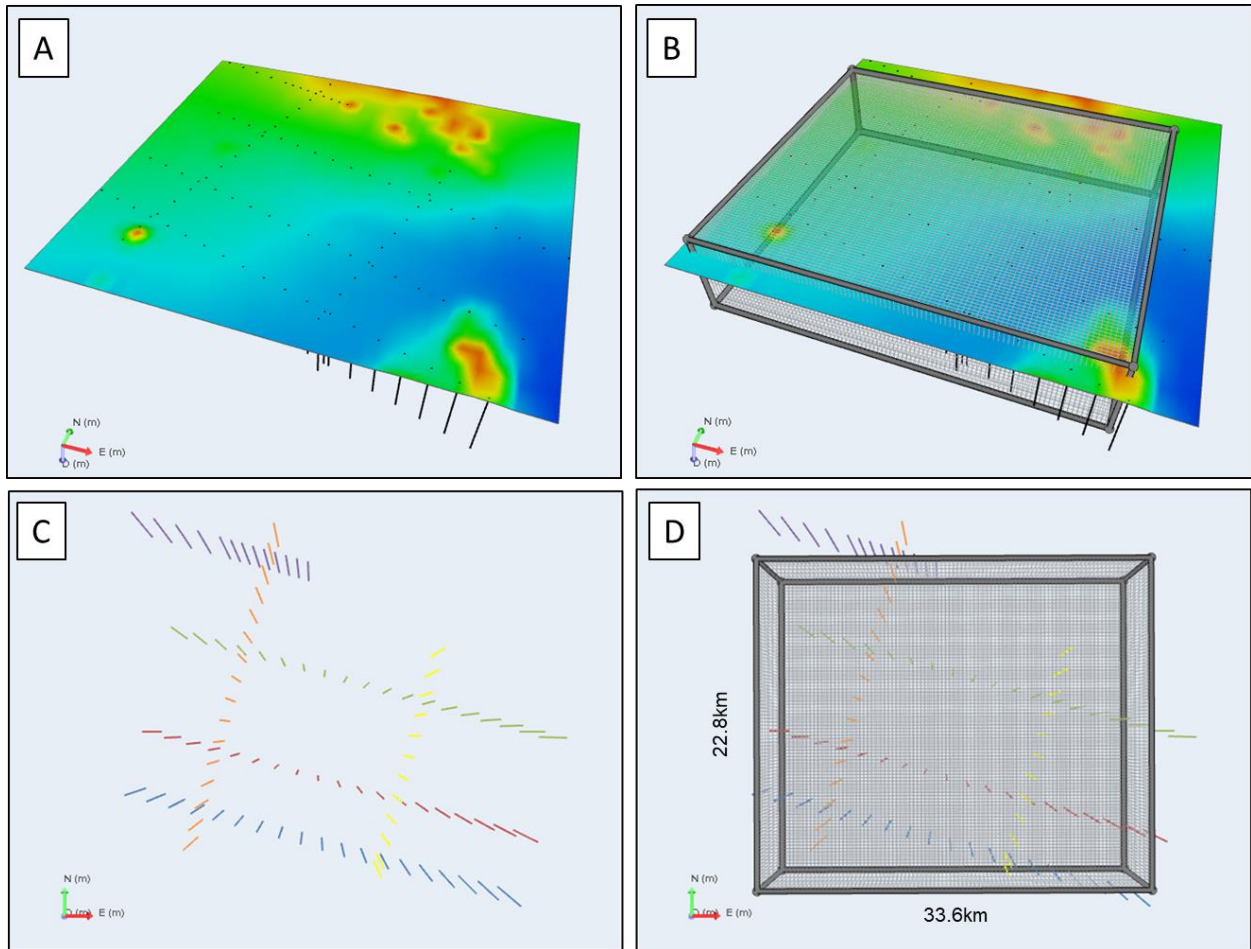


Figure 6-1 (A) JewelSuite representation of synthetic vertical wells from the structural cross sections intersecting the ground surface derived from the digital elevation model; (B) Outline of model box superimposed on ground elevation; (C) Map view perspective of 3-dimensional well trajectories located along the six structural cross sections; (D) Outline of model box for the GFM superimposed on well trajectories with GFM dimensions (33.6 x 22.8 km).

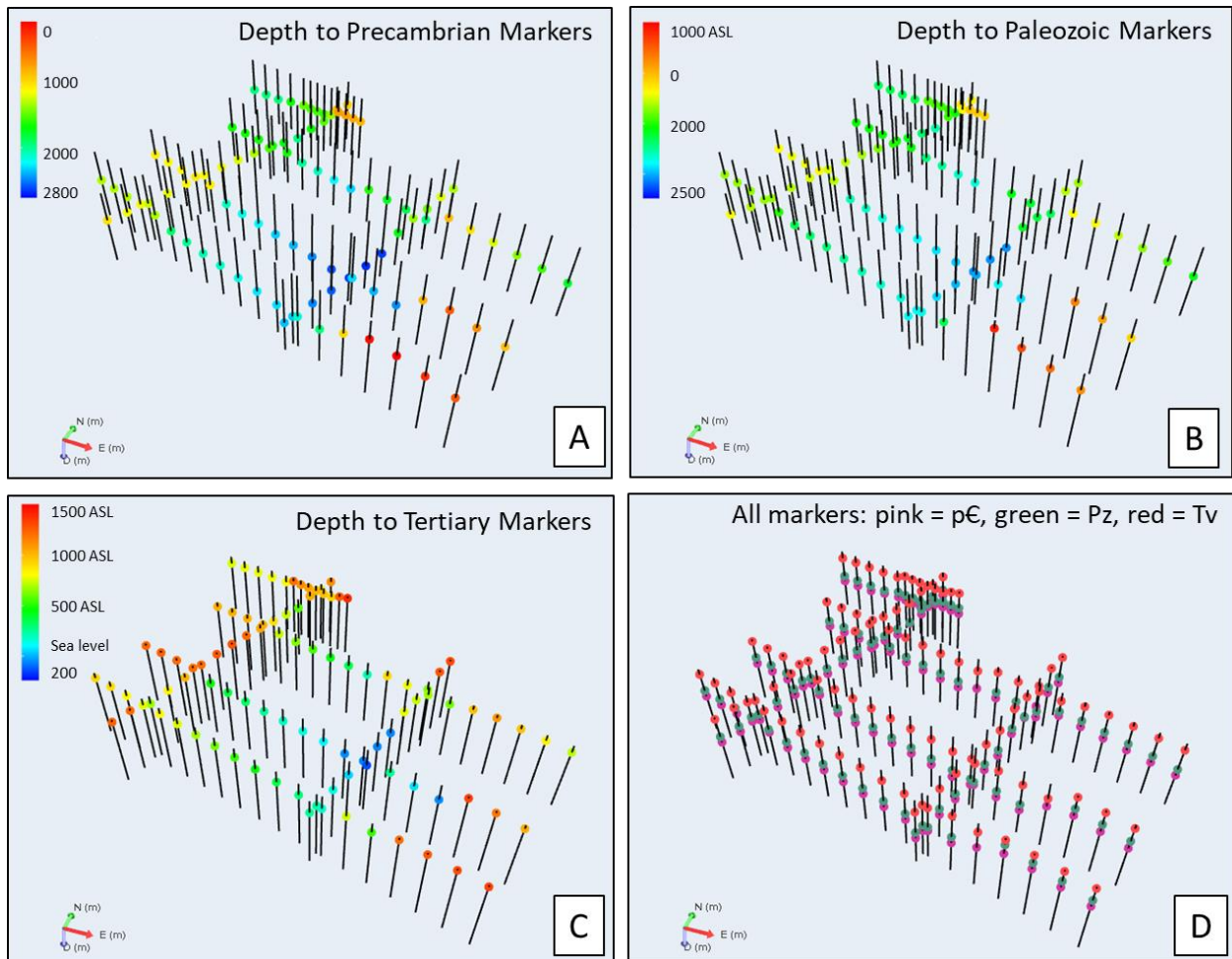


Figure 6-2 Tops of bedrock units ("markers") from well data extracted from the six structural cross sections. (A) Top of Precambrian; (B) Top of Paleozoic; (C) Top of Tertiary; (D) All marker tops for all bedrock units.

6.3 Surfaces

Two types of surfaces were created in JewelSuite: faults and stratigraphic horizons. For this first iteration of the GFM we modeled two main normal faults: the basin-bounding fault, which dips to the west and southwest, and the antithetic fault that dips to the east. These are identified as Fault #1 and Fault #3, respectively, in Figure 5-13. The faults were created in the following steps:

- Digitize the fault surface traces in ArcGIS to create polylines.
- Import the polylines into JewelSuite to create a fault surface trace.
- Create a duplicate polyline of the fault trace and then manually offset this copy such that the dip angle is representative of the basin-bounding faults (~60°).
- Triangulate the two polylines to create a meshed fault surface.

The marker data for each bedrock unit were similarly triangulated to create meshed surfaces for each horizon top. The surfaces were created in the following steps:

- Select the marker set that will be used as the surface representation
- Define the output geometry such that the surface extent matches the desired areal extent of the GFM
- Select interpolation method and power

This model defined the interpolation method as inverse distance weighted (IDW) with a power of 4. IDW is a simple interpolation method that determines cell values based on a linearly weighted combination of a set of sample points; the weight of nearby points is controlled by the power value. While the default power value is 2, we found that using a slightly higher power value of 4 – which assigns more weight to the nearest points – helped smooth the surfaces and prevent large peaks and valleys due to slight variations in marker depth.

The results are shown in 3D (oblique perspective) and 2D (map view) for the faulted bedrock units (Figure 6-3) and for the tops of three horizontal alluvium units (Figure 6-4). A cross sectional perspective looking to the north of all GFM surfaces portrays the wide, full graben basin geometry in the south and the narrowing of the basin to the north as the trend of the eastern boundary fault changes from N to NW.

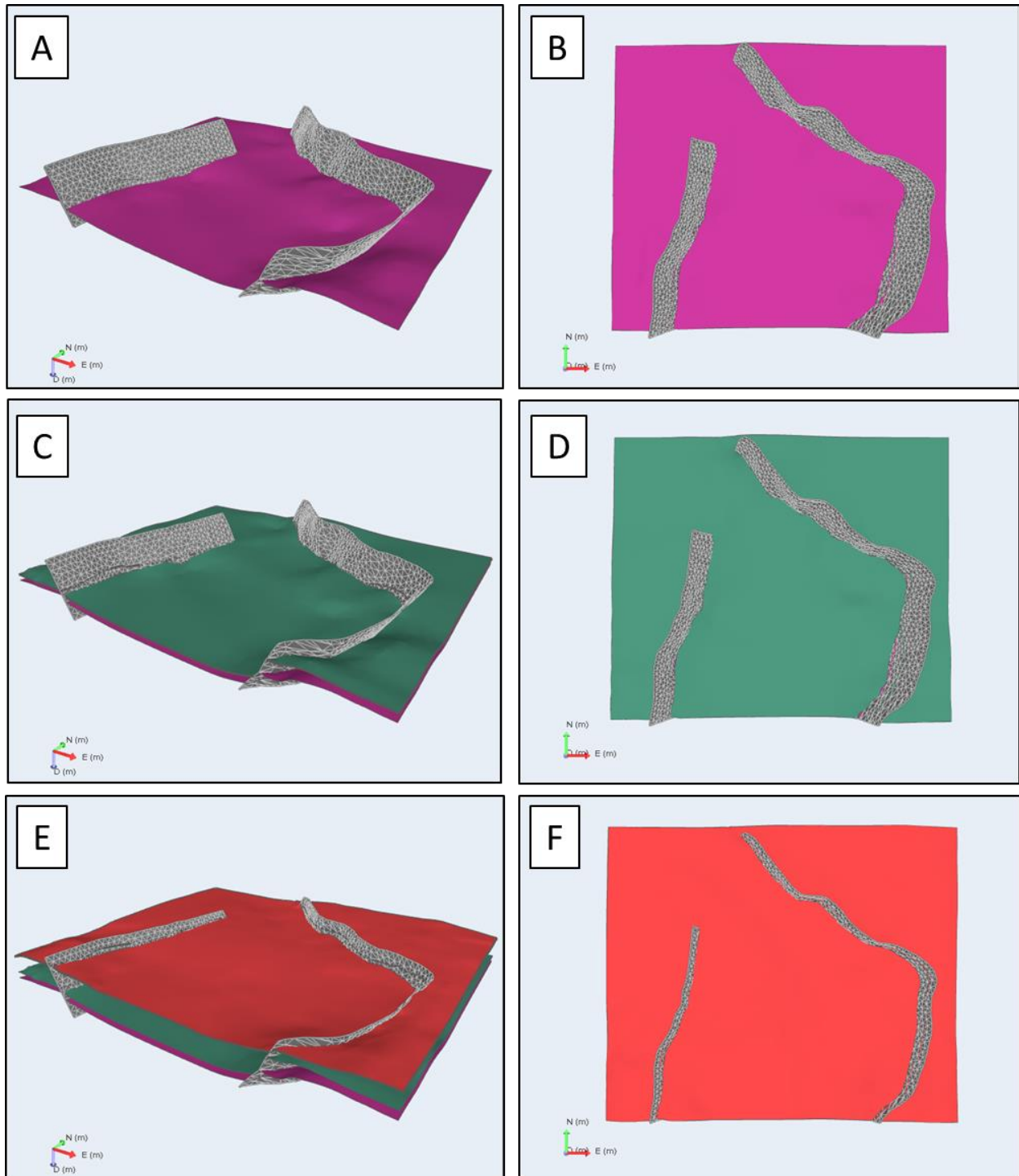


Figure 6-3 Fault and bedrock horizon surfaces created for the GFM presented in 3D perspective and 2D map view for top of Precambrian (A,B), tops of Precambrian and Paleozoic (C,D), tops of Precambrian, Paleozoic and Tertiary volcanics (E,F).

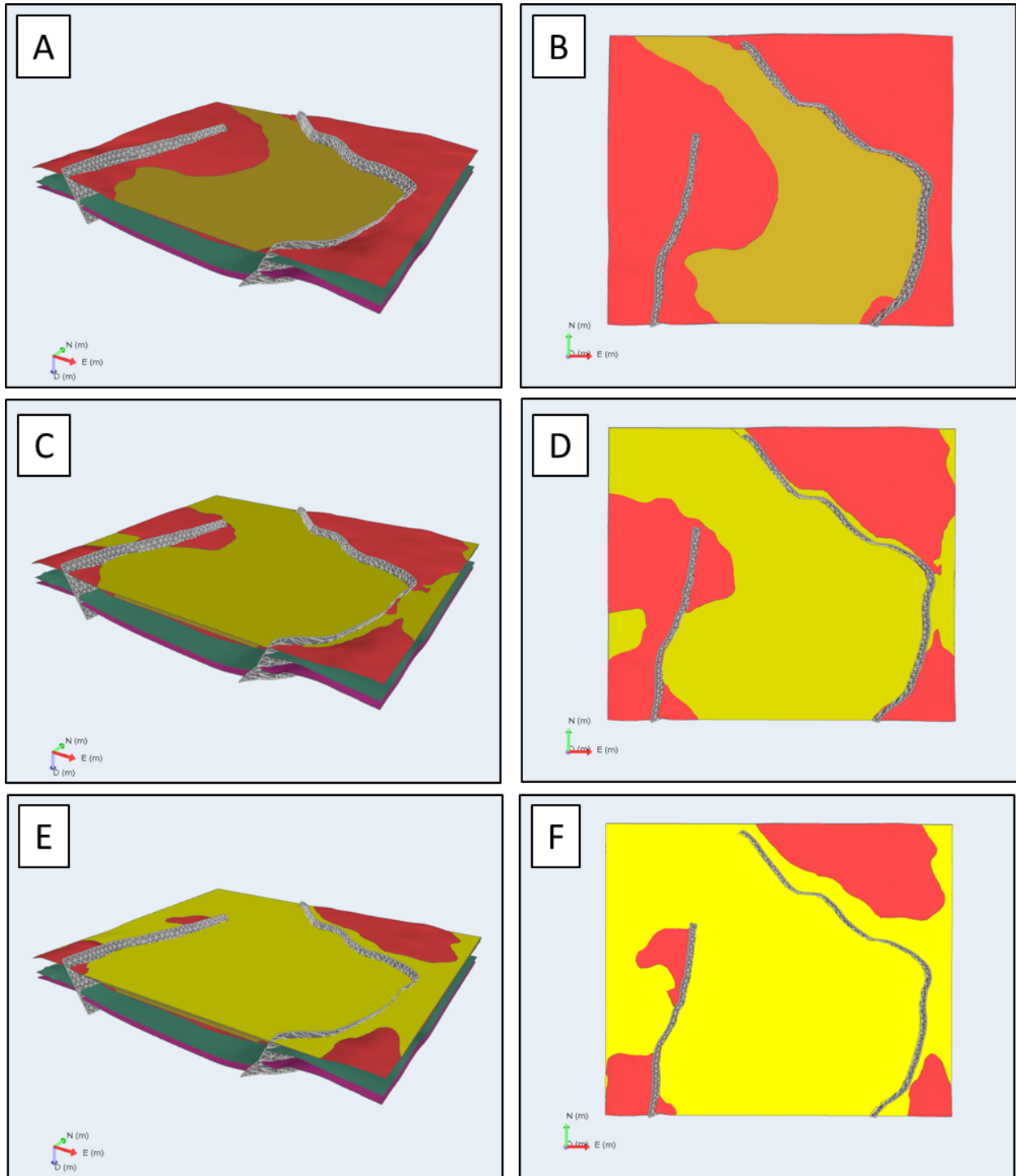


Figure 6-4 Fault and horizon surfaces of bedrock and alluvium created for the GFM presented in 3D perspective and 2D map view for tops of bedrock and alluvium unit 1 (A,B), tops of bedrock, alluvium unit 1 and alluvium unit 2 (C,D), tops of bedrock, alluvium unit 1, alluvium unit 2 and alluvium unit 3 (E,F).

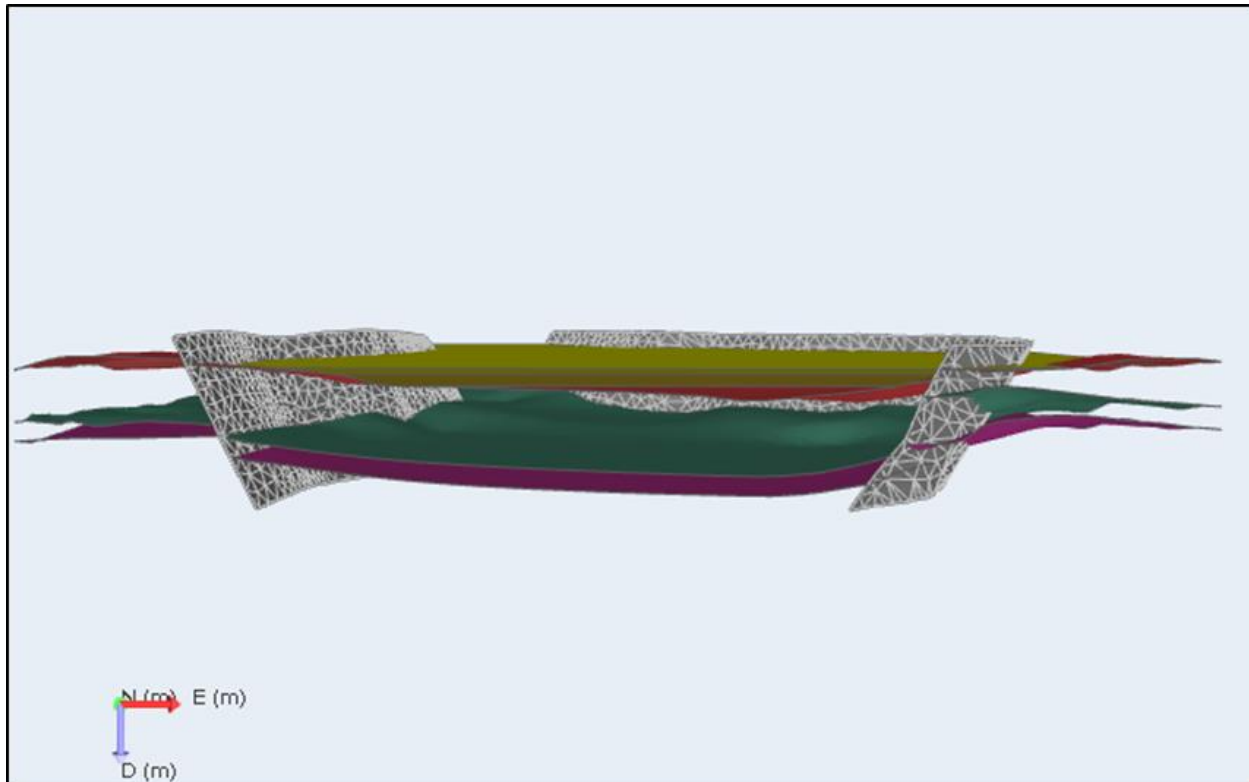


Figure 6-5 Cross sectional view looking to the north of all horizon and fault surfaces in the GFM.

6.4 Volumes

Before creating the three-dimensional mesh for the GFM volume, the model must be made watertight, i.e., any holes at fault/horizon and horizon/horizon boundaries must be removed. JewelSuite has a number of tools to help the modeler achieve a watertight volume, which often require multiple iterations to arrive at a watertight solution. Where horizons cross faults (rather than being truncated by a fault), the “Clear Intersection” tool will retract the horizon. Where horizons do not fully extend to the fault, the “Extend to Other Surfaces” tool will extend the horizon to create a watertight connection. Once the model is watertight, the next step in JewelSuite is to create the Stratigraphic, Fault and 3D Structural models. Upon validation of these three models, the 3D Mesh workflow can be initiated to create a 3D mesh of the model volume. The 3D mesh was created in the following steps:

- Assign data to the model, including both faults (from the Fault Model) and surfaces (from the 3D Structural Model)
- Create boundary: this is auto-created in JewelSuite assuming the model is watertight
- Set element sizes: we used a maximum element size of 500m to allow for moderate model resolution without significantly slowing down processing speed
- Mesh surfaces

Upon completion of the 3D Mesh workflow, the surfaces are used to create meshed volumes.

The 3D mesh volumes for the bedrock units are shown in Figure 6-6 and Figure 6-7. Although the bedrock units are truncated and offset by faults, their subparallel structure throughout the model is ideal for mesh generation. The criteria that must be satisfied to create a watertight model within the alluvial units are more complex, because these units are truncated both by faults and the Tertiary volcanics unit; as such, these units must be treated as both a horizon and an unconformity and require a considerable amount of automated and manual modeling.

At present we have not achieved watertight status for the alluvium horizons, and therefore we are currently unable to generate meshed volumes for these units. It is interesting to note the topography on the top of the Tertiary volcanics (Figure 6-6E; Figure 6-7A). The regions of lowest elevation correspond to the thickest accumulation of overlying alluvial sediments.

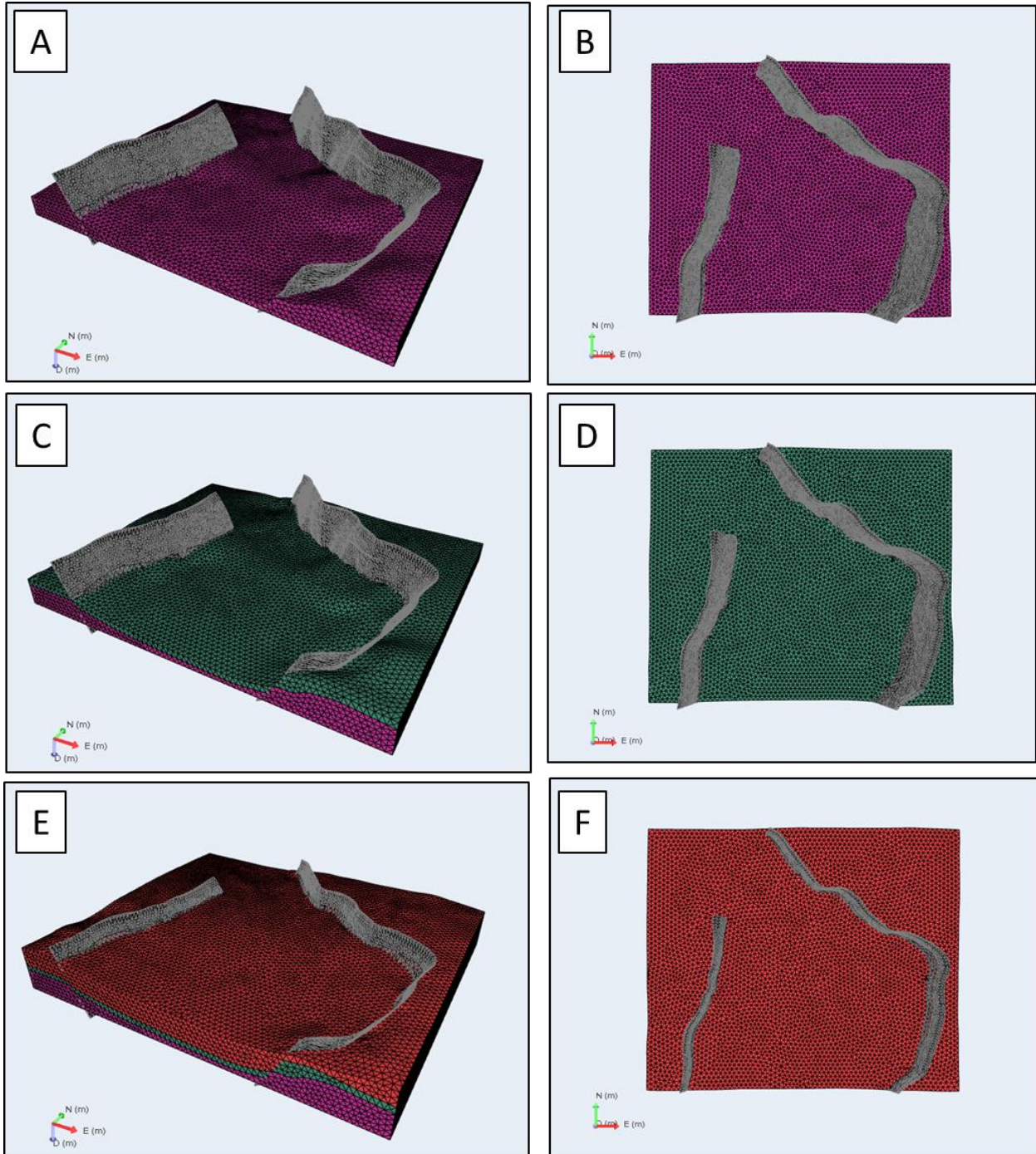


Figure 6-6 Three-dimensional gridded volumes of the GFM in oblique perspective and map view for the Precambrian (A, B), Precambrian and Paleozoic (C, D) and Precambrian, Paleozoic and Tertiary volcanics (E, F).

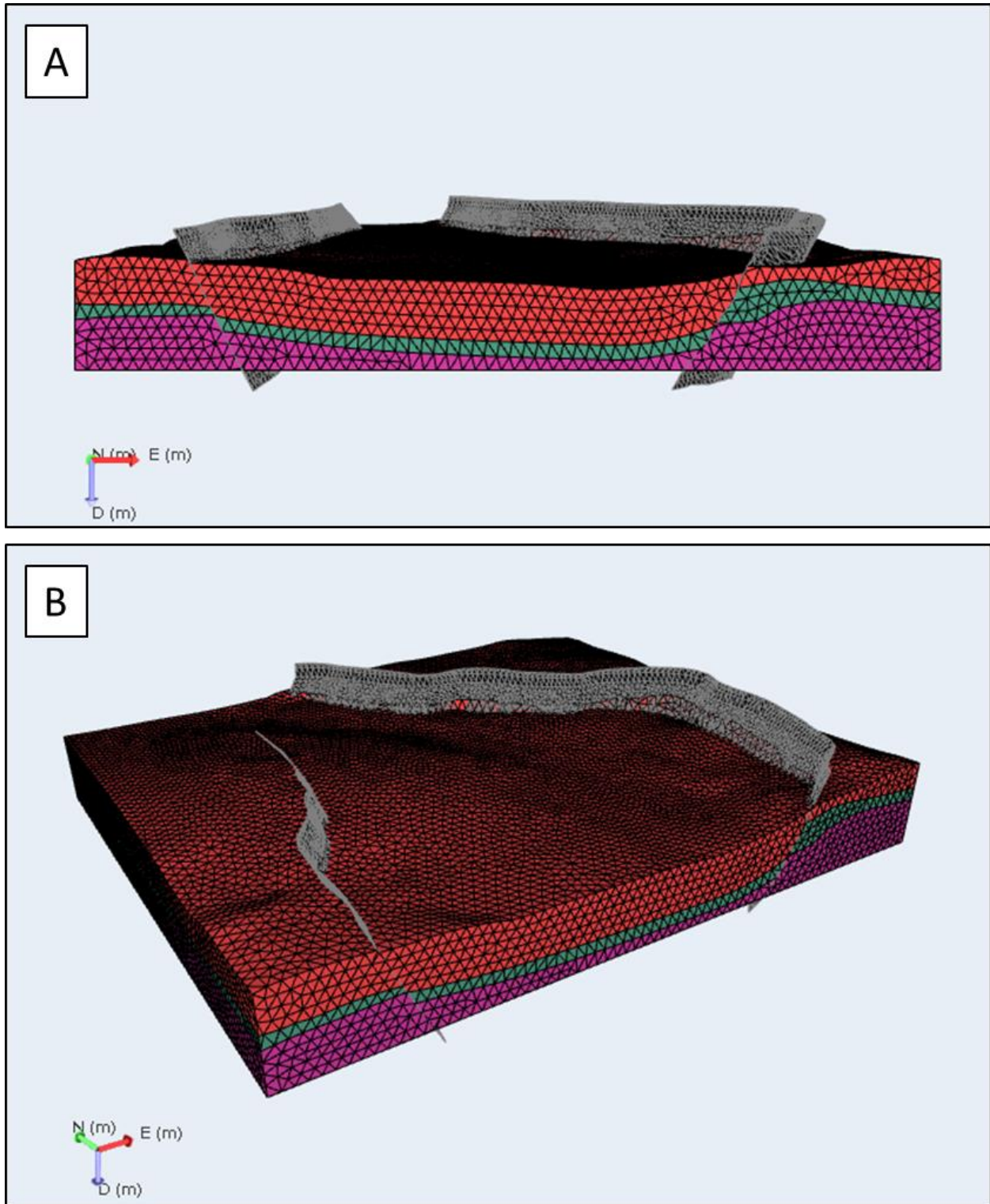


Figure 6-7 Three-dimensional gridded volumes of the GFM for all bedrock units as viewed in cross section (A) and oblique (B) perspectives. Note the symmetric graben geometry in the wide south portion of the basin as well as the topography on top of the Tertiary volcanics.

6.5 GFM Assessment

Insofar as a model is an approximation of the subsurface geology, it is important to evaluate whether the GFM captures the important elements of the subsurface characterization, and if not, to provide strategies to improve the GFM. Comparing cross sectional (Figure 6-8) and map views (Figure 6-9), one may conclude that the model captures the geometry of basin-bounding faults (amount of displacement, curving fault trace) and overall graben geometry of the Deming sub-basin. Further, the fault traces, bedrock outcrops, and top of alluvium in the GFM (Figure 6-9C) are in good agreement with the published geologic map (Figure 6-9A) and the fault map from this study (Figure 6-9B). The top of Tertiary volcanics (Tv) (Figure 6-7) is a good match with the distribution of alluvium thickness (Figure 4-10).

On the other hand, bedrock unit thickness is not uniform (with the exception of eroded Tv) as portrayed in the structural cross sections, most notably for the Paleozoic unit in the footwall of Fault #1 (block A) in the GFM (Figure 6-8). The consistent eastward dip (2° - 5°) of the bedrock, i.e., block rotation for structural blocks A, B and C, is not captured in the GFM, in part because Fault #2 was not included in the model. The next model iteration will include this important synthetic normal fault, as well as a more detailed distribution of basin-fill alluvial sediments described in (Section 5.2.5).

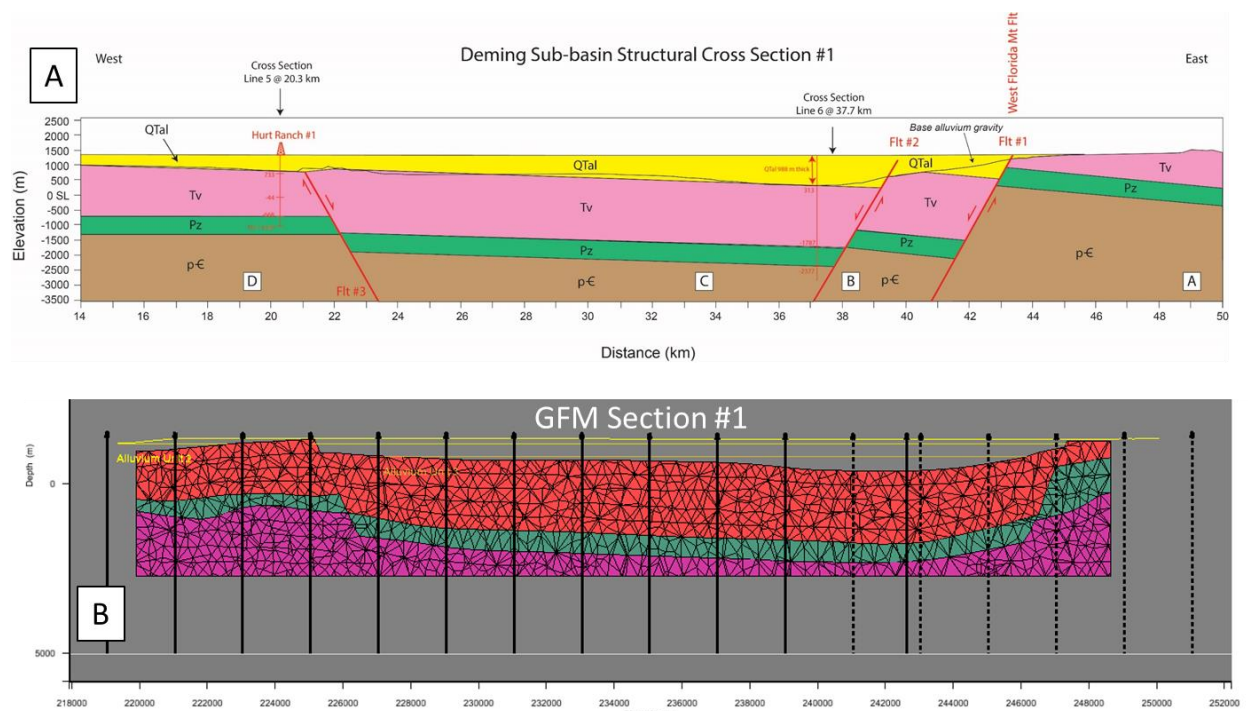


Figure 6-8 Comparison of structural Cross Section #1 (A) to the GFM cross section at the same location (B). The vertical black lines in the GFM are the synthetic wells and the horizontal yellow lines are the three alluvium tops.

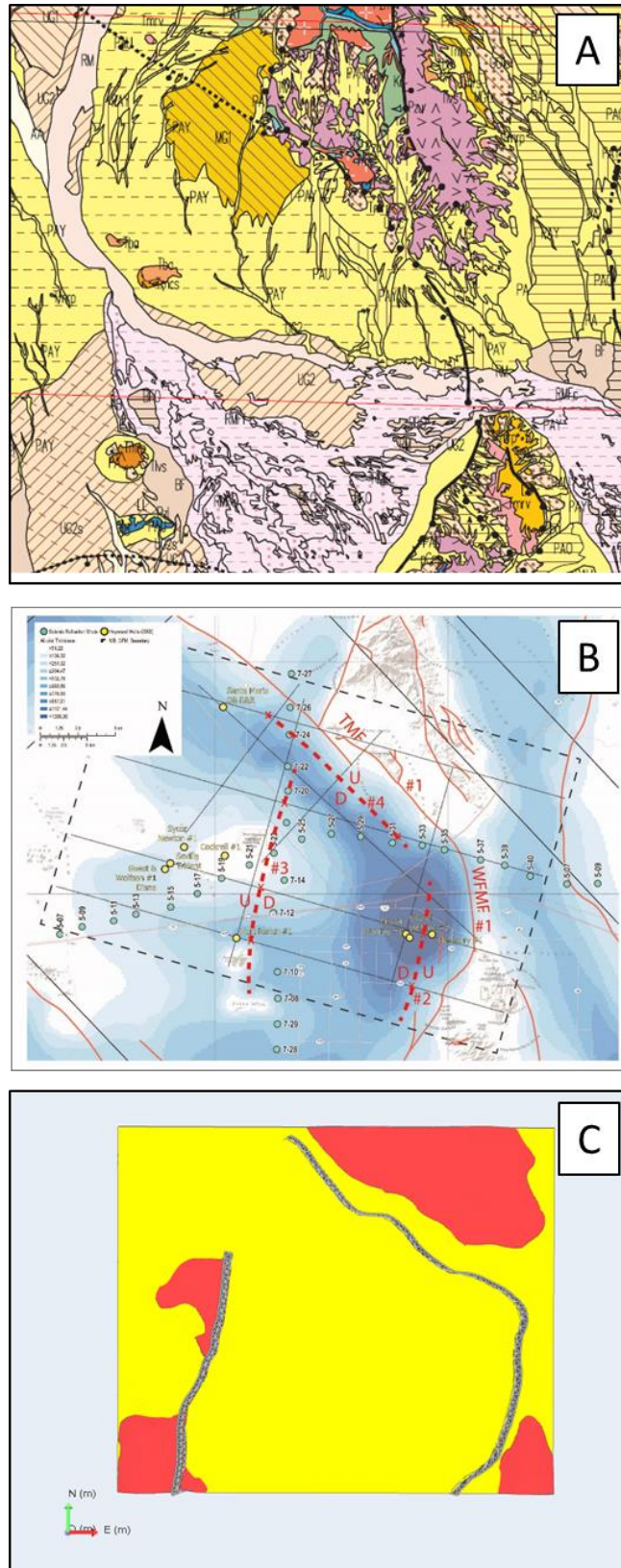


Figure 6-9 2D perspective map view of (A) surface geology from Hawley et al, 2001; (B) Fault traces and contours of alluvium thickness from this study; and (C) Surface geology and faults from the GFM.

7 The Hydrologic Framework Model (HFM)

The geologic framework discussed in earlier sections is critical to begin to model flow and transport, offering broad bounds on flow parameters. Yet geologic characteristics alone cannot give all the information needed for hydrologic flow models. This translation of geologic data to hydrologic parameters cannot be done by existing software. Instead, it is entirely done via site-specific measurements, where available, and judgement calls from subject matter experts. Model calculations can sometimes help with translation of measurable data into flow model inputs. For example, we cite studies in the following sections that modeled water well levels to obtain calculated hydraulic conductivity. However, this covers only a small part of creating a hydrologic framework model.

Accurate hydrologic models require that most of the properties described below be measured at the particular site of interest. In the absence of site-specific measurements, estimates of hydrologic parameters can be made based on grain size, cementation, chemistry, and regional and local geology. Each of these aspects is discussed in more detail below.

It is important to note that our understanding of the link between the geology and the hydrologic parameters is incomplete, and the ranges and errors could likely be reduced with a focused study. In addition, site-specific measurements would reduce uncertainties for a given basin, if those measurements exist. Below is the current status of knowledge for this link between the geology and the necessary flow model inputs, listed by input. This is intended to show our current process for using geologic data to inform model inputs.

7.1 Porosity

Porosity is important to define the volume of water that contains solute and heat in transport models (Masbruch et al., 2014). It can be measured from rock cores directly, although this is not commonly done for water wells. Porosity of alluvial deposits comes in two primary forms: the porosity between clasts, “inter-grain”, where flow is most likely, and the porosity within clasts. Volcanic clasts in particular have a fair amount of porosity that will likely have a lesser role in flow properties. The inter-grain porosity is more likely to decrease under a lithostatic load than the porosity within clasts. While we are aware of these second-order effects, reported data (where present) usually does not distinguish these different types, and so we present here a single value of porosity that includes all porosity. Porosity will also be dependent on cementation, with more highly cemented samples having reduced porosity (also discussed in 7.2.2).

Porosities for coarse grained alluvial deposits have been reported to range between 16% to 42% (mean of 31%), (Smyth et al., 1979); 38-43% (Kwicklis et al., 2006); and 30-50% (Mariner et al., 2018). Anderson (1992) calculated porosities based on density to be between 17-33%. We take the uncemented value of coarse-grained alluvial deposits to be approximately 40%, decreasing to 25% in deeper, more cemented and compacted layers. Fine-grained playa

deposits have been reported to have porosities of 35%-50% (Davis, 1969), 51% (Thomas et al., 1989), and 26-57% (Mariner et al., 2018).

For the Mimbres basin, we were unable to find any reported values for porosity in alluvial units within the study area. In an area of the Mimbres Basin more than 30 km northwest of our study area, porosity was reported to be between 18 and 25% (Trauger and Lavery, 1976, as cited by Hanson et al., 1994).

Hydrologic properties for units below the alluvium are important for determining regional interbasin flow and for evaluating the potential impacts of changing climate on the future water table. Thus, we include some values relevant to Tertiary volcanic rocks, Paleozoic carbonates, and the Precambrian basement rocks. Tertiary volcanic rocks in the area of southern Nevada have an average porosity of ~30% (e.g. Diment et al., 1958). Paleozoic carbonates commonly underlie basins throughout the Basin and Range, and can accommodate significant inter-basin flow (Heilweil and Brooks, 2010), and these carbonates in the Great Basin have porosities of 5-10% (Harrill and Prudic, 1998). Metamorphosed pre-Cambrian basement rocks have much lower porosity, around 1% (Masbruch et al., 2014).

7.2 Permeability

Permeability is one of the most important flow model inputs. Permeability in alluvial units varies by many orders of magnitude, and will also vary based on the scale of the measurement. Model simulations require regional-scale measurements of permeability, and this will be the only type of data discussed here. Information about the geology can guide estimates of permeability of alluvial units, but this will not work well for highly fractured rocks. Some of the important geologic characteristics that control the permeability include grain size, cementation, depth, fracturing and faulting (Smyth et al., 1979). Permeabilities are not often reported directly for alluvial units, but where measured, are given as hydraulic conductivities, which describe the flow of water with units of meters per day.

Permeabilities of alluvial deposits vary between horizontal and vertical flow, usually by about one or two orders of magnitude, with the horizontal flow occurring primarily in the more permeable gravels, and the vertical flow being impeded by clay layers (Thomas et al., 1989; Harrill and Preissler, 1994). This year's models do not incorporate anisotropic permeabilities, but this will be an important future consideration. An additional important consideration in the regional permeability structure is the role of faults and fractures, which may serve as conduits of flow and also may retard flow, as discussed in section 7.2.4.

7.2.1 Grain Size

Permeabilities of alluvial units can vary between $\sim 10^{-10}$ to 10^{-15} m² (Belcher et al., 2001). Within this range, the larger grain size units such as the coarse sand and gravel with occasional beds of silt tend to have higher permeabilities ($\sim 6 \times 10^{-11}$ to 3×10^{-12} m², average of 10^{-11} m², based on values from Thomas et al., 1989; average of 1×10^{-12} m² from Harrill and Preissler, 1994), and

smaller grained sizes units such as silts and clays have lower permeabilities (average of 3×10^{-15} m², based on values from Thomas et al., 1989; average of 3×10^{-14} m², based on Harrill and Preissler, 1994). The coarser units are generally found near basin margins, while finer units are generally found near basin axes (Section 5.2.3). The Mimbres Basin contains mostly sand-size grains, with some gravels and clays. Thus, permeabilities likely range between 10^{-10} to 10^{-15} m².

7.2.2 Cementation

Another strong influence on the permeability is the degree and type of cementation between the clasts. When deposits are initially laid down, whether by slope transport or alluvial processes, the gaps between them are initially open. Over time, typically due to the interactions with water, some of the pore spaces fill with cement. This cement can be calcite, silica, clay, or other material. Basin-fill deposits tend to be uncemented near the surface, but become more cemented and indurated with depth, particularly below the water table (Belcher et al., 2001). For the Mimbres Basin, the deposits are unlithified to moderately lithified, with calcite composing the dominant cement type, with subordinate silica and limonite (hydrated iron oxides and hydroxides) (Hanson et al., 1994).

7.2.3 Depth of Burial

At increased depth, the volume between clasts decreases due to the increase in lithostatic load, compacting the rock. The depth can be compared to permeability (or hydraulic conductivity, as done by Belcher et al, 2001), but it is difficult to separate out the role of depth from increased cementation. These authors found that, across all rock types, hydraulic conductivity spans from .001 to 1000 m/d for rocks buried less than 500 m, and .000001 to 1 m/d for rocks between 1500 and 2000 m depth.

7.2.4 Faults and Fractures

Faults can have permeabilities that differ from their host rocks, affecting groundwater flow (e.g. Sweetkind et al., 2010; Fenelon et al., 2012). In the current model, the faults do not have unique hydrologic properties, but this may be important to include in future models. It is difficult to estimate fault hydrologic properties based on the geology. Generally, faults are assumed to have fine-grained fault gouge cores with a lower permeability than the host rock, and a fractured “damage zone” with permeability that is higher than the host rock, where increased fracture density increases flow (e.g. Caine et al., 1996; Evans, 1997), but exceptions occur (Chester and Logan, 1986). Permeability may also be affected by fault orientation, with those aligned perpendicular to the present-day minimum principal stress likely having a greater aperture and permeability than those aligned with more compression across the faults (Fenelon et al., 2012; Faunt, 1997). Fault permeability would have to be addressed by site-specific research.

7.2.5 Permeabilities in study area basin

The ranges of hydraulic conductivities for the alluvial basins in the Death Valley Regional Flow System, derived from 25 single well and 18 multiple-well aquifer tests, vary from 0.001 to 130

m/d (Belcher et al., 2001). This is equivalent to permeabilities between $\sim 10^{-10}$ to 10^{-15} m². The 0.003 to 34 m/d for the finer-grained “alluvial confining unit” based on 15 analyses also fall within this range. The values used by Sandia National Laboratories for their alluvial basin models (hydraulic conductivities of 0.54 - 3.5 m/d, and permeabilities of 10^{-11} to 10^{-14} m²) are well within this range (Meridian et al, 2018; Sevougian et al., 2019, based on data from Cochran et al., 2001).

Hydraulic conductivities were calculated for the Mimbres Basin alluvial units by Hanson et al., 1994, based on a model constrained by well water levels, estimates of outflows, and estimates of recharge. In the entire basin model, hydraulic conductivity values range from 0.001 m/d to 18.9 m/d. The parts of the basin selected for the study area model here have hydraulic conductivities ranging between 0.2 and 1.2 m/ day (Hanson et al., 1994), with the larger values in one cell covering the entire central part of the basin (Figure 7-1).

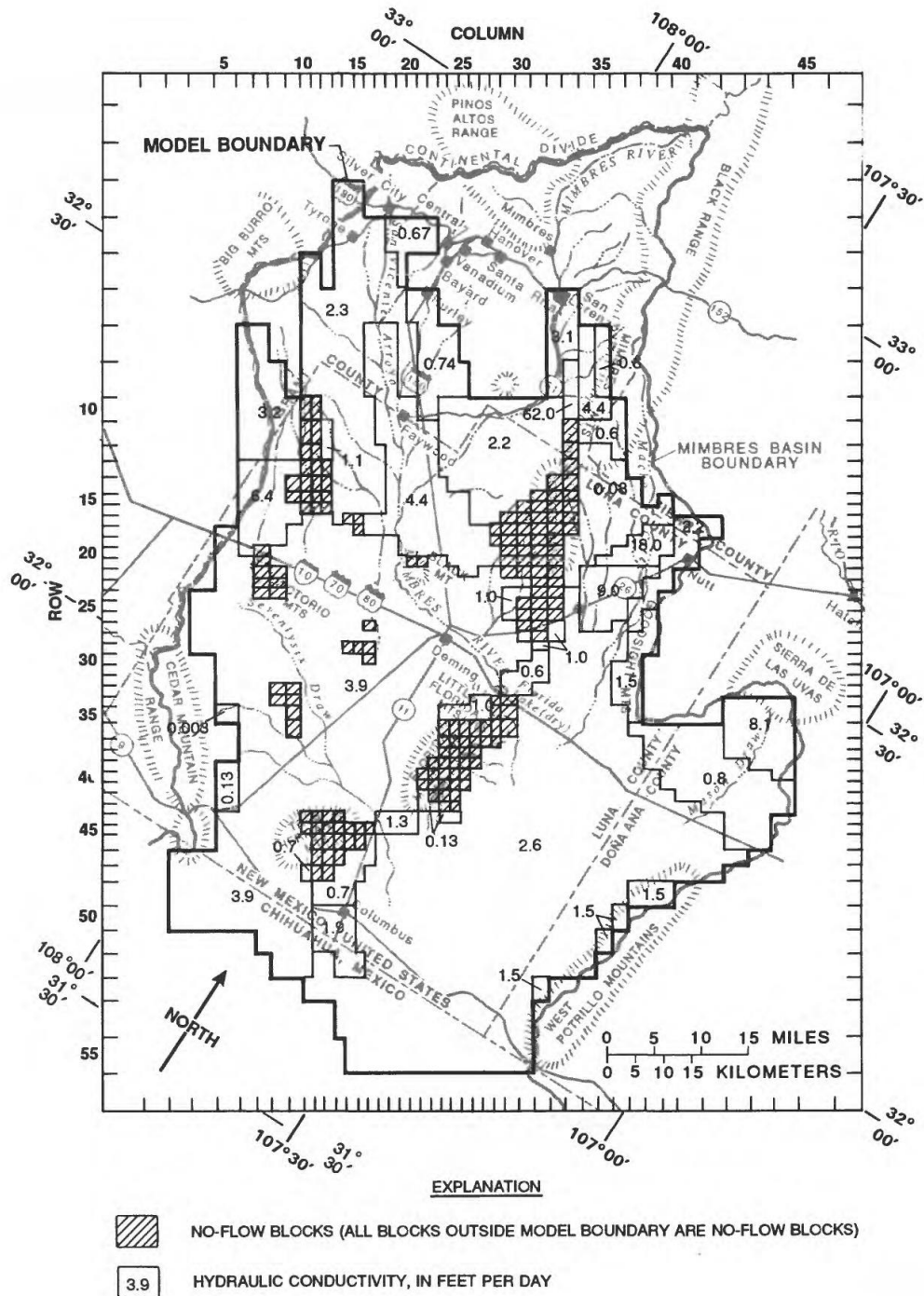


Figure 7-1 Map of model-produced values for hydraulic conductivity of the aquifer in ft/day from Hanson et al, 1994 (text converts to m/d).

Hydraulic conductivities were also calculated for the Mimbres Basin by Finch et al. (2008). They integrated data from Hanson et al., 1994 with other data into a 3-D regional groundwater flow model, and produced estimates of hydraulic conductivity of not just the alluvial part of the basin, but the lower layers as well (Table 7-1).

Table 7-1 Hydrogeologic properties from bedrock and basin-fill sediments in the Mimbres Basin (from Finch et al, 2008). Last column is added to show in m/d for better comparison with other data sources.

Age	Key Formations	Thickness, ft	Rock Type	Hydraulic Conductivity, ft/d	Hydraulic Conductivity, m/d
Paleozoic	Lake Valley Ls	300 to 400	limestone		
	Oswaldo Fm	300 to 400	dolomite	0.01 to 900	0.003 to 300
	Abo Fm	up to 640	shale, siltstone, limestone		
Cretaceous	Colorado Fm	up to 1000	shale, limestone, sandstone	0.0005 to 1.4	0.0002 to 0.4
	Beartooth Quartzite	65 to 140	quartzite		
Tertiary	Sugarlump Tuff Rubio Peak Fm Hurley Sill	up to 3600	volcanic, volcanoclastic, shallow intrusive	0.002 to 0.4	0.0006 to 0.1
Tertiary to Quaternary	Gila	up to 3500	poorly consolidated	0.01 to 100	0.003 to 30
	Conglomerate alluvium	less than 100	sediments	10 to 400	3 to 100

Both Finch et al., 2008 and Hanson et al., 1994 show similar ranges in hydraulic conductivity for the alluvial section in the Mimbres Basin, 0.003 to 30 m/d vs 0.001 to 20 m/d, respectively. However, both of these datasets are based on the water wells, which generally do not penetrate deep into the basin. It would be expected that the deeper layers would have lower permeability due to their depth and cementation.

Belcher et al., 2001 reported a range in hydraulic conductivity values for Tertiary volcanic rocks, based on 159 analyses, from 0.000001 to 180 m/d, with a geometric mean of 0.1 m/d and an arithmetic mean of 4 m/d. They also found that altered tuffs have approximately one order of magnitude lower hydraulic conductivity than unaltered tuffs. Plume (1996) reported a range in hydraulic conductivity for Paleozoic carbonates between 0.002 and 300 m/d, with a median of 0.2 m/d and a mean of 20 m/d. In Table 7-1, Finch et al., (2008) show a range from .002 to 0.4 m/d. Clearly, a wide variety of permeabilities would be acceptable for the Tertiary volcanic rocks, and more information is needed about the welding and alteration states to make an adequate estimate. Better estimates would require permeability data on the volcanic rocks from the Mimbres Basin.

Paleozoic carbonates tend to have hydraulic conductivities that are dependent on the extent of fracturing, but can be as high as 800-900 m/day (permeability of 10^{-9}), and average 90 m/day (permeability of 10^{-10} m²) (Belcher, 2002). We chose the average value, which agrees with calculations by Finch et al. (2008) for the Mimbres Basin.

7.3 Saturation

The level of saturation is difficult to predict from the geologic setting. The surface is usually unsaturated, unless under a lake or river, and saturation generally increases with depth until the water table is reached. Complexities arising from the presence of low-permeability layers may result in perched water tables (where the saturated rock does not directly connect to the aquifer below). Faults and other features that juxtapose geologic features with high permeability contrast can dramatically impact fluid pathways, and therefore create large offsets in the water table, within a basin.

The top of the saturated zone is often recorded in water wells, as it is the target of the majority of the wells in the Mimbres Basin. However, saturation levels for unsaturated rocks are not commonly measured, and are of importance for transport modeling. In addition, it is unlikely to see records of perched water tables from existing well logs. For the Mimbres Basin, there are reports of a perched water table in the Tyrone Mine area, which is located in a “granite-like” rock containing the ore body (New Mexico Office of Resources Trustee, 2012). However, this rock type is not found in the study area, and no other mention has been made regarding a very low-permeability unit. Therefore, we assume that there are no perched water tables, and the rock is entirely saturated below the top of the water table.

7.4 Sorption Properties

Sorption properties, the ability of the rock to adsorb radionuclides and slow their transport, affect a site’s transport properties. Since sorption properties are not commonly measured in wells dug for water or oil, it is unlikely that a literature review of a site’s geologic data will produce useful values. Each site must be sampled and analyzed specifically for measuring sorption properties. However, there are some broad trends that may help down select for favorable basins.

Clastic units dominate the Mimbres Basin alluvium and these will consist dominantly of quartz, feldspar and rock fragments derived from the surrounding highlands. Quartz and Feldspar typically have small sorption coefficients, whereas rock fragments sorption coefficients may vary considerable depending on their composition. Clay minerals and zeolites are present in most of the alluvial units and will be abundant in some, especially the finer grained units. The clay minerals, and particularly zeolites, typically will have high sorption coefficients and thus may control the sorption properties of the units. Zeolites may also be common when basins fill with material derived from volcanic rock, and sit below the water table for an extended period of time. Volcanic clasts are associated with both a greater clay proportion within the matrix, and greater zeolite content, and thus generally have a greater capacity to adsorb radionuclides (Hoffman et al., 1977).

Mariner et al. (2018) compiled a list of sorption coefficients from several sources, calculated based on data from the Nevada National Security Site, another alluvial basin in the Basin and

Range that contains a relatively large proportion of clasts derived from volcanic rocks. Their values are presented in Table 7-2. Sorption data are not available for units in the Mimbres Basin, but these would be important data to gather for any propose repository site.

Table 7-2 Sorption properties for alluvium provided by Mariner et al. (2018) in their Table 5-7. Radionuclide sorption coefficients in mL/g for alluvium at the Nevada National Security Site.

Species	(Value, probability)	Best value (range)	Best value (range)	Mean value ± st dev (range)	Value
Pu	mean = 100; range = 50 to 300; standard deviation = 15	0.9 (1.4 – 0.4) ($O_2 = 10^{-5}$) 1.3 (1.8 – 0.8) ($O_2 = 10^{-10}$) 1.9 (2.3 – 1.4) ($O_2 = 10^{-15}$)	2.1 ($O_2 = 0.2$)	4,091 ± 4,448 (230 – 21,000)	
Am	Range = 1,000 to 10,000; mean = 5,500; standard deviation = 1,500	3.7 (4.1 – 3.4)	4.2 (4.7 – 3.7)	174,469 ± 214,582 (3,200 – 1,400,000)	
Np	(1.8, 0.) (4.0, 0.05) (8.7, 0.95) (13, 1.0)	0.7 (1.1 – 0.3)	1.5 (2.0 – 1.1)	8.57 ± 5.08 (1.83 – 22)	25 to 30 over pH 7.5 to 8.5
U	(0, 0.) (5.39, 0.05) (8.16, 0.95) (20, 1.0)	0.4 (0.8 – 0.03)	0.8 (1.3 – 0.3)	6.36 ± 5.04 (0.9 – 60)	
Am	Range = 1,000 to 10,000; mean = 5,500; standard deviation = 1,500	3.7 (4.1 – 3.4)	4.2 (4.7 – 3.7)	174,469 ± 214,582 (3,200 – 1,400,000)	
Tc	0			2.16 ± 3.48 (0 – 12)	
Material	Alluvium, devitrified	Alluvium	Alluvium	Alluvium*	Alluvium
Location	Yucca Mountain	Frenchman Flat	Frenchman Flat	Nevada Test Site	Fortymile Wash
		calculated	calculated	measured	measured
Reference	Sandia National Laboratories (2008)	Zavarin (2004)	Tompson et al. (2001)	Hu et al. (2008)	Bertetti and Werling (2004)

7.5 Unsaturated Hydraulic Properties

Properties of the rock that describe how the moisture content affects the pressure head and unsaturated hydraulic conductivity (Cochran et al., 2001) are critical to model flow through the unsaturated zone. Such properties are difficult to predict based on geology alone, and need to be calculated based on data from site-specific samples. Most of the available data for alluvial hydraulic properties come from the NNSS, a coarser-grained basin with a deeper water table. However, these data are the most relevant available data to our study area, so we will use them directly. Mariner et al. (2018) list the applicable hydraulic parameters from the NNSS that they

used in their basin models, and their Table 5-2 is repeated here (Table 7-3) for ease of reference. For further discussion, the reader is referred to their report.

Table 7-3 Unsaturated alluvium hydraulic properties values from the Greater Confinement Disposal Boreholes, Nevada National Security Site (Table 5-2 in Mariner et al., 2018).

Parameter	Mean value	Value
Saturated hydraulic conductivity (m/d)	0.82	0.72
Residual moisture content (unitless)	0.06	0.065
Saturated moisture content (unitless)	0.33	0.36
van Genuchten fitting parameter (cm^{-1})	0.071	0.036
van Genuchten fitting parameter (unitless)	1.4	1.94
Reference	Cochran et al. (2001)	Shott et al. (1998)

7.6 Hydraulic Gradient

Of the hydraulic properties needed for flow models, the simplest one to calculate based on data that might be readily available from existing literature is the hydraulic gradient. The hydraulic gradient can be readily calculated from the GIS presentation of water table data. The difference in elevation of the water table (in m) at two points spanning the area of interest is divided by the distance between the two points (in m). For the study area, there's a 300 m difference in elevation over 45 kilometers of distance, giving a hydraulic gradient of .007 m/m (Figure 7-2). This value is within the ranges presented in Hanson et al. (1994) for various parts of the Mimbres Basin. Recharge, or the amount and distribution of water that enters the subsurface, is a critical component for modeling subsurface flow. Recharge for the Mimbres Basin is ~29,000-56,000 acre-feet, as discussed in section 3.5.

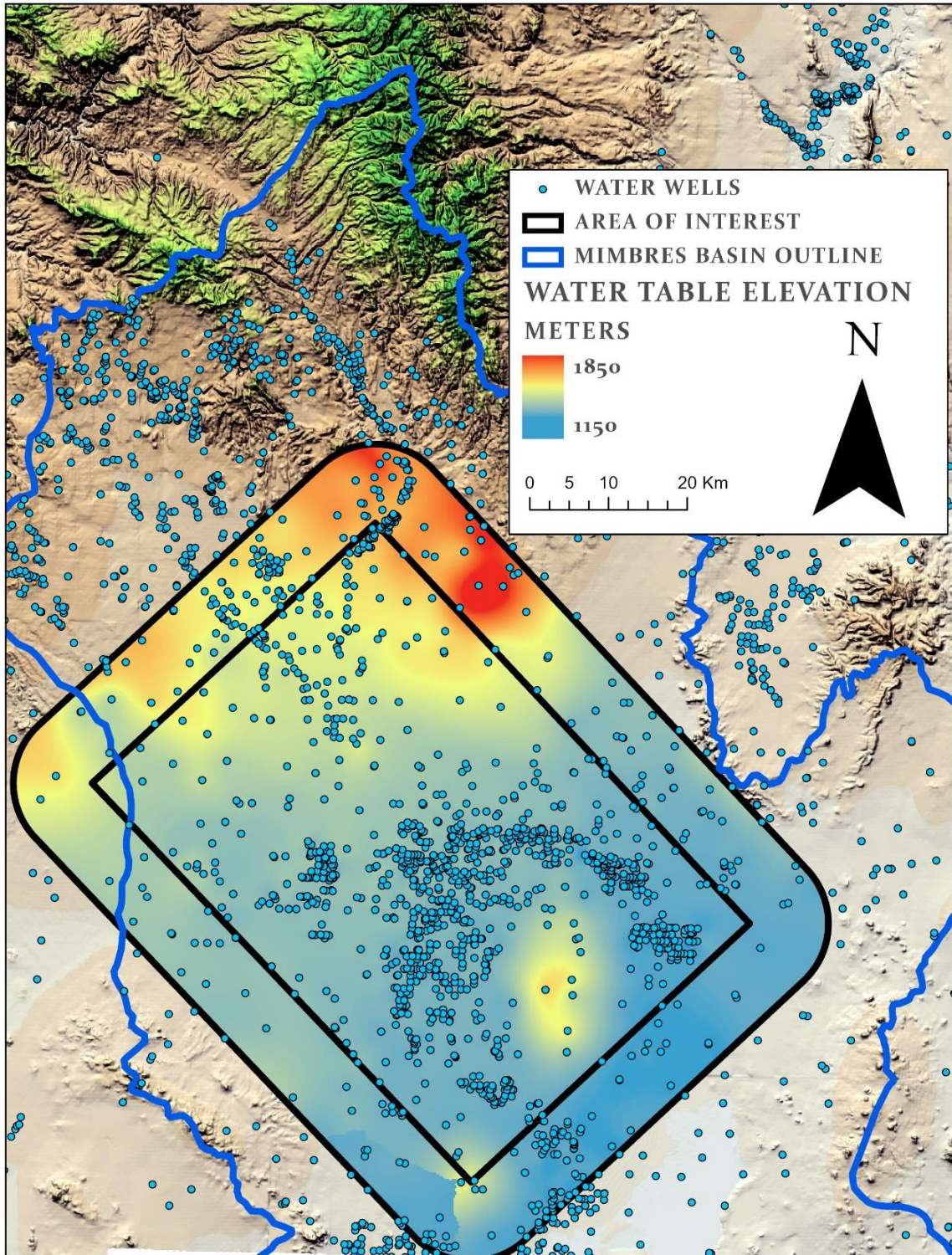


Figure 7-2 Map of the water table elevation over the study area, based on the data from the water wells indicated with black dots.

8 Meshing Workflow for Alluvial Basin Case

We used four test cases to explore the integration of geologic applications into a workflow for modeling an alluvial basin. Four common geologic features are used for these tests. These include horizontal layers, sloped layers with a pinch out that creates a wedge feature, internal bodies such as a lens, and an inclined fault creating offset layers. These tests are synthetic representations with planar cube shaped exterior boundaries. These are small with x,y,z extents no more than 20 meters in each direction. See Table 8-1 for the computational mesh sizes.

Geologic models represent complex stratigraphy and geologic structures such as inclined layers, faults, erosion and deposition. Software applications have been developed to represent these complicated geometries and to run simulations of subsurface flow and transport processes. The modeling process involves the integration of the characterization data, a conceptual model, a computational mesh, and modeling simulations.

The following approach was used for these test cases: (1) The site data and conceptual model are combined to create a Geologic Framework Model (GFM) with JewelSuite; (2) Using the conceptual model, a computational mesh and model setup files are created using LaGriT; (3) This computational mesh is then verified for modeling by running simulations with FEHM (FEHM, 2019).

Once the GFM is built, it is used to design and build a computational mesh and setup files for simulations. Modeling software such as FEHM and PFLOTRAN have mesh requirements that ensure the accuracy of simulations used on the mesh. Meshing software such as LaGriT have the tools to build the appropriate computational mesh and to write setup files that meet the modeling software requirements (boundary conditions, initial conditions, and properties such as the material distribution).

The following are steps used for the integration of the Meshing Workflow with JewelSuite. These steps are iterative from building the GFM to meshing, to the modeling simulations. Each step may reveal changes to be made at an earlier step so that all the next steps have to be repeated. The necessity for the process being iterative also makes it important that as much of the workflow as possible be automated.

- 1) Designing a standard conforming interface between the JewelSuite GFM and LaGriT for meshing is the first step. The GFM is used to inform the meshing workflow about the model geometry and topology. Meshing can use surfaces exported from the GFM, meshed volumes, or by a query method that interpolates material properties from the GFM to a mesh. The JewelSuite application can export air tight surface tessellations that represent the exterior bounding surface of each material volume. The mesh formats available for output from JewelSuite were explored: Abaqus, MESH3D (JewelSuite mesh3D format) and GOCAD TSolid TETRA format. The file formats for Abaqus and MESH3D are similar and include much more information than needed, such as multiple copies of the mesh and vertex and cell listings for zones that are not used. The files are unnecessarily large and the file format is inconsistent. The GOCAD file format

is much more consistent and concise. The GOCAD files are therefore used here for exporting the GFM information for the Meshing Workflow.

For this workflow we use LaGriT to import the GFM from JewelSuite and extract the boundary surfaces as well as the internal interfaces representing the geologic features. These surfaces are used in the meshing process to build a computational mesh. LaGriT is also used to extract and create a valid triangulated surface that can be used by the VoroCrust software.

- 2) The meshing step includes the design and the building of an appropriate computational mesh for simulations that is appropriate for the particular constraints for accuracy and numerical stability imposed by the modeling software. The design is chosen with consideration of the physics to be modeled, mesh size restrictions (number of degrees of freedom) versus mesh resolution needed for model features, and the mesh and model information needed by the model application.

For modeling applications with complex stratigraphy, depending on the mesh, you can get a stable but inaccurate solution to the physics (Zyvoloski and Vesselinov, 2006). We choose a mesh design and meshing method that gives the best possible performance from the modeling application, with respect to the difficulty in generating the mesh.

LaGriT is used to generate meshes with control volume discretization such that the underlying control volumes are Voronoi tessellations. Developed by Los Alamos National Laboratory as open source software, LaGriT provides a variety of meshing tools with capabilities specific to geologic applications and Voronoi control volume solvers. Examples of methods used for geologic applications include unstructured and structured, both with adaptive refinement to geological features. The unstructured approach allows the creation of meshes that exactly conform to the geometric model, but requires some expertise in building the mesh such that it will also meet the Delaunay criteria. The easier method is to use a structured mesh with fine resolution, or a coarser mesh that uses octree refinement to increase resolution in user specified regions of interest. These result in stair-stepped geometries instead of smooth, but can be acceptable for where the geometry spacing is small relative to the full model domain. (Sentis and Gable, 2017)

- 3) Write computational mesh and model setup files. This is the final step for modeling that checks that the mesh satisfies the design criteria, the mesh is Delaunay, and that required model setup files are correctly written. The domain size and resolution are chosen to limit the mesh size and increase computational speed while maintaining the geometry and topology of the GFM.

The model files include the geometric coefficients for the voronoi volumes, zone lists that can be used separately or together to identify vertices of various materials, and zone lists for vertices on the boundaries. Vertex or cell sets are written if needed for the simulation, such as a line of vertex to represent a well or fault feature.

The computational mesh statistics and quality measurements are included to aid in model setup and to understand the quality of the mesh that is being used. This information includes a

summary of vertex counts for the various zones, spacing and quantity counts, and the cell and vertex Voronoi volumes. The numbers for the geometric coefficient matrix are reported and can give an indication of local orthogonality by checking for negative coupling coefficients and negative voronoi volumes.

- 4) FEHM simulations to verify mesh and model setup. It is important that the computational mesh be checked and that resolution and setup files are checked to ensure that mesh affects are minimal within the design expectations. Even though the mesh satisfies the Delaunay criteria and model setup files are correct, this step is needed to confirm the mesh work is satisfactory. Often simulations at this stage will reveal results that require a new mesh design and a new computational mesh.

Here we describe the meshing workflow used for each of the four GFM test cases. A summary of the computational mesh created for each test is shown in Table 8-1. Meshing workflow steps 1, 2, and 3 are described for each test GFM in sections 8.1, 8.2, 8.3 and 8.4. The step 4 covering mesh verifications follow in Chapter 9.

Table 8-1 Cube Tests 1-4 Computational Mesh Summary

Test	Method	Dimensions X Y Z m	Vertices	Cells	Zones	Volume
1 Layers	Stacked Surfaces	20 x 20 x 12.0766	7546	38934	4	4830.64
2 Wedge	Octree Refined	20 x 20 x 12	182154	1036237	3	4800.00
3 Lens	Octree Refined	20 x 20 x 10	72329	420897	3	4000.00
4 Fault	Octree Refined	20 x 20 x 10	253688	1459249	5	4000.00

8.1 Cube Test 1: Horizontal Layers

Models are commonly represented with a layering of stratigraphy with the layers represented by surface elevations. As long as the layers are non-intersecting and are of reasonable thickness, these models are the easiest to mesh.

8.1.1 JewelSuite GFM exports for Meshing Workflow

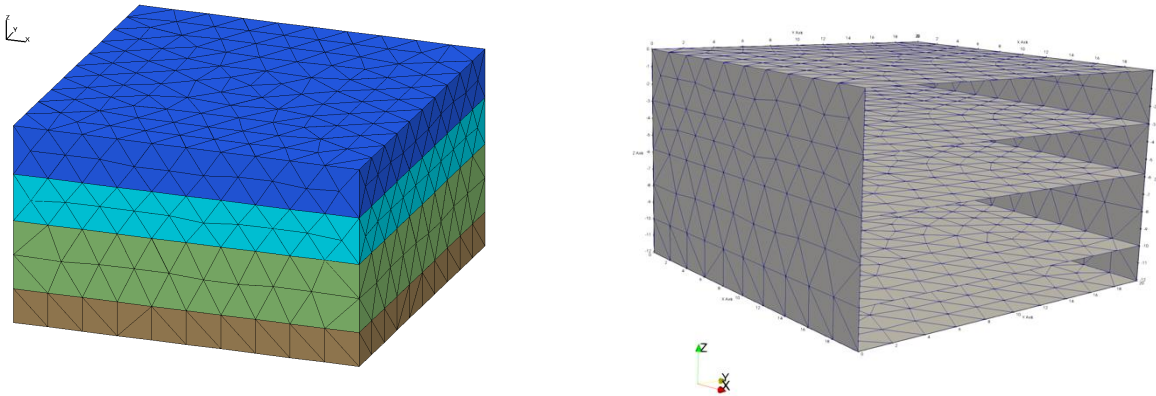


Figure 8-1 Exported GFM tetrahedral mesh representing 4 material zones (left) and extracted boundary surfaces and internal interfaces (right).

8.1.2 Mesh Generation

This model has four horizontal material layers represented by 5 flat surfaces; top, bottom, and 3 layers. For a model with horizontal non-intersecting surfaces, we can create a computational mesh with conforming interfaces by using a stacked mesh method. We first create a Delaunay triangulated surface of the domain, interpolate surface elevations to each layer, create refinement layers, then stack into a 2 ½ Dimension prism mesh. As long as we select a vertical resolution with respect to the triangulated surface spacing, the point distribution can be connected into a tetrahedral Delaunay mesh. Note the elevation values are interpolated from the GFM layer surfaces so that the minimum and maximum Z extents are the same as the input GFM.

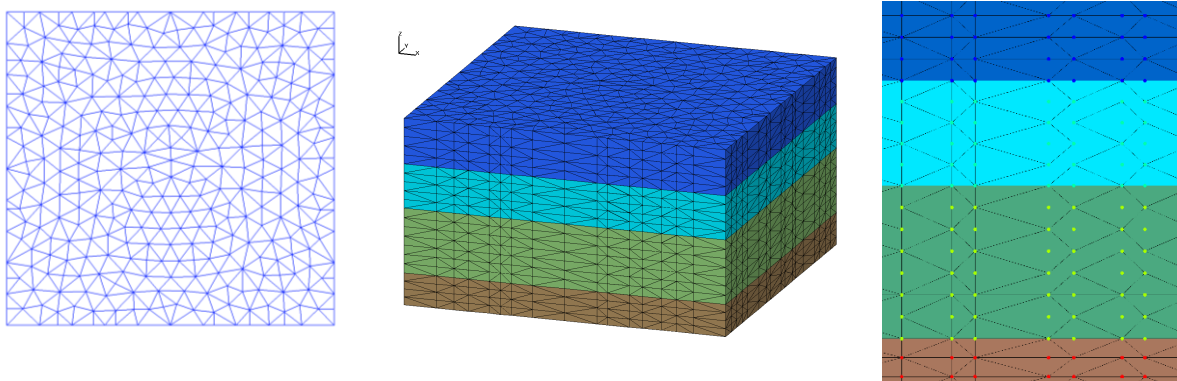


Figure 8-2 shows the Delaunay triangulation used for stacking (left), the stacked point distribution connected into a Delaunay mesh with material zones (middle), and a detail showing the mesh vertices and elements with material zone colors (right).

8.1.3 Computational Mesh and Model Setup Files

The mesh quality is confirmed by checking that all tetrahedral cells have positive volumes and the Voronoi volumes and coupling coefficients are not negative. The model mesh and setup files include the sparse matrix file, lists of mesh vertices for each material zone, and boundary zone files. The boundary of the mesh is a flat faced cube and boundary vertices are identified and written for each of the 6 directions- bottom, top, front, right, back and left. We include quality measurements and mesh statistics to aid setup for the modeling simulations and analyses.

Mesh and Model Setup Files

```
-rw-r--r-- 1 tamiller sft 2132119 May 13 14:14 tet.fehmn
-rw-r--r-- 1 tamiller sft 1938367 May 13 14:14 tet.stor
-rw-r--r-- 1 tamiller sft 34331 May 13 14:13 tet_interface.zone
-rw-r--r-- 1 tamiller sft 83150 May 13 14:13 tet_material.zone
-rw-r--r-- 1 tamiller sft 125336 May 13 14:13 tet_multi_mat.zone
-rw-r--r-- 1 tamiller sft 24743 May 13 14:13 tet_outside.zone
-rw-r--r-- 1 tamiller sft 142005 May 13 14:14 tet_outside_vor.area
```

Mesh Statistics

```
number of nodes = 7546
number of elements = 38934
```

Size	MIN	MAX	DIFFERENCE
X coord	0.000000000E+00	2.000000000E+01	2.000000000E+01
Y coord	0.000000000E+00	2.000000000E+01	2.000000000E+01
Z coord	-1.207660000E+01	0.000000000E+00	1.207660000E+01
edgemax	9.774372609E-01	2.087009355E+00	1.109572095E+00
edgemin	5.191500000E-01	5.963288100E-01	7.717880996E-02
eratio	2.512485123E-01	6.067646919E-01	3.555161796E-01

```
Material Zone 1 has 2058 nodes. #nodes/nnodes is 0.272727280855
Material Zone 2 has 1715 nodes. #nodes/nnodes is 0.227272734046
Material Zone 3 has 2401 nodes. #nodes/nnodes is 0.318181812763
Material Zone 4 has 1372 nodes. #nodes/nnodes is 0.181818187237
```

```
top 1 has 343 nodes.
Sum Voronoi Area x y z = 0.1186440E+02 0.1186440E+02 0.4000000E+03
bottom 2 has 343 nodes.
Sum Voronoi Area x y z = 0.1038300E+02 0.1038300E+02 0.4000000E+03
left_w 3 has 374 nodes.
Sum Voronoi Area x y z = 0.2415320E+03 0.1854734E+02 0.2004362E+02
front_s 4 has 374 nodes.
Sum Voronoi Area x y z = 0.1262067E+02 0.2415320E+03 0.1914060E+02
right_e 5 has 396 nodes.
Sum Voronoi Area x y z = 0.2415320E+03 0.2415320E+02 0.2048326E+02
back_n 6 has 396 nodes.
Sum Voronoi Area x y z = 0.1840780E+02 0.2415320E+03 0.1995058E+02
```

Mesh Quality Checks for positive cell volumes, Voronoi volumes, and geometric coefficients.

Voronoi Volume min: 9.9034663E-02
 Voronoi Volume max: 1.0499972E+00
 Voronoi Volume total: 4830.6400+00
 Coefficient abs(area/distance) min = 0.0000000E+00
 Coefficient abs(area/distance) max = 3.3916380E+00
 Maximum number connection to a node = 11
 Total number of Negative Coefficients = 0

Tetrahedral Volume min: 3.876904103E-02
 Tetrahedral Volume max: 2.130117153E-01
 Tetrahedral Volume total: 4830.6400E+00

8.2 Cube Test 2: Wedge

Models become more complex as they represent dipping beds, erosion, and outcrops. Instead of non-intersecting horizontal layers, these layers can intersect or become coincident where the thickness becomes zero, or where the layer pinches out.

8.2.1 JewelSuite GFM exports for Meshing Workflow

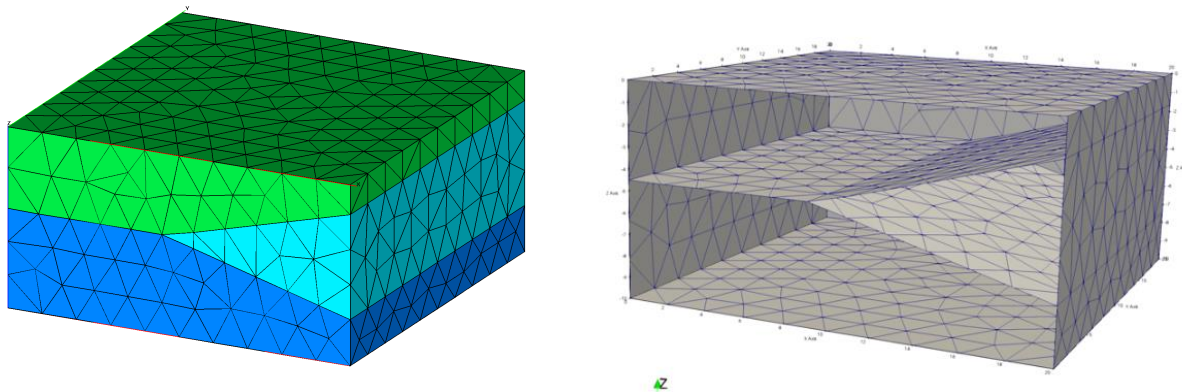


Figure 8-3 Exported GFM tetrahedral mesh representing 3 material zones (left) and extracted boundary surfaces and internal interfaces (right).

8.2.2 Mesh Generation

This test represents a pinch out with two internal surfaces that are coincident for part of the model, creating 3 zones, where the middle zone has a wedge shape. For a model with intersecting internal surfaces, a mesh that conforms with the material layers is more difficult, especially in 3 dimensions. Rather than using an unstructured mesh requiring careful design and discretization, we create a structured mesh and use octree refinement to capture the material

geometry. We start with a hexahedral mesh with 1 meter spacing. LaGriT is used to intersect the extracted interfaces with the coarse hex mesh, the intersected cells are refined with the octree method multiple times to achieve the desired resolution at these interfaces. This point distribution is then connected into a tetrahedral Delaunay mesh. The material zones are interpolated from the JewelSuite GFM mesh to this Delaunay tetrahedral mesh. The extents of the mesh are selected such that the x, y coordinates are within the GFM domain and aligned along integer values. The vertical extent is slightly taller so the refinement along the layers do not extend onto the top of the mesh. This makes the calculation of the top faces all the same and easier for the modeler to set boundary conditions.

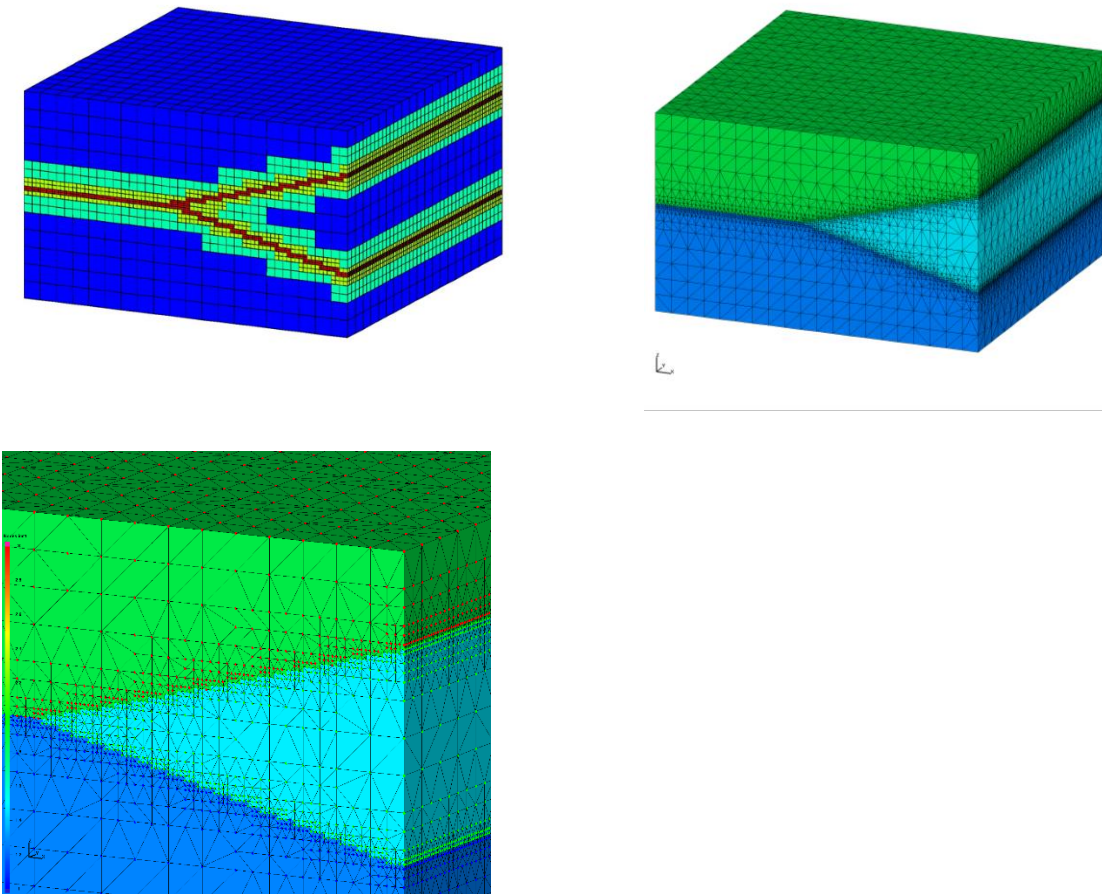


Figure 8-4 The hexahedral mesh with 3 levels of octree refinement (top left), the point distribution connected into a Delaunay mesh with interpolated material zones (top right), and detail showing the mesh vertices and elements with material zone colors (bottom).

8.2.3 Computational Mesh and Model Setup Files

The mesh quality is confirmed by checking that all tetrahedral cells have positive volumes and the Voronoi volumes and coupling coefficients are not negative. The model mesh and setup files include the sparse matrix file, lists of mesh vertices for each material zone, and boundary zone files. The boundary of the mesh is a flat faced cube and boundary vertices are identified and written for each of the 6 directions bottom, top, front, right, back, and left. We include quality measurements and mesh statistics to aid setup for the modeling simulations and analyses.

Mesh and Model Setup Files

```
-rw-r--r-- 1 tamiller sft 55418710 Jun  4 12:12 tet.fehmn
-rw-r--r-- 1 tamiller sft 42350504 Jun  4 12:12 tet.stor
-rw-r--r-- 1 tamiller sft  2003805 Jun  4 12:12 tet_material.zone
-rw-r--r-- 1 tamiller sft  1035759 Jun  4 12:12 tet_interface.zone
-rw-r--r-- 1 tamiller sft  5642394 Jun  4 12:12 tet_multi_mat.zone
-rw-r--r-- 1 tamiller sft   78962 Jun  4 12:12 tet_outside.zone
-rw-r--r-- 1 tamiller sft  454997 Jun  4 12:12 tet_outside_vor.area
```

Mesh Statistics

```
number of nodes = 182154
number of elements = 1036237
```

Size	MIN	MAX	DIFFERENCE
X coord	0.000000000E+00	2.000000000E+01	2.000000000E+01
Y coord	0.000000000E+00	2.000000000E+01	2.000000000E+01
Z coord	-1.100000000E+01	1.000000000E+00	1.200000000E+01
edgemax	1.767766953E-01	1.732050808E+00	1.555274112E+00
edgemin	1.250000000E-01	1.000000000E+00	8.750000000E-01
eratio	3.333333333E-01	1.000000000E+00	6.666666667E-01

```
Material Zone 1 has 64141 nodes. #nodes/nnodes is 0.352125138044
Material Zone 2 has 79317 nodes. #nodes/nnodes is 0.435439229012
Material Zone 3 has 38696 nodes. #nodes/nnodes is 0.212435632944
```

```
top 1 has 441 nodes.
Sum Voronoi Area x y z = 0.1186440E+02 0.1186440E+02 0.4000000E+03
bottom 2 has 441 nodes.
Sum Voronoi Area x y z = 0.2000000E+02 0.2000000E+02 0.4000000E+03
left_w 3 has 1079 nodes.
Sum Voronoi Area x y z = 0.2400000E+03 0.9480469E+01 0.2000000E+02
front_s 4 has 1594 nodes.
Sum Voronoi Area x y z = 0.8158203E+01 0.2400000E+03 0.2000000E+02
right_e 5 has 2006 nodes.
Sum Voronoi Area x y z = 0.2400000E+03 0.6832682E+01 0.2000000E+02
back_n 6 has 1594 nodes.
Sum Voronoi Area x y z = 0.8158203E+01 0.2400000E+03 0.2000000E+02
```

Mesh Quality Checks for positive cell volumes, Voronoi volumes, and geometric coefficients.

Voronoi Volume min: 4.8828125E-04
Voronoi Volume max: 1.0000000E+00
Voronoi Volume total: 4800.0000E+00
Coefficient abs(area/distance) min = 0.0000000E+00
Coefficient abs(area/distance) max = 1.1250000E+00
Maximum number connection to a node = 31
Total number of Negative Coefficients = 0

Tetrahedral Volume min: 3.255208333E-04
Tetrahedral Volume max: 1.666666667E-01
Tetrahedral Volume total: 4800.0000E+00

8.3 Cube Test 3: Lens

Models sometimes consist of internal volumes such as lava flow bodies, cavities, or lenses. This test represents a lens with 2 surfaces that are coincident except for where they describe the bottom and top of the lens.

8.3.1 JewelSuite GFM exports for Meshing Workflow

This model represents a single internal lens that does not touch any boundary surfaces. JewelSuite exports this as a mesh with 3 material zones, the internal lens, the volume above the surfaces and the volume below the surfaces (*Figure 8-5*).

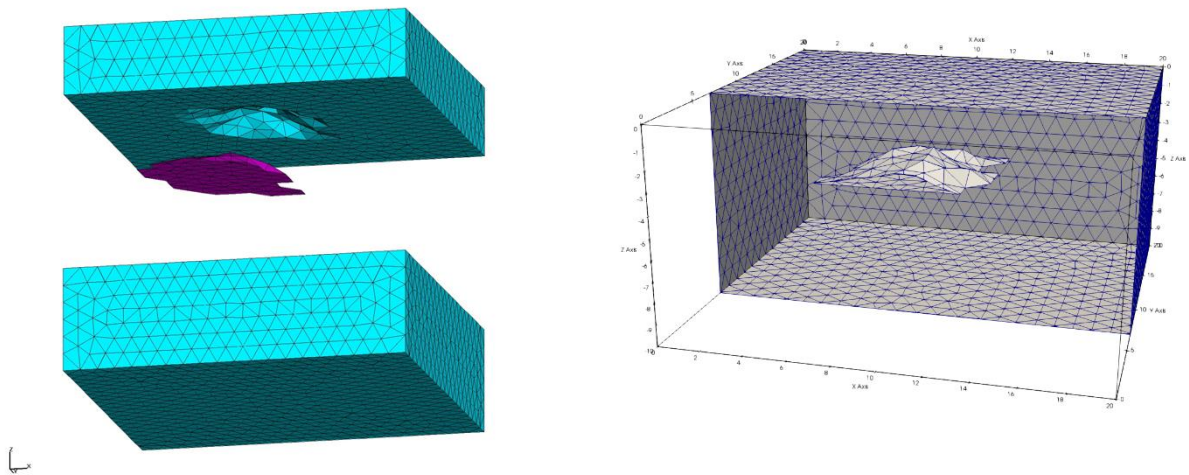


Figure 8-5 Exported GFM tetrahedral mesh exploded to show the internal body (left) and the extracted boundary and internal surface (right).

8.3.2 Mesh Generation

For this model, the top and bottom volumes are combined into a single material surrounding the internal lens. When LaGriT extracts surfaces from this mesh, the result is the bounding box and the surface of the internal lens not connected to the external boundary.

For a model with internal surfaces representing volumes not connected to the boundary, we can create a computational mesh conforming to the volume surface, or we can use a structured mesh with octree refinement along the interfaces (*Figure 8-6*). For simplicity, we use the octree method starting with a hexahedral mesh with 1 meter spacing. LaGriT is used to intersect the extracted interfaces with the coarse hex mesh, the intersected cells are refined with the octree method multiple times to achieve the desired resolution at these interfaces. This point distribution is then connected into a tetrahedral Delaunay mesh. The material zones are interpolated from the GFM mesh to this Delaunay tetrahedral mesh.

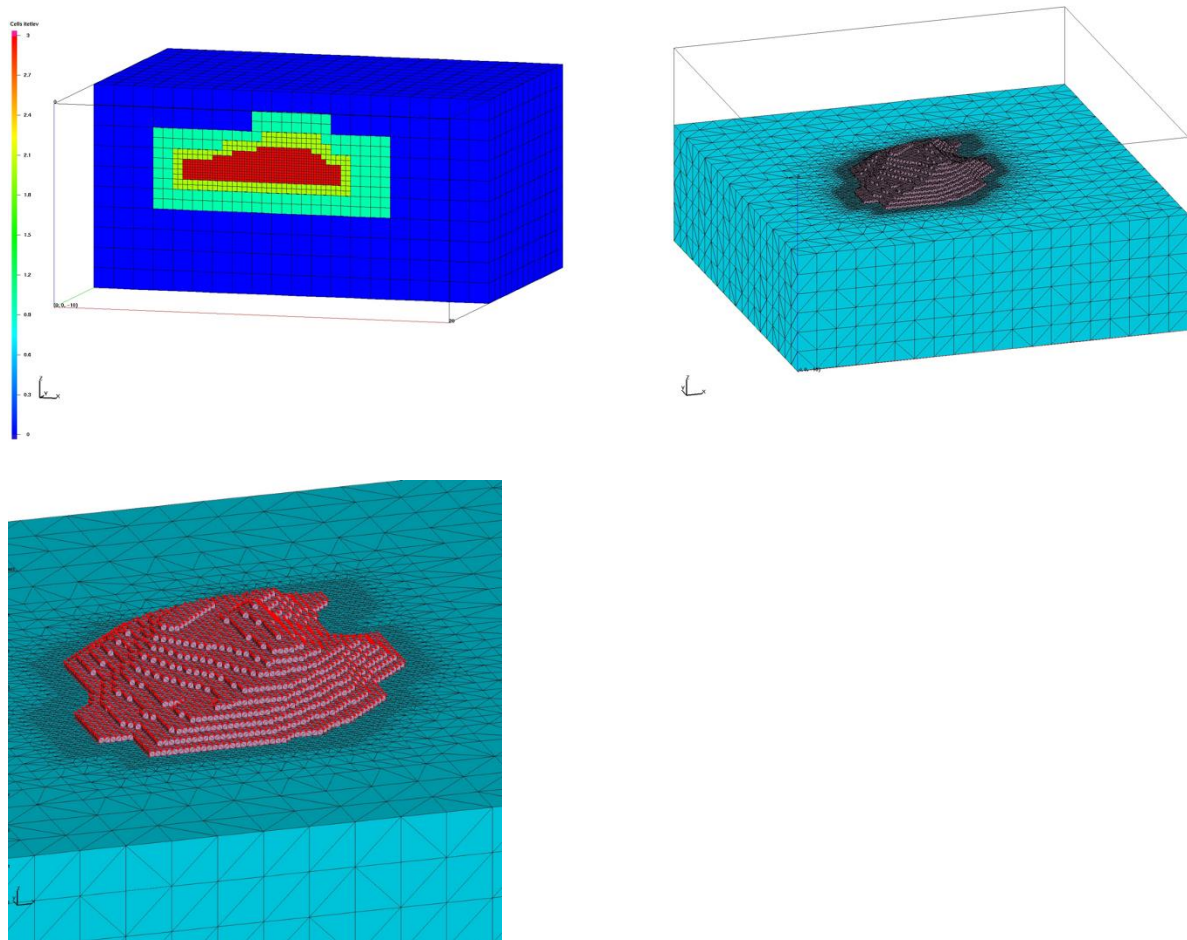


Figure 8-6 The hexahedral mesh with 3 levels of octree refinement (top left), the point distribution connected into a Delaunay mesh with interpolated material zones (top right), and detail showing the mesh vertices and elements with material zone colors (bottom). The mesh has been clipped to show the internal lens.

8.3.3 Computational Mesh and Model Setup Files

The mesh quality is confirmed by checking that all tetrahedral cells have positive volumes and the Voronoi volumes and coupling coefficients are not negative. The model mesh and setup files include the sparse matrix file, lists of mesh vertices for each material zone, and boundary zone files. The boundary of the mesh is a flat faced cube and boundary vertices are identified and written for each of the 6 directions bottom, top, front, right, back, and left. We include quality measurements and mesh statistics to aid setup for the modeling simulations and analyses.

Mesh and Model Setup Files

```
-rw-r--r-- 1 tamiller sft 22392195 Jun  5 09:37 tet.fehmn
-rw-r--r-- 1 tamiller sft 15281683 Jun  5 09:37 tet.stor
-rw-r--r-- 1 tamiller sft  795730 Jun  5 09:37 tet_material.zone
-rw-r--r-- 1 tamiller sft  213420 Jun  5 09:37 tet_interface.zone
-rw-r--r-- 1 tamiller sft 1185626 Jun  5 09:37 tet_multi_mat.zone
-rw-r--r-- 1 tamiller sft   20123 Jun  5 09:37 tet_outside.zone
-rw-r--r-- 1 tamiller sft  115337 Jun  5 09:37 tet_outside_vor.area
```

Mesh Statistics

```
number of nodes = 72329
number of elements = 420897
```

Size	MIN	MAX	DIFFERENCE
X coord	0.000000000E+00	2.000000000E+01	2.000000000E+01
Y coord	0.000000000E+00	2.000000000E+01	2.000000000E+01
Z coord	-1.100000000E+01	0.000000000E+00	1.000000000E+01
edgemax	1.767766953E-01	1.732050808E+00	1.555274112E+00
edgemin	1.250000000E-01	1.414213562E+00	1.289213562E+00
eratio	3.333333333E-01	1.000000000E+00	6.666666667E-01

```
Material Zone 1 has 27223 nodes. #nodes/nnodes is 0.376377373934
Material Zone 2 has 28338 nodes. #nodes/nnodes is 0.391793042421
Material Zone 3 has 16768 nodes. #nodes/nnodes is 0.231829553843
```

```
top 1 has 441 nodes.
Sum Voronoi Area x y z = 0.1186440E+02 0.1186440E+02 0.4000000E+03
bottom 2 has 441 nodes.
Sum Voronoi Area x y z = 0.2000000E+02 0.2000000E+02 0.4000000E+03
left_w 3 has 231 nodes.
Sum Voronoi Area x y z = 0.2000000E+03 0.1000000E+02 0.2000000E+02
front_s 4 has 231 nodes.
Sum Voronoi Area x y z = 0.1000000E+02 0.2000000E+03 0.2000000E+02
right_e 5 has 231 nodes.
Sum Voronoi Area x y z = 0.2000000E+03 0.1000000E+02 0.2000000E+02
back_n 6 has 231 nodes.
Sum Voronoi Area x y z = 0.1000000E+02 0.2000000E+03 0.2000000E+02
```

Mesh Quality Checks for positive cell volumes, Voronoi volumes, and geometric coefficients.

Voronoi Volume min: 1.9531250E-03
 Voronoi Volume max: 1.0000000E+00
 Voronoi Volume total: 4000.0000E+00
 Coefficient abs(area/distance) min = 0.0000000E+00
 Coefficient abs(area/distance) max = 1.1250000E+00
 Maximum number connection to a node = 28
 Total number of Negative Coefficients = 0

Tetrahedral Volume min: 3.255208333E-04
 Tetrahedral Volume max: 3.333333333E-01
 Tetrahedral Volume total: 4000.0000E+00

8.4 Cube Test 4: Fault

Models are often represented as layers offset by a fault plane or fault surface. These models can be very complex with dozens of faults all intersecting layers or each other so that stratigraphic layers are often offset or clipped by the fault.

8.4.1 JewelSuite GFM exports for Meshing Workflow

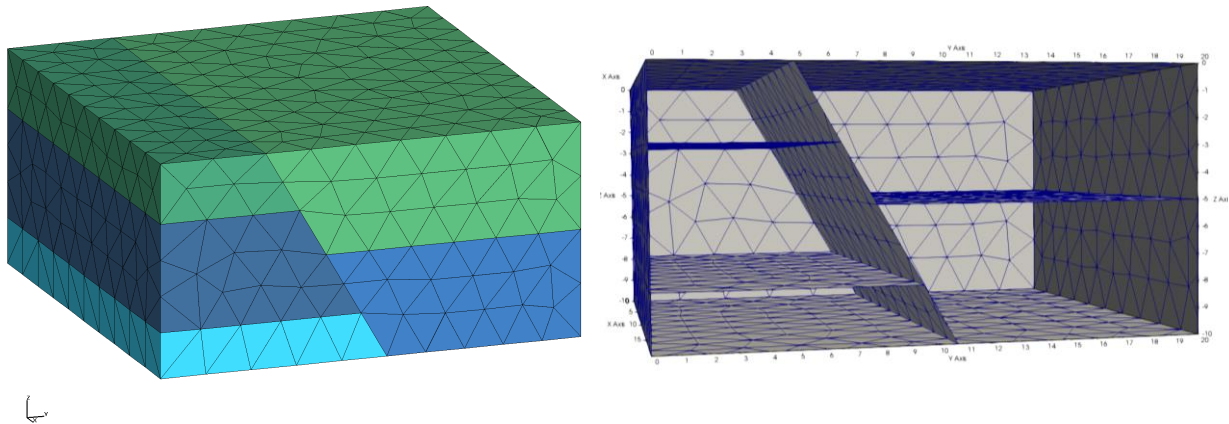


Figure 8-7 Exported GFM tetrahedral mesh represented as 5 material zones (left) and the extracted boundary and interface surfaces (right).

8.4.2 Mesh Generation

This test represents horizontal layers intersected by one inclined fault (*Figure 8-7*). The fault plane breaks the layers into components on either side of the fault and offset to each other. JewelSuite assigns a separate component id to each layer on each side of the fault plane. This model has one inclined fault intersecting 3 horizontal layers. The layers are offset by the fault

plane such that there are 3 layers under the fault (footwall block) and 2 layers on the opposite side (hanging wall block).

For simplicity, we use the octree method starting with a hexahedral mesh with 1 meter spacing (*Figure 8-8*). LaGriT is used to intersect the extracted fault and layer interfaces with the coarse hex mesh, the intersected cells are refined with the octree method multiple times to achieve the desired resolution at these interfaces. The interfaces are broken into zones on either side of the fault and numbered with unique integer values. The modeler can combine or keep separate each of these zones. This point distribution is connected into a tetrahedral Delaunay mesh. The 5 material zones are interpolated from the GFM mesh to this Delaunay tetrahedral mesh.

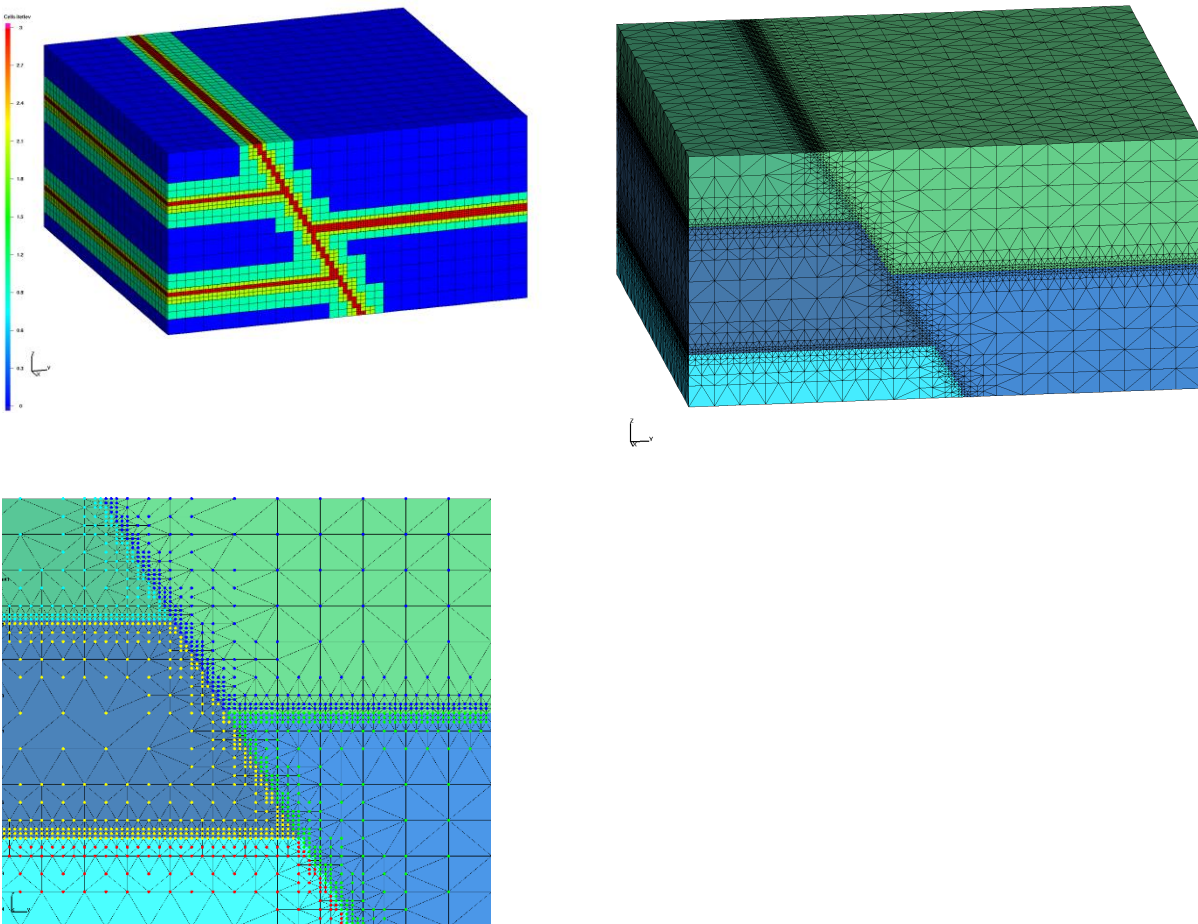


Figure 8-8 The hexahedral mesh with 3 levels of octree refinement (top left), the point distribution connected into a Delaunay mesh with interpolated material zones (top right), and detail showing the mesh vertices and elements with material zone colors (bottom).

8.4.3 Computational Mesh and Model Setup Files

The mesh quality is confirmed by checking that all tetrahedral cells have positive volumes and the Voronoi volumes and coupling coefficients are not negative. The model mesh and setup files include the sparse matrix file, lists of mesh vertices for each material zone, and boundary zone files. The boundary of the mesh is a flat faced cube and boundary vertices are identified and written for each of the 6 directions bottom, top, front, right, back, and left. We include quality measurements and mesh statistics to aid setup for the modeling simulations and analyses.

Mesh and Model Setup Files

```
-rw-r--r-- 1 tamiller sft 77841116 Jun  5 15:58 tet.fehmn
-rw-r--r-- 1 tamiller sft 2790745 Jun  5 15:58 tet_material.zone
-rw-r--r-- 1 tamiller sft 1376671 Jun  5 15:58 tet_interface.zone
-rw-r--r-- 1 tamiller sft 6298006 Jun  5 15:58 tet_multi_mat.zone
-rw-r--r-- 1 tamiller sft 114404 Jun  5 15:58 tet_outside.zone
-rw-r--r-- 1 tamiller sft 659594 Jun  5 15:58 tet_outside_vor.area
-rw-r--r-- 1 tamiller sft 58201688 Jun  5 15:58 tet.stor
```

Mesh Statistics

```
number of nodes = 253688
number of elements = 1459249
```

Size	MIN	MAX	DIFFERENCE
X coord	0.000000000E+00	2.000000000E+01	2.000000000E+01
Y coord	0.000000000E+00	2.000000000E+01	2.000000000E+01
Z coord	-1.000000000E+01	0.000000000E+00	1.000000000E+01
edgemax	1.767766953E-01	1.641476300E+00	1.464699605E+00
edgemin	1.041666667E-01	1.301708279E+00	1.197541613E+00
eratio	3.492151479E-01	9.204467514E-01	5.712316036E-01

```
Material Zone 1 has 63219 nodes. #nodes/nnodes is 0.249199807644
Material Zone 2 has 29352 nodes. #nodes/nnodes is 0.115701176226
Material Zone 3 has 78157 nodes. #nodes/nnodes is 0.308083146811
Material Zone 4 has 69252 nodes. #nodes/nnodes is 0.272980988026
Material Zone 5 has 13708 nodes. #nodes/nnodes is 0.540348775685E-01
```

```
top 1 has 1488 nodes.
Sum Voronoi Area x y z = 0.1455658E+02 0.1666667E+02 0.4000000E+03
bottom 2 has 1609 nodes.
Sum Voronoi Area x y z = 0.1383643E+02 0.1591667E+02 0.4000000E+03
left_w 3 has 2068 nodes.
Sum Voronoi Area x y z = 0.2000000E+03 0.7000781E+01 0.1738672E+02
front_s 4 has 1885 nodes.
Sum Voronoi Area x y z = 0.5740625E+01 0.2000000E+03 0.2000000E+02
right_e 5 has 2068 nodes.
Sum Voronoi Area x y z = 0.2000000E+03 0.7000781E+01 0.1738672E+02
back_n 6 has 1259 nodes.
Sum Voronoi Area x y z = 0.8260938E+01 0.2000000E+03 0.2000000E+02
```

Mesh Quality Checks for positive cell volumes, Voronoi volumes, and geometric coefficients.

Voronoi Volume min: 4.0690104E-04
Voronoi Volume max: 8.3333333E-01
Voronoi Volume total: 4000.0000E+00
Coefficient abs(area/distance) min = 0.0000000E+00
Coefficient abs(area/distance) max = 1.2000000E+00
Maximum number connection to a node = 28
Total number of Negative Coefficients = 0

Tetrahedral Volume min: 2.712673611E-04
Tetrahedral Volume max: 2.777777778E-01
Tetrahedral Volume total: 4000.0000E+00

9 FEHM Verification of Mesh and Model Setup

Once generated, computational meshes need to be tested using flow simulators to ensure that the meshes are able to correctly propagate numerical solutions. Typically one starts with simple flow solutions such as single phase, isothermal water and/or heat only solutions. For analysis of the four representative geological test case meshes, we begin with simple single-phase water, isothermal conditions using a single value of permeability and add complexity. The simple cases can be solved analytically and provide an excellent validation check on the numerical solutions. Initial simulations are performed using FEHM as the mesh files can be directly dumped from LaGriT into FEHM format. However, because the GDSA workflow will ultimately use PFLTORAN for flow solutions, we present cases where PFLOTTRAN and FEHM are compared for simulations using the same boundary conditions and computational meshes. The test cases in this section are not comprehensive and further testing in the next FY (2020) will be necessary to fully understand important physical processes such as chemical transport, reactive chemistry, and multiphase heat/mass flow.

Here we present results for 16 simulations on the four representative geological test cases designed to confirm the ability of the computational meshes to correctly propagate numerical solutions. For each test case, the porous flow simulator FEHM (FEHM, 2019) is used to generate a set of 4 different simulation scenarios. The simulations are grouped into fully saturated (2) and unsaturated (2) for each geological test case. For both saturated and unsaturated simulations, a scenario with constant material properties is run followed by a scenario with variable rock properties (e.g. permeability and capillary functions). PFLOTTRAN is used to exactly recreate a subset of 8 of these test cases (i.e., the saturated examples).

We use the numerical mesh files created within LaGriT and set up boundary and initial conditions that generate flow solutions which can, in some cases, be compared to analytical solutions. For some of the 16 simulations presented (4 geological test cases times 4 scenarios each), there are no analytical solutions and we present images of pressure and saturation field that can be examined to understand the behavior of the meshes under different forcing conditions. Detailed information on the 16 scenarios is given in Table 9-1. All numerical meshes are 20 m x 20 m laterally and range from 10 to 12 m deep. All simulations are run to steady-state, where mass flow into the domain is balanced by mass flow out of the domain.

Table 9-2 lists the relevant hydrologic parameters used for each of the four scenarios. For the saturated cases with variable rock properties, permeability is given either a high value ($1e^{-12} \text{ m}^2$) or a low value ($1e^{-18} \text{ m}^2$) with no capillary pressure model. For the unsaturated cases, the hydraulic properties of the simulated materials are based on two known rock types, the Santa Fe Group aquifer (high permeability and low capillary suction) and the Otowi member of the Bandelier Tuff (lower permeability and high capillary suction). For all isotropic scenarios in the unsaturated scenarios, the Santa Fe Group properties are used, while for all isotropic saturated scenarios a permeability of $1e^{-12} \text{ m}^2$ (sand) is used.

All saturated simulations use full thermal solutions, however temperatures are initialized to 20°C and boundaries are fixed at 20°C, very small temperature increases are seen due to Joule-Thomson heating during depressurization of liquid water (Stauffer et al., 2014).

All unsaturated simulations presented herein use the air water macro in FEHM that forces isothermal conditions on the two-phase system. The reference temperature of the domain is 20°C and the reference pressure is 0.1 MPa. In this formulation there is no condensable gas phase (i.e., water vapor) present (FEHM, 2019).

Table 9-1 Information for the 16 test case scenarios.

Scenario	Geologic Test Case	Phase State	Permeability	Flow field	Gravity on?	Top Boundary	Bottom Boundary
1.1	1 - Layered	Saturated	Isotropic	Upflow	NO	Fixed P	Fixed P
1.2	1 - Layered	Saturated	Variable	Upflow	NO	Fixed P	Fixed P
1.3	1 - Layered	Unsaturated	Isotropic	Infiltration	YES	Fixed flux	Fixed sat
1.4	1 - Layered	Unsaturated	Variable	Infiltration	YES	Fixed flux	Fixed sat
2.1	2 - Wedge	Saturated	Isotropic	Upflow	NO	Fixed P	Fixed P
2.2	2 - Wedge	Saturated	Variable	Upflow	NO	Fixed P	Fixed P
2.3	2 - Wedge	Unsaturated	Isotropic	Infiltration	YES	Fixed flux	Fixed sat
2.4	2 - Wedge	Unsaturated	Variable	Infiltration	YES	Fixed flux	Fixed sat
3.1	3 - Lens	Saturated	Isotropic	Upflow	NO	Fixed P	Fixed P
3.2	3 - Lens	Saturated	Variable	Upflow	NO	Fixed P	Fixed P
3.3	3 - Lens	Unsaturated	Isotropic	Infiltration	YES	Fixed flux	Fixed sat
3.4	3 - Lens	Unsaturated	Variable	Infiltration	YES	Fixed flux	Fixed sat
4.1	4 - Fault	Saturated	Isotropic	Upflow	NO	Fixed P	Fixed P
4.2	4 - Fault	Saturated	Variable	Upflow	NO	Fixed P	Fixed P
4.3	4 - Fault	Unsaturated	Isotropic	Infiltration	YES	Fixed flux	Fixed sat
4.4	4 - Fault	Unsaturated	Variable	Infiltration	YES	Fixed sat	Fixed sat

Table 9-2 Hydrologic properties for the 4 test case scenarios.

Rock Case	Permeability (m2)	Porosity	α (1/m)	n	Residual saturation	Max saturation
Saturated High Perm	1.e-12	0.1	NA	NA	NA	NA
Saturated Low Perm	1.e-18	0.1	NA	NA	NA	NA
Santa Fe Group	2.65e-12	0.35	5.0	2.68	0.01	1.0
Otowi Member	2.32e-13	0.44	0.59	1.76	0.043	1.0

9.1 Test Case 1 – Horizontal Layers

9.1.1 Scenario 1.1

The first scenario for the layered case shows that the pressure gradient for an upwelling flow-field is perfectly flat. Gravity is turned off for this scenario so that there is no impact of gravitational potential energy and the flow field will be exactly proportional to the spacing of the constant pressure lines shown in black on Figure 9-1. The mass flow rate (\dot{m}) for this simulation (3.3 kg/s) is in line with the analytical flow solution, given as

$$\dot{m} = A \cdot \rho \cdot \frac{k}{\mu} \nabla P \quad \text{Eq. 1}$$

Assuming $A = 400 \text{ m}^2$, $\rho = 998.6 \text{ kg/m}^3$, $k = 1.e^{-12} \text{ m}^2$, $\mu = 1e^{-3} \text{ Pa s}$, and $\nabla P = (1.e^5 \text{ Pa/12 m})$, Eq. 1 yields 3.33 kg/s leaving the top of the model domain. PFLOTRAN gives the same mass flow rate for this problem.

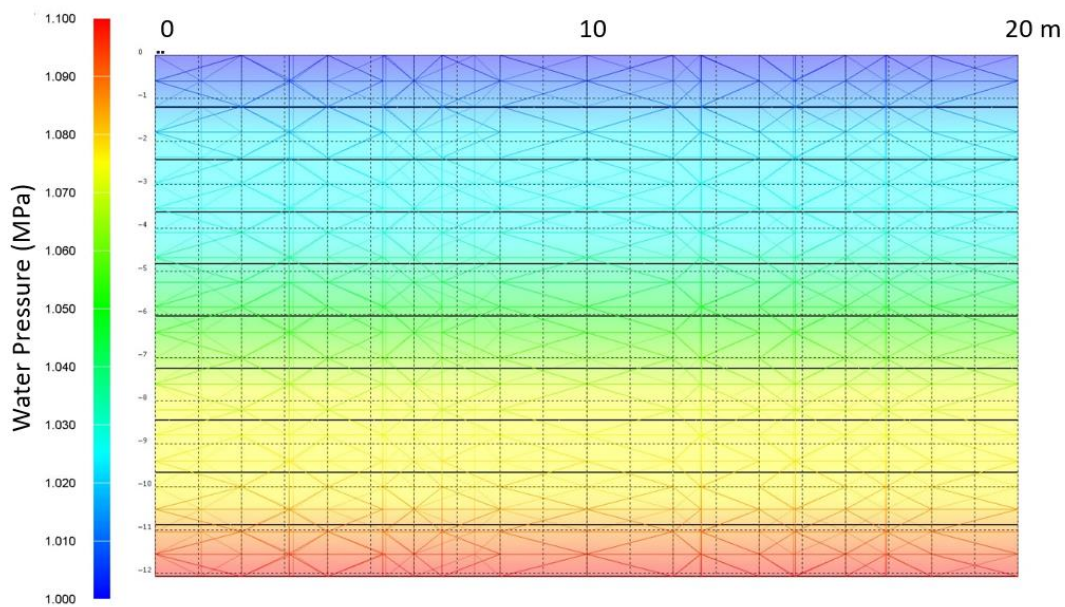


Figure 9-1 Scenario 1.1. Water pressure contours for up flowing single phase water in the absence of gravity (FEHM).

9.1.2 Scenario 1.2

This case presents a layered system with properties shown in Table 9-3. The layered permeability upwelling case is similar in appearance to the previous scenario; however the constant pressure contours are not at constant spacing because of the impact of variable permeability Figure 9-3. The bulk of the pressure loss occurs over the relatively low permeability layer (red in Figure 9-2). Comparing FEHM results to PFLOTTRAN (PFLOTTRAN, 2019) shows that the two simulators are producing visually identical results (Figure 9-4). The analytical solution for this scenario uses a harmonic average of the permeability of each layer scaled by the layer thickness relative to the total thickness of the layered system as (Fetter, 1980):

$$k_{vavg} = \frac{d}{\sum_{m=1}^n \left(\frac{d_m}{k_{vm}} \right)} \quad \text{Eq. 2}$$

With the values for the layer thicknesses and permeabilities given in Table 9-3, Eq. 2 yields an average vertical permeability for the layered system of $2.97\text{e-}14$ m². Using this permeability value in Eq. 1 gives an estimate of mass flow for the domain of 0.096 kg/s, compared to 0.096 kg/s in the steady-state simulation. PFLOTTRAN gives the same mass flow rate for this problem.

Table 9-3 Thicknesses and permeabilities for the layers in Scenario 1.2

Layer	Thickness (m)	k	d/k
1 - Top	3.25E+00	1.00E-12	3.25E+12
2	2.87E+00	1.00E-11	2.87E+11
3	4.14E+00	1.00E-14	4.14E+14
4 - Bottom	1.74E+00	5.00E-12	3.48E+11

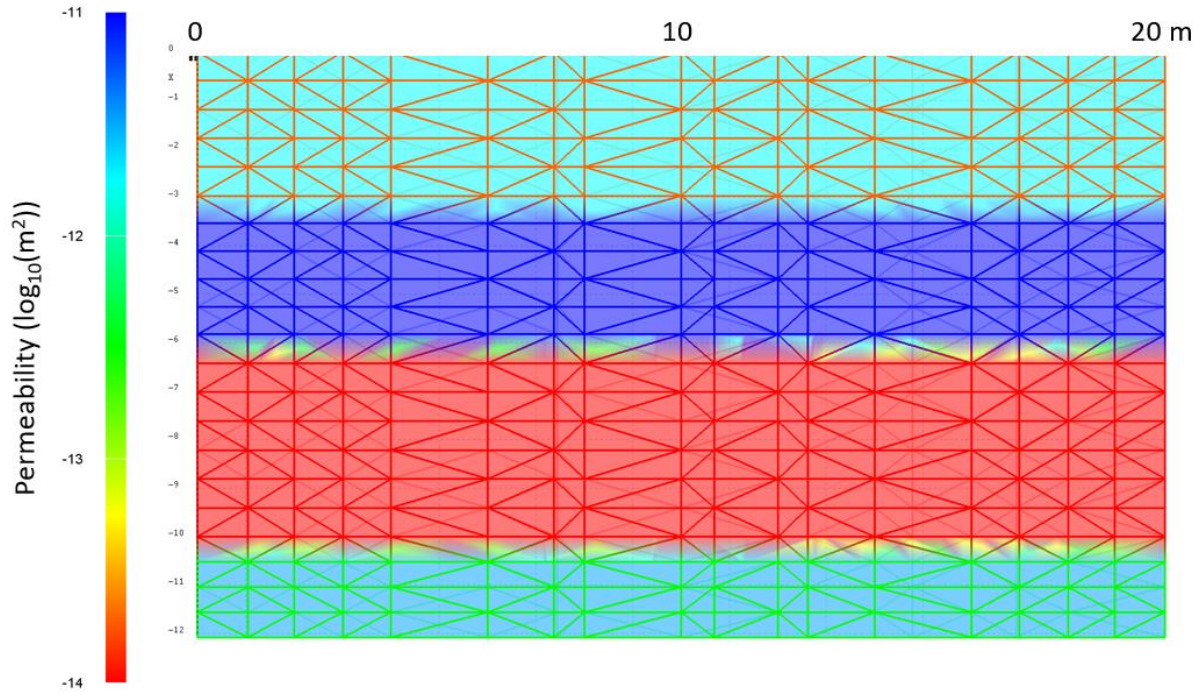


Figure 9-2 Layered permeability for the saturated layered case 1.2 (FEHM).

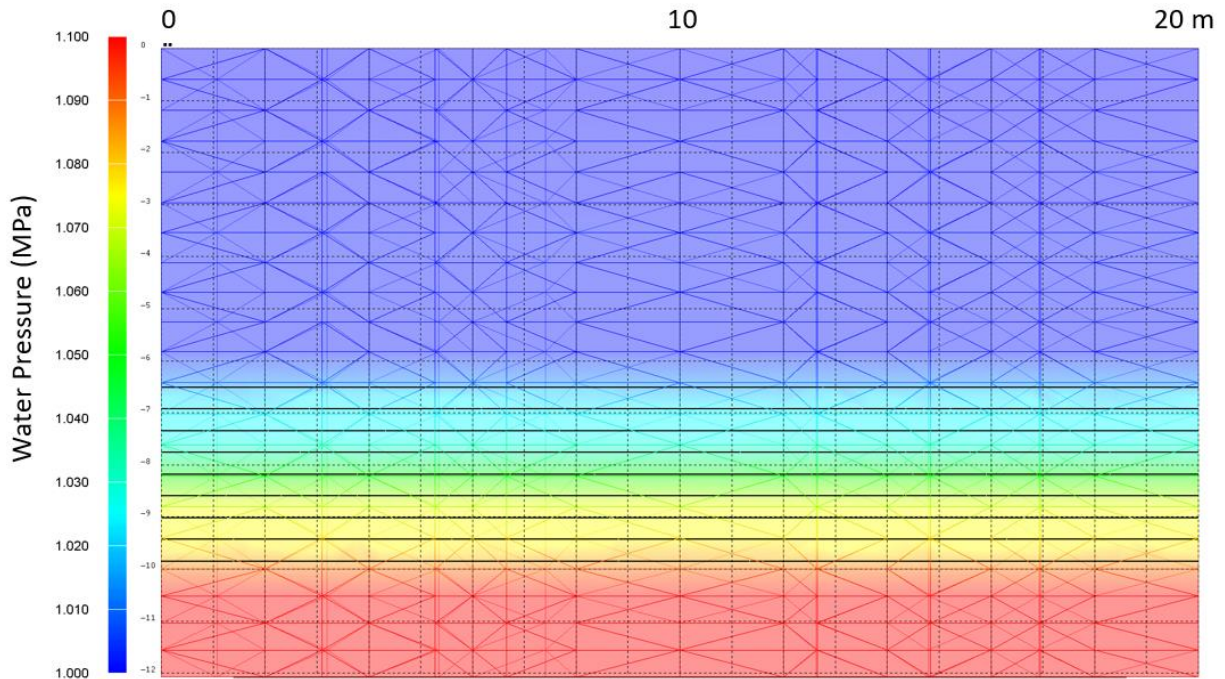


Figure 9-3 Scenario 1.2. Pressure contours for upwelling in a layered permeability field (FEHM).

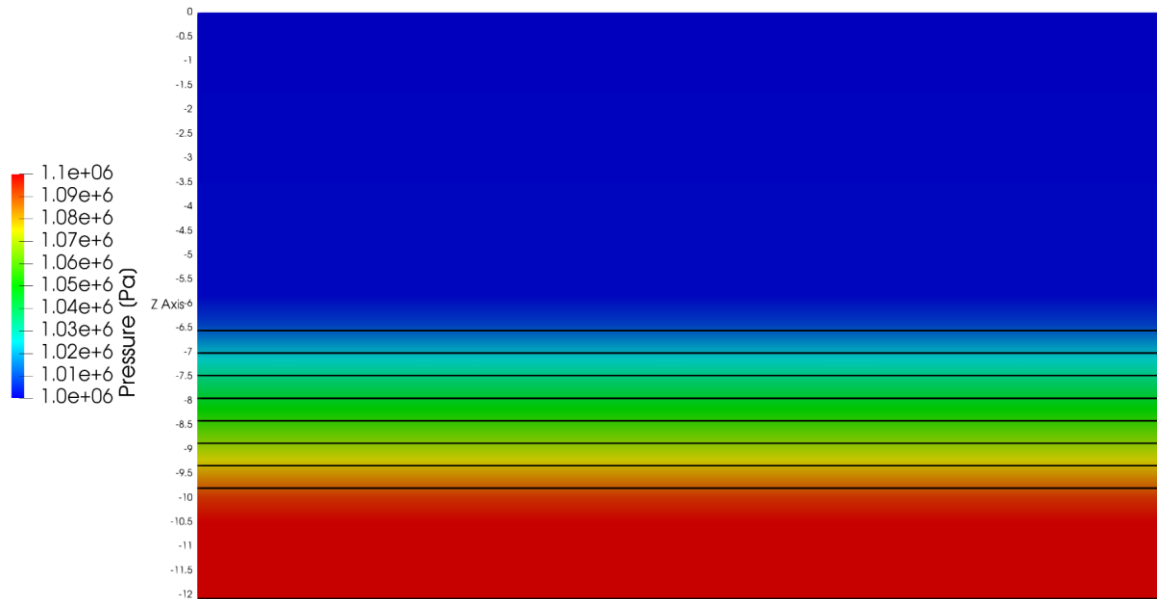


Figure 9-4 Scenario 1.2. Pressure contours for upwelling in a layered permeability field as generated by PFLOTRAN.

9.1.3 Scenario 1.3

This scenario presents an unsaturated domain with an isotropic permeability field on the layered mesh. The boundaries include a constant infiltration flux and fixed pressure (0.1 MPa) at the top of the domain and a fixed saturation at the bottom of the domain. Infiltration is distributed evenly on the top of the model domain by area, where center, edge, and corner

nodes have areas of 1.0, 0.5, and 0.25 m² respectively. Saturation contours are flat, showing no impact of the mesh on the solution. Steady-state saturation results for an infiltration flux of 10 mm/yr (4000 kg/yr over a 20 x 20 m surface) are shown in Figure 9-5.

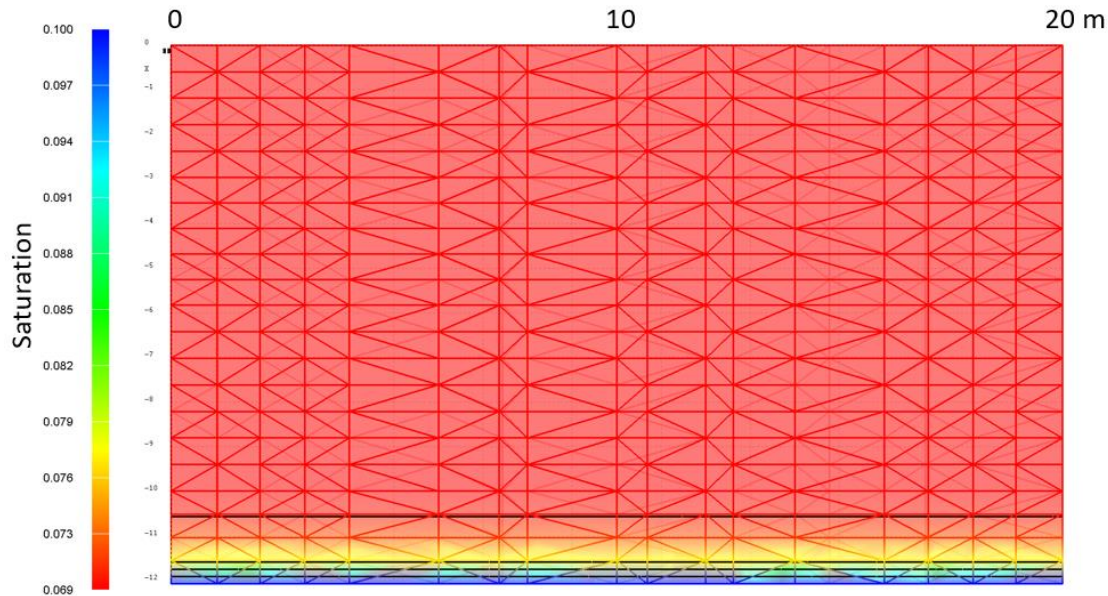


Figure 9-5 Scenario 1.3. Saturation profile for 10 mm/yr infiltration flux on an isotropic material property field (Santa Fe Group).

9.1.4 Scenario 1.4

This scenario presents an unsaturated domain with a layered permeability field on the layered mesh. Boundary conditions include a constant infiltration flux and fixed pressure (0.1 MPa) at the top of the domain and a fixed saturation at the bottom of the domain. The top and bottom layers have properties of the Santa Fe Group, while the middle two layers are assigned Otowi properties (Table 9-2).

Steady-state saturation for an infiltration flux of 10 mm/yr (4000 kg/yr over a 20 x 20 m surface) is shown in *Figure 9-6*

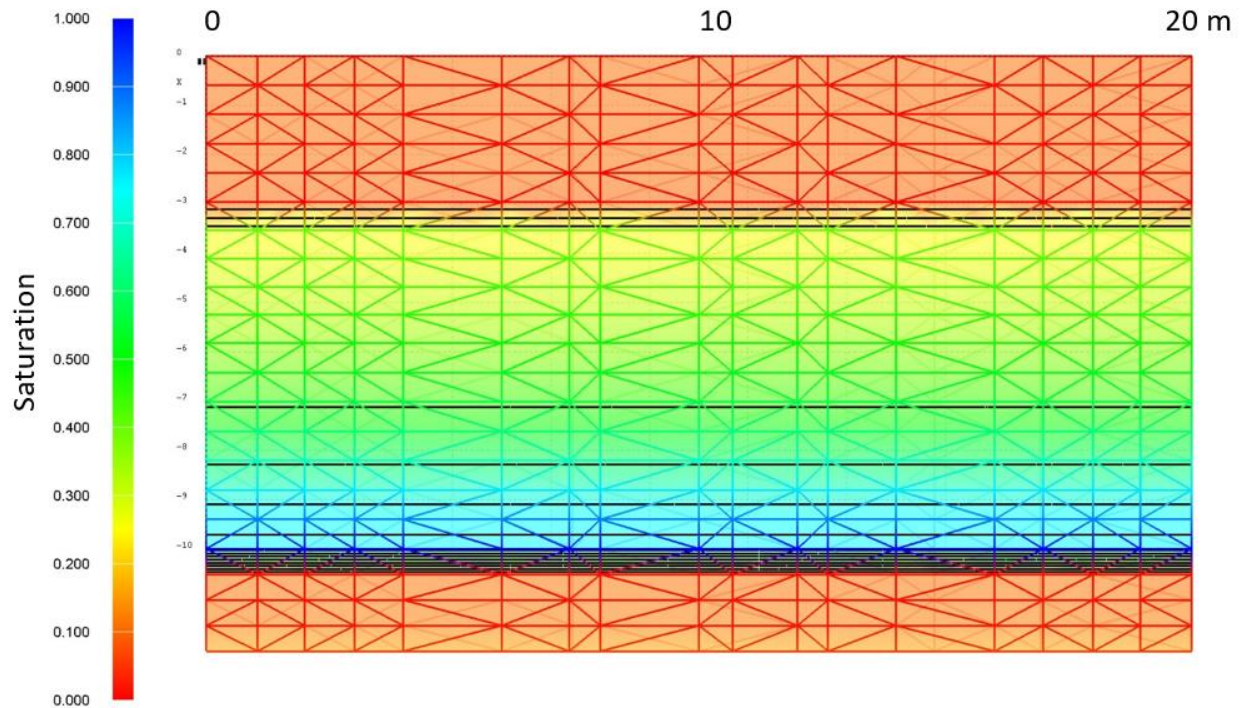


Figure 9-6 Scenario 1.4. Saturation profile for 10 mm/yr infiltration flux on a layered material property field (Santa Fe Group top and bottom, Otowi in the middle).

Because of the higher suction properties of the Otowi, the middle of the domain saturates to a much greater extent than the top and bottom which have the low suction properties of the Santa Fe Group.

9.2 Test Case 2 – Wedge

9.2.1 Scenario 2.1

The first scenario for the wedge mesh shows that the pressure gradient for an upwelling flow-field is perfectly flat. Gravity is turned off for this scenario so that there is no impact of gravitational potential energy and the flow field will be exactly proportional to the spacing of the constant pressure lines shown in black on Figure 9-7. The calculated mass flow rate (Eq. 1) for this problem is again 3.33 kg/s and the simulation matches this value closely (3.30 kg/s). PFLOTRAN also achieves 3.30 kg/s.

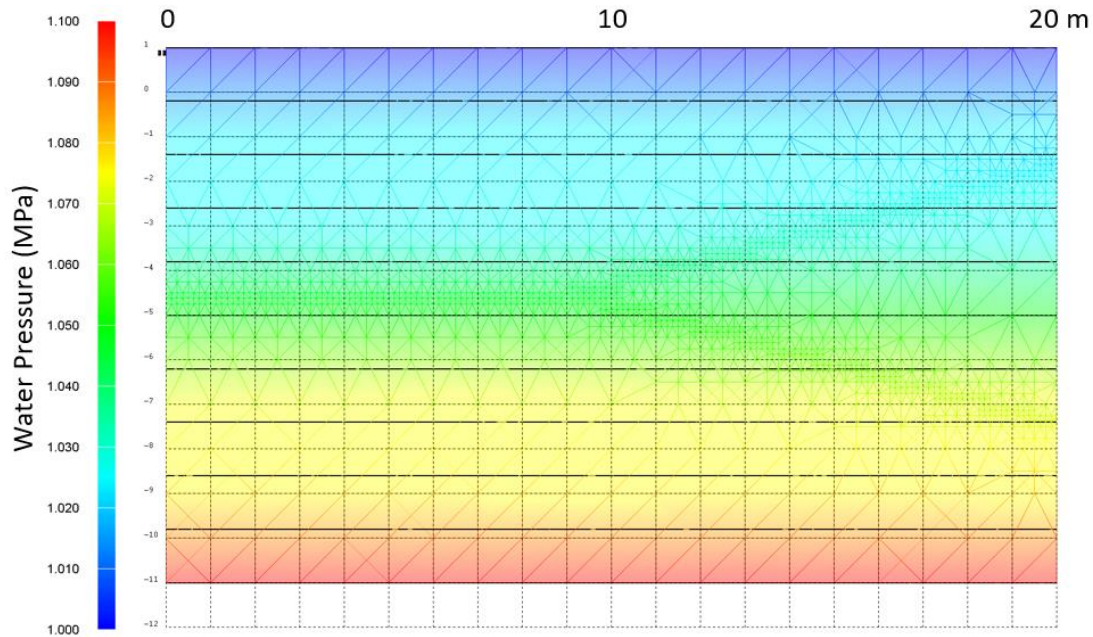


Figure 9-7 Scenario 2.1. Up flowing single phase water in the absence of gravity for the wedge mesh (test case 2).

9.2.2 Scenario 2.2

The wedge mesh permeability upwelling case introduces a low permeability wedge into the domain (Figure 9-8). The low permeability wedge causes pressure contours to bend around the low permeability section (Figure 9-9). Results generated by PFLOTRAN show a visually identical response (Figure 9-10). The mass flow rate for this problem does not have an analytical solution, however the simulated flow rate of 1.89 kg/s is slightly more than half of the value (57%) for the isotropic permeability field (3.33 kg/s) which makes intuitive sense because the low permeability wedge is blocking about half of the vertical flow path. PFLOTRAN calculates the same mass flow rate for this problem.

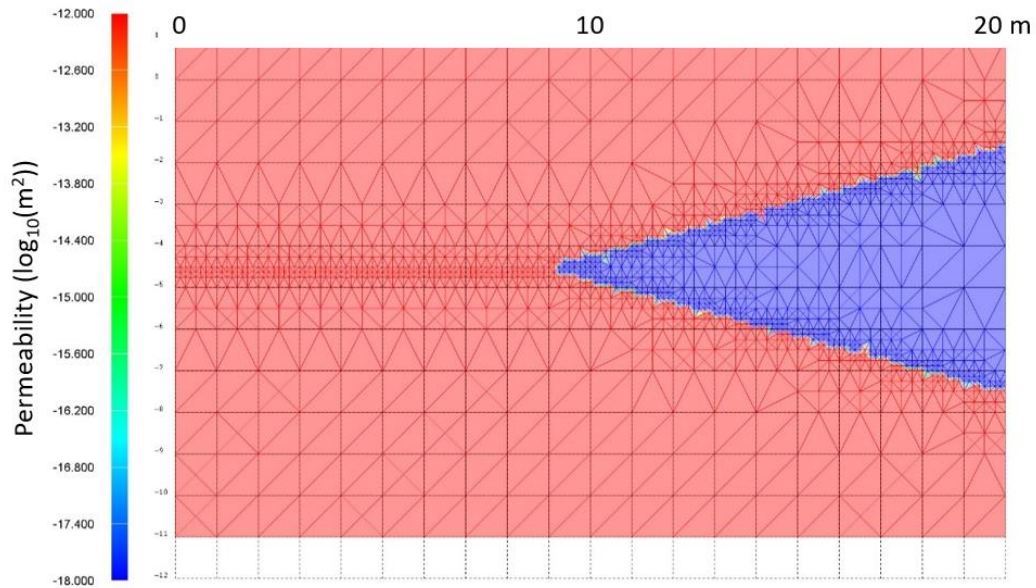


Figure 9-8 Wedge permeability ($\log_{10}(\text{perm m}^2)$) for the saturated case 2.2. Slice is at $y = 10$ m, through the center of the 3-D domain.

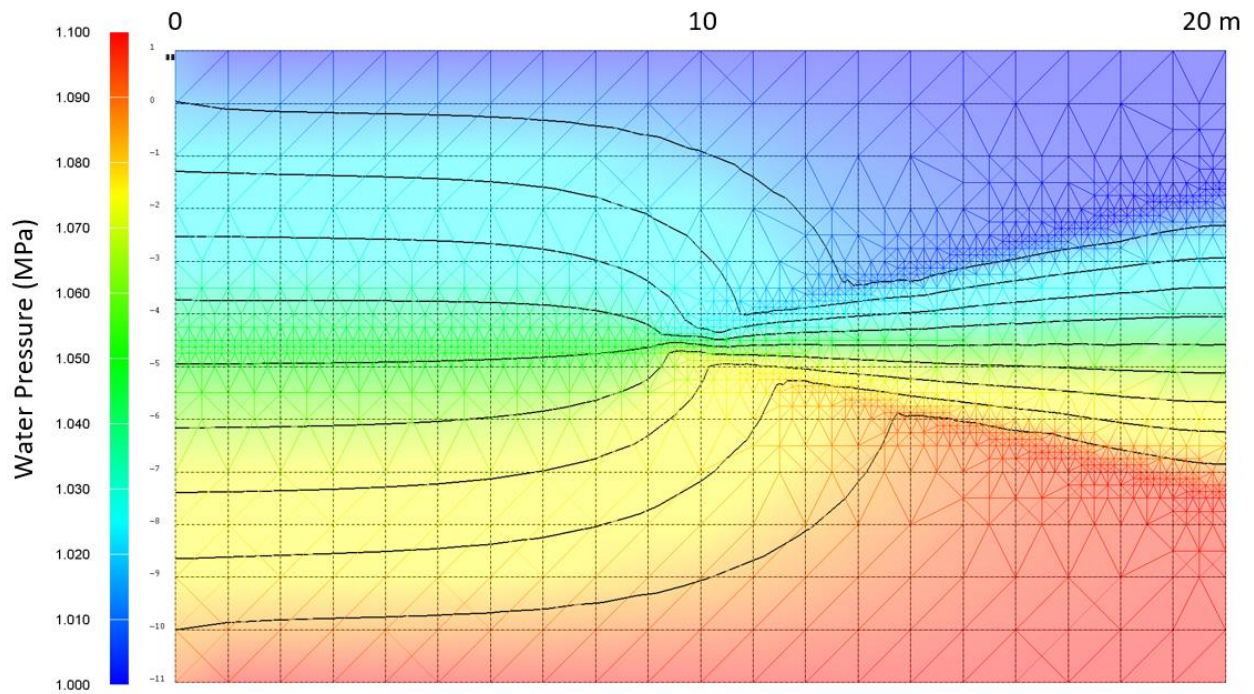


Figure 9-9 Scenario 2.2. FEHM version of pressure contours for upwelling with the low permeability wedge. Slice is at $y = 10$ m, through the center of the 3-D domain.

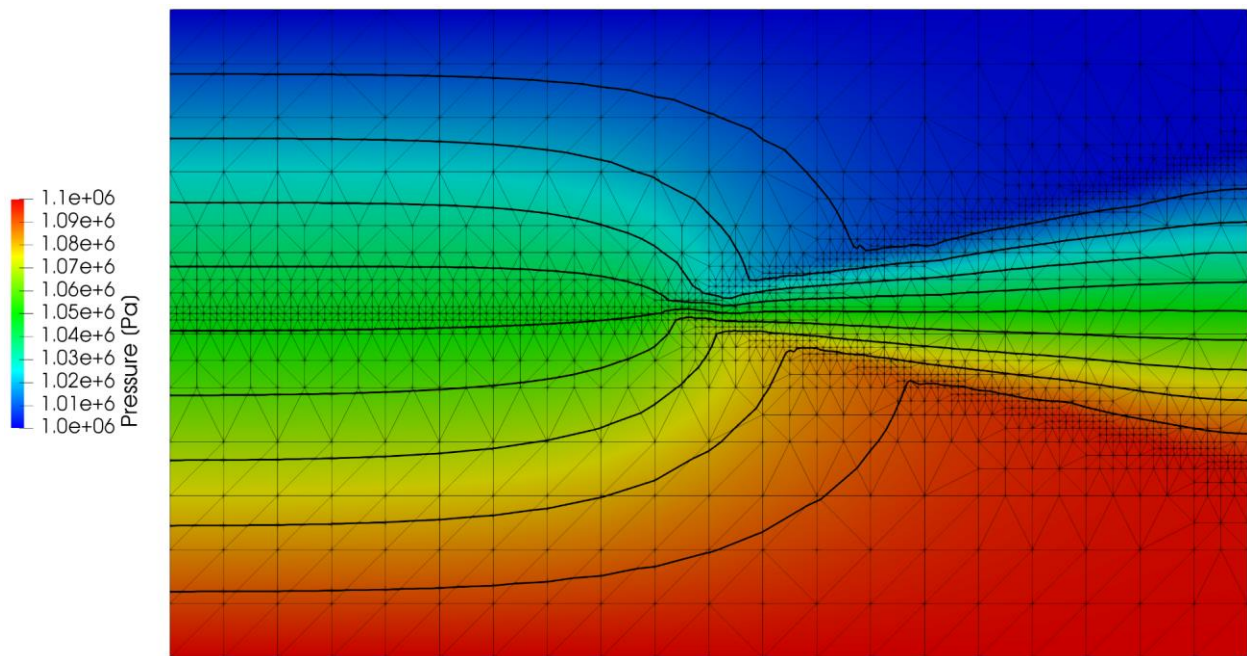


Figure 9-10 Scenario 2.2. PFLOTTRAN version of pressure contours for upwelling with the low permeability wedge. Slice is at $y = 10$ m, through the center of the 3-D domain.

9.2.3 Scenario 2.3

This scenario presents an unsaturated domain with an isotropic permeability field on the wedge mesh with a constant infiltration flux and fixed pressure (0.1 MPa) at the top of the domain and a fixed saturation (0.1) at the bottom of the domain. Steady-state saturation results for an infiltration flux of 10 mm/yr (4000 kg/yr over a 20 x 20 m surface) are shown in Figure 9-11. Infiltration is distributed evenly on the top of the model domain by area, where center, edge, and corner nodes have areas of 1.0, 0.5, and 0.25 m² respectively. Saturation contours are flat, showing no impact of the mesh on the solution.

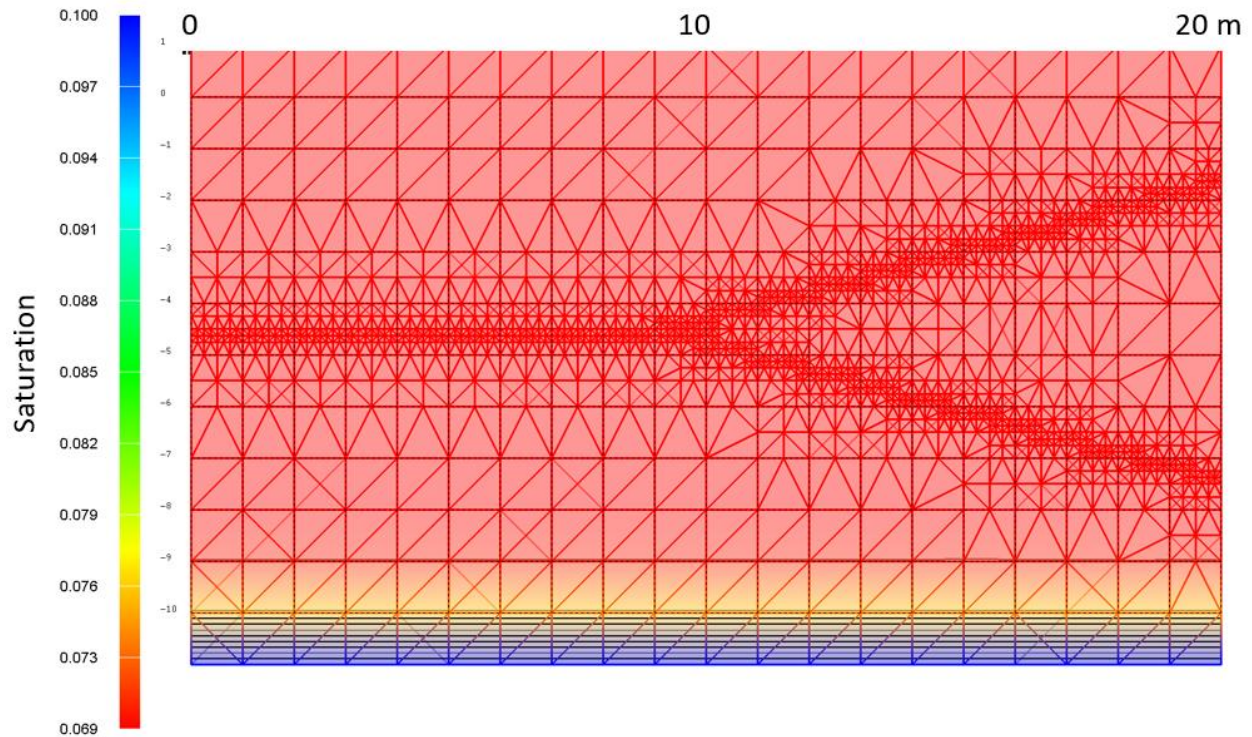


Figure 9-11 Scenario 2.3. Saturation profile for 10 mm/yr infiltration flux on an isotropic material property field (Santa Fe Group).

9.2.4 Scenario 2.4

This scenario presents a layered permeability field on the wedge mesh with a constant infiltration flux and fixed pressure (0.1 MPa) at the top of the domain and a fixed saturation (0.1) at the bottom of the domain. Steady-state saturation results for an infiltration flux of 10 mm/yr (4000 kg/yr over a 20 x 20 m surface) are shown in Figure 9-12. The higher suction properties in the wedge of Otowi lead to higher saturations at steady state relative to the Santa Fe Group.

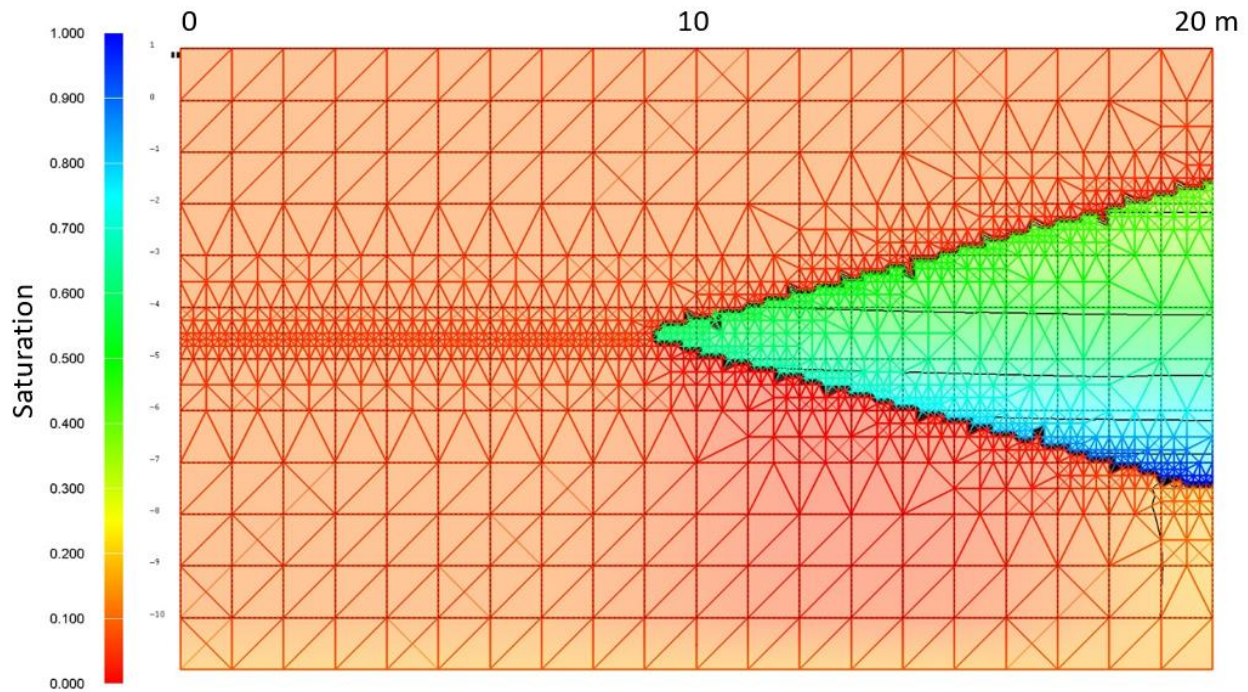


Figure 9-12 Scenario 2.4. Saturation profile for 10 mm/yr infiltration flux. The wedge is composed of Otowi tuff and the rest of the domain is Santa Fe Group. The slice plane is at $y = 10$ m.

9.3 Test Case 3 – Lens

9.3.1 Scenario 3.1

The first scenario for the lens mesh shows that the pressure gradient for an upwelling flow-field is perfectly flat. Gravity is turned off for this scenario so that there is no impact of gravitational potential energy and the flow field will be exactly proportional to the spacing of the constant pressure lines shown in black on. Using Eq. 1 yields a predicted analytical flow rate of 4.0 kg/s while FEHM and PFLOTRAN simulations result in 3.99 kg/s.

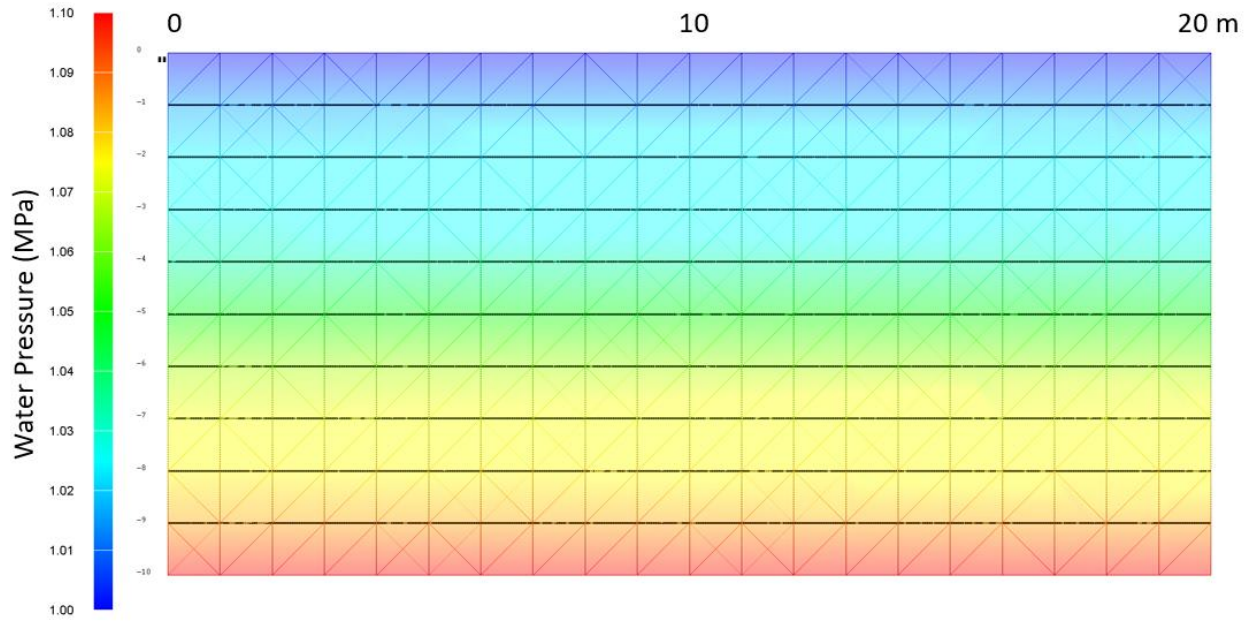


Figure 9-13 Scenario 3.1. Up flowing single phase water in the absence of gravity for the lens mesh (test case 3). Slice plane is $y = 10$ m.

9.3.2 Scenario 3.2

The lens mesh permeability upwelling case introduces a low permeability lens into the domain (Figure 9-14). The low permeability wedge causes pressure contours to bend around the low permeability section (Figure 9-15). The mass flow rate for this case (3.81) is again below the isotropic rate (3.99 kg/s) because the lens is blocking part of the vertical flow path.

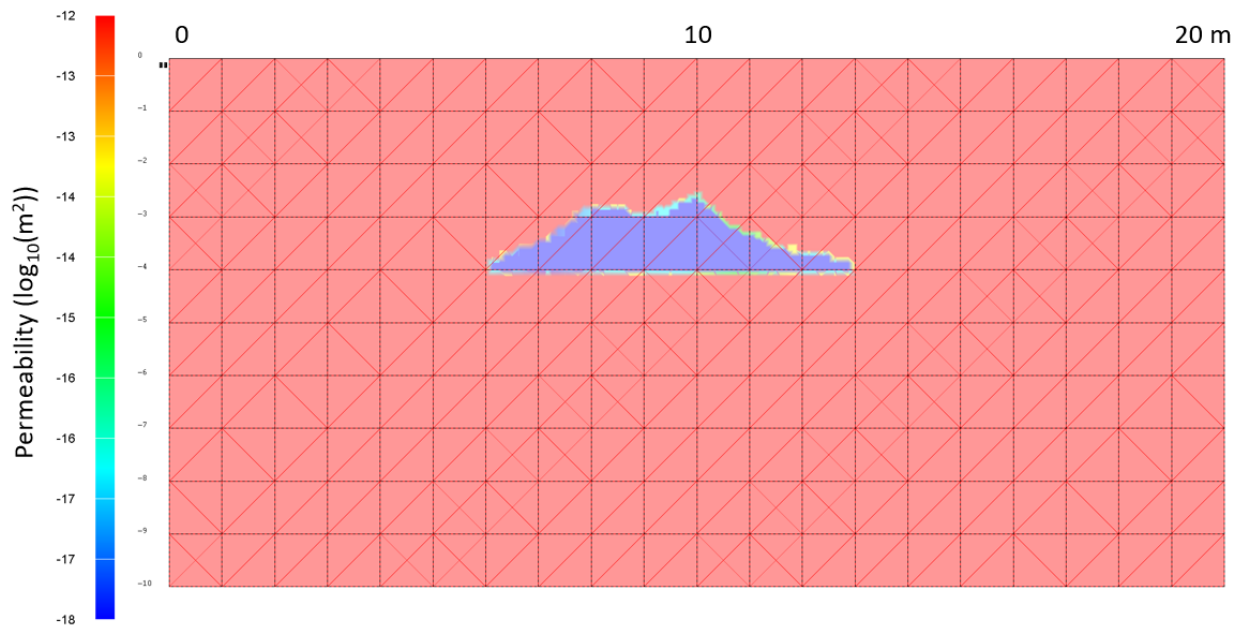


Figure 9-14 Lens permeability ($\log_{10}(\text{perm } m^2)$) for the saturated case 3.2. Slice is at $y = 10$ m, through the center of the 3-D domain.

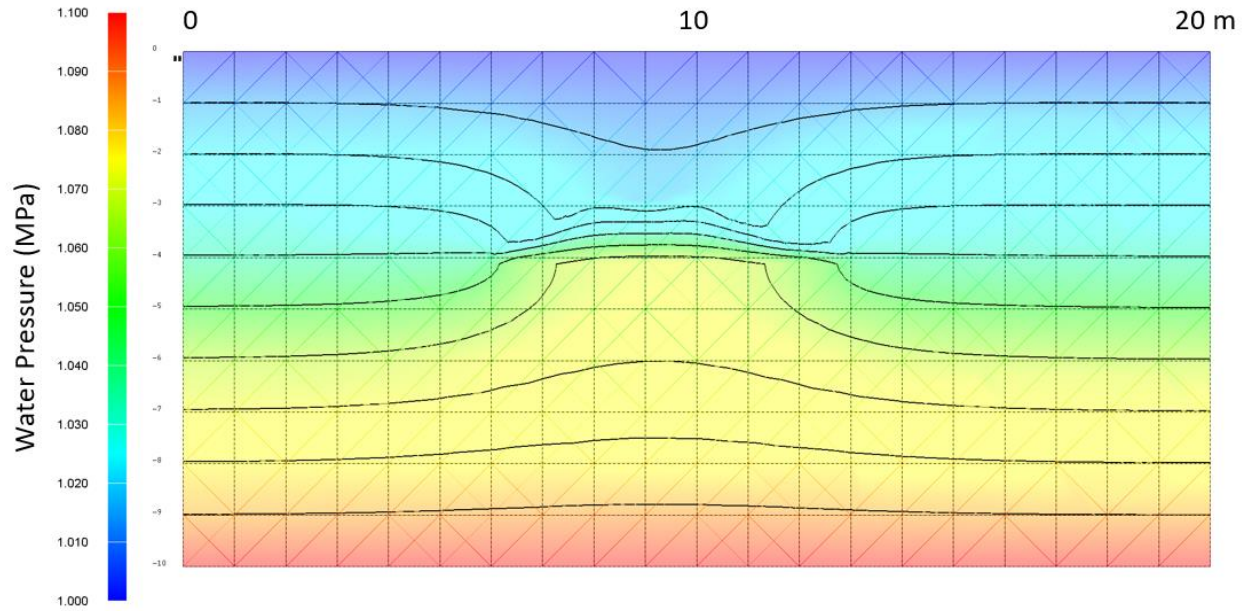


Figure 9-15 Scenario 3.2. Pressure contours for upwelling with the low permeability lens. Slice is at $y = 10$ m, through the center of the 3-D domain. (FEHM)

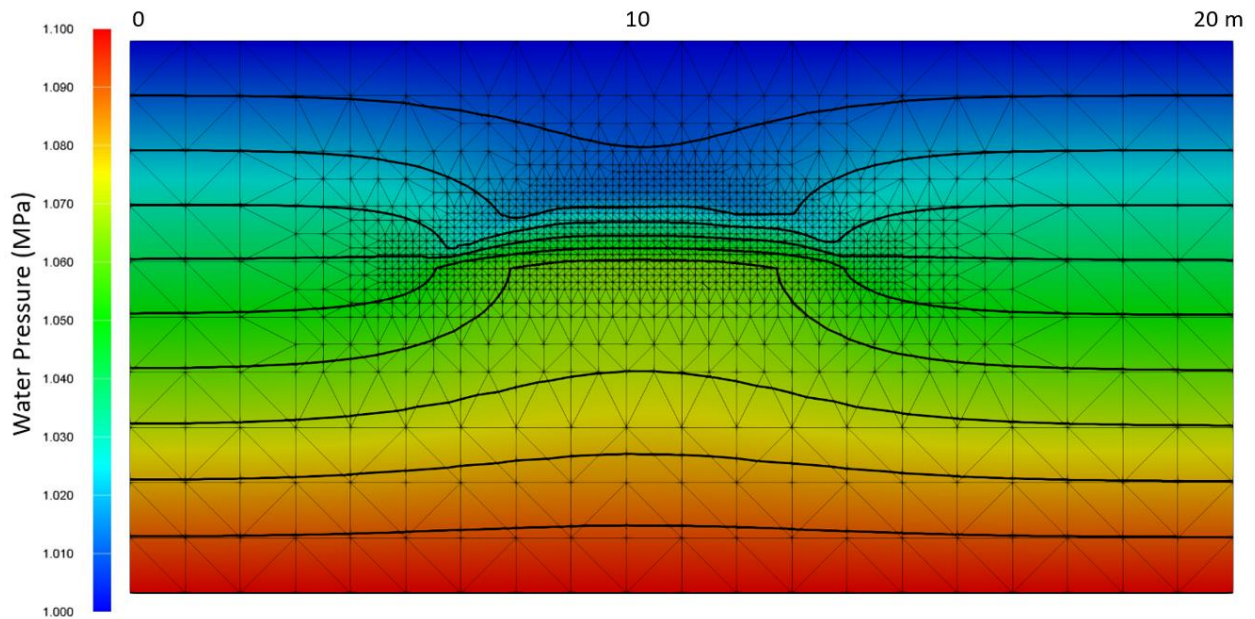


Figure 9-16 Scenario 3.2. PFLTRAN simulation showing pressure contours for upwelling with the low permeability lens. Slice is at $y = 10$ m, through the center of the 3-D domain.

9.3.3 Scenario 3.3

This scenario presents an unsaturated domain with an isotropic permeability field on the lens mesh with a constant infiltration flux and fixed pressure (0.1 MPa) at the top of the domain and a fixed saturation (0.1) at the bottom of the domain. Steady-state saturation results for an infiltration flux of 10 mm/yr (4000 kg/yr over a 20 x 20 m surface) are shown in Figure 9-17.

This image shows the $x = 10$ m slice plane that goes through the lens and there are no perturbations in the flat saturation profile.

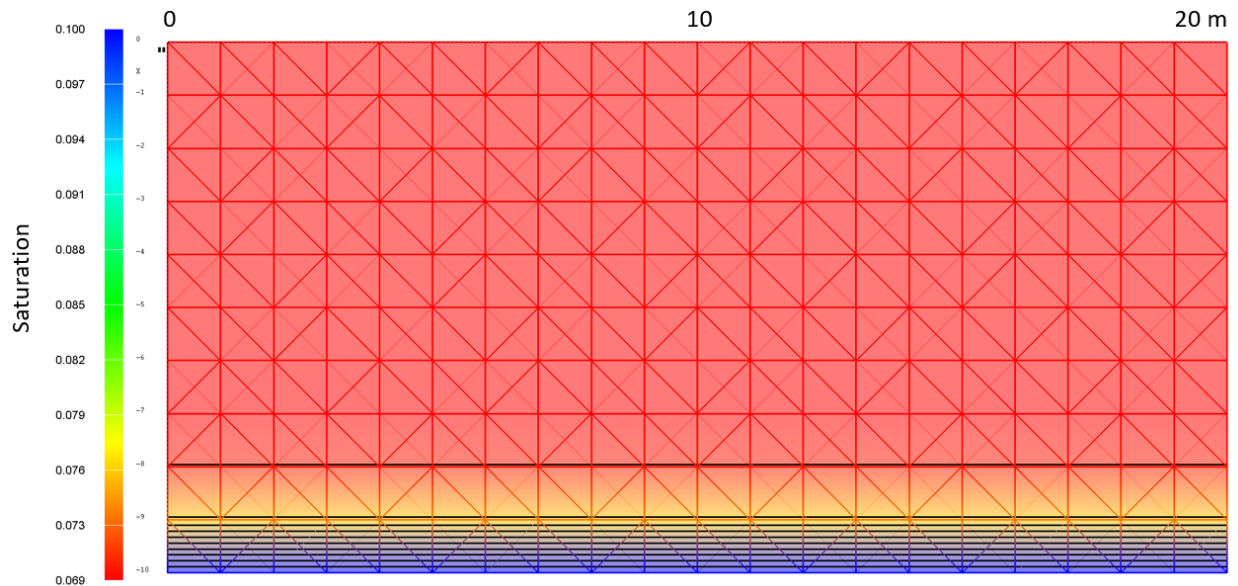


Figure 9-17 Scenario 3.3. Saturation profile for 10 mm/yr infiltration flux on an isotropic material property field (Santa Fe Group). Slice plane through the lens at $X = 10$ m.

9.3.4 Scenario 3.4

This scenario presents an unsaturated domain with two sets of unsaturated properties on the lens mesh with a constant infiltration flux and fixed pressure (0.1 MPa) at the top of the domain and a fixed saturation (0.1) at the bottom of the domain. Steady-state saturation results for an infiltration flux of 10 mm/yr (4000 kg/yr over a 20 x 20 m surface) are shown in Figure 9-18. The higher suction properties in the lens of Otowi lead to higher saturations at steady state relative to the Santa Fe Group.

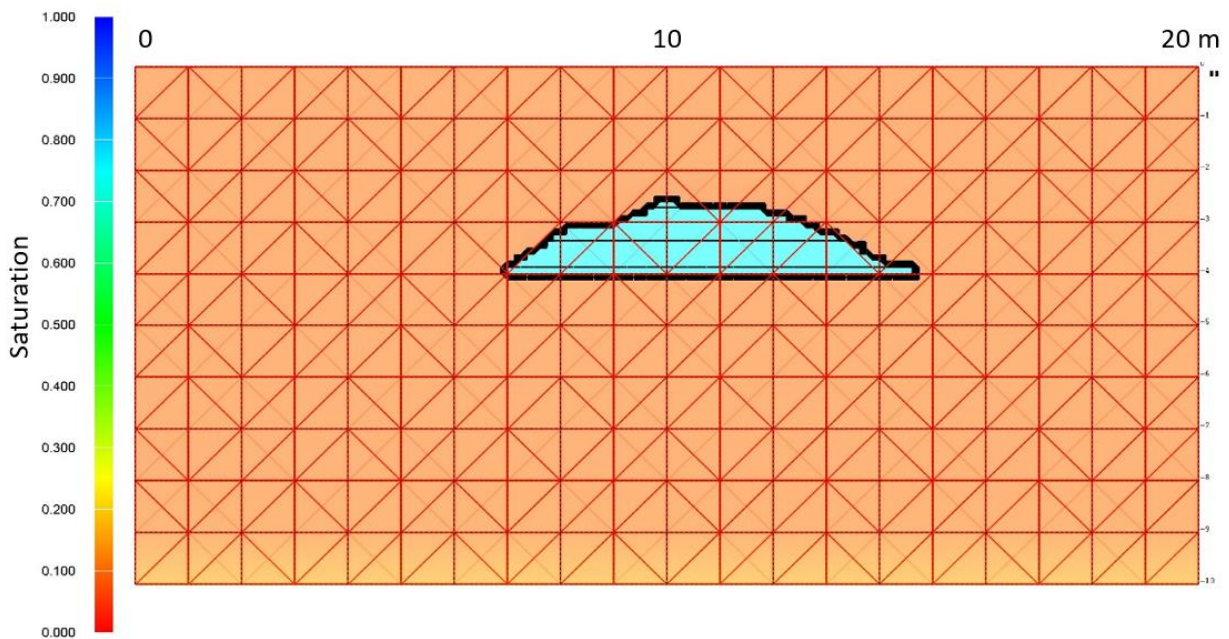


Figure 9-18 Scenario 3.4. Saturation profile for 10 mm/yr infiltration flux. The wedge is composed of Otowi tuff and the rest of the domain is Santa Fe Group.

9.4 Test Case 4 – Fault

9.4.1 Scenario 4.1

The first scenario for the fault mesh shows that the pressure gradient for an upwelling flow-field is perfectly flat. Gravity is turned off for this scenario so that there is no impact of gravitational potential energy and the flow field will be exactly proportional to the spacing of the constant pressure lines shown in black on Figure 9-19. Using Eq. 1 yields a predicted analytical flow rate of 4.0 kg/s while FEHM and PFLOTRAN simulations result in 3.99 kg/s.

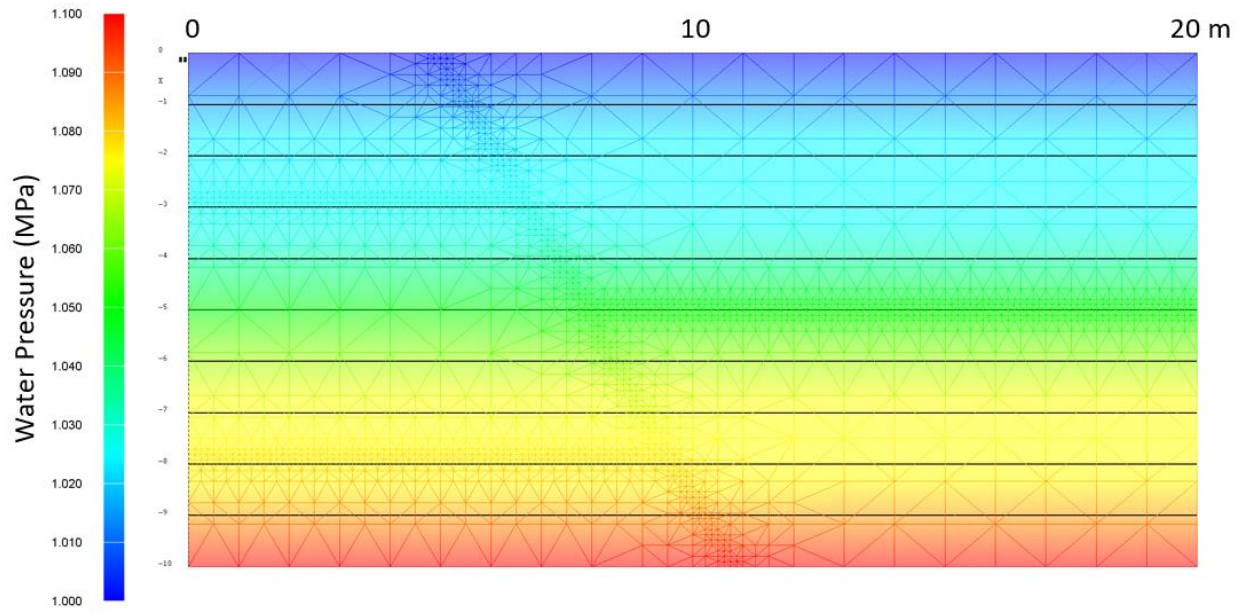


Figure 9-19 Scenario 4.1. Up flowing single phase water in the absence of gravity for the fault mesh (test case 4). Slice plane is $x = 10$ m.

9.4.2 Scenario 4.2

The fault mesh is next modified for the upwelling case to introduce low permeability layers into the domain (Figure 9-20). The low permeability layers causes pressure contours to bend such that flow follows the higher permeability layers from the lower right ($y = 20$ m) upwards through the mesh toward the upper left corner ($y = 0$ m) (Figure 9-21). The pressure contours in PFLOTTRAN (Figure 9-22) look visually identical to those from FEHM (Figure 9-21).

The mass flow rate for this case (0.59) is again below the isotropic rate (3.99 kg/s) because much of the vertical flow path is blocked by the lower permeability units. Interestingly, the narrow gap in permeability is about 3 m, or 1/7 (0.14) of the lateral domain, while the reduction in flow rate is of the same magnitude ($0.592/3.99 = 0.148$).

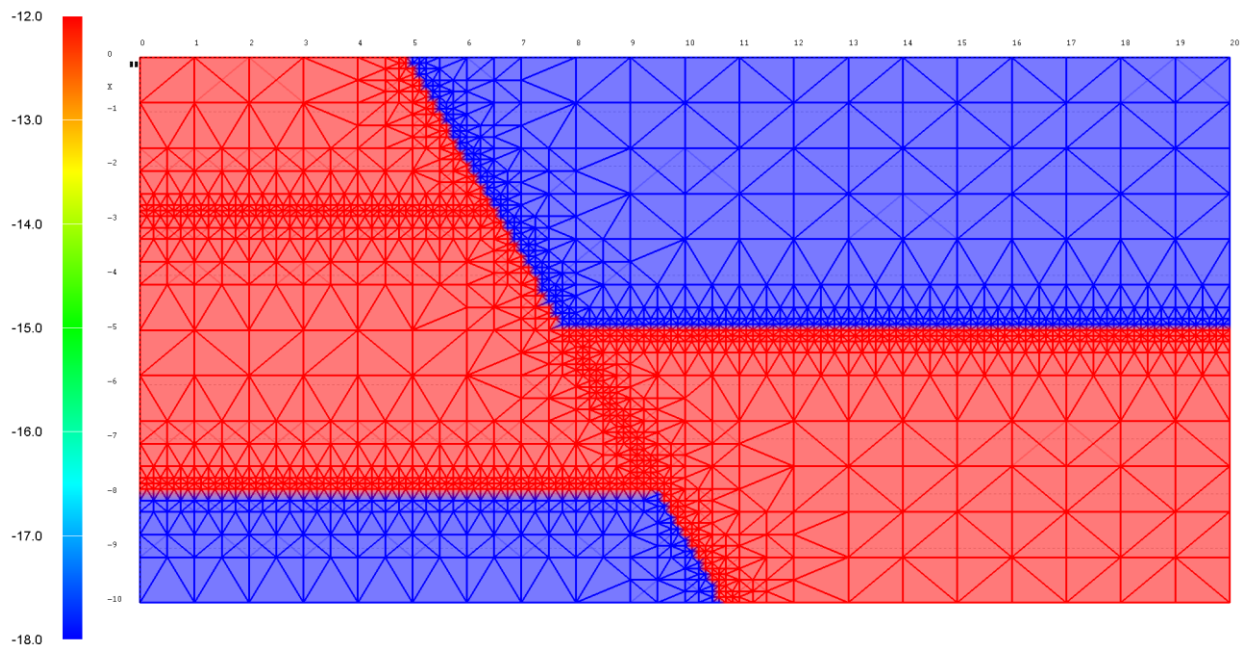


Figure 9-20 Fault permeability ($\log_{10}(\text{perm m}^2)$) for the saturated case 4.2. Slice is at $x = 10$ m, through the center of the 3-D domain.

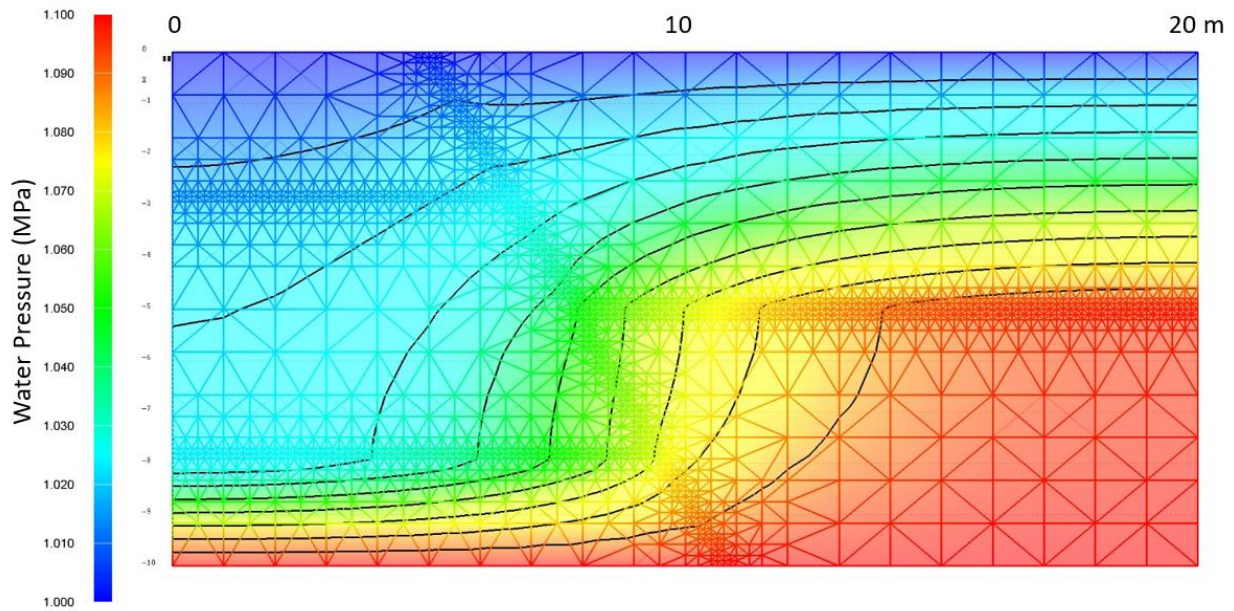


Figure 9-21 Scenario 4.2. Pressure contours for upwelling with low permeability layers forcing flow up from the lower left to the upper right. Slice is at $x = 10$ m, through the center of the 3-D domain.

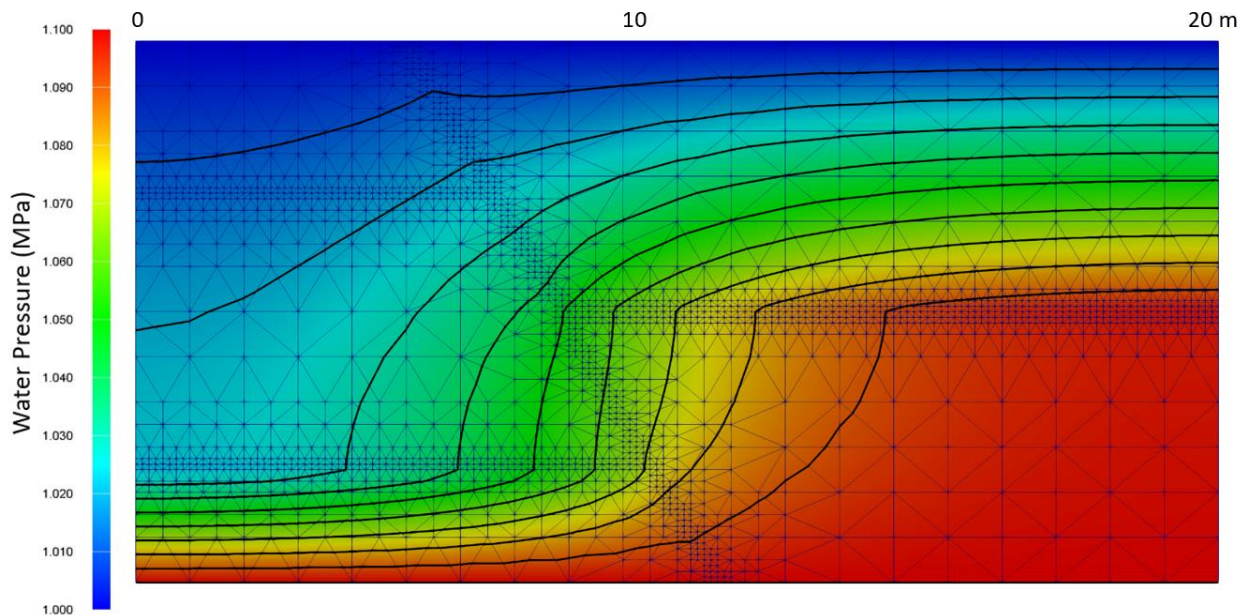


Figure 9-22 Scenario 4.2. PFLOTRAN simulation of pressure contours for upwelling with low permeability layers forcing flow up from the lower left to the upper right. Slice is at $x = 10$ m, through the center of the 3-D domain.

9.4.3 Scenario 4.3

This scenario presents an unsaturated domain with an isotropic permeability field (Santa Fe Group) on the fault mesh with a constant infiltration flux and fixed pressure (0.1 MPa) at the top of the domain and a fixed saturation (0.1) at the bottom of the domain. The infiltration flux

for this scenario is 10 mm/yr (4000 kg/yr over a 20 x 20 m surface). Steady-state saturation contours for a slice plane of $X = 10$ m are shown in Figure 9-23. The slightly non-uniform saturation seen near $Y = 5$ m is caused by the use of an internal FEHM algorithm that distributes fluxes on a boundary as a function of node volume divided by the Z distance of the volume.

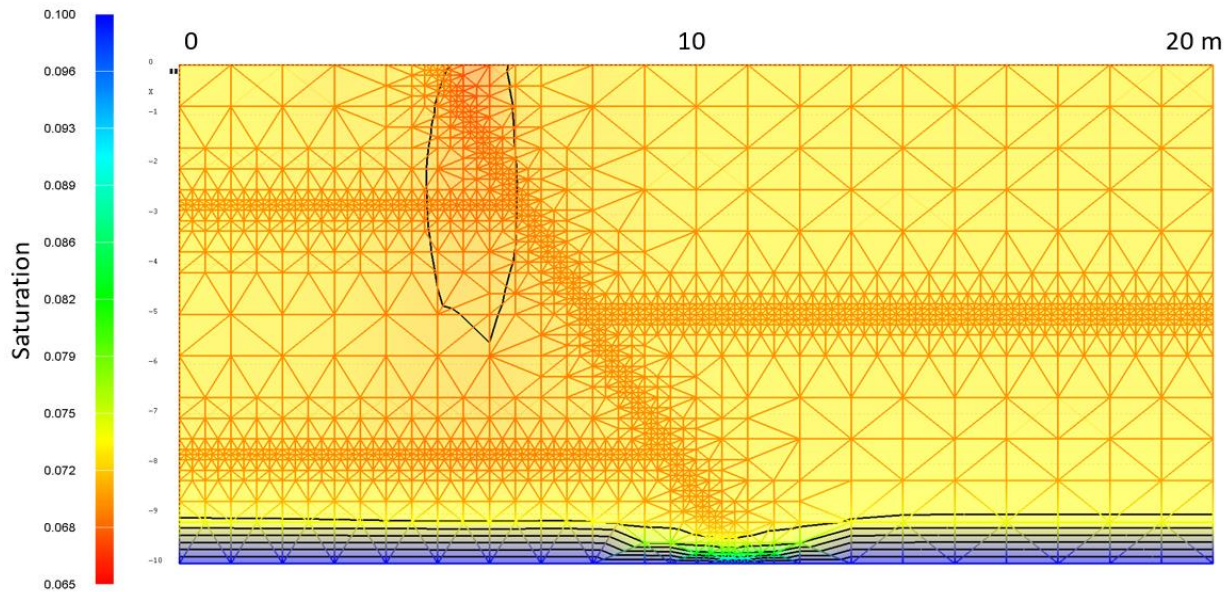


Figure 9-23 Scenario 4.3. Saturation profile for 10 mm/yr infiltration flux on an isotropic material property field (Santa Fe Group).

9.4.4 Scenario 4.4

This scenario presents a variable permeability field on the fault mesh with a fixed saturation (0.07) on both the top of and the bottom of the domain. The permeability follows the pattern in Figure 9-20 with Santa Fe Group properties applied to the red colored regions and Otowi properties applied to the blue regions. To help with numerical convergence, the entire top and bottom of the domain are also given Santa Fe Group properties. This limits high suction that would pull water out of the domain if the Otowi were fixed to a saturation of 0.07.

The infiltration flux for this scenario is higher than in the previous examples at approximately 12.4 mm/yr (approximately 5000 kg/yr over a 20 x 20 m surface). The higher suction properties in the Otowi layers lead to higher saturations at steady state relative to the Santa Fe Group.

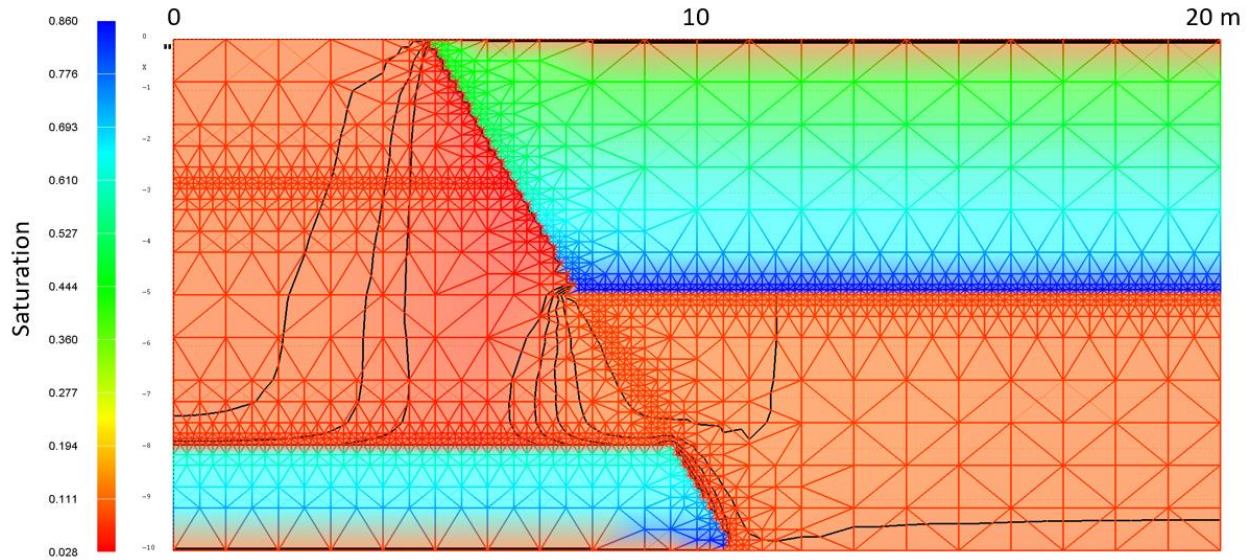


Figure 9-24 Scenario 3.4. Saturation profile for 10 mm/yr infiltration flux. The wedge is composed of Otowi tuff and the rest of the domain is Santa Fe Group.

9.5 Diagnostic output data

Diagnostic output for the 16 scenarios is shown in Table 9-4. Saturated flow rates are lower for the variable permeability cases because part of the domain has a lower permeability than used for the isotropic cases. Unsaturated flow rates are nearly constant because of the fixed top boundary infiltration flux of 4000 kg per year ($= 0.126750E-03$ kg/s). An exception is the Fault scenario 4.4 where the top and bottom boundary saturations are both fixed. For the meshes that are 12 m deep, the flow rate, at the same pressure gradient, is proportionally smaller than the 10 m deep meshes by the ratio of $10/12 = 0.833$.

Table 9-4 Diagnostic output information for the 16 test case scenarios

Scenario	Geologic Test Case	Permeability Structure	Phase State	Steady-state flowrate (kg/s) FEHM	Steady-state flowrate (kg/s) PFLOTTRAN	Final Simulation Time (yrs)	Model Depth (m)
1.1	1 - Layered	isotropic	Saturated	3.30E+00	3.30E+00	100.	12.
1.2	1 - Layered	variable	Saturated	9.55E-02	9.55E-02	100.	12.
1.3	1 - Layered	isotropic	Unsaturated	1.27E-04		1000.	12.
1.4	1 - Layered	variable	Unsaturated	1.27E-04		1000.	12.
2.1	2 - Wedge	isotropic	Saturated	3.32E+00	3.32E+00	100.	12.
2.2	2 - Wedge	variable	Saturated	1.89E+00	1.89E+00	100.	12.
2.3	2 - Wedge	isotropic	Unsaturated	1.27E-04		1000.	12.
2.4	2 - Wedge	variable	Unsaturated	1.27E-04		1000.	12.
3.1	3 - Lens	isotropic	Saturated	3.99E+00	3.99E+00	100.	10
3.2	3 - Lens	variable	Saturated	3.81E+00	3.82E+00	100.	10
3.3	3 - Lens	isotropic	Unsaturated	1.27E-04		1000.	10
3.4	3 - Lens	variable	Unsaturated	1.27E-04		1000.	10
4.1	4 - Fault	isotropic	Saturated	3.99E+00	3.99E+00	100.	10
4.2	4 - Fault	variable	Saturated	5.92E-01	5.93E-01	100.	10
4.3	4 - Fault	isotropic	Unsaturated	1.27E-04		1000.	10
4.4	4 - Fault	variable	Unsaturated	1.57E-04		1000.	10

9.6 Conclusions

All four representative geological test case computational meshes have been shown to correctly propagate numerical solutions using the FEHM porous flow simulator for cases of saturated and unsaturated flow with isotropic and heterogeneous permeability distributions. Further, PFLOTTRAN has been shown to give nearly identical results for the 8 saturated test problems.

Moving forward, we are in the process of building the unsaturated PFLOTRAN cases to compare to the FEHM results. The test cases in this section are not comprehensive and further testing in the next FY (2020) will be necessary to fully understand important physical processes such as chemical transport, reactive chemistry, and multiphase heat/mass flow. Specifically, numerical dispersion around the high resolution sections of the test case meshes will give an idea of how such dispersion could impact results in larger domains for both FEHM and PFLOTRAN. Particle simulations that are not impacted by numerical dispersion will be useful in understanding the magnitude of numerical dispersion.

10 References

- Ackermann, H.D., Pankratz, L.W. and Klein, D.P., 1994, Six regionally extensive upper-crustal seismic refraction profiles in southwest New Mexico: U.S. Geological Survey Open-file Report 94-695, 18 p.
- Addicott, W.O., 1966. Late Pleistocene marine paleoecology and zoogeography in central California, U.S. Geol. Surv. Prof. Pap., 523-C: 1-21.
- Amato, J.M., 2000, Structural relationships in the Florida Mountains, southwestern New Mexico – a review, in New Mexico Geological Society Guidebook, 51st Field Conference, p. 103-108.
- Anderson, K., Nelson, S., Mayo, A., Tingey, D., 2006. Interbasin flow revisited: The contribution of local recharge to high-discharge springs, Death Valley, CA. *Journal of Hydrology*, 323, 276-302.
- Anderson, T.W., 1979. Development of ground-water models of alluvial basins in south-central Arizona, *in* Proceedings of the 23rd Annual Arizona Water Symposium: Arizona Department of Water Resources Report 2, p. 13-17.
- Anderson, T. W., 1995. Summary of the Southwest Alluvial Basins, Regional Aquifer-System Analysis, south-central Arizona and parts of adjacent states. Professional Paper 1406-A. 44 p.
<https://pubs.er.usgs.gov/publication/pp1406A>
- Anderson, T.W., Freethey, G.W., Tucci, P., 1992. Geohydrology and Water Resources of Alluvial Basins in South-Central Arizona and Parts of Adjacent States. Professional Paper 1406-B. 77 p.
<https://pubs.er.usgs.gov/publication/pp1406B>
- Atwater, T., 1970. Implications of plate tectonics for the Cenozoic evolution of North America: *Geol. Soc. Am. Bull.*, 81, 3513–3536. [https://doi.org/10.1130/0016-7606\(1970\)81\[3513:IOPTFT\]2.0.CO;2](https://doi.org/10.1130/0016-7606(1970)81[3513:IOPTFT]2.0.CO;2)
- Atwater, T. and Stock, J., 1998, Pacific-North America plate tectonics of the Neogene southwestern United States: and update: *International Geology Review*, v. 40, p. 375-402.
- Baldrige, W.S., Perry, F.V., Vaniman, D.T., Nealy, L.D., Leavy, B.D., Laughlin, A.W., Kyle, P., Bartov, V., Steinz, G., Gladney, E.S., 1989. Magmatism associated with lithospheric extension: Middle to Late Cenozoic magmatism of the southeastern Colorado Plateau and central Rio Grande rift, New Mexico and Arizona, *N.M. Bur. Min. Miner. Resour. Mem.*, 46, 187-202.
- Belcher, W.R., Sweetkind, D.S., Elliott, P.E., 2002. Probability distributions of hydraulic conductivity for the hydrogeologic units of the Death Valley Regional Ground-Water Flow System, Nevada and California. U.S. Geological Survey Water-Resources Investigations Report 02-4212, 24 p.
- Belcher, W.R., Elliott, P.E., and Geldon, A.L., 2001. Hydraulic-property estimates for use with a transient ground-water flow model for the Death Valley regional ground-water flow system, Nevada and California: U.S. Geological Survey Water-Resources Investigations Report 2001-4210, 28 p.
<https://pubs.usgs.gov/wri/wri014210/>

- Belcher, W.R., Bedinger, M.S., Back, J.T., Sweetkind, D.S., 2009. Interbasin flow in the Great Basin with special reference to the southern Funeral Mountains and the source of Furnace Creek springs, Death Valley, California. *US. Journal of Hydrology*, 369, 30-43 p.
- Bielicki, J., Blackwell, D., Harp, D., Karra, S., Kelley, R., Kelley, S., Middleton, R., Pepin, J., Person, M., Sutula, G., Witcher, J., 2015, Hydrogeologic windows: regional signature detection for blind and traditional geothermal play fairways: Final Report submitted to the Department of Energy, Los Alamos National Laboratory Report LA-UR-15-28360.
- Broadhead, R.F., Mansell, M. and Jones, G., 2009, Carbon dioxide in New Mexico: geologic distribution of natural occurrences: New Mexico Bureau of Geology and Mineral Resources, Open File Report No. 514, 131p., 1 Plate.
- Brown, G.A. and Clemons, R.E., 1983, Florida Mountains section of southwest New Mexico overthrust belt – a reevaluation: *New Mexico Geology*, v. 5, p. 26-29.
- Bussod, G.Y., and Williams, D.R., 1991. Thermal and kinematic model of the southern Rio Grande rift: inferences from crustal and mantle xenoliths from Kilbourne Hole, New Mexico, *Tectonophysics*, v. 197, p. 373-389.
- Caine, J.S., Evans, J.P., Forster, C.B., 1996. Fault zone architecture and permeability structure. *Geology*, 24, 1025-1028.
- Chapin, CE, 1979. Evolution of the Rio Grande Rift: A Summary, In: *Rio Grande Rift: Tectonics and Magmatism*, Riecker, R.E. [ed], Am. Geophys. Union Spec. Publ., 1-7.
- Chapman, J.B., Dafov, M.N., Gehrels, G., Ducea, M.N., Valley, J.W. and Ishida, A., 2018, Lithospheric architecture and tectonic evolution of the southwestern U.S. Cordillera: constraints from zircon Hf and O isotopic data: *Geological Society of America Bulletin*, v. 130, p. 2031-2046.
- Chester, F.M., Logan, J.M., 1986. Implications for mechanical properties of brittle faults from observations of the Punchbowl fault zones. *California: Pure and Applied Geophysics (PAGEOPH)*, 124, 79–106.
- City of Deming 40-Year Water Plan, 2009, Report by Daniel B. Stephens & Associates, Inc., 104 p.
- Clemons, R.E., 1986, Petrography and stratigraphy of Seville-Trident exploration wells near Deming, New Mexico: *New Mexico Geology*, v. 8, p. 5-11.
- Cochran, J.R, and 16 others, 2001, Compliance assessment document for the transuranic wastes in the greater confinement disposal boreholes at the Nevada Test Site, v. 2: Sandia National Laboratories, Albuquerque, New Mexico, SAND2001-2977, 811 p.
- Contaldo, G.J. and Mueller, J.E., 1991, Earth fissures of the Mimbres Basin, southwestern New Mexico: *New Mexico Geology*, v. 13, p. 69-74.

- DeCelles, P.G., 2004, Late Jurassic to Eocene evolution of the Cordilleran thrust belt and foreland basin system, western U.S.A.: *American Journal of Science*, v. 304, p. 105-168.
- De los Santos, M.G., Lawton, T.F., Copeland, P., Licht, A. and Hall, S.A., 2018, Magnetostratigraphy, age and depositional environment of the Lobo Formation, southwest New Mexico: implications for the Laramide orogeny in the southern Rocky Mountains: *Basin Research*, v. 30, p. 401-423.
- Dickinson, W.R., 1991, Tectonic setting of faulted Tertiary strata associated with the Catalina core complex in southern Arizona: *Geological Society of America Special Paper* 264, 106 p.
- Dickinson, W.R., 2006. Geotectonic evolution of the Great Basin: *Geosphere* , 2, 353-368, <https://doi.org/10.1130/GES00054.1>
- Diment, W. H., and others, 1958, Properties of Oak Spring formation in Area 12 at the Nevada Test Site: U.S. Geol. Survey TEI-672, open-file report.
- Drewes, H., Houser, B. B., Hedlund, D. C., Richter, D. H., Thorman, C. H. and Finnell, T. L., 1985. Geologic map of the Silver City 1° x 2° Quad., New Mexico and Arizona, U.S. Geol. Surv., *Miscell. Invest. Ser. Map, I-1310-C*, scale 1 : 250,000
- Eakin, T.E., Price, D. and Harill, J.R., 1976, Summary appraisals of the nation's groundwater resources-Great Basin region: U.S. Geological Survey Professional Paper, 37 p.
- Eberly, L.D., and Stanley, T.B., 1978. Cenozoic stratigraphy and geologic history of southwestern Arizona, *GSA Bull.*, v. 89, p. 921-940.
- Eppelbaum, L., Kutasov, I., and Pilchin, A., 2014, *Applied Geothermics*: Springer, 183 p.
- Faunt, C.C., 1997. Effect of Faulting on Ground-Water Movement in the Death Valley Region, Nevada and California. U.S. Geological Survey Water-Resources Investigations Report 95-4132, 51 p.
- FEHM (2019), FEHM Website, <https://fehm.lanl.gov/> accessed June 28th, 2019.
- Fenelon, J.M., Sweetkind, D.S., Elliot, P.E., Lacznia, R.J., 2012. Conceptualization of the Predevelopment Groundwater Flow System and Transient Water-Level Responses in Yucca Flat, Nevada National Security Site, Nevada. U.S. Geological Survey Scientific Investigations Report 20 U.S. Geological Survey Scientific Investigations Report 2012-5196, 72 p.
- Fetter (2001), *Applied Hydrogeology – Fourth Edition*, Prentice Hall.
- Finch, S.T. Jr., McCoy, A. and Melis, E., 2008, Geologic controls on ground-water flow in the Mimbres Basin, southwestern New Mexico in *Geology of the Gila Wilderness-Silver City area, New Mexico Geological Society Guidebook, 59th Field Conference*, p. 1889-198.
- Fleischhauer, H. L., and Stone, W. J., 1982. Quaternary geology of Lake Animas, Hidalgo County, New Mexico, *New Mexico Bur. Mines Mineral. Res. Circular* 174, 25 p.

- Forester R. M., 1991. Ostracode assemblages from springs in the western United States: Implications for paleohydrology, *Mem. Entomolog. Soc. Canada*, 155 181–201.
- Frostick, L.E. and Reid, I., 1989. Climatic versus tectonic controls of fan sequences: lessons from the Dead Sea, Israel, *Jour. Geol. Soc. Lond.*, 146, 527–538.
- Geologic Map of New Mexico, 2003, New Mexico Bureau of Geology and Mineral Resources in cooperation with the U.S. Geological Survey (scale: 1:500,000).
- Gilbert, G.K., 1875, Report upon the geology of portions of Nevada, Utah, California, and Arizona, examined in the years 1871 and 1872, *in* Report on the geographical and geological explorations and surveys west of the One Hundredth Meridian (Wheeler): U.S. Geological and Geographical Survey, Publication of the Wheeler Survey, v. 3, pt. 1, p. 17-187.
- Gile, L. H., Hawley, J. W. and Grossman, R. B., 1981. Soils and geomorphology in a Basin-and-Range area of southern New Mexico-Guidebook to the Desert Project, New Mexico Bur. Mines Mines Miner. Resour. Bull., 142, 96p.
- Gulluly, J., 1956. General geology of central Cochise county Arizona, *Geol. Surv. Profess. Paper* 281, 169 pp.
- Hanson, R.T., McLean, J.S. and Miller, R.S., 1994, Hydrogeologic framework and preliminary simulation of ground-water flow in the Mimbres Basin, southwestern New Mexico: U.S. Geological Survey Water-Resources Investigations Report 94-4011, 118 p.
- Hardin, E., T. Hadgu, D. Clayton, R. Howard, H. Greenberg, J. Blink, M. Sharma, M. Sutton, J. Carter, M. Dupont and P. Rodwell, 2012. Repository reference disposal concepts and thermal load management analysis. FCRD-UFD-2012-00219 Rev. 2. U.S. Department of Energy, Used Fuel Disposition Campaign. 345 p.
- Harrill J.R. and Preissler A.M., 1994. Ground-water flow and simulated effects of development in Stagecoach Valley, a small, partly drained basin in Lyon and Storey counties, western Nevada. Professional Paper 1409-H. 83 p. <https://pubs.er.usgs.gov/publication/pp1409H>
- Harrill, J.R. and Prudic, D.E., 1998. Aquifer systems in the Great Basin region of Nevada, Utah, and adjacent states; summary report. Professional Paper 1409-A. <https://pubs.er.usgs.gov/publication/pp1409A>
- Harry, D.L., Sawyer, D.S., and Leeman, W.F., 1993. The mechanics of continental extension in western North America: Implications for the magmatic and structural evolution of the Great Basin, *Earth Planet. Sci. Lett.* , 117, 59–71.
- Hawley, J. W., 1975. Quaternary history of Doña Ana County region south-central New Mexico, *New Mexico Geol.Soc. Guidebook* 26, 138- 150.

- Hawley, J. W., Haase, C. S. and Lozinsky, R. P., 1995. Hydrogeologic framework of the northern Albuquerque basin, In: Klett, C. T. (ed.), *The water future of Albuquerque and Middle Rio Grande basin*, New Mexico Water Res. Research Inst., Tech. Report 290, 37- 55.
- Hawley, J.W., Hibbs, B.J., Kennedy, J.F., Creel, B.J., Remmenga, M.D., Johnson, M., Lee, M.M. and Dinterman, P., 2000, Trans-International Boundary aquifers in southwestern New Mexico: New Mexico Water Resources Research Institute, New Mexico State University, prepared for U.S. Environmental Protection Agency, Region 6, and International Boundary and Water Commission; Technical Completion Report-Interagency Contract X-996350-01-3, 126 p.
- Heilweil, V.M., and Brooks, L.E., eds., 2010. Conceptual model of the Great Basin carbonate and alluvial aquifer system. U.S. Geological Survey Scientific Investigations Report 2010-5193, 191 p. <https://pubs.usgs.gov/sir/2010/5193/>
- Heywood, C.E., 2002, Estimation of alluvial-fill thickness in the Mimbres ground-water basin, New Mexico, from Interpretation of isostatic residual gravity anomalies: U.S. Geological Survey Water-Resources Investigations Report 02-4007, 15 p.
- Hoffman, D.C., Stone, R., Dudley, W.W. Jr., 1977, Radioactivity in the underground environment of the Cambrian nuclear explosion at the Nevada Test Site. Los Alamos Scientific Laboratory, LA-6877-MS, 92p. <https://www.osti.gov/biblio/60209>
- Karlstrom, K.E., Amato, J.M., Williams, M.L., Heizler, M., Shaw, C.A., Read, A.S. and Bauer, P., 2004, Proterozoic tectonic evolution of the New Mexico region: a synthesis, in Mack, G.H. and Giles, K.A., eds., *The Geology of New Mexico: A Geologic History*, New Mexico Geological Society, p. 1-34.
- Kennedy, J.F., Hawley, J.W. and Johnson, M.M., 2000, The hydrogeologic framework of basin-fill aquifers and associated ground-water-flow systems in southwestern New Mexico – an overview, in *New Mexico Geologic Society Guidebook, 51st Field Conference*, p. 235-244.
- Klein, D.P., Abrams, G.A. and Hill, P.L., 1995, Structure of the Basins and Ranges, southwest New Mexico, an interpretation of seismic velocity sections: U.S. Geological Survey Open File Report 95-506, 60 p.
- Kwicklis, E.M., A.V. Wolfsberg, P.H. Stauffer, M.A. Walvoord, and M.J. Sully. 2006. Multiphase, multicomponent parameter estimation for liquid and vapor fluxes in deep arid systems using hydrologic data and natural environmental tracers. *Vadose Zone J.* 5:934– 950. doi:10.2136/vzj2006.0021
- Lawton, T.F., 2004, Upper Jurassic and Lower Cretaceous strata of southwestern New Mexico and northern Chihuahua, Mexico, , in Mack, G.H. and Giles, K.A., eds., *The Geology of New Mexico: A Geologic History*, p. 153-182.
- Leopoldt, W. and Kortemeier, C.P., 1984. Zircon-fission-track ages of Neogene air-fall ashes from the Gila Group and the Camp Rice Formation, Grant and Doña Ana Counties, New Mexico, *Isotopes*, 41, 15–18.
- Los Alamos Grid Toolbox, LaGriT, Los Alamos National Laboratory, (<https://lagrit.lanl.gov>), 2019.

- Love, D.W. and Seager, W.R., 1996, Fluvial fans and related basin deposits of the Mimbres drainage: *New Mexico Geology*, v. 18, p. 81-92.
- Lucas, S., 2004, The Triassic and Jurassic systems in New Mexico, in Mack, G.H. and Giles, K.A., eds., *The Geology of New Mexico: A Geologic History*, p. 137-152.
- Mack, G.H., 2004, Middle and Late Cenozoic crustal extension, sedimentation, and volcanism in the southern Rio Grande rift, Basin and Range, and southern transition zone of southwestern New Mexico, *in* Mack, G.H. and Giles, K.A., eds., *The Geology of New Mexico: A Geologic History*, p. 389-406.
- Mack, G.H., Love, D.W., and Seager, W.R., 1997. Spillover models for axial rivers in regions of continental extension – the Rio Mimbres and Rio Grande in the southern Rio Grande rift, USA, *Sedimentology*, 44, 637-652.
- Mack, G.H., and Seager, W.R., 1990. Tectonic control on facies distribution of the Camp Rice and Palomas Formations (Pliocene-Pleistocene) in the southern Rio Grande rift, *Geol. Soc. Am. Bull.*, 102, 45-53.
- Mack, G.H., Seager, W.R. and Leeder, M.R., 2003, Synclinal-horst basins: examples from the southern Rio Grande rift and southern transition zone of southwestern New Mexico, USA: *Basin Research*, v. 15, 365-377.
- Mack, G.H. and Stout, D.M., 2005, Unconventional distribution of facies in a continental rift basin: the Pliocene-Pleistocene Mangas Basin, south-western New Mexico: *Sedimentology*, v. 52, p. 1187-1205.
- Mariner, P.E., Stein, E.R., Sevougian, S.D., Cunningham, L.J., Frederick, J.M., Hammond, G.E., Lowry, T.S., Jordan, S., and Basurto, E. 2018. Advances in Geologic Disposal Safety Assessment and an Unsaturated Alluvium Reference Case. SFWD-SFWST-2018-000509, SAND2018-11858 R.
- Masbruch, M.D., Gardner, P.M., and Brooks, L.E., 2014, Hydrology and numerical simulation of groundwater movement and heat transport in Snake Valley and surrounding areas, Juab, Millard, and Beaver counties, Utah, and White Pine and Lincoln counties, Nevada: US Geological Survey Scientific Investigations Report 2014-5103, 122 p.
- Matthew, J. W., Fremd, T. J., 2008. Miocene tectonics and climate forcing of biodiversity, western United States, *Geology* 36 (10), 783-786.
- Menges, C.M. and McFadden, L.D., 1981. Evidence for the latest-Miocene to Pliocene transition from Basin-Range tectonic to post-tectonic landscape evolution in southeastern Arizona: *Arizona Geological Society Digest*, 13, 151-160.
- Menges, C.M. and Pearthree, P.A., 1989. Cenozoic Tectonism in Arizona and its impact on regional landscape evolution, In: Jenney, J. P., and Reynolds, S. J., (eds), *Geologic evolution of Arizona: Tucson, Arizona Geological Society Digest* 17, 649-680.

- Miller, D.M., Nilsen, T.H., and Bilodeau, W.L., 1992, Late Cretaceous to early Eocene geologic evolution of the U.S. Cordillera, *in* Burchfiel, B.C., Lipman, P.W., and Zoback, M.L., eds., *Geology of North America, Cordilleran orogen: Conterminous U.S.*, G-3. 205-260.
- Molnar, P. and England, P., 1990. Late Cenozoic uplift of mountain ranges and global climate change: Chicken or egg?, *Nature*, 346, 29-34.
- Neher, R. E., and Buchanan, W. A, 1980. Soil survey of Luna County, New Mexico, U S Depart. Agri. Soil Conserv. Service, 80 pp.
- New Mexico Office of Resources Trustee, 2012. Final Groundwater Restoration Plan for the Chino, Cobre, and Tyrone Mine Facilities, www.env.nm.gov/wqcc/documents/NMAGExh11.pdf
- Parsons, T., 2006, The Basin and Range Province. *Developments in Geotectonics*, v. 25, p. 277-324.
- Pazzaglia, F.J. and Hawley, J.W., 2004, Neogene (rift flank) and Quaternary geology and geomorphology, *in* Mack, G.H. and Giles, K.A., eds., *The Geology of New Mexico: A Geologic History*, p. 407-437.
- Perry, F.V., Kelley, R.E., Dobson, P.F., and Houseworth, J.E., 2014. Regional geology: a GIS database for alternative host rocks and potential siting guidelines. FCRD-UFD-2014-000068. U.S. Department of Energy, Used Fuel Disposition Campaign, Los Alamos Unlimited Release LA-UR-14-20368, 168p.
- Perry, F.V., Swanson, E., Milazzo, D.M., Bussod, G.Y.A. and Kelley, R.E., 2018. Regional geologic evaluations for disposal of HLW and SNF: alluvial basins of the Basin and Range Province. SFWD-SFWST-2018-000512. U.S. Department of Energy, Used Fuel Disposition Campaign, Los Alamos Unlimited Release LA-UR-18-28909, 46p.
- PFLOTRAN (2019), <https://www.pfлотran.org/>, last accessed June 28, 2019.
- Plume, R.W., 1996. Hydrogeologic Framework of the Great Basin Region of Nevada, Utah, and Adjacent States. U.S. Geological Survey Professional Paper 1409-B, 78 p.
- Ratté, J.C., and Finnell, T.L., 1978. Roadlog from Silver City to Reserve via Glenwood and the Mogollon mining district, In: Chapin, C.E., and Elston, W.E., (eds.), *Field guide to selected cauldrons and mining districts of the Datil-Mogollon volcanic field, New Mexico*, New Mexico Geol. Soc. Spec. Publication 7, 49–64.
- Reeves, C. C., 1969. Pluvial Lake Palomas, northwestern Chihuahua, Mexico, In: Cordoba, D. A., Wengerd, S.A, and Shomaker, J.W. (eds.), *The Border Region: New Mexico Geol. Soc. Guidebook 20*, 143-154.
- Remeikam, P., Fischbein, I.W., and Fischbein, S.A., 1988. Lower Pliocene petrified wood from the Palm Spring Formation, *Rev. Paleobotany Palynology*, 56, pp.30.
- Rinehart, A., Timmons, S., Felix, B. and Pokorny, C., 2015, Groundwater level and storage changes – regions of New Mexico: Technical completion report by the New Mexico Bureau of Geology and Mineral Resources, Socorro NM, 40 p.

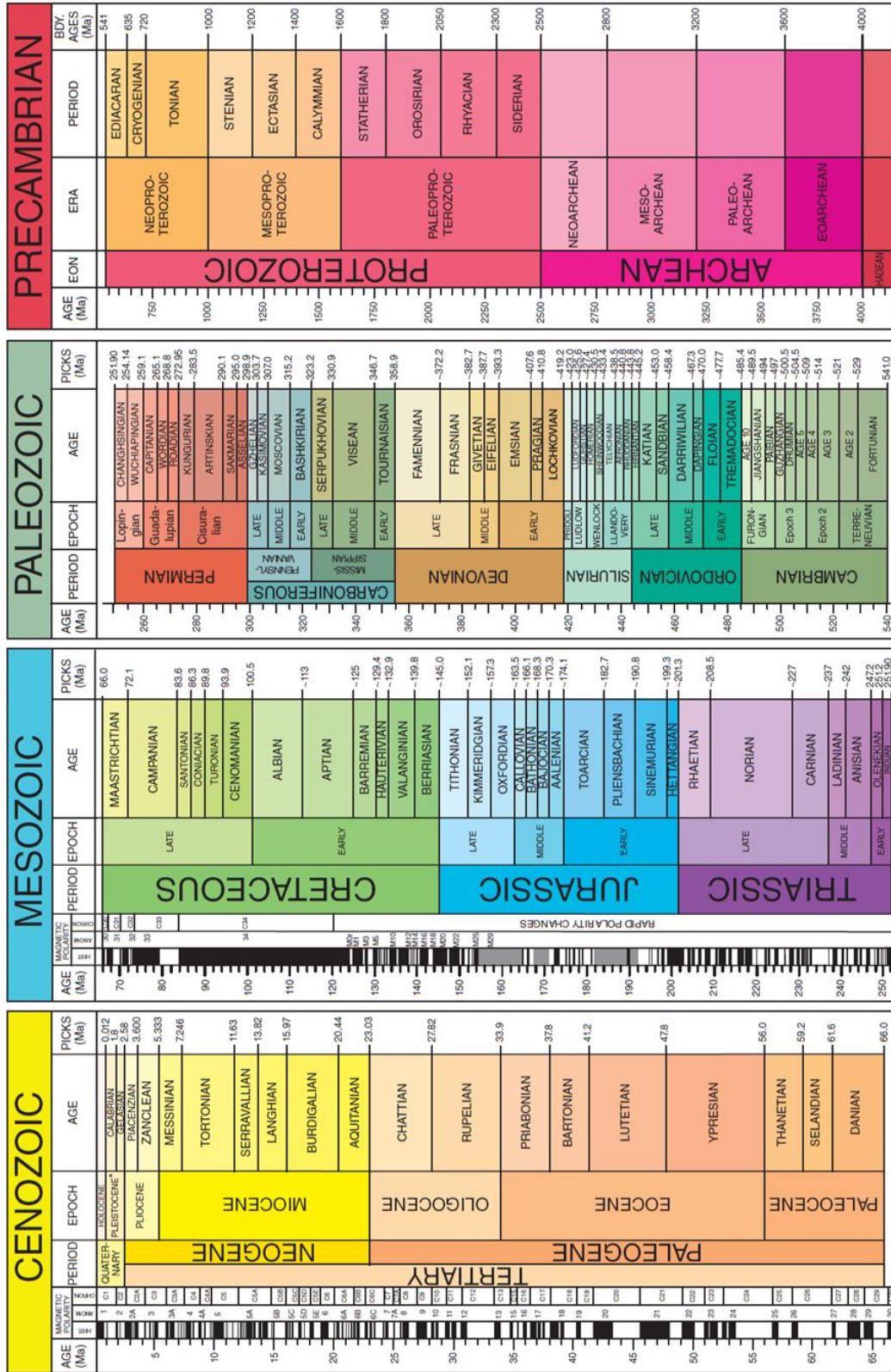
- Saleeby, J., 2003, Segmentation of the Laramide slab—Evidence from the southern Sierra Nevada region: Geological Society of America Bulletin, v. 115, p. 655–668.
- Schwennesen, A.T, 1919. Geology and water resources of the Gila and San Carlos Valleys in the San Carlos Indian Reservation, Arizona, In: Grover, N.C., Contribution to the Hydrology of the United States, 1919, 1-27.
- Seager, W.R., 1995, Geology of southwest quarter of Las Cruces and northwest El Paso 1° x 2° sheets (scale 1:125,000), New Mexico: New Mexico Bureau of Mines & Mineral Resources Geologic Map GM-60.
- Seager, W.R., Clemons, R.E., Hawley, J.W. and Kelley, R.E., 1982, Geology of northwest part of Las Cruces 1° x 2° sheets (scale 1:125,000), New Mexico: New Mexico Bureau of Mines & Mineral Resources Geologic Map GM-53.
- Sentis, M.L., Gable, C.W., Coupling LaGrit unstructured mesh generation and model setup with TOUGH2 flow and transport: A case study, Computers & Geosciences, 2017, DOI:doi.org/10.1016/j.cageo.2017.06.012.
- Seager, W.R., Hawley, J. W., Kottowski, F. E. and Kelley, S. A., 1987. Geology of the east half of Las Cruces and northeast El Paso 1° x 2° quad., New Mexico, New Mexico Bur. Min. Mineral Res., Geol. Map GM-57, scale 1:125,000.
- Sevougian, S.D., Stein, E.R., LaForce, T., Perry, F.V., Lowry, T.S., Cunningham, L.J., Nole, M., Haukwa, C.B., Chang, K.W., and Mariner, P.E., 2019, GDSA Repository Systems Analysis Progress Report. M2SF-19SN010304051 SAND2019-5189 R.
- Shafiqullah, M., Damon, P.E., Lynch, D.J., Reynolds, S.J., Rehrig, W.A, and Raymond, R.H., 1980. K-Ar geochronology and geologic history of southwestern Arizona and adjacent areas: Arizona Geological Society Digest, 12, 201-260.
- Smith, G. A., 1994. Climatic influences on continental deposition during late-stage filling of an extensional basin, southeastern Arizona, Geol. Soc. Am. Bull., 106, 1212-1228.
- Smyth, J.R., Crowe, B.M., Halfeck, P.M., Reed, A.W., 1979. A Preliminary Evaluation of the Radioactive Waste Isolation Potential of the Alluvium-Filled Valleys of the Great Basin. U.S. Department of Energy, Los Alamos Scientific Laboratory, Los Alamos Informal Report LA-7962-MS, 26 p.
- Stauffer, P.H., K.C. Lewis, J.S. Stein, B.J. Travis, P. Lichtner and G.A. Zyvoloski, (2014), Joule-Thomson Effects on the Flow of Liquid Water, Transport in Porous Media, Vol. 105 (3), December 2014. DOI 10.1007/s11242-014-0379-3.
- Stone, P. H., 1984. Climate Processes and Climate Sensitivity, Geophys. Monogr. 29, 6-17.
- Sweetkind, D.S., Masbruch, M.D., Heilweil, V.M., Buto, S.G., 2010a. Groundwater Flow. U.S. Geological Survey Scientific Investigations Report 2010-5193, Chapter C, in Heilweil, V.M., and Brooks, L.E., eds., 2011. Conceptual model of the Great Basin carbonate and alluvial aquifer system: U.S.

- Geological Survey Scientific Investigations Report 2010-5193, 191 p.
<http://pubs.usgs.gov/2010/5193>
- Sweetkind, D.S., Cederberg, J.R., Masbruch, M.D., V.M., Buto, S.G., 2010b. Hydrogeologic Framework. U.S. Geological Survey Scientific Investigations Report 2010-5193, Chapter B, in Heilweil, V.M., and Brooks, L.E., eds., 2011. Conceptual model of the Great Basin carbonate and alluvial aquifer system: U.S. Geological Survey Scientific Investigations Report 2010-5193, 191 p.
<http://pubs.usgs.gov/2010/5193>
- Thompson, J. C., and Morgan, G. S., 2001. Late Pleistocene mammalian fauna and environments of the Sandia mountains, New Mexico, *Cur. Res. Pleistocene*, 18, 113-115.
- Thompson, S., 3rd., 1977, Geology, petroleum source rocks, and thermal metamorphism in KCM No. 1 Forest Federal well, Hidalgo County, New Mexico: Socorro, New Mexico Bureau of Mines and Mineral Resources Circular 152, 62 p.
- Thompson, S. 3rd, Tovar, R.J.C. and Conley, J.N., 1978, Oil and gas exploration wells in the Pedregosa Basin: New Mexico Geological Society 29th Annual Fall Field Conference Guidebook, p. 331-342.
- Thomas, J.M., Carlton S.M., and Hines L.B., 1989. Ground-water hydrology and simulated effects of development in Smith Creek valley, a hydrologically closed basin in Lander County, Nevada. Professional Paper 1409-E. <https://pubs.er.usgs.gov/publication/pp1409E>
- Trauger, F.D., 1965. Geologic structure pattern of Grant County, New Mexico. *In: Southwestern New Mexico II*, Fitzsimmons, J. P., Balk, C. L. [eds.], New Mexico Geological Society 16th Annual Fall Field Conference Guidebook, 184-187.
- Trauger, F.D., 1972. Water resource and general geology of Grant County, New Mexico, New Mexico Bur. Mines Min. Res., Hydrol. Report 2, 211 p.
- Trauger, F.D., and Lavery, N.G., 1976, Geohydrology of the Upper Pipe Line Draw Area, Grant County, New Mexico: Consultant report to Exxon Company, U.S.A., April 1976, 48 p.
- Wahba, G. 1990. Spline models for Observational data. Paper presented at CBMS-NSF Regional Conference Series in Applied Mathematics. Philadelphia: Soc. Ind. Appl. Maths.
- Wernicke, B.P., 1992. Cenozoic extensional tectonics of the U.S. Cordillera, In: Burchfiel, B.C., Lipman, P.W., and Zoback, M.L., [eds], *The Cordilleran Orogen: Conterminous U.S.: Boulder*, Geol. Soc. Am., 3, 553pp.
- Wernicke, B., Axen, G.J. and Snow, J.K., 1988, Basin and Range extensional tectonics at the latitude of Las Vegas, Nevada: *Geological Society of America Bulletin*, v. 100, p. 1738-1757.
- Wernicke, B., and Snow, J. K., 1998. Cenozoic tectonism in the central Great Basin and Range: Motion of the Sierran-Great Valley Block, *Int. Geol. Rev.*, 40, 403–410.

- Whitmeyer, S.J. and Karlstrom, K.E., 2007, Tectonic model for the Proterozoic growth of North America: *Geosphere*, v. 3, p. 220-259.
- Winograd, I.J., 1981. Radioactive Waste Disposal in Thick Unsaturated Zones. *Science, New Series* 212, 1457-1464 p.
- Winograd, I.J., Szabo, B.J., Coplen, T.B., Riggs, A.C., and Kolesar, P.T., 1985. 2 million year record of deuterium depletion in Great Basin ground waters, *Science*, 227, 519–522.
- Wolfe, J.A., and Hopkins, D.M., 1967. Climatic changes recorded by Tertiary land floras in northwestern northwestern North America, In: *Tertiary correlations and climatic changes in the Pacific*, Pacific Sci. Cong., 11th, Tokyo, 1966, 67-76.
- Wolfe, J.A., 1971. Tertiary climatic fluctuations and methods of analysis of Tertiary floras. *Palaeogeogr., Palaeo-climatol., Palaeoecol.* 9, 27-57.
- Vorocrust, (2019), <https://ip.sandia.gov/technology.do/techID=208>, last accessed April 5, 2019.
- Zyvoloski, G.A., B.A. Robinson, Z.V. Dash, S. Kelkar, H.S. Viswanathan, R. J. Pawar, P. H. Stauffer, T. A. Miller, S. Chu, 2015. Software Users Manual (UM) for the FEHM Application Version 3.1 - 3.X, Los Alamos National Laboratory document LA-UR-12-24493.
- Zyvoloski, G.A., Vesselinov, V.V., 2006, An investigation of numerical grid effects in automated calibration: *Ground Water*, v.44, p.814-825.

11 Appendix 1 – Geological Time Scale

GSA GEOLOGIC TIME SCALE v. 5.0



12 Appendix 2 – File Format for Exporting Data from Structural Cross-Sections to JewelSuite.

Well Description File for Structural Cross Section #2:

WellID	UWI	Northing	Easting	TVDSS	DFE	MD	Inclination	Azimuth
2-50000	2-50000	3567830	257559	-1281.21	1281.21	0	0	0
2-50000	2-50000	3567830	257559	5000	1281.21	6281.21	0	0
2-48000	2-48000	3568370	255634	-1317.04	1317.041	0	0	0
2-48000	2-48000	3568370	255634	5000	1317.041	6317.041	0	0
2-46000	2-46000	3568920	253710	-1410.38	1410.38	0	0	0
2-46000	2-46000	3568920	253710	5000	1410.38	6410.38	0	0
2-44000	2-44000	3569460	251785	-1289.96	1289.96	0	0	0
2-44000	2-44000	3569460	251785	5000	1289.96	6289.96	0	0
2-42000	2-42000	3570000	249860	-1293.31	1293.31	0	0	0
2-42000	2-42000	3570000	249860	5000	1293.31	6293.31	0	0
2-40000	2-40000	3570550	247935	-1297.31	1297.31	0	0	0
2-40000	2-40000	3570550	247935	5000	1297.31	6297.31	0	0
2-38000	2-38000	3571090	246010	-1302.71	1302.71	0	0	0
2-38000	2-38000	3571090	246010	5000	1302.71	6302.71	0	0
2-36000	2-36000	3571630	244086	-1308.4	1308.4	0	0	0
2-36000	2-36000	3571630	244086	5000	1308.4	6308.4	0	0
2-34000	2-34000	3572180	242161	-1314.4	1314.4	0	0	0
2-34000	2-34000	3572180	242161	5000	1314.4	6314.4	0	0
2-32000	2-32000	3572720	240236	-1320.81	1320.81	0	0	0
2-32000	2-32000	3572720	240236	5000	1320.81	6320.81	0	0
2-30000	2-30000	3573260	238311	-1323.84	1323.84	0	0	0
2-30000	2-30000	3573260	238311	5000	1323.84	6323.84	0	0
2-28000	2-28000	3573810	236386	-1334.57	1334.57	0	0	0
2-28000	2-28000	3573810	236386	5000	1334.57	6334.57	0	0
2-26000	2-26000	3574350	234462	-1339.43	1339.43	0	0	0
2-26000	2-26000	3574350	234462	5000	1339.43	6339.43	0	0
2-24000	2-24000	3574890	232537	-1346.76	1346.8	0	0	0
2-24000	2-24000	3574890	232537	5000	1346.8	6346.76	0	0
2-22000	2-22000	3575440	230612	-1351.61	1351.61	0	0	0
2-22000	2-22000	3575440	230612	5000	1351.61	6351.61	0	0
2-20000	2-20000	3575980	228687	-1356.91	1356.91	0	0	0
2-20000	2-20000	3575980	228687	5000	1356.91	6356.91	0	0
2-18000	2-18000	3576520	226762	-1360.51	1360.51	0	0	0
2-18000	2-18000	3576520	226762	5000	1360.51	6360.51	0	0
2-16000	2-16000	3577070	224838	-1365.81	1365.81	0	0	0
2-16000	2-16000	3577070	224838	5000	1365.81	6365.81	0	0
2-14000	2-14000	3577610	222913	-1371.79	1371.79	0	0	0
2-14000	2-14000	3577610	222913	5000	1371.79	6371.79	0	0

Formation Top File for Structural Cross Section #2:

Well	Lith	TVDSS	DFE	MD
2-50000	Top Alluvium	-1281.21	1281.21	0.00
2-50000	Top Tertiary Volcanics	-1110.00	1281.21	171.21
2-50000	Top Paleozoic	150.00	1281.21	1431.21
2-50000	Top Precambrian	875.00	1281.21	2156.21
2-48000	Top Alluvium	-1317.04	1317.04	0.00
2-48000	Top Tertiary Volcanics	-1267.47	1317.04	49.57
2-48000	Top Paleozoic	-100.00	1317.04	1217.04
2-48000	Top Precambrian	620.00	1317.04	1937.04
2-46000	Top Tertiary Volcanics	-1410.38	1410.38	0.00
2-46000	Top Paleozoic	-300.00	1410.38	1110.38
2-46000	Top Precambrian	390.00	1410.38	1800.38
2-44000	Top Alluvium	-1289.96	1289.96	0.00
2-44000	Top Tertiary Volcanics	0.00	1289.96	1289.96
2-44000	Top Precambrian	800.00	1289.96	2089.96
2-42000	Top Alluvium	-1293.31	1293.31	0.00
2-42000	Top Tertiary Volcanics	-120.00	1293.31	1173.31
2-42000	Top Paleozoic	1900.00	1293.31	3193.31
2-42000	Top Precambrian	2500.00	1293.31	3793.31
2-40000	Top Alluvium	-1297.31	1297.31	0.00
2-40000	Top Tertiary Volcanics	-315.00	1297.31	982.31
2-40000	Top Paleozoic	1780.00	1297.31	3077.31
2-40000	Top Precambrian	2400.00	1297.31	3697.31
2-38000	Top Alluvium	-1302.71	1302.71	0.00
2-38000	Top Tertiary Volcanics	90.00	1302.71	1392.71
2-38000	Top Paleozoic	2040.00	1302.71	3342.71
2-38000	Top Precambrian	2300.00	1302.71	3602.71
2-36000	Top Alluvium	-1308.40	1308.40	0.00
2-36000	Top Tertiary Volcanics	0.00	1308.40	1308.40
2-36000	Top Paleozoic	1940.00	1308.40	3248.40
2-36000	Top Precambrian	2620.00	1308.40	3928.40
2-34000	Top Alluvium	-1314.40	1314.40	0.00
2-34000	Top Tertiary Volcanics	-150.00	1314.40	1164.40
2-34000	Top Paleozoic	1875.00	1314.40	3189.40
2-34000	Top Precambrian	2500.00	1314.40	3814.40
2-32000	Top Alluvium	-1320.81	1320.81	0.00
2-32000	Top Tertiary Volcanics	-200.00	1320.81	1120.81
2-32000	Top Paleozoic	1800.00	1320.81	3120.81
2-32000	Top Precambrian	2400.00	1320.81	3720.81
2-30000	Top Alluvium	-1323.84	1323.84	0.00
2-30000	Top Tertiary Volcanics	-250.00	1323.84	1073.84
2-30000	Top Paleozoic	1790.00	1323.84	3113.84
2-30000	Top Precambrian	2350.00	1323.84	3673.84
2-28000	Top Alluvium	-1334.57	1334.57	0.00
2-28000	Top Tertiary Volcanics	-300.00	1334.57	1034.57
2-28000	Top Paleozoic	1700.00	1334.57	3034.57
2-28000	Top Precambrian	2250.00	1334.57	3584.57
2-26000	Top Alluvium	-1339.43	1339.43	0.00
2-26000	Top Tertiary Volcanics	-380.00	1339.43	959.43
2-26000	Top Paleozoic	1650.00	1339.43	2989.43
2-26000	Top Precambrian	2190.00	1339.43	3529.43
2-24000	Top Alluvium	-1346.76	1346.76	0.00
2-24000	Top Tertiary Volcanics	-430.00	1346.76	916.76
2-24000	Top Paleozoic	1600.00	1346.76	2946.76
2-24000	Top Precambrian	2100.00	1346.76	3446.76
2-22000	Top Alluvium	-1351.61	1351.61	0.00
2-22000	Top Tertiary Volcanics	-525.00	1351.61	826.61
2-22000	Top Paleozoic	600.00	1351.61	1951.61
2-22000	Top Precambrian	1050.00	1351.61	2401.61
2-20000	Top Alluvium	-1356.91	1356.91	0.00
2-20000	Top Tertiary Volcanics	-1300.00	1356.91	56.91
2-20000	Top Paleozoic	410.00	1356.91	1766.91
2-20000	Top Precambrian	1025.00	1356.91	2381.91
2-18000	Top Alluvium	-1360.51	1360.51	0.00
2-18000	Top Tertiary Volcanics	-1300.00	1360.51	60.51
2-18000	Top Paleozoic	450.00	1360.51	1810.51
2-18000	Top Precambrian	1100.00	1360.51	2460.51
2-16000	Top Alluvium	-1365.81	1365.81	0.00
2-16000	Top Tertiary Volcanics	-1330.00	1365.81	35.81
2-16000	Top Paleozoic	450.00	1365.81	1815.81
2-16000	Top Precambrian	1100.00	1365.81	2465.81
2-14000	Top Alluvium	-1371.79	1371.79	0.00
2-14000	Top Tertiary Volcanics	-1310.00	1371.79	61.79
2-14000	Top Paleozoic	400.00	1371.79	1771.79
2-14000	Top Precambrian	1050.00	1371.79	2421.79